UAB
Universitat Autònoma de Barcelona

Department of Microelectronics and Electronic Systems

Implementation of high-resolution MRSI methods in a pre-clinical scanner, and optimization for brain longitudinal studies of therapy response in mice glioma models

PhD Thesis in Electronic and Telecommunication Engineering

by

ZOONA JAVED

Thesis advisors:
Dr. Silvia Lope Piedrafita and Prof. Carles Arús Caraltó
Servei de Ressonància Magnètica Nuclear & Departament de Bioquímica i Biologia Molecular
Universitat Autònoma de Barcelona

Tutor
Dr. Francesc Serra Graells

JUNE 2023

Dissertation presented By

Zoona Javed

Submitted for the PhD degree in Electronic and Telecommunication Engineering at the

Universitat Autònoma de Barcelona

Of the Doctoral Program in

Department of Microelectronics and Electronic Systems

Supervised By

Signature of the Supervisors

Dr.Silvia Lope Piedrafita	**Prof. Carles Arús Caraltó**

Signature of Tutor

Dr. Francesc Serra Graells

Signature of PhD Thesis Author

Zoona Javed

Cerdanyola del Valles, June 2023

In the name of Allah most Beneficient Most Merciful [Al Quran]

DEDICATION

This thesis is dedicated to the unwavering support of my husband, who stood by me through thick and thin, my twin daughters Zimal and Emaan, whose love and sacrifices have been the foundation upon which I built my dreams, to my mother and father, whose prayers and words of wisdom have supported me through challenging times and to my late son, whose presence will always be missed.

Contents

List of Figures

List of Tables

ABSTRACT

Magnetic resonance spectroscopy and magnetic resonance spectroscopic imaging (MRS/MRSI) are non-invasive diagnostic techniques that use a strong magnetic field and radio waves to examine the chemical composition of living tissue. Working on the same principles as Magnetic Resonance Imaging (MRI), instead of producing images, MRS generates a spectrum of signals that can be used to identify the type and amount of molecules present in a tissue. The utility of MRS and MRSI has already been established in many studies, providing useful information about the chemical makeup of different regions of the brain, and allowing diagnosis of conditions such as Alzheimer's disease, multiple sclerosis, and brain Glioblastoma (GB) tumors.

Preclinical glioblastoma studies looking forward to improving therapeutic outcomes are necessary since clinical GB has no current cure. These studies can greatly benefit from improved spatial resolution and homogeneity of the acquired MRSI grids. Hence, we can work towards improved acquisition schemes enhancing the quality of acquired data using MRS and MRSI. There exists a methodological consensus among spectroscopy experts where the Localized Adiabatic Spin Echo Refocused (semiLASER) data acquisition strategy has been ranked as the most likely localization technique to improve (pre) clinical MRS. SemiLASER uses adiabatic pulses to selectively excite and refocus the signal from a localized volume of interest in the brain. This results in a higher signal-to-noise ratio (SNR) and better spatial resolution compared to conventional data acquisition sequences.

Partial volume effects can occur in MRSI when the voxel (a 3D volume of interest) being measured contains a mixture of different neighbouring tissue types or compartments, such as grey and white matter or cerebrospinal fluid. This can lead to inaccurate quantification of metabolites, as the signal from one tissue can mix with the signal from another and affect overall pattern recorded. SemiLASER is designed to minimize partial volume effects by using adiabatic pulses to selectively excite and refocus the signal from a small region of interest within the voxel. This allows for more accurate quantification of metabolites within the region of interest, while reducing the contamination of the signal by other tissue types. In addition, semiLASER also employs an outer-volume suppression (OVS) technique to further reduce contamination from outside the region of interest. This involves using additional adiabatic pulses to selectively saturate the signal from outside the volume of interest, so that it does not contribute to the MRSI signal. Overall, the combination of selective excitation and OVS in semiLASER can help improve the accuracy of MRSI measurements and reduce partial volume effects.

Although, the clinical utility of semiLASER has been acknowledged, the pre-clinical use and implementation of semiLASER still remains a less explored area. Our group has a long record of using MRSI in therapy response monitoring of a murine model glioblastoma (the GL261 cell line) using a commercially available MRSI acquisition sequence. In our efforts towards bridging the barriers between pre-clinical and clinical research, we have implemented the clinically verified semiLASER sequence on a pre-clinical 7T Bruker Biospec USR scanner running the ParaVision 5.1 software package, which provides a graphical user interface for sequence programming and data acquisition. The single and multi-voxel semiLASER sequences were implemented with the idea that the developments generated during this PhD project will be replicable by other interested users.

The implemented SV-semiLASER and MRSI-semiLASER sequences for preclinical acquisitions were optimised to perform high resolution MRSI of living mouse brain. For this, sequences were duly verified and tested first in phantoms and later in-vivo, in wild-type (wt) and tumor bearing (GL261) mice. To do so, the Bruker pulse sequence implementation was first studied in detail to become familiar with the Bruker programming environment and a test sequence PRESS_Slice to

localize the slice dimension was developed by modifying the Bruker stock PRESS sequence for single voxel localization. After careful evaluation of test sequence results, the semiLASER single and multi-voxel sequences were also implemented using a similar strategy. The implemented SV-semiLASER sequence provided a ca. 1.4-fold improvement in SNR in phantoms and ca. 1.3-fold improvement in SNR for in-vivo subjects, in comparison to the stock Bruker PRESS (single volume acquisition) sequence. The MRSI-semiLASER sequence resulted in a ca. 1.2-1.3-fold improvement of SNR in phantoms and in-vivo subjects compared to the stock Bruker CSI-PRESS sequence. Combined with phase encoding strategies and volume reduction methods, higher spatial resolution and SNR was achieved for the implemented MRSI-semiLASER. The quantification analysis of the results was done using MATLAB based post-processing tools specially designed to process Bruker datasets and solutions for a faster post processing pipeline were proposed. The single voxel MRSI-semiLASER sequences were further simulated using NMRSCOPE-B virtual simulator, a jMRUI plug-in which positively correlated with the experimental results. Preliminary nosological images obtained using MRSI-semiLASER datasets and the SpectraClassifier tool previously developed in our group, and trained with GL261 tumors using already available CSI-PRESS data, suggested those classifiers could be robust enough to recognize the tumor region acquired with the semi-LASER sequence. Still, classifiers may require retraining for the evaluation of response to therapy, which is an ongoing project within the group.

List of Abbreviations

ACQ	Acquisition
AFP	Adiabatic full-passage
BW	Bandwidth
Cho	Choline
CPU	Central Processing Unit
Cr	Creatine
CH3	Methyl group
CSDE	Chemical Shift Displacement Error
CSI	Chemical Shift Imaging
CV	Coefficient of Variance
D2O	Deuterium Oxide
FASTMAP	Fast Automatic Shimming Technique by Mapping Along Projections
FE	Frequency encoding
FID	Free Induction Decay
FOV	Field of View
FWHM	Full-width at half-maximum
GB	Glioblastoma
GOIA	Gradient offset independent adiabatic
GUI	Graphical User Interface
HS	Hyperbolic secant
jMRUI	Java-based Magnetic Resonance User Interface
LASER	Localization by Adiabatic Selective Refocusing
Lac	Lactate
LB	Line broadening
LW	Linewidth in Hz
µ $\bar{x}$	Mean of means
MI	Myo-inositol
ML	NMR-visible mobile lipids
MM	Macromolecules
MRI	Magnetic Resonance Imaging
MRS	Magnetic Resonance Spectroscopy
MRSI	Magnetic Resonance Spectroscopy Imaging
MSME	Multi-spin Multi echo
NA	Number of Accumulations
NAA	N-Acetyl Aspartate
NMR	Nuclear Magnetic Resonance
Npoints	Number of datapoints
OVS	Outer Volume Suppression
PCr	Phosphocreatine
PE	Phase encoding
p.i.	post inoculation
Ppg	Pulse program
ppm	Parts-per-million
PRESS	Point Resolved Spectroscopy
PSF	Point Spread Function

PV	ParaVision
PVM	ParaVision method
RARE	Rapid Acquisition with Relaxation Enhancement
RF	Radio Frequency
RG	Receiver Gain
RMSD	Root Mean Square Deviation
ROI	Region of Interest
Rx	Receiver
Sech	Hyperbolic secant
SNR	Signal to noise ratio
SRF	Spatial response function
std	Standard deviation
SV	Single voxel
SVS	Single voxel Spectroscopy
SW	Spectral Width
TAT	Total Acquisition Time
TRI	Tumor Response Index
TE	Echo time
TR	Repetition time
TSP	Trimethylsilyl propionate
T2w	T2 weighted
Tx	Transmitter
VAPOR	Variable Power RF pulses with Optimized Relaxation delay
VOI	Volume of Interest
wt	Wild Type

Acknowledgements

Thesis Overview

This PhD work was developed under the framework of the Horizon 2020 action MSCA-ITN-ETN (European Training Networks) and **H2020-MSCA-ITN-2018** call. The project name is "**Integrating Magnetic Resonance Spectroscopy and Multimodal Imaging for Research and Education in Medicine**" (INSPIRE-MED), grant agreement number 813120, from January 1st, 2019, to June 30th, 2023. My PhD research project is enclosed in WP1 of INSPIRE-MED: "Next generation methodology for enhanced MRS(I) in (pre-)clinical research and use". The goal of this project was to develop and evaluate next generation high-speed MRSI methods for pre-clinical use.

This thesis document is organized into five main chapters.

Chapter 1 introduces a technical description of the fundamental concepts of MRS and MRSI that constitute the bases of this thesis. The reader is guided through the basic theoretical knowledge of MRS/MRSI acquisitions as well as a comprehensive description of programming in the Bruker ParaVision 5.1 environment on a 7T Bruker Biospec 70/30 USR preclinical scanner.

Chapter 2 presents the motivation and objectives of the work.

Chapter 3 provides an overview of the general materials and methods which encompass the data collection techniques and methods. The acquisition parameters for in-vivo and in-vitro experiments are recorded and the quantifying parameters and analysis tools are elaborated.

Chapter 4 contains all the experiments performed and results obtained during the PhD duration and is hence the core of this thesis consisting of six subchapters. All these subchapters contain the individual experiments and results performed for a certain goal.

Sub-chapter 4.1 presents the studies and results for a test single slice sequence called PRESS_Slice. This sequence was developed on the 7T Bruker Biospec running ParaVision 5.1 by modifying the stock Bruker PRESS sequence. The main motivation for the development of this sequence was to improve understanding of Bruker pulse sequence programming environment and gain command over the sequence implementation techniques. These goals were successfully achieved.

Sub-chapter 4.2 describes a short study performed to evaluate the prepared phantom solutions using the 300MHz High Resolution NMR spectrometer installed at the *Servei de Ressonància Magnètica Nuclear* (SeRMN) of UAB. The purpose of this study was to validate the preparation of reproducible and reliable phantoms, which can help validate in-vitro the PhD work implemented sequences on the Bruker Biospec scanner.

In sub-chapter 4.3, the implementation of the single voxel semiLASER pulse sequence, which was developed on a 7T Bruker BioSpec 70/30 USR spectrometer running ParaVision 5.1, is discussed. The main goal of this sequence implementation was to provide alternative and higher Signal-to-noise ratio (SNR) single voxel magnetic resonance spectroscopy acquisitions in wt mouse and tumor models. This chapter guides the reader through the steps and challenges faced in sequence implementation and their solutions, the verification tests for evaluation of the implemented sequence and the improved results obtained both in-vivo and in-vitro experiments.

After having verified the semiLASER sequence for single voxel, the semiLASER technique was extended to multi-voxel acquisitions reported in sub-chapter 4.4. This subchapter studies the

improvements in spatial resolution, SNR and homogeneity in phantom and in-vivo applications using the implemented MRSI-semiLASER sequence.

Sub-chapter 4.5 focuses on the various MATLAB based post processing tools which were developed during the course of the PhD project. A new approach to optimize the existing pipeline for post processing of MRSI data acquisitions have also been proposed in this chapter.

Sub-chapter 4.6 describes the simulations for the SV-PRESS and SV-semiLASER pulse sequences using the NMS-SCOPE B jMRUI plug-in. This work was performed as part of the secondment which took place at the Department of Magnetic Resonance and Cryogenics, Institute of Scientific Instruments of the Czech Academy of Sciences, under the supervision of Dr Zenon Starčuk and Dr Jana Starčukova in Brno (Czech Republic) from 9th to 21st October 2022.

Chapter 5 presents a global discussion of all results and observations and some possible avenues for future work.

Finally, Chapter 6 lists the main conclusions of this PhD thesis work.

The scientific contributions and the publications derived from this thesis are also listed in chapter 6, followed by the bibliography section.

The steps required for adiabatic pulse shape generation for refocusing pulses in ParaVision 5.1 using the TOPSPIN stdisp tool are described in appendix A. The MATLAB scripts for single and multi-voxel Bruker data post processing are included in APPENDIX B. The implemented SV-semiLASER and MRSI-semiLASER sequence codes and method modifications are provided in APPENDIX C. The MRSI-semiLASER acquisition protocol is given in APPENDIX D.

Chapter 1: Introduction to MRS/MRSI and Bruker Pulse Programming

Nuclear Magnetic Resonance spectroscopy and imaging (MRS/MRSI) [1] are completely non-invasive methods that can be used to study metabolic brain disorders and enable the simultaneous imaging and quantification of metabolites inside a tissue. For example, ^{1}H MRSI helps in the detection of metabolic changes caused by tumors, MS lesions, epilepsy and other neurodegenerative diseases and hence finds applications in both research and preclinical diagnosis [2]. Animal models of human brain tumors [3] have been developed to facilitate the studies of tumor characterization, progression and response to therapy. Previous studies have shown associations between regionally altered N-Acetyl Aspartate (NAA) and Lactate (Lac) concentrations in the presence of abnormal glial cells. In addition, associations between altered concentrations of Choline and Creatine (Cho/Cr ratio) have also been reported [4]. Hence, these techniques can be used to closely observe the metabolic changes occurring as a result of disease and therefore, serve as an efficient diagnosis tool for therapy response monitoring in mouse glioma models.

MRSI uses a sequence of radio-frequency (RF) and magnetic field gradient pulses to measure chemical shift distribution across an, usually, rectangular grid (voxel). The signal is measured in time domain but visualized in the frequency domain in the form of a spectrum. The major disadvantages of MRSI include long acquisition times (in the order of 20-40 minutes and up to 60-80 minutes for 3D acquisitions), lack of adequate signal-to-noise ratio (SNR), insufficient water and lipid suppression and limited spatial coverage; which pose major constraints and limitations in the acquisition and processing of spectroscopic data [5]. Moreover, these problems get even more pronounced in mouse brain studies due to small size of the mouse brain and low spatial resolution.

In preclinical research MRS/MRSI applications, there is a great desire to attain high spatial resolution in a short measurement time, and at the same time with large brain coverage. However, in terms of these factors, there are limits to what is technically possible while ensuring the measurement remains reliable. MRSI methods in particular would greatly benefit from a reduction in scan-time and an increase in spatial resolution, in order to become more viable in preclinical environments.

This introduction chapter provides a technical description of the fundamental concepts of MRS and MRSI that constitute the bases of this thesis.

1. A brief background of Nuclear Magnetic Resonance (NMR) Spectroscopy

NMR (Nuclear Magnetic Resonance) technologies have revolutionized many fields, including chemistry, physics, and medicine. MR spectroscopy and MR imaging are similar techniques both of which have originated from NMR. The principle of NMR was first described in 1946 by Edward Purcell [6], who was a Nobel prize Laureate from Harvard University and Felix Bloch [7] of Stanford University, simultaneously. Back then, NMR was only used by physicists in order to determine the magnetic time moment of atomic nuclei. The in-vivo use of NMR started much later in the mid-1970's after Lauterbur [8], Mansfield and Grannell [9] applied gradients into the magnetic field, hence determining the spatial localization of the signal and generating MR images. In vivo NMR was renamed MR imaging since the word 'nuclear' led to negative associations and for the very reason, NMR spectroscopy used in vivo is now called Magnetic Resonance Spectroscopy. The first MR imaging Medical scanner was introduced in the 1980's. During the 1980s and 90s MRI technology evolved with the development of stronger magnets, faster acquisitions and better images. MRI has become a useful medical tool for diagnosing

tissue and organ abnormalities and to monitor many conditions. Its non-invasiveness and ability to provide detailed tissue arquitecture and function information make it an important tool in medical imaging.

Over the past two decades, MRI technology has continued to evolve with advances in hardware, and software. High-field MRI scanners with a magnetic field of 3 Tesla or higher are becoming more common, providing better images and faster scan times. New measurements such as diffusion tensor imaging (DTI) and magnetic resonance spectroscopy (MRS) have expanded the potential of MRI to examine the link between brain and metabolism.

An MR scanner consists mainly of a magnet that creates the fixed magnetic field B_0, Gradient coils, radio frequency (RF) coils, and a computer system. The magnetic flux density of the scanner magnet is measured in Tesla (T). The MR scanner uses three orthogonal linear gradients to obtain spatial localization of the MR signal. These gradients are produced by coils mounted on a cylindrical insert placed within the magnet bore parallel to the main magnetic field. In the case of a cylindrical magnet, the z-axis lies in the direction of the bore, the top–bottom direction is the y axis and the right–left direction is the x-axis. Contrary to the main magnetic field B_0, these additional fields are not active continuously, but switch on and off in short, well-controlled gradient pulses. The fast switching of these coils inside the B_0 field generates strong forces on the coils and hence produces the loud noise associated with MRI examinations.

The RF system comprises of the transmitter and receiver coils. The transmitter is used to generate pulses of current matching the Larmor frequency of resonance (see section 1.1.1). On the application of this current at the transmitter coil an alternating field is generated. The receiver coil detects the MR signal. The reconstruction and post processing of the signal for acquiring the MR image is performed in the computer system. It also contains the data acquisition and post processing consoles.

In this section, we will discuss some major ingredients of NMR acquisitions.

1.1.1   NMR Signal

The phenomenon of NMR occurs when nuclei which have spin (such as protons, ^{1}H) placed in a static magnetic field (B_0, usually applied in the z-direction), are subjected to a second oscillating electromagnetic field in the form of radio frequency radiation, which causes the nuclei to absorb energy (resonate). In the presence of a magnetic field, B_0, there will be a macroscopic net magnetization, M_0, parallel to B_0. This is known as the equilibrium state. When an RF pulse at the Larmor (resonance) frequency (ω) is applied in an orthogonal direction to B_0, the magnetization will flip to the transverse plane and hence the excitation of the spins occurs. Once rotated away from the z axis, M_0 precesses about B_0 with an angular frequency equal to the Larmor frequency (ω) which can be expressed in angular frequency units (radians/sec) as $\omega_0 = \gamma B_0$ where γ is the gyromagnetic ratio (27×10^7 rads^{-1} for ^{1}H). The oscillating magnetization induces a current in a receiver coil located in the transverse plane: the NMR signal or "Free Induction Decay" (FID). The FID or free induction decay is the time domain representation of an MRS signal. Figure 1.1.1 shows a schematic representation of the FID acquisition process.

Plotting detected current as a function of time gives a sinusoidal wave. This wave decays with time due to relaxation processes.

To visualize the information obtained by an FID, a spectrum is obtained which is the Fourier transformed frequency domain representation of an NMR signal. Proton NMR spectra yield a great deal of information about molecular structure because most organic molecules contain many hydrogen atoms, and the hydrogen atoms absorb energy of different wavelengths depending on their nuclear/bonding environment. A spectrum can be represented by equation 1.1;

$$F(\omega)= \int_{-\infty}^{\infty} f(t)e^{-i\omega t} \, dt \qquad \text{[1.1]}$$

Where ω is the Larmor frequency, t is time.
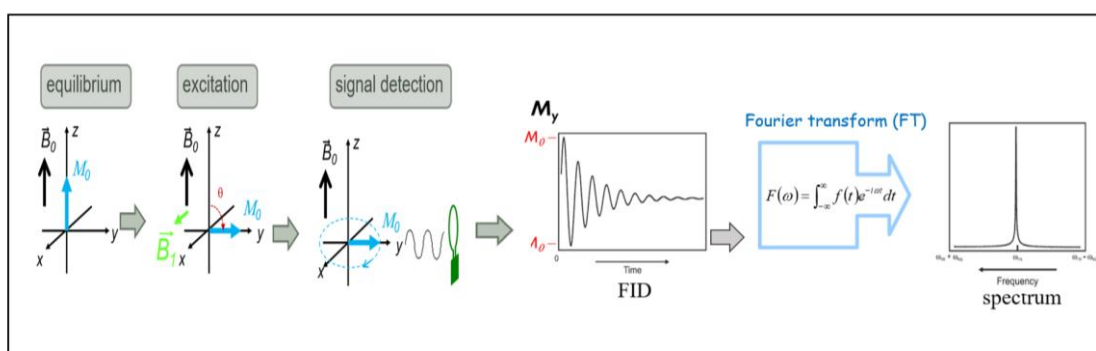
Figure 1.1.1 NMR signal generation

1.1.2   NMR Spectral Characteristics

The most important piece of information provided by an NMR spectrum is the chemical shift of hydrogen atoms which reveals a great deal about the nature of the bonds around each hydrogen. NMR absorbances appear in a spectrum as a series of sharp spikes or peaks. The vertical scale of the spectrum represents the relative height or intensity of each peak. The horizontal scale does not normally show proton resonances in simple frequency units. Instead, the position of each peak is normally measured relative to the absorption of the protons in parts per million or ppm, which is independent of the spectrometer frequency. The area under the peak of the proton signal is proportional to the number of equivalent hydrogen nuclei giving rise to the peak. Due to spin-spin coupling, each proton resonance (or peak) may split into several peaks depending on the number of non-equivalent neighbouring protons that the nucleus couples to. If there are no neighbouring hydrogen atoms, the resonance will be a single peak (singlet)

Figure 1.1.2 shows the summary of the four main pieces of information that can be obtained when looking at a ^{1}H NMR spectrum [10]**.** The first information is the functional groups that are present in the molecule. This is determined based on the ppm positions (shown in red) of the signals on the spectrum. The ppm scale is normally plotted from 0-12ppm. The second information that can be obtained is the number of protons represented by each signal (shown

in blue). This can be obtained by finding the area under each peak using integration. The third important piece of information which can be derived from a spectrum is the number of different types of protons present in the molecule. This is determined by the number of NMR signals (shown in purple). Only non-equivalent protons give different signals. Chemically equivalent protons give one NMR signal regardless of their number. The spin-spin splitting tells how many protons are connected to the neighbouring carbons. This is determined by the number of the peaks (signal multiplicity) (shown in green) within the signal based on n+1 rule, n being the number of neighbouring protons. This splitting of spectral peaks into doublets, triplets or higher order multiplets hence results from an electron-mediated interaction of two nuclear spins residing on the same molecule. This phenomenon is known as J-coupling.
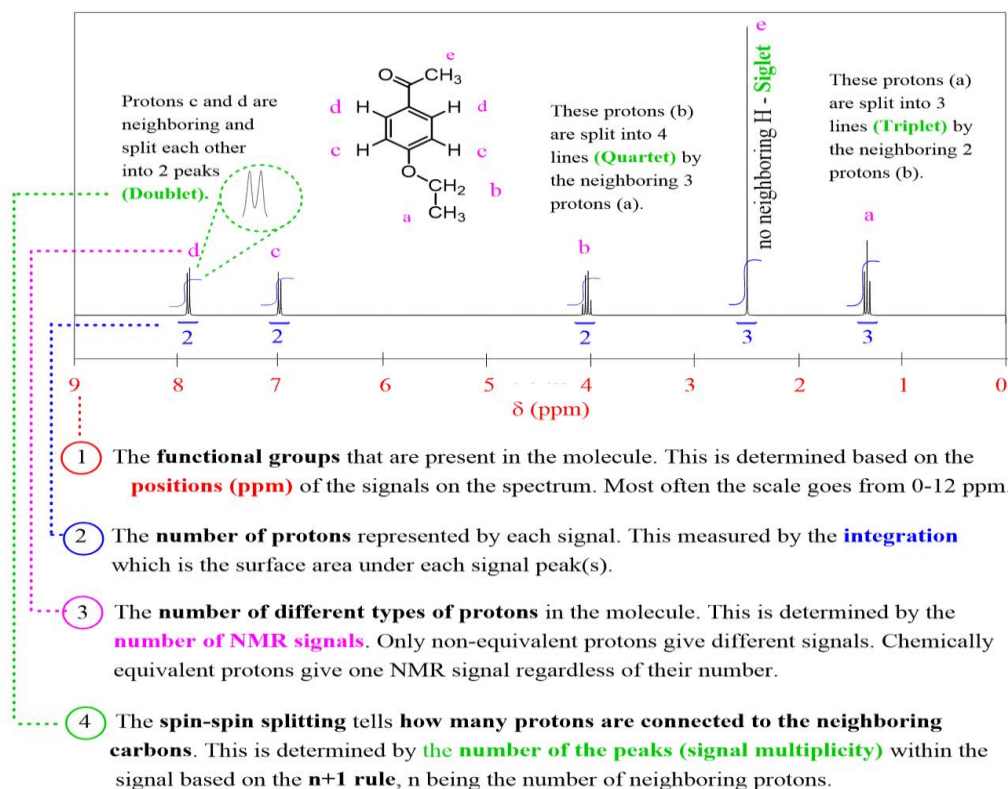
Figure 1.1.2 Summary of main information obtained from an NMR spectrum [10]

1.1.3   ppm scale

The NMR spectrum scale on the x axis is reported in units of parts per million (ppm) and increases from right to the left. The position on the plot at which the nuclei absorbs is called the chemical shift (δ). Since the ppm value is an arbitrarily assigned value, a standard reference point must be used. The spectra shown in this work were referenced to NAA at 2.01ppm and in the absence of NAA, to the water resonance at 4.7 ppm. The chemical shift of a resonance in a sample, δsample , in ppm is defined as follows in equation 1.2:

$$\delta\text{sample} = \frac{v_{sample} - v_{reference}}{v_{reference}} \times 10^6 \qquad \textbf{[1.2]}$$

where v_{sample} is the absolute frequency of the sample resonance and $v_{reference}$ is the

absolute frequency of an agreed upon a reference compound.

This scale is useful in particular since it is independent of a single absolute frequency and hence does not depend on the magnetic field strength, which varies between scanners of different field strengths. Therefore, spectra recorded using magnets of unequal field strength can be compared more easily.

1.1.4 Radiofrequency (RF) pulses

As already described, MR acquisitions require RF pulses with spectral or spatial selectivity based on the type of acquisition. A radio frequency pulse is described by the following parameters [11]:

• duration (= pulse width)

• frequency

• phase

• power (=amplitude) and shape

The RF pulses can be broadly divided into excitation and refocusing pulses. Several types of rectangular excitation pulses are available such as the SINC pulse, Gauss pulse and Hermite pulse etc. SINC pulses [12] have been widely used for selective excitation, saturation, and refocusing. A SINC pulse consists of several adjacent lobes of alternating polarity. The central lobe has the highest amplitude and is also twice as wide as every other lobe. The amplitude of the lobes progressively decreases on either side of the central lobe, as their polarity alternates. The Fourier transform of a SINC function is a box function, so if a long low power SINC shaped rf pulse is used one obtains a narrow flat box shaped excitation profile. A frequently used alternative to the SINC pulse for selective excitation is the Gaussian shaped pulse. The Fourier transform of a Gaussian is a Gaussian and one therefore will obtain a narrow Gaussian shaped excitation profile when a long low power Gaussian shaped pulse is used. Figure 1.1.3 shows the comparison of the excitation profiles for the Gaussian and SINC pulses.
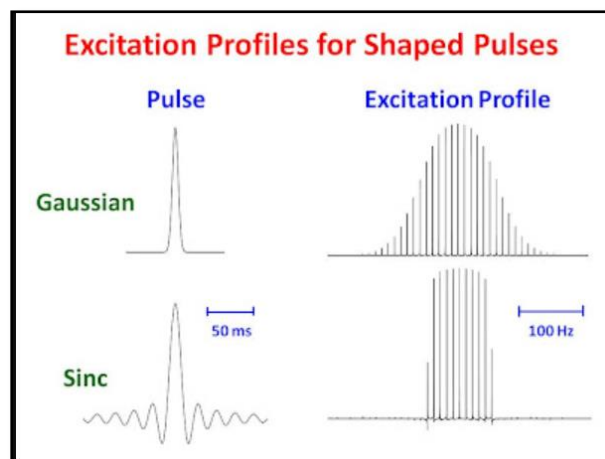
Figure 1.1.3 Excitation profiles for shaped pulses [13]

Although a single "best pulse shape" does not exist, the choice of optimal pulse depends on the experimental requirements, such as the need for uniform excitation versus the need for

localized effects or narrowest possible band-width. For single voxel spectroscopic acquisitions, Hermite pulses, which consist of a Gaussian profile, is adequate for narrow band excitations. The Hermite pulse represents a good compromise between the requirements of a simple pulse shape with low power requirements and a good slice profile. Compared to the SINC pulse, the Hermite provides much improved profiles, steeper edges and flatter tops. The excitation profile of the SINC and Hermite pulses can be seen in the Figure 1.1.4 adapted from [14].
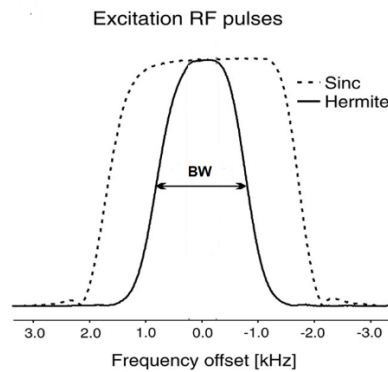
Figure 1.1 4 Pulse profiles of SINC and Hermite excitation pulses [14]

The conventional rectangular pulses are also not perfect at inverting all of the lines in a spectrum with a wide spectra width. In such cases a better choice is shaped adiabatic pulses. Adiabatic pulses can be categorized as excitation, refocusing, and inversion pulses. No matter what their use is, adiabatic pulses behave differently than non-adiabatic pulses.

The adiabatic refocusing pulses are a special class of RF pulses that rotate the transverse (as well as longitudinal) magnetization vector by 180° about an axis in the transverse plane. The word adiabatic originated from Greek meaning 'impassable to heat' and was used mostly in thermodynamics. One of the most prevalent adiabatic pulses used in MRI is a spatially selective adiabatic inversion pulse, also known as a hyperbolic secant (sech) pulse which is explained within [15]. A general hyperbolic secant pulse is given by equation 1.3:

$$\boldsymbol{B_1(t) = [A_o sech\ (\beta t)]^{1+i\mu}}$$ **[1.3]**

Where

A_o = maximum B_1 field amplitude
"β" = modulation angular frequency
μ = phase modulation parameter (dimensionless)

Figure 1.1.5 (A) shows the amplitude and (B) frequency modulation for a hyperbolic secant refocusing pulse which has the same profile as an inversion pulse. Note that the amplitude starts low, increases to a maximum and then returns to zero, and that the frequency is swept above and below several hundred of Hz [16]. The adiabatic principle, plane rotations and in-vivo applications in NMR have already been described in much detail in literature [17] [18]. All adiabatic pulses have the remarkable advantage of being insensitive to B1 inhomogenities which make them particularly suitable for in-vivo spectroscopy applications. .
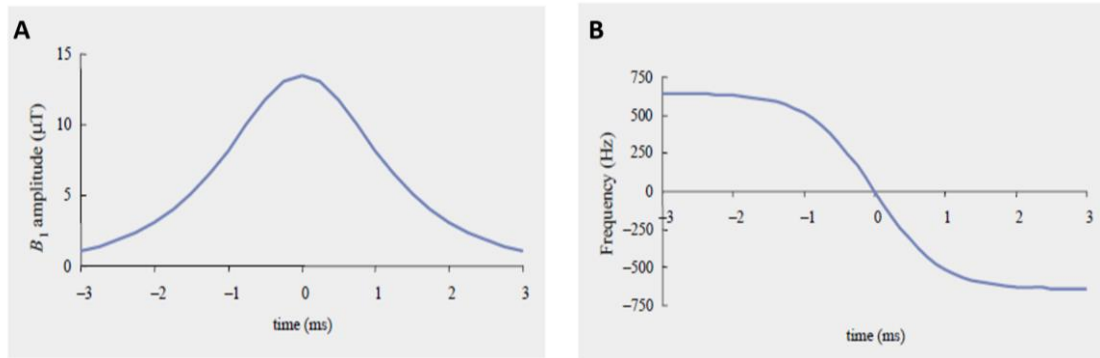
Figure 1.1.5 (A) Amplitude (B) Frequency modulation, for a hyperbolic secant adiabatic refocusing pulse. Figure is adapted from [16]

To induce adiabatic refocusing of the transverse magnetization, the amplitude and frequency of an RF pulse must be modulated (i.e., varied) throughout the pulse in accordance with the adiabatic condition. The differences between adiabatic and non-adiabatic pulses are summarized in table 1.1.

.

Table 1.1 Comparison between adiabatic and non-adiabatic pulses.

ADIABATIC VS. NON-ADIABATIC PULSES

ADIABATIC PULSES	NON-ADIABATIC PULSES
• The flip angle is independent of the applied B_1 field $$\theta \neq \int_0^t B_1 (t)\, dt$$	• The flip angle is dependent on the applied B_1 field $$\theta = \int_0^t B_1 (t)\, dt$$
• Amplitude and frequency phase modulation	• Amplitude modulation, constant carrier frequency, (constant phase)
• Long duration(2-12ms)	• Short duration(0.3 ms to 1ms)
• Higher B_1 amplitude	• Lower B_1 amplitude
• Generally not multi-purpose(e.g inversion pulse cannot be used for refocusing	• Generally multipurpose

1.1.5   Slice selection

Often, the first step in producing an MR image is to reduce a 3D object to a smaller volume or "plane" of interest from which to receive signal; this is called selective excitation [19]. To selectively excite spins in a slice, two things are essential: a gradient field and a shaped radio frequency pulse.

Slice selection is used to selectively excite the spins in a well-defined plane. The slice dependence of the Larmor frequency (ω) in the presence of a gradient can be used to selectively excite the spins within a slice perpendicular to the gradient direction. When a gradient in the z-direction (Gz, slice select gradient) is applied, it causes the field strength to vary linearly with

distance from the center of the magnet. At the same time a 90° RF excitation pulse is also applied at a resonance frequency F=ω_0+$\Delta\omega$ exciting only the spins at a particular plane z=z_0. To excite a slice with some thickness Δz, the RF pulse must possess a bandwidth of frequencies that matches the bandwidth of resonance frequencies of the spins in the slice of interest. Only spins located within that specified slice will contribute to the signal. The slice thickness (Δz) is directly proportional to the bandwidth (BW) of the applied RF pulse and inversely proportional to the steepness of the applied gradient (Gz) given by equation 1.4.

$$\Delta z = \frac{BW}{\gamma G_z}$$ [1.4]

Figure 1.1.6 A shows how a shallow gradient produces a thicker slice for a chosen transmit Bandwidth (BW) while (B) shows that a steeper gradient produces a narrow slice for the same transmit BW. Once a given slice is selectively excited, the signals arising from each volume element within that section must be spatially encoded in the other two orthogonal directions. In routine MR imaging, one of these in-plane dimensions is encoded by changes in frequency, whereas the other is encoded by differences in phase.

The iso-center is the point where all three gradient coils intersect and produce a net zero additional magnetic field. This point is typically the same as the iso-center of the magnet. Usually the desired slice plane does not pass through the iso-center. In this case, the desired slice offset z_0 is obtained by shifting the carrier frequency of the RF by an amount Δf. The required amount of frequency shift is proportional to the desired offset (e.g., in centimetres) and the amplitude of the slice-selection gradient. The spins thus precess with a spatially dependent frequency. The offset frequency v_{RF} is given by equation 1.5:

$$v_{RF} = v_0 + slice\ position(cm) * G_z(kHz\ cm^{-1})$$ [1.5]
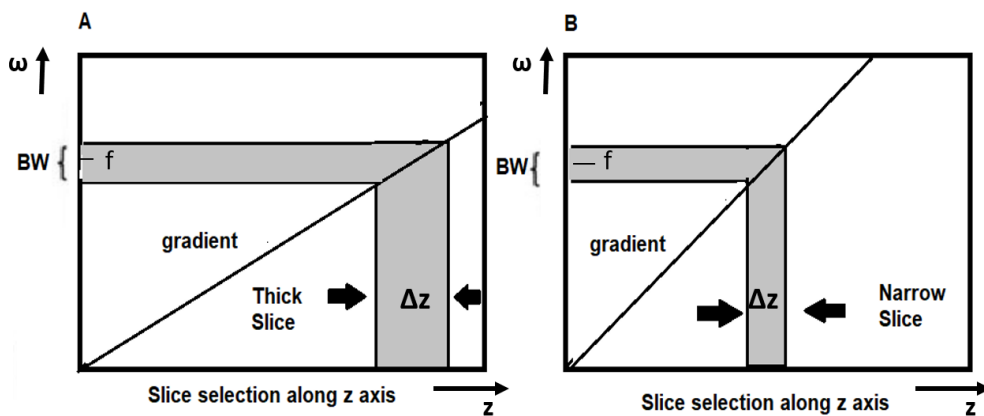
Figure 1.1.6 Representation of slice selection along z axis (A) Shallow gradient produces a thicker slice for a chosen transmit Bandwidth (BW). (B) Steeper gradient produces a narrow slice for the same transmit BW. Figure adapted from [20]

In Bruker ParaVision 5.1, the available slice excitation planes are named as RL (right-left) which represents the x-direction, AP (anterior-posterior) which represents the y-direction and HF (head-foot) which represents the z-direction.

1.1.6 Slice-select gradients and Crushers

As seen in the previous section, a very important ingredient for slice selection in localized MR acquisitions are the slice select gradients. The slice-select gradients are constant gradients played concurrently with a selective RF pulse. To recapitulate, a slice select gradient defines the center frequency and frequency range for a given slice. The amplitude of the slice-selection gradient and RF pulse bandwidth determine the slice thickness. However, when programming the pulse sequence, the slice selective gradients are also accompanied by a rephasing lobe. The purpose of a rephasing lobe is to correct for phase dispersion of the transverse magnetization due to the primary slice select gradient. Without the slice-rephasing gradient lobe, there is intravoxel phase dispersion across the slice and signal loss results, as if a spoiler gradient were present.

In general, to fully correct for the phase dispersion introduced by the slice select gradient, the rephasing lobe area must be equal to half the area of the slice select gradient. Thus, the strength of the rephasing lobe can be calculated by finding the ratio of the area under the gradient and the gradient duration. Figure 1.1.7 shows the pulse timing diagram of a slice selective gradient Gz and the rephasing lobe applied together with a 90° RF excitation pulse. The rephasing lobe was applied once the RF pulse was turned off. The duration of the slice selective gradient was Ts while the duration of the rephasing part was Ts/2, thus, in this example both gradients have the same amplitude.
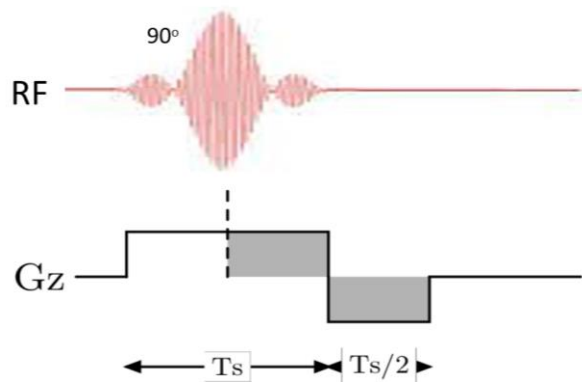
Figure 1.1.7 Graphical representation of a rectangular slice selective gradient Gz and the rephasing lobe applied together with a 90º excitation pulse.

Another important type of gradient are crusher gradients which serve as correction gradients that preserve desired signal pathways and eliminates the unwanted ones by manipulating the phase of the signal [21]. The crushers are mainly applied along the slice selection gradient axis, but can also be applied in all three dimensions. Depending on signal pathway, left and right crushers may have same or different areas.

Unbalanced crushers can be caused by improperly adjusted crusher slopes. An unbalanced slope manifests itself as a shift in the echo peaks, resulting in a distorted Lorentzian lineshape of the spectrum. This can be corrected post-acquisition by first-order phasing, but the root cause can also introduce other artefacts.

1.2 ^{1}H Magnetic Resonance Spectroscopy (MRS)

Magnetic resonance spectroscopy (MRS) is a useful diagnostic tool to assess tissue biochemistry complementary to anatomical information provided by Magnetic Resonance Imaging (MRI) and has been used in a variety of clinical research applications on the brain [22]. In pre-clinical settings this technique has proved to be a handy tool to assess tissue biochemistry in conditions that result in large changes in metabolite levels [2]. By excluding the overwhelming signals from water and fat, MRS can detect small metabolites existing in millimolar (mM) concentrations. These metabolites can be differentiated because they resonate at slightly different frequencies based on their local chemical environments. As described in section 1.1.2, the degree of frequency separation between two molecular species is characterized by their chemical shift (δ), and the relative areas under each peak are proportional to the number of equivalent nuclei in that particular chemical environment [10]. Figure 1.2.1 shows a ^{1}H single volume/voxel (SV) spectrum acquired from rat brain with water signal suppression and repeated accumulations (NA=128) to improve signal intensities from metabolites (the individual peaks that are labelled). The spectrum is plotted in ppm scale (see section 1.1.3).
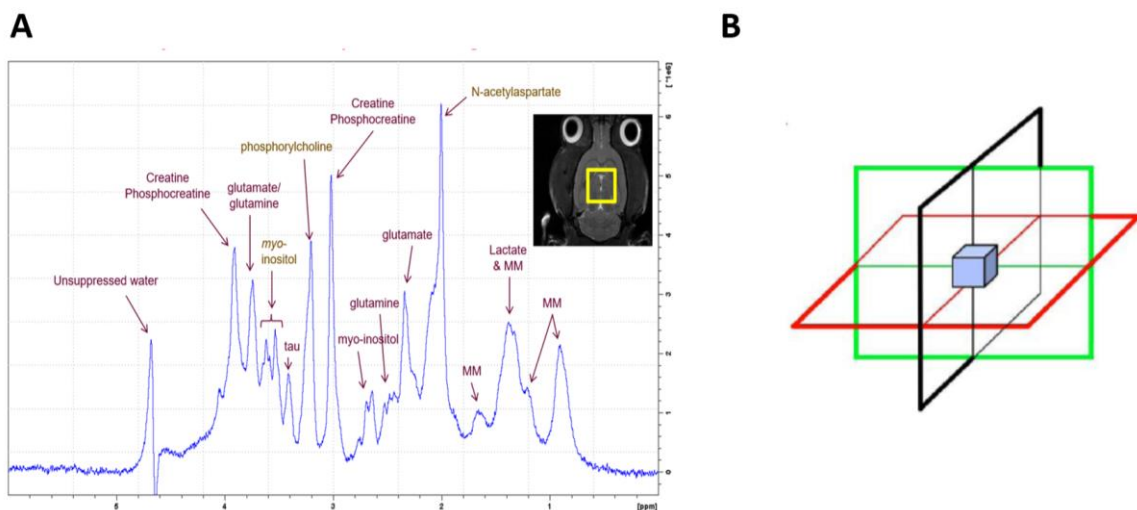
Figure 1.2.1(A) single voxel spectrum acquired from rat brain (B) Single voxel (blue) localization by applying three orthogonal gradients in the x, y and z directions. Figure B adapted from [23]

The spatial localization in single voxel spectroscopy is achieved by applying three orthogonal RF slice selective pulses and collecting the echo signal from the excited volume of interest called a ''voxel'' by using a suitable pulse sequence *[4]*. The sequence is designed such that only the signal inside the voxel is detected to convert into useful information. Figure 1.2 B shows a voxel (blue) localized by three orthogonal gradients applied in the x, y and z directions. Several techniques have been reported in literature for this volume selection *[24] [25]*.

Before making the MRS measurement, it is important that the magnetic field within the voxel is homogeneous. Therefore, a shimming procedure is performed using shim coils in order to correct for any field inhomogeneity. Poor shimming of the voxel can be observed in the resulting spectrum by a widening of the resonances, which complicates the resolution and quantification of the metabolite concentrations.

1.2.1 Spin echo sequence

As already mentioned, the basic principle underlying nearly all single voxel techniques is to apply three mutually orthogonal slice-selective pulses and design the pulse sequence to only collect the echo signal at the point of intersection (voxel volume) [4].

Immediately after the excitation RF pulse, excited protons in the tissue generate a signal which decays due to the T_2 relaxation process. The transverse magnetization (T_2) decays much faster than the recovery of the longitudinal magnetization (T_1). Imperfections in the main magnetic field, application of gradient coils, and tissue inhomogeneity further accelerate the loss of transverse magnetization. This problem is overcome by applying 180° refocused RF pulses to generate what is called a ''spin echo''. In this manner signal loss due to static inhomogeneities of the magnetic field is recovered. Figure 1.2.2 shows a spin echo sequence consisting of a 90° excitation pulse and a 180° refocusing pulse. The total time to acquire one spin echo is called the echo time (TE) and the intervals between the 90° and 180° pulses and 180° and acquire are equal to TE/2 [26].
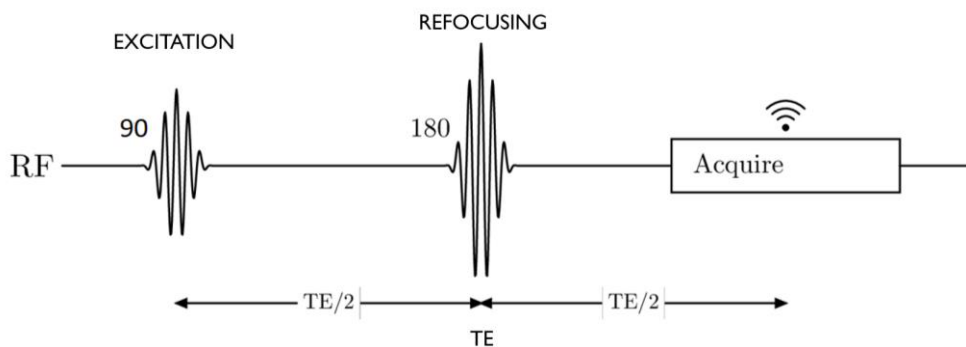
Figure 1.2.2 RF pulse diagram showing a spin echo sequence consisting of a 90o excitation pulse and a 180o refocusing pulse. The total time from excitation to acquire one spin echo is called the echo time (TE) and the intervals between the 90o and 180o pulses and 180o and acquire are equal to TE/2.

1.2.2 Point resolved spectroscopy (PRESS)

The correct choice of pulse sequence and the associated acquisition parameters are often the key factors in determining the success of an MRS study. Point Resolved Spectroscopy (PRESS) is one of the simplest spin echo single voxel localization sequences. It has three RF pulses, a slice selective excitation followed by two slice selective refocusing pulses. Figure 1.2.3 shows the simplified pulse sequence diagram of a PRESS sequence [23]. The first pulse is a slice-selective excitation pulse with a flip angle of 90° followed by second and third refocusing pulses with flip angle of 180°. Crusher gradients are applied around these pulses in order to select the desired spin echo. Typically, the echo time is about 12-20ms, and signal loss is primarily due to T2 relaxation. The standard protocol uses Hermite excitation and refocusing RF pulses.

The PRESS sequence encounters a challenge wherein the RF pulses utilized to excite and refocus the 1H spins operate at frequencies that result in interference effects. Additionally, the conductive tissue attenuates these RF pulses, leading to an inhomogeneous magnetic field B_1 despite the utilization of volume RF excitation coils. This inhomogeneity can give rise to intravoxel variation of flip angles (in cases of large volume selections) or introduce a bias in the intended flip angle for a specific voxel location, depending on the size and position of the spectroscopic volume of interest (VOI). Consequently, inaccurate flip angles lead to changes in the shape of the VOI, incomplete refocusing, diminished signal-to-noise ratio (SNR), and the emergence of undesired coherences due to excitation occurring outside the intended VOI [27].

Also, the chemical shift difference between different resonances causes a chemical shift displacement error (CSDE) which results, in some cases, in unacceptably large differences in the localization of the volume of origin of different resonances. This is due to the bandwidth-limited refocusing pulses present in the sequence and the partial slice excitation. At the edges of the refocused slice, the proton spins may be excited rather than refocused. This leads to signal loss near the edges of the slices as well as significant unwanted excitation outside of the desired voxel. The unwanted excitation can be suppressed through spoiler gradients, OVS and phase cycling. Phase cycling is a common strategy used in MRS protocols to combat unwanted signals generated by spectrometer hardware and coherent noise contribution from tissue external to the VOI. The cycling scheme also affects the selection of coherence transfer pathways. When the phase of the excitation pulse is cycled, the phase of the resulting signal will change accordingly, allowing the NMR signal to be distinguished from phase-invariant background interference. The receiver phases are alternated accordingly, so that when the FID is added, unwanted background interference is suppressed while the desired VOI signal is added coherently [28]. Nonetheless the signal loss can be harder to attenuate. Hence, sequences that utilize RF pulses with sufficiently broad bandwidths to minimize CSDE are essential.
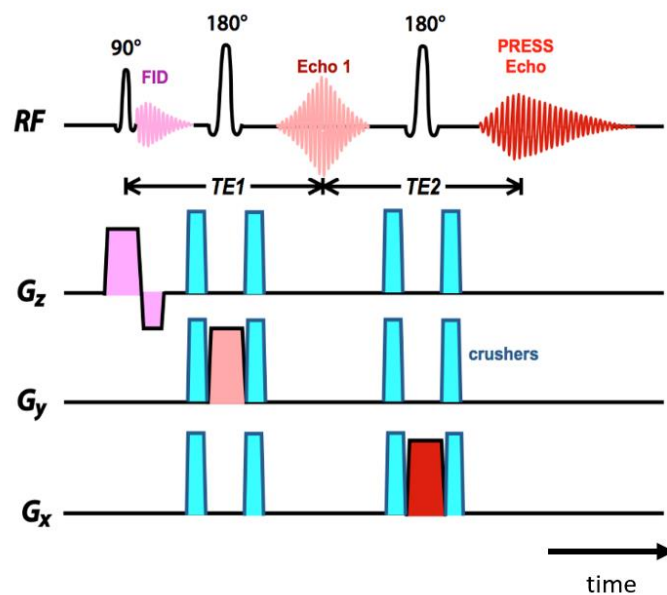
Figure 1.2.3 The single voxel PRESS sequence [23]

A solution to these problems is using adiabatic RF pulses to combat the effects of B1 inhomogeneity by improving SNR and reducing the unwanted coherences occurring due to excitation outside the intended VOI.

1.2.3 Localization by semi-adiabatic selective refocusing (semiLASER)

The semi-adiabatic localization by adiabatic selective refocusing (semiLASER) sequence is a robust localization technique for ^{1}H-MRS which can be used as an alternative to the PRESS sequence and is now widely used in clinical applications. The semiLASER sequence provides single-shot full intensity signal with clean localization and minimal chemical shift displacement error and was recommended by the international MRS Consensus Group as the preferred localization sequence at high and ultra-high fields [27]. This sequence, consisting of pairs of adiabatic passages (AFP) gives excellent refocusing performance across the entire slice, which significantly decreases partial slice excitation issues. The adiabatic pulses also have relatively high bandwidths and their flip angles are insensitive to transmit B1-inhomogeneities. In addition, adiabatic refocusing pulses have sharp slice selection profiles to produce a localized spin echo. The use of adiabatic pulses has significant advantages when using surface transceiver coils, which cannot otherwise produce good refocusing pulses due to their inhomogeneous B1 fields.

Figure 1.2.4 shows a single voxel semiLASER sequence reported in the literature [29]. The sequence consists of a slice-selective excitation pulse, T_{EXC} , followed by two pairs of adiabatic refocusing pulses, T_{REF}. The adiabatic refocusing pulses are used in pairs to prevent phase dispersion which occurs across the slice. The intervals between the pulses are defined as T_1, T_2, T_3, T_4, and T_5 , the sum of which is equal to the total TE. The gradients and crusher pairs are also placed concurrently with the RF pulses in the G_x, G_y and G_z planes. The sequence has been reported with a minimum echo time TE=20.1ms for human brain at 3T [29].

There are however a few drawbacks reported for the single voxel semiLASER sequence when compared to PRESS. The echo times for these sequences are long, typically at least double than seen in PRESS. This is less of a concern at lower fields, when T2 relaxation is typically slower, but can represent a more significant signal loss at higher fields. Despite that, the benefits of the semiLASER sequence make it a suitable choice over the conventional PRESS sequence.
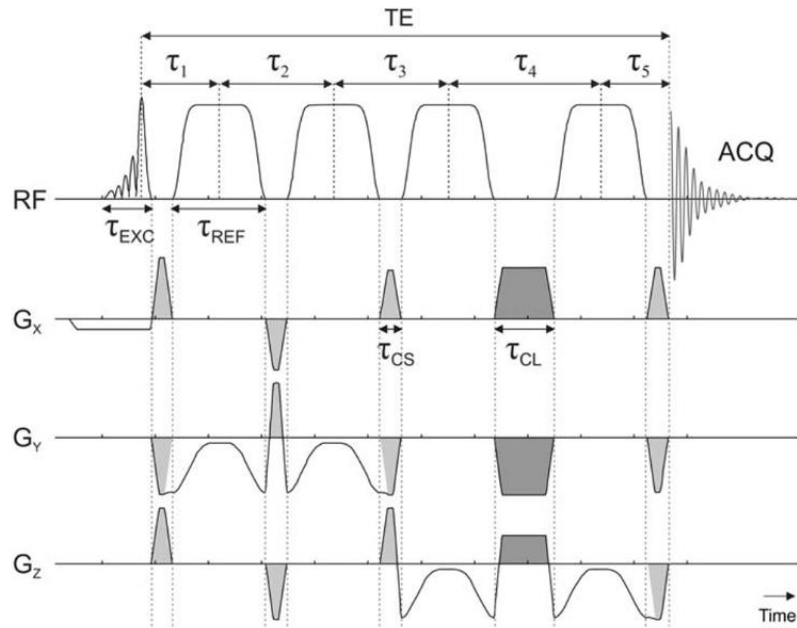
Figure 1.2.4 A semiLASER pulse sequence diagram reported in Literature [29]. T_1, T_2, T_3, T_4 and T_5 represent the delay intervals and τ_{EXC} and τ_{REF} are the excitation and refocusing pulses. The light grey color represents the crusher gradients with short duration (T_{CS}) and the dark grey represents the long duration crushers (T_{CL}).

1.3 ^{1}H Multi-voxel spectroscopic Imaging (^{1}H-MRSI)

Proton Multi-voxel spectroscopic imaging, also named ^{1}H-Magnetic Resonance Spectroscopy Imaging, and formerly known as Chemical Shift Imaging (CSI) is a versatile diagnostic technique that provides non-invasive metabolic information about living tissues non-invasively. Conventional two-dimensional (2D) MRSI is based on volume selective MR spectroscopy (MRS) in combination with phase encoding gradients in the y and z planes. The phase encodes help in segmenting the larger stimulated volume into multiple smaller voxels. The phase encodes are applied as a series of gradient pulses along the phase encoding direction to encode spatial information. This allows for the acquisition of a set of spectra that represent different regions of the brain. The amplitude and duration of the gradient pulse determines the spatial resolution and the number of spatial locations sampled. Figure 1.3.1 shows a simplified CSI-PRESS pulse sequence diagram with slice-selective excitation pulses in three planes with phase-encoding gradients along y and z axes. The sequence has been simplified by leaving out preparatory suppression modules such as water suppression VAPOR and OVS, and crusher gradients.
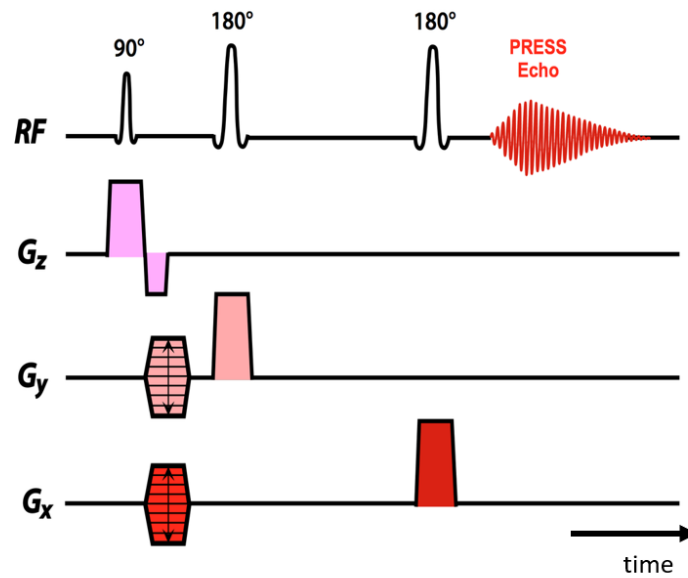
Figure 1.3.1 2D CSI-PRESS pulse sequence diagram adapted from [23]

.

CSI phase-encoding can be combined with any type of excitation and signal generation method. In the simplest possible case, the entire volume could be excited with a non-selective RF-pulse, with sampling of an FID signal after each phase-encoding step. More commonly, excitation is performed using spatially selective RF-pulses and gradients similar to PRESS.

Furthermore, the use of enhanced MRSI protocols improve the non-invasive characterization of brain tumors at a preclinical level. The main sources of error in preclinical MRSI occur mainly due to the small rodent brain, long acquisition times and low signal to noise ratio.

1.4 Single voxel Spectroscopy (SVS) vs Multi-voxel Spectroscopy (MRSI)

As already described, the SVS techniques are valuable tools which allow quantification of chemical biomarkers for tissues of interest and help to improve diagnostic specificity. However, due to the heterogeneous nature of brain tumor lesions, complex metabolic changes cannot be explained by a single spectrum obtained using single voxel spectroscopy. Therefore, multi-voxel techniques are used to excite a large volume of brain tissue while excluding signal from lipid in the scalp and/or regions of poor field homogeneity and then phase encoding gradients are used to localize spectra from the volume of interest (MRSI inner grid) within the excited region [30].

Figure 1.4.1 shows examples of single and multi-voxel acquisitions. The single voxel spectrum was acquired by placing a small voxel inside the tumor region of a GL261 tumor growing in C57BL/6 mice. The SV spectrum shows the metabolites at their resonance positions but not all peaks can be seen clearly because some signals overlap, since tumors are very heterogeneous, inducing field heterogeneities which produce broader signals in bigger VOI. The multi-voxel technique allows to acquire a bigger grid consisting of smaller sub-voxels and hence provides more detailed insight into the spectra acquired and additional/different metabolite peaks may

be identified. It is also a possibility to obtain visually different spectral patterns as well as more resolved metabolite peak in multi-voxel MRS in comparison to single voxel.
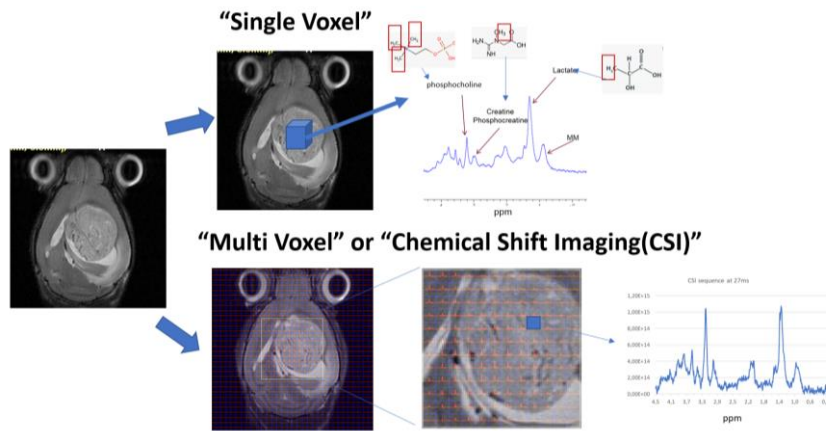
Figure 1.4.1 Spectroscopy techniques: Single versus Multi-voxel comparison in a GL261 tumor mouse. The top row shows the single voxel represented by a blue cube positioned inside the tumor region overlaid on a T2w mouse image and the corresponding spectral pattern. The bottim row shows the MRSI grid covering the tumor region and a sub-voxel spectra from within the MRSI grid.

The MRSI technique offers two potential advantages over the SVS:

1) A larger total coverage area (since the size of the entire multivoxel grid is greater), and
2) Higher spatial resolution (since the individual voxels are smaller) [23].

 A wide coverage area is important for large, heterogeneous lesions like the brain tumors where the SVS technique provides data from only a small portion of the mass. The multi-voxel sequence can hence provide a volumetric approach for tumor area coverage.

Although the SVS acquisition is fairly rapid and easy, it provides limited information about the regional distribution of brain metabolites. On the other hand, the MRSI technique has its own set of drawbacks such as that conventional slice-selective 180° refocusing pulses do not have particularly good slice profiles and hence not all signal is fully refocused resulting in lower SNR and lower quality near the MRSI grid edges. Also, MRSI techniques tend to be more complex and time consuming compared to single voxel acquisitions. The problems faced in MRSI may be particularly overcome by applying high-bandwidth adiabatic refocusing pulses [31] to sharpen the edges of the excitation profile.

Overall, MRSI is an interesting and useful approach to complement MRS in evaluating tumor response to therapy. Table 1.2 summarizes the comparison of single vs multi-voxel spectroscopy techniques [32]**.**

SINGLE VOXEL SPECTROSCOPY	MULTI VOXEL SPECTROSCOPY
Easy to use	Hard to use
Shorter time	Longer time
Easy to interpret	Hard to interpret
More Signal	Less Signal
Large voxel volume	Small voxel volume
Low Spatial Resolution	High Spatial Resolution
Voxel placement critical	Allows metabolite & quantification maps

1.5 Brain Metabolites

The brain is a complex structure containing several metabolites in the millimolar range which are small molecules that are involved in various metabolic processes that occur within the brain. These metabolites can be measured using various techniques, such as MRS/MRSI, which allow researchers to noninvasively measure the levels of several of those metabolites. Using MRS/MRSI, the metabolites which can be detected in the brain tissue include total trimethylamine containing compounds: free choline, phosphocholine, glycerophosphocholine, being the major ones, jointly labelled as total choline or to simplify even further, Choline (Cho), total Creatine (creatine+phosphocreatine), simplified as (Cr), N-acetyl aspartate (NAA), lactate (Lac), myoinositol (mI), glutamine/glutamate (Gln/Glu, sometimes simplified as Glx), NMR visible mobile lipids (ML), and amino acids in peptides ans small proteins (MM). Brain lesions contain abnormal levels of these metabolites as compared to normal brain tissue.

Table 1.3 shows the ^{1}H chemical shifts of major metabolites detected in rat brain [33].

Table 1.3 ¹H Chemical Shifts of Cerebral Metabolites detected in Rat brain. See the original reference for further details [33].

No.	Compound		Carbon position	*in vivo* spectra (ppm)	Fitted model spectra (ppm)
				¹H chemical shift	
1	*N*-Acetylaspartate	CH₃		2.009 (Ref.)	
2		αCH	C2		4.377
3		βCH₂	C3	2.489 + 2.674	
4		NH		7.82	
5	*N*-Acetylaspartylglutamate	CH₃		2.046	
6	γ-Aminobutyric acid	αCH₂	C2	2.28	
7		βCH₂	C3	1.89	
8		γCH₂	C4		3.01
9	Alanine	αCH	C2		3.777
10		βCH₃	C3	1.468	
11	Aspartate	αCH	C2		3.88
12		βCH₂	C3	2.79	2.66 + 2.79
13	Choline compounds	(CH₃)₃		3.209	
14	Creatine	CH₂		3.911	
15		CH₃		3.027	3.024
16	Phosphocreatine	CH₂		3.931	
17		CH₃		3.027	3.030
18	α-Glucose	[1]CH	C1	5.226	
19	Glutamine	αCH	C2		3.76
20		βCH₂	C3	2.12	
21		γCH₂	C4	2.45	
22	Glutamate	αCH	C2	3.75	
23		βCH₂	C3		2.08
24		γCH₂	C4	2.349	
25	Glutathione	Gly CH + Glu αCH	C2		3.77
26		Glu βCH₂	Glu C3		2.16
27		Glu γCH₂	Glu C4		2.54
28		Cys βCH₂	Cys C3		2.95
29	Glycerophosphorylcholine	NCH₂ + Glyc CH₂			3.66
30		OCH₂			4.31
31		Glyc OCH₂ + CH			3.90
32	*myo*-Inositol	[1,3]CH	C1,C3	3.525	
33		[2]CH	C2	4.060	
34		[4,6]CH	C4,C6	3.622	
35		[5]CH	C5	3.275	
36	*scyllo*-Inositol	CH		3.345	
37	Lactate	αCH	C2	4.11	
38		βCH₃	C3	1.318	
39	Phosphorylcholine	NCH₂			3.58
40		OCH₂			4.16
41	Phosphorylethanolamine	NCH₂			3.22
42		POCH₂		3.98	
43	Taurine	SCH₂		3.418	
44		NCH₂		3.246	

1.5.1 N-Acetyl Aspartate (NAA)

NAA is the largest signal in the normal brain spectrum, its N-acetyl group (CH₃) resonates at 2.01 ppm with a usually unresolved contribution from N-acetyl aspartyl glutamate (NAAG). Other additional NAA resonances are βCH2 at 2.48 ppm and 2.67 ppm and αCH at 4.47ppm [34]. NAA decreased levels are measured in numerous neuropathological conditions ranging from brain injury, tumors, stroke, Alzheimer's disease etc. This fact makes NAA a potential diagnostic molecule for doctors treating patients with brain damage or disease. Figure 1.5.1 shows the simulated spectrum obtained for NAA resonances using NMRSCOPE-B.
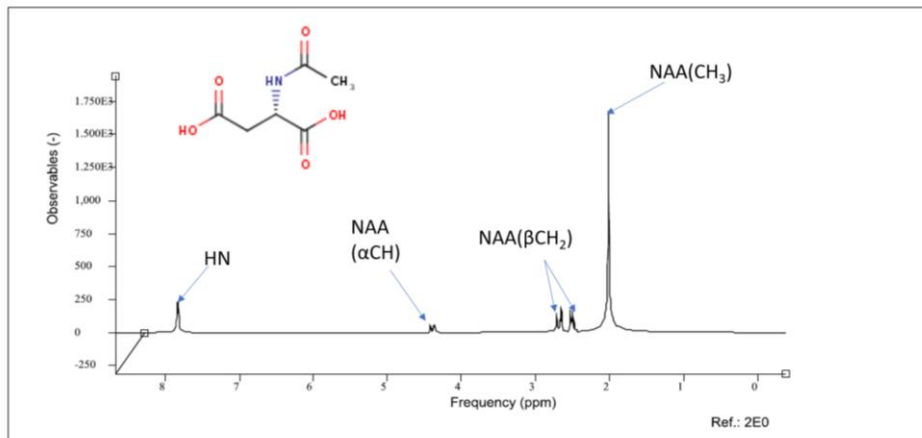
Figure 1.5.1 N-Acetyl Aspartate spectrum simulated using NRMSCOPE-B showing NAA CH$_3$ peak at 2.01ppm, βCH$_2$ at 2.48ppm+2.67 ppm, αCH at 4.47ppm and HN at 7.8ppm.

1.5.2 Total creatine (Phosphocreatine + creatine)

Phosphocreatine(PCr), also known as creatine phosphate, is a phosphorylated creatine molecule that serves as a rapidly mobilizable reserve of high-energy phosphates in skeletal muscle, myocardium and the brain to recycle consumed adenosine triphosphate, the energy currency of the cell. It shows a main resonance at 3.03 ppm and a second resonance/s are also observed at ca. 3.91-3.94 ppm at 7T [35]. Since creatine is produced in the liver and transported to brain, chronic liver diseases may lead to low cerebral total creatine concentration. Total creatine also shows large regional variations with lower levels in white matter and high levels in cerebellum. In brain tumors also, total creatine concentrations are reduced. Figure 1.5.2 shows a Phosphocreatine simulated spectrum showing CH$_3$ peak at 3.03ppm and CH$_2$ peak at 3.9ppm.
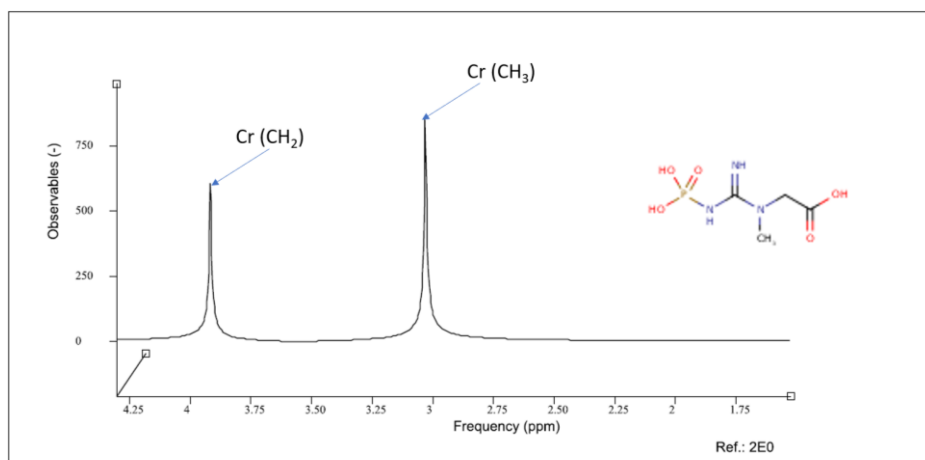
Figure 1.5.2 Phosphocreatine spectrum simulated using NMRSCOPE-B showing the CH$_3$ peak at 3.03ppm and CH$_2$ peak at 3.9ppm.

1.5.3 Lactate

Lactate is found in very low concentrations in normal brain tissue and its methyl resonance (CH_3) at 1.3ppm is hard to detect [36]. However, in tumor brain, the Lactate peak is significantly increased and can be detected by MRS. Figure 1.5.3 shows the Lactate simulated spectrum containing Lac (CH_3) peak at 1.3ppm and (αCH) peak at 4.1ppm. The Lactate peak at 1.3ppm is a doublet and the scalar coupling gives rise to a phase evolution of this methyl doublet, which depends on the echo time and hence may show reduced or absent intensities at long echo times. Moreover, it overlaps with a short-T2 lipid signal (ML) that will be more attenuated with a longer TE due to T2 relaxation.
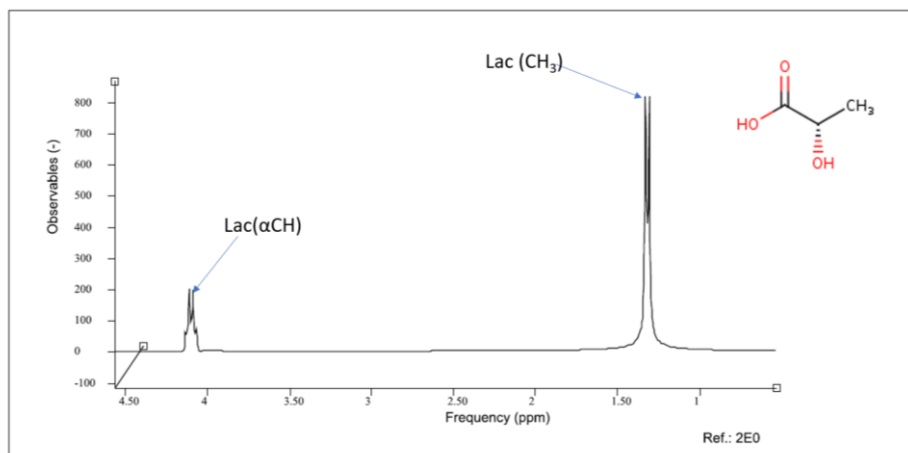
Figure 1.5.3 Lactate simulated spectrum showing Lac (CH_3) peak at 1.3ppm and (αCH) peak at 4.1ppm.

1.6   MRS and MRSI applications in Glioblastoma (GB) Tumors

In tumor studies, MRS/MRSI can be used to detect changes in the metabolite levels of cancerous tissues compared to healthy tissues, providing valuable information about the metabolic profile of tumors. For example, changes in the levels of certain metabolites, such as lactate, choline, and creatine, can be indicative of tumor growth and progression. Glioblastoma (GB) tumors are the most common primary malignancy of the central nervous system in adults with an extremely poor prognosis that has not improved significantly despite the development of new diagnostic strategies and innovative therapies [37]. Surgery followed by combination chemotherapy such as temozolomide (TMZ) plus radiation therapy has been used as the standard adjuvant treatment option with a median survival of 14.6 months [38]. For the assessment of treatment response in GB, the most common monitoring method is magnetic resonance imaging (MRI), which is the preferred modality to obtain information on tumor size and local extension of tumor tissue [39]. Our group has a long history of working in pre-clinical models of GB tumors, since pre-clinical studies in glioma tumor research are essential for advancing our understanding of the disease, identifying new therapeutic targets, optimizing treatment approaches, and improving outcomes. Our group has several contributions towards laying the foundation for future advancements in glioma treatment. In our previous studies, the multi-slice MRSI

technique has allowed us to observe response to treatment using nosological images in GL261 tumor-bearing mice treated with TMZ [2].The MRSI technique provides spatial mapping of the metabolite profiles throughout the different regions of the mouse brain and tumor [40].

1.6.1 Nosological images

The MRSI signal obtained from different types of tissue can be automatically categorized by pattern recognition (PR) techniques creating nosological maps potentially useful to detect and characterize therapy response in a non-invasive way [41] [42]. In this respect, the tumor responding index (TRI) is an evaluation parameter, introduced by our group, that has been put forward to measure the extent of response to treatment using the obtained nosological images [2]. To produce the nosological images the spectral (metabolomic) information is analysed, classified and converted into a coloured image according to different conditions [43]. The method uses semi-supervised non-negative matrix factorization (NMF) strategies to extract significant source signals from tumors. From a biochemical perspective, source extraction techniques for classifying MRS data assume the presence of a mixture of heterogeneous tissues and their metabolites in each voxel, from which the contribution of each source can be derived. A classifier was trained using these extracted sources from previous CSI-PRESS acquisitions. The spectra classifier identifies pixels of normal brain parenchyma, actively proliferating tumor and treatment-responsive tumor tissue and represents this information as nosological maps (Figure 1.6.1). Green color coding is used when GB pattern contributing most was the source ot tumor responding to treatment, normal brain parenchyma is blue, red codes for actively proliferating GB, and black is for indeterminate tissue.
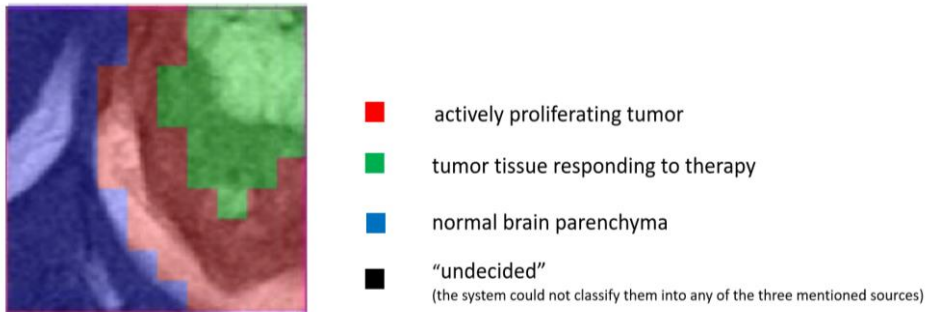
Figure 1.6.1 Example of a semi-supervised nosological map corresponding to C971 mouse (GL261 Gb responding to TMZ). The Cxxx notation corresponds to the internal GABRMN unique mouse identifier code. The color coding consists of the the red, green and blue regions which correlate to the unresponding, treated and normal brain parenchyma.Figure adapted from [43].

The tumor responding index (TRI) is calculated as given in equation (1.6);

$$\textbf{Tumor responding index (TRI) (percentage)} = \frac{responding\ tumor\ voxels}{total\ tumor\ voxels} \times \textbf{100} \qquad \textbf{[1.6]}$$

1.6.2   Multi-slice MRSI acquisitions

One step beyond into unravelling response to therapy in GB is to acquire multiple MRSI slices to cover a bigger tumor volume. Consecutive grids can be acquired across the tumor in a 3D like volumetric approach which is both feasible for preclinical models and can provide additional insight into therapy response. Our group has a long track of using CSI-based nosological images to provide metabolomic information for treatment monitoring in murine brain tumors. Figure 1.6.2 shows multi-slice MRSI acquisitions and the corresponding nosological images in a tumor mouse undergoing TMZ treatment in one of our previous studies [2]. Four consecutive grids (Grid1-Grid4) were placed covering the tumor region (plane B) such that Grid2 and Grid 3 have dimensions 12x12 while Grid1 and Grid4 have smaller dimensions 10x10 to avoid sampling the scalp. The acquired MRSI grids superimposed on the anatomic axial images are visible in plane C. The grids were then exported to spectra classifier [44] to obtain the nosological images as shown in the Figure 1.6.2 . Multiple images give a better visualization of the responding and non-responding parts of the tumor and can help to better diagnose and evaluate tumor response to therapy [43] [45] .
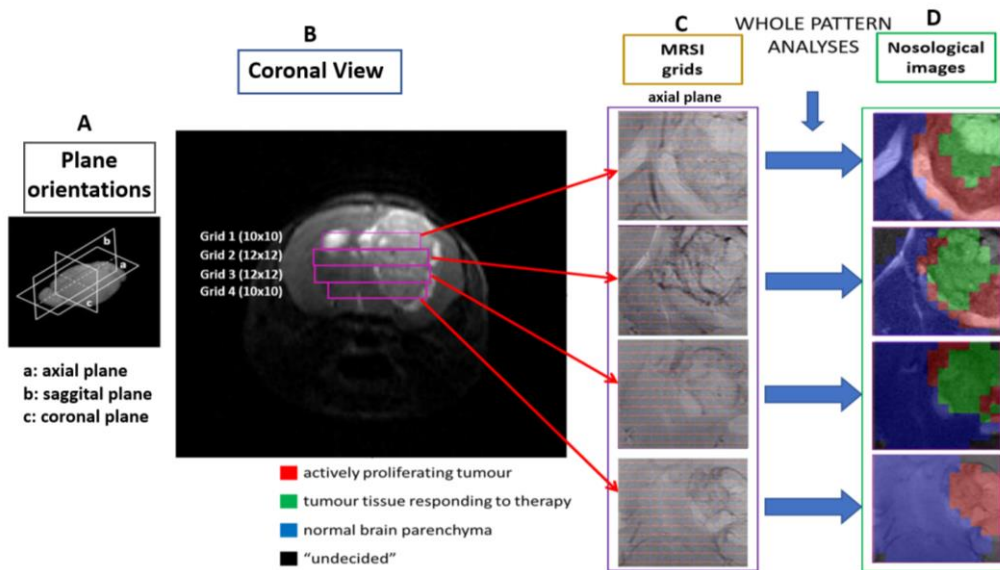
Figure 1.6.2 (A) The three plane orientations i.e. axial, sagittal and coronal defined for mouse brain. (B) Coronal T2w MRI of mouse C971 (bearing C971 a unique animal identifier within the GABRMN) brain harbouring a GL261 GB tumor, with the position of the four MRSI slices, (C) MRSI grids overlaid on axial T2w images, and blue arrows point to (D) the nosological images obtained with the source contribution analysis system [2].

1.6.3   State-of-the-art in MRSI and current practices

Over the last few years, with continuous enhancement and refinement in MRS/MRSI methods, including faster data acquisition and processing and higher magnetic field strength magnets, spatial as well as temporal resolution have improved significantly. For more global coverage, the 2D MRSI can be extended to 3D which allows fast and higher resolution MRSI as reported by Li

et al [46] and can be further combined with spatiospectral encoding schemes such as SPICE which is SPectroscopic Imaging by exploiting spatiospectral CorrElation [47]. Furthermore, several new approaches improving MRSI of the brain have been reported which include combining other techniques such as Compressed Sensing [48] and parallel imaging such as SENSE with MRSI . The SENSE-MRSI was applied to clinical studies in brain tumor patients [49] and shortly afterwards SENSE-MRSI was also implemented as a commercial option by a major vendor and is utilized in clinical diagnostics today on a regular basis [50].To overcome long scan times associated with MRSI, several acceleration schemes have also been proposed which include undersampling the k-space and using non-caretsian trajectories such as radial, rosette etc however their use is limited since the spectral aliasing is more problematic.Most of these advanced strategies have been proposed for clinical applications and their pre-clincal equivalents remain scanty. Translating clinical MRSI techniques to the preclinical settings involves addressing various technical challenges including adjustments in hardware, software, and acquisition protocols. The limited SNR and resolution due to small animal sizes adds to the hurdles. Overcoming these technical challenges in the preclinical setting requires extensive engineering efforts and validation studies. Hence, we anticipate that our efforts in improving resolution and SNR in preclinical studies will contribute towards facilitating the advanced preclinical strategies.

1.7 Bruker Pulse Sequence Programming

1.7.1   Introduction to Bruker pulse programming

In this section, we introduce some of the main concepts of Bruker pulse programming that were required to implement the pulse sequences on the Bruker 7T preclinical scanner as part of the work done for this PhD project.

Before moving on to complex sequences, let us remember that most MR methods require the application of sequences of RF pulses, magnetic field gradients, and delay times between them, and the combination of these elements is termed a pulse sequence. A pulse sequence is hence a sequence of events including RF pulses, gradient waveforms, and data acquisition. The purpose of the pulse sequence is to manipulate the magnetization to produce the desired signal. The sequence of pulses actually executed during the measurement is defined by the parameters selected directly by the operator and the variables defined in the method files [51]. In Bruker ParaVision (PV5.1), all pulse programs basically include synchronization of pulse trains, RF pulse generation, data acquisition, control of data flow expressions, control of other hardware units and gradient control [51].

The flexibility of MR is largely due to the capability to combine such elements in different sequences to perform different functions. The simplest sequence to obtain a spectrum would be a delay (to establish spin equilibrium) followed by a single RF pulse followed by data acquisition (Figure 1.7). More complex patterns of combinations of multiple pulses, gradients, and delays are used for such purposes as measuring relaxation times, obtaining T1- or T2-weighted images, and for water signal suppression.
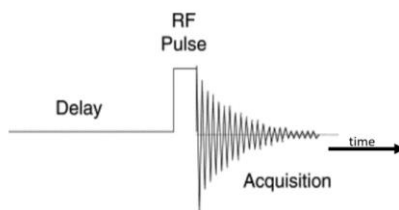
Figure 1.7.1.Pulse sequence diagram for a pulse and acquire sequence [51]

For MR studies our group has access to a 7T Bruker BioSpec 70/30 USR scanner, located at the SeRMN of UAB, which runs on a Linux computer using ParaVision 5.1 software (Bruker BioSpin GmbH, Ettlingen). The ParaVision 5.1 software package enables acquisition and reconstruction of datasets employing standard techniques as well as user-defined schemes. The package includes TOPSPIN 2.0 for NMR data acquisition, processing, plotting, analysis and simulation as well as MRS techniques, such as localized single voxel spectroscopy and Spectroscopic imaging (CSI).

The pulse sequence in *ParaVision* is set up using a text editor and stored as a text file**.** By convention, filenames containing pulse programs usually have a suffix .ppg. Pulse programs are ASCII text files stored in the directory exp/stan/nmr/lists/pp for Bruker methods and prog/curdir/<user>/ParaVision/exp/lists/pp for User methods in the ParaVision File Tree. Pulse program commands correspond to (base level) parameters. The single Parameter Editor allows to inspect and change any base level parameter. The training method baselevel Acquisition allows easy access to all relevant base level parameters.

1.7.2   Method structure and how to create a new Method

Methods are programmable components of ParaVision providing a user-friendly interface. The acquisition and reconstruction of data are two basic parts of a ParaVision Method (PVM). In general, the role of a method is to provide high-level parameters for experiment description, assign initial values to the parameters in a New Scan, decide which parameters should be visible, editable and saved in protocol files, respond to loading a protocol, respond to changes of parameters made by the user in the Geometry Editor, Scan Editor, Method Editor, or by a shell command, check if the new parameter values are allowed, and if all parameters are compatible with each other and derive base-level parameters from high-level parameters [51]. Examples for ParaVision Methods include MSME, FLASH, EPI, CSI, etc**.**

The method source code is written in the C language with a few extensions (e.g. the syntax of parameter definition) and is divided into several files, all contained in one directory. Table 1.4 gives the list and description of some common parameters used in Method files.

Table 1.4 Bruker pulse sequence Method parameters

FILE NAME	DESCRIPTION
methodname.c	A glue file always bearing method name. Not modified.
Method.h	Provides the link to necessary header files and is identical for all methods, needs no modification.
relProtos.h	Provides the link to function prototypes. Identical for all methods, needs no modification.
parsTypes.h	Contains user defined parameter types
parsDefinition.h	Contains definitions of parameters. Can be modified for new parameter definitions.
parsLayout.h	Defines the layout in the method editor. Can be modified for layout changes.
callbackDefs.h	Redirection of global (predefined) parameter relations.
InitMeth.c	Contains code of the initMeth function (required)
loadMeth.c	Contains code of the loadMeth function (required)
parsRelations.c	Contains all parameter relations. Can be modified to introduce new relations.
BaselevelRelations.c	Contains functions for setting ACQP parameters. Can be modified for function descriptions.
RecoRelations.c	Contains functions for setting RECO parameters. Can be modified.
Makefile	Not modified.

The structure of a method can be divided into two parts i.e. the internal PV code and the PV method code. The PVM part consists of definitions of global parameters and their very simple default relations. At this level all parameters remain independent. In the method part, it is first decided which of the global parameters should have their relations redirected to some local code. Such redirections can be made for single parameters and for group handlers. Additionally, local parameters and their relations are defined in the method code, as well as the loadMeth and the initMeth files. All local relations as well as initMeth make a call of the backbone routine, in which all dependencies between parameters are programmed. Toolbox functions may be used for this purpose, in particular the group updaters. Finally, at the end of backbone(), local functions are called to set the ACQP and RECO parameters SetBaseLevelParam() and SetReco-Param(). Figure1.7.2 presents the Bruker Method arrangement graphically [51]**.**
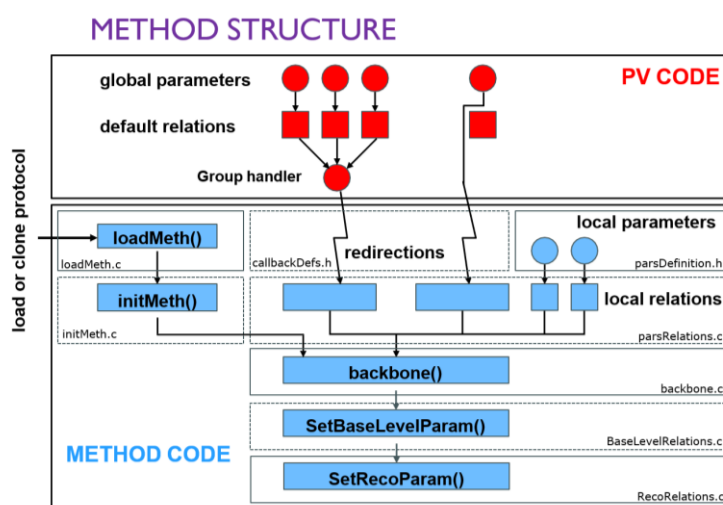
Figure 1.7.2 Bruker PVM Method structure [51]

The steps required to setup or create a new method from an existing Bruker method are listed as follows;

1. Go to System tools----> Terminal(bash)
2. In bash type, **cd/opt/Pv5.1/prog/parx/src/Method name**
3. Once the directory changes to selected method, write the command **/opt/Pv5.1/prog/bin/copyMethod**
4. Follow the instructions
5. Compile the method by first typing **make clean cproto depend** followed by **make install**. The first step is needed for the first compilation and each time a new function is added. Any other changes in the code need only the second step, which is much faster.
6. The .ppg file of the new created method must be copied to **opt/ Pv5.1/ exp/ stan/ nmr/lists/pp**
7. The method.so file must be copied to **opt/ Pv5.1/ prog/ parx/methods**
8. ParaVision 5.1 needs to restart to make the newly compiled method available to the user.

1.7.3   Bruker pulse sequence timing diagram

The pulse sequence timing diagram is a graphical representation of the pulse sequence which enables the viewer to visualize all the delays and applied RF and gradient pulses. The sum of delays and pulse lengths starting from the middle of the excitation pulse till acquisition time gives the total Echo time (TE). Figure 1.7.3 shows, as an example, a section of the timing diagram for an implemented single voxel (SV)-semiLASER sequence (discussed in chapter 4.3). The diagram depicts the exact timing of the RF pulses, phases and amplitudes as well as the delay intervals. It also shows the gradient and crusher amplitudes and hence is a useful tool for pulse sequence programming to visualize the incorporated changes in the sequence.
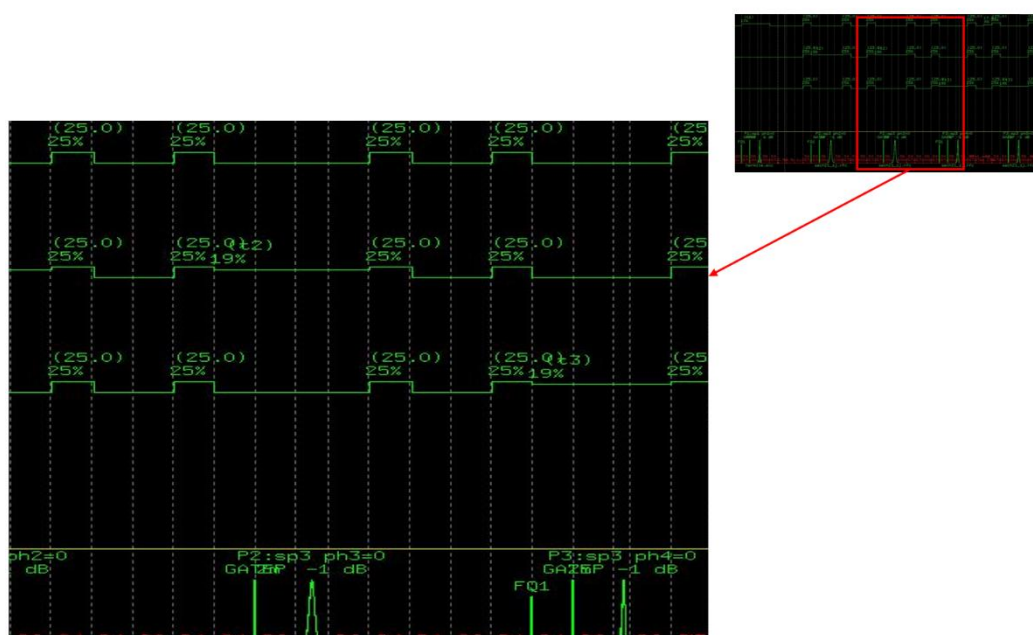
Figure 1.7.3 Screenshot of a section of the Bruker timing diagram for SV-semiLASER sequence

1.7.4 Delays

The pulse program controls the exact timing of an MR-Experiment. The starting point and duration of each action are specified with the help of delay commands which dedicate an amount of time to an action. In Bruker programs, the delays are written with prefix D0-D63 (64 predefined delays). These delays can be divided into the following:

1. Fixed delays
2. Variable delays
3. User-Defined delays

The fixed delays specify the absolute time for a duration. They are built out of a non-negative fixed-point number and a time unit. Valid time units are s for seconds, m for milliseconds and u for microseconds. The time unit must be added to the length without a blank e.g. 1u, 17.3m etc. Variable delays that depend on other parameters and user defined delays can also be used.

1.7.5 Gradients

In Bruker systems, the gradient characteristics are defined by the information stored in the preemphasis file. The preemphasis parameters include the gradient strength, the gradient ramp and rise times, the amplifier and gradient filter characteristics, the gradient ramp shape, etc. The default preemphasis file (filename default) is used by all PVM imaging and spectroscopy methods. Some methods allow the activation of method or protocol specific dedicated preemphasis files. These preemphasis files have different names and are user defined. All preemphasis files reside in the directory:

$XWINNMRHOME/exp/stan/nmr/parx/preemphasis/<grad_status>/

The correct setting of preemphasis parameters has an important impact on the image geometry, the pulse program timing and on the image quality. Therefore, preemphasis parameters are normally set by the BRUKER service team upon installation of the system.

The time that is physically used to ramp up or down a gradient pulse is called the **Gradient Ramp Time**. The Gradient ramp time is defined for each of the x, y and z gradients. The **Gradient Rise Time** is a nominal delay that equals the areas under the gradient ramp to a value given by 0.5*RiseTime*GradientAmplitude. This nominal time is used in the PVM methods for accurate gradient calculations. The **duty cycle** macro can also be run to see the performance of the gradient.

1.7.6 Adiabatic pulse generation using TOPSPIN

The Bruker ParaVision 5.1 contains built-in blocks for adiabatic excitation and inversion pulses only. Hence to use adiabatic refocusing pulses, the shaped pulses need to be generated by the user. The hyperbolic secant (sech) pulses show good adiabatic behaviour and have a pulse profile identical to inversion pulses.. In contrast to the conventional pulse shapes such as Hermite, the sech pulse uses amplitude as well as phase modulation of the B1 field. On the 7T Bruker scanner, the sech refocusing pulses can be generated using the TOPSPIN tool 'stdisp'. The steps to generate an adiabatic refocusing pulse are explained in detail in appendix (i).

Chapter 2 :Thesis Objectives

2.1 MOTIVATION

Our group has a long track of using CSI-based nosological images to provide metabolomic information for treatment monitoring in murine brain tumors. However, tumor inhomogeneities and the small mouse brain volume may compromise spectrum quality when using the Bruker commercially available PRESS-CSI sequences. There are other MRSI pulse sequences, which are not implemented in our scanner, that may be less sensitive to field inhomogeneities and offer better excitations profiles. One such example is the semiLASER sequence which is a robust localization technique for ^{1}H-MRS and can be used as an alternative to PRESS and CSI sequences for single and multi voxel localization.The clinical MRS community recommends the use of semiLASER due to its recent validation studies and increasing availability on clinical systems, as both research work-in-progress sequences and commercial product [52] [53]. Furthermore, in consensus surveys, semiLASER was ranked as the most likely localization technique to improve clinical MRS. Although in wide use clinically, the preclinical uptake of semiLASER still remains a question especially for old scanner setups and requires expensive hardware and software upgrades. Hence, the need arises to perform an inhouse implementation of the semiLASER sequence to provide an alternative data acquisition technique in addition to the stock Bruker methods. It was aimed to implement this current best-practice (semiLASER based) and latest research (reduced and alternative k-space) MRSI acquisition methods on a pre-clinical scanner for brain longitudinal studies in mouse glioblastoma models. The evaluation of the methodology performance limits, repeatability and reproducibility compared to stock Bruker Biospec MRSI sequences and the assessment of speed-up MRSI methods in a 7-Tesla pre-clinical scanner was also performed.

2.2 Objectives

The main objective of this thesis was the implementation of high-resolution MRSI methods in a pre-clinical 7T Bruker Biospec scanner, and its optimization for brain longitudinal studies of therapy response in mice glioma models

The specific objectives of this thesis have been the following:

O1. Implementation of Single voxel (SV) and multi-voxel (MRSI) semiLASER sequences and evaluation of their performance limits, repeatability and reproducibility.

O2. Comparison of newly implemented vs. stock Bruker BioSpec sequences.

O3. Assessment of speed-up MRSI methods in a 7-Tesla pre-clinical scanner.

2.3 Thesis Methodology or Scope

The current thesis was originally motivated by our interest in high resolution spectroscopic acquisition methods and their implementation and optimization on ParaVision 5.1 which runs the 7T Bruker Biospec scanner at the SeRMN of UAB. A pre-requisite to learn and understand the operation of the Bruker Biospec spectrometer is to gain expertise over the working of ParaVision 5.1 software. Obtaining basic MR images using the MSME and RARE methods, acquiring single voxel spectra using localization techniques such as the PRESS sequence and analysing the obtained spectrum using TopSpin was the first learning step.

The next milestone was to implement sequences on ParaVision using Bruker pulse programming. To lay the grounds for understanding the Bruker pulse programming, a test sequence named PRESS_Slice was implemented to perform a single-slice MRS acquisition by creating a spin echo with the help of a 90° slice-selective excitation pulse and a 180 degree refocusing pulses. The method codes were modified to adjust the echo times and the method was compiled successfully. This learning helped in fulfilling one of the main thesis objectives which is the Implementation of single and multi-voxel semiLASER methods.

To facilitate the sequence implementation and testing process, different types of phantoms (control samples) were designed and prepared in order to test performance of the different MRS/MRSI sequences and protocols depending on the expected outcomes. For example, to begin our investigations, we started the pulse sequence implementation by using simple phantoms containing only water and ethanol. Other phantoms were also prepared for specific experimental goals. Later on, to mimic the metabolites present in mouse brain, control phantoms were made containing metabolites at physiological concentrations such as 12.5mM N-Acetyl Aspartate (NAA), 10mM Creatine (Cr) and 10mM Lactate (Lac) were used.

To evaluate the performance comparison between the vendor and the implemented sequences, several quantifying parameters were identified. The Signal to Noise ratio (SNR) is a limiting factor due to low metabolite concentration and sensitivity. The SNR of an MRS spectrum is mainly governed by the effective voxel volume and the number of signal averages. The SNR between methods was compared under similar scan times and parameters. Differences between the spatial spectral homogeneity were identified as well as by using different parameters such as SNR maps, intensity maps, and histogram and boxplot analysis. The repeatability and reproducibility of the results was also determined for the implemented SV-semiLASER and MRSI-semiLASER sequences. The performance of the sequences was quantitatively evaluated using control samples (phantoms) and in-vivo wt and tumor mouse brain.

The increased SNR provided by the MRSI-semiLASER allowed us to extend our limits and increase the MRSI spatial resolution acquiring an extra slice within the same tumor volume by reducing the slice thickness. Five consecutive 0.8 mm slice thickness grids were acquired individually across the tumor in a GL261 tumor-bearing mice. These five slices covered the same volume as the four 1mm slices that would be acquired with our previous protocol. The sequence was further improved by combining with k-space weighting techniques such as elliptical, weighted and standard.

Several inhouse post processing scripts were also developed to facilitate the analysis and quantitation of the acquired datasets using the implemented pulse sequences. The scripts were specifically written with the goal to facilitate the processing of BRUKER acquired 2dseq files in MATLAB. The data processing included post processing of the MRS and MRSI acquired data as well as the processing of the spectra from multiple locations simultaneously leading to a large amount of data to be processed. The different scripts were developed in combination with other post processing softwares such as the FID-A to meet the needs of more efficient data processing and spectra analysis tasks. Lastly the implemented SV-semiLASER and Bruker PRESS sequences were simulated using NMRSCOPE-B jMRUI plug-in and different test conditions were also visualized.

Chapter 3: General Materials and Methods

In this chapter, the general materials and methods used during this PhD work are described. The data collection techniques and methods are defined in general, the acquisition parameters are recorded for both in-vivo and in-vitro studies and the quantifying parameters used to test the efficacy of implemented methods are also presented. The UAB NMR facility has a 7 T Bruker BioSpec 70/30 USR spectrometer for MRI/MRSI in-vitro and in-vivo preclinical studies, as well as several high field NMR spectrometers and a DNP hyperpolarizer, among other equipment. The mice used for experiments are housed in the animal facility of the *Universitat Autònoma de Barcelona*. For my research, the software tools utilized for data acquisition and processing include JMRUI, Paravision 5.1 and Matlab2013 (Mathworks, USA).

3.1 Bruker 7T Biospec preclinical scanner and 300MHz High Resolution NMR spectrometer

3.1.1 Bruker 7T Biospec scanner

In vivo MRSI studies were performed at the joint nuclear magnetic resonance facility of the *Universitat Autònoma de Barcelona* and *Centro de Investigación Biomédica en Red-Bioingeniería, Biomateriales y Nanomedicina* (CIBER-BBN) (Cerdanyola del Vallès, Spain), Unit 25 of NANBIOSIS (www.nanbiosis.es). All MRS/MRSI experiments were performed on a 7T Bruker Biospec 70/30 USR preclinical scanner using ParaVision 5.1 (Bruker BioSpin GmbH, Ettlingen, Germany) equipped with a mini-imaging gradient set (400 mT/m) (Figure 3.1 (A)). The scanner is installed at the *Servei de Ressonància Magnètica Nuclear* (SeRMN) at the *Universitat Autònoma de Barcelona* (UAB). Different coil setup configurations were used depending on the specific study, which are described later.

A 7T Bruker BioSpec 70/30 USR scanner   **B** 300 MHz NMR High Resolution spectrometer

Figure 3.1.1 (A) 7T Bruker Biospec 70/30 USR scanner and (B) High resolution 300MHz AVANCE NEO spectrometer at the SeRMN UAB.

3.1.2 High Resolution 300 MHz spectrometer

Figure 3.1 (B) shows the High resolution 300MHzNEO console spectrometer equipped with TOPSPIN software, also installed at the SeRMN. The spectrometer includes a Nanobay AVANCE

nanoNEO console, ultra-shielded ASCEND magnet and a BBFO probe head, and was used for comparative studies and verification of phantom sample solutions.

3.2 Phantoms

Phantoms designed to mimic specific in vivo features are essential in medical imaging, and are employed in many MRI/MRSI applications [54]. Phantoms can be used to perform the validation of specific scan methodologies and help in the preparation of scan protocols. Reproducible and reliable phantoms were prepared to help in the in-vitro validation of the implemented sequences of this PhD work.

Initial phantoms were prepared using spherical glass containers since the spherical design improves magnetic field homogeneity and uniformity characteristics inside MRI scanners [55]. Figure 3.2.1 shows pictures taken from the various phantoms used in this thesis. Their composition and research purpose are summarized in table 3.1. Phantom 1, namely a T1 spherical phantom, contained a copper sulphate ($CuSO_4$ in $2H_2O$ (2g/l)) solution with 5mM Gadolinium (Gd) to reduce the T1 relaxation time. Phantom 1 was used in the initial stages of pulse sequence implementation where a well-defined and symmetric peak, with no spurious signals in the spectrum baseline, was expected if the sequence was properly performing. Phantom 2 was named the Ethanol-H_2O spherical phantom and consisted of alcohol (ethanol) dissolved in water in a 1:3 ratio. Phantom 3 was used in sequence implementation experiments for visualizing more than one resonance, i.e. water as well as ethanol, in the obtained spectra.

To facilitate experiments testing voxel localization, a two-compartment phantom (phantom 4) was prepared in a 15 mL Falcon tube using red-coloured 2% agarose in water to form a distinguishable water layer, and colourless baby oil as fat layer. The water layer was prepared using 0.1 g agarose dissolved in 50 mL of water and some red food colour to differentiate between the two layers. 7mL of this solution was added to the 15mL falcon tube and left overnight in the refrigerator to solidify. The fat layer was prepared using baby oil and was added in the phantom just before the experiment to avoid diffusion of the two layers. Even though the baby oil was slowly and carefully added, some small air bubbles were still noticeable in the fat layer. Figure 3.2.1 shows the two-compartment phantom prepared in-house.

For experiments to test the chemical shift displacement effect, a two-chamber cylindrical phantom (phantom 7) filled with two different metabolite solutions was prepared. The inner chamber consisted of a 5mm diameter NMR tube cut to a short length (not recorded) to fit inside the cylindrical 1.5cm diameter syringe used as container (Figure 3.2.1). The inner chamber was completely filled with NAA (12.5mM) solution in PBS and the outer chamber was completely filled with Cr (20mM) solution in PBS by carefully avoiding any air bubbles.
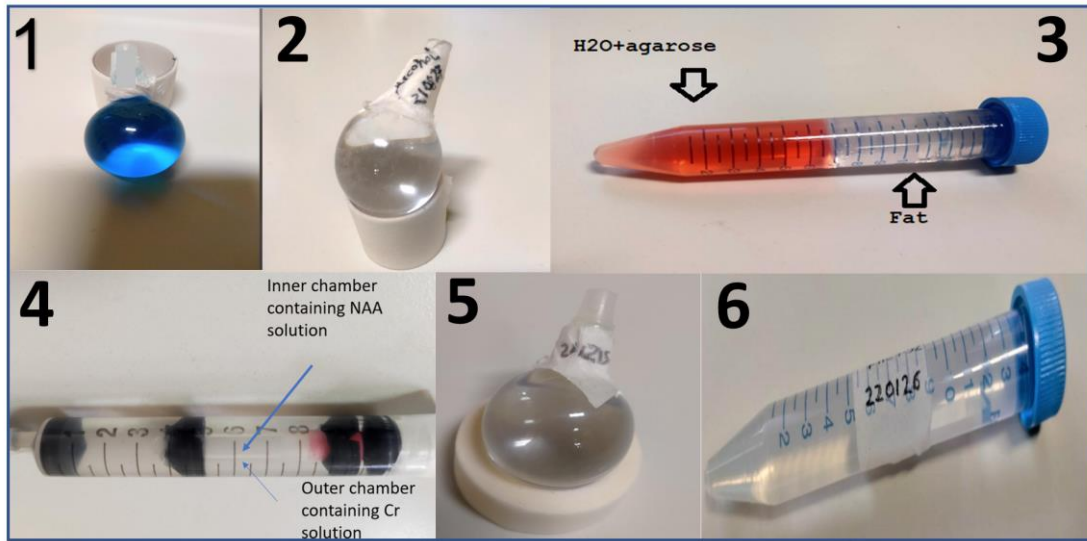
Figure 3.2.1 Phantoms containing metabolite solutions used during this thesis. See text and table 3.1 for further details. The number at top left for each one allows further tracking.

Table 3.1 Metabolic concentrations present in phantoms

Phantom number	Phantom Name	Composition	Purpose
1	T1 spherical phantom	$CuSO_4$ (2g/l) in ^2H_2O, with 5mM Gd chloride	Used in initial tests for well-defined single water resonance detection
2	Ethanol (CH_3-CH_2OH) in H_2O spherical phantom	1:3 ratio	Used in sequence implementation testing
3	Two-compartment phantom	2% agarose in water and baby oil (fat)	Used for voxel localization tests
4	Two-chamber phantom	12.5mM NAA (inner chamber) and 10mM Cr (outer chamber) in distilled water	Used for Chemical shift displacement (CSDE) tests
5	High metabolite concentration spherical phantom **(Phantom A)**	125mM NAA, 20mM Cr , 50mM Lac, Phosphate Buffer (PBS) containing 157 mM Na^+, 140 mM Cl^-, 4.45mM K^+, 10.1 mM HPO_4^{2-}, 1.76 mM H_2PO4 and 4.1 mM Sodium Azide (NaN_3). pH adjusted at 7.07.	High concentration phantom used for Volume Tx/Rx configuration tests
6	Low metabolite concentration cylindrical phantom **(Phantom B)**	12.5mM NAA, 10mM Cr , 5mM Lac, Phosphate Buffer (PBS) containing 157 mM Na^+, 140 mM Cl^-, 4.45mM K^+, 10.1 mM HPO_4^{2-}, 1.76 mM H_2PO4 and 4.1 mM Sodium Azide (NaN_3).pH adjusted at 7.52.	Brain phantom used for volume Tx and surface Rx configuration and repeatability and reproducibility tests

Once the sequences were fully implemented, in order to evaluate their performance, reproducibility and repeatability, we prepared more stable and reproducible phantoms. In particular, two phantoms, namely **Phantom-A (phantom 5)** consisting of high concentration metabolites in a spherical glass container and **Phantom-B (phantom 6)** having low concentration metabolites in a cylindrical falcon tube were also prepared to obtain the final experimental results.

The high metabolite concentration spherical phantom, Phantom-A, contained a high concentration metabolite solution in a spherical glass container (9 mm in diameter) (Figure 3.2.1) with a total volume of 12mL. The spherical shape was selected for its improved magnetic field homogeneity and uniformity as stated earlier. The phantom solution preparation was based on the protocol for "the Realistic head-shaped phantom" [54] with some modifications. Three mouse brain-mimicking metabolites, N-Acetyl Aspartate (NAA, 125 mM), Creatine (Cr, 20 mM) and Lactate (Lac, 50 mM) were added to the phantom at higher than physiological concentrations and within solubility limits for those metabolites. Full composition for phantom 7 can be check in Table 3.1. These metabolites were particularly chosen because they are routinely observed in mouse brain MRS. Their concentrations are clearly higher than in healthy brain tissue, but this was a compromise to be able to acquire test spectra fast, by reducing scan accumulations, when using the more homogenous 7.2 cm volume coil, which provides less SNR than the mouse brain surface coil used in in-vivo mouse brain experiments.

In the design of the phantom object, it is important to consider whether the phantom is stable over the time period that is needed to complete the study. The phantom's solvent may slowly evaporate or the signal generating metabolites in the phantom may change over time as a result of micro-organism activity. To prevent bacterial growth, Sodium Azide (NaN$_3$)(0.27 g/L) (4.1mM) was added to prolong the lifetime of phantoms A and B, allowing pattern stability along time.

A phosphate buffer saline (PBS) solution was prepared using the recipe given in literature [56]. The resultant 1× PBS has a final concentration of 157 mM Na$^+$, 140mM Cl$^-$, 4.45mM K$^+$, 10.1 mM HPO$_4$ $^{2-}$, 1.76 mM H$_2$PO4$^-$ and a pH of 7.96. The buffer saline was added to the Phantom-A solution to maintain a constant pH. The pH of the Phantom-A after adding the PBS was recorded at 7.07.

The low metabolite concentration cylindrical phantom, Phantom-B, (Figure 3.2.1) was prepared by using the same recipe as Phantom-A but having lower concentrations of the metabolites of interest as detailed in Table 3.1. (12,5 mM NAA, 10 mM Cr, 5 mM Lac). Such lower concentrations were chosen to better mimic the mouse brain (or mouse brain tumor) actual metabolite concentrations and to be used when acquiring spectra with the in-vivo mouse brain surface coil configuration. A cylindrical Falcon tube (15mL) was used as a container for Phantom-B construction, because it perfectly fits the mouse brain surface coil. The final pH of Phantom-B was recorded at 7.52 after adding PBS. No further changes were made to the phantom contents.

Minor variations of the before described phantoms were also used (see section 4.3.3.1) and will be detailed when required.

The phantoms can be replicated using the same preparation strategy in the future, if needed. Phantoms were utilized for evaluating the performance of new implemented MRS acquisition pulse sequences.

3.3 Animal preparation

In-vivo experiments were performed using C57BL/6 female mice (figure 3.3.1) which were obtained from the Charles River Laboratories (France) and housed at the animal facility of the Universitat Autònoma de Barcelona (*Servei d'Estabulari*). All animal studies were approved by the local ethics committee, according to the regional and state legislation (protocol DARP3255/CEEAH-530). GL261 mouse glioma cells were obtained from the Tumor Bank Repository at the National Cancer Institute (Frederick/MD, USA) and were grown and implanted into the mouse brain as previously described by our group [2] [57].

For MR scanning, mice were positioned in a bed, which allowed delivery of anaesthesia (isoflurane, 1.5%-2.0% in O_2 at 1 L/min), with an integrated heating water circuit for body temperature regulation. Respiratory frequency was monitored with a pressure probe and kept between 60 and 80 breaths/min.

Figure 3.3.1 C57BL/6 female mouse

3.4 Single voxel and MRSI acquisition parameters

3.4.1 MRS studies

To visualize the anatomical structure of the mouse brain and check the accurate placement of voxel position, high resolutionT2w coronal images were acquired using a Rapid Acquisition with Relaxation Enhancement (RARE) sequence. The acquisition parameters were as follows: repetition time (TR)/effective echo time (TEeff) = 4200/36ms; echo train length (ETL) = 8; field of view (FOV) = 19.2 × 19.2 mm; matrix size (MTX) = 256 × 256 (75 × 75μm/pixel); number of slices (NS) = 10; slice thickness (ST) = 0.5 mm; inter-ST = 0.1 mm; number of averages (NA) = 4; total acquisition time (TAT) = 6 min and 43 s [2] **.**

The single voxel PRESS and SV-semiLASER studies with water suppression were performed using the following acquisition parameters: echo time (TE) = 12 or 20ms for PRESS and TE=16ms or 20ms for SV-semiLASER; repetition time (TR) = 2500ms; Dummy scans (DS) = 4; number of averages (NA) = 128; VAPOR water suppression and outer volume suppression (OVS); voxel size = $(3mm)^3$; Npoints = 2048; SW = 13.34 ppm (4006.41 Hz); spoiler strength = 25% and total acquisition time (TAT)=5min 30s.

3.4.2 MRSI studies in wt mouse

Single MRSI gird consisting of matrix size of 8x8 interpolated to 32 x 32, thus resulting in a voxel matrix size of 12 x 12 was acquired. To ensure quality of the acquired data, shimming was performed individually for each MRSI grid. The acquisition parameters were kept as follows; TE = 14ms for CSI-PRESS and TE=27ms for MRSI-semiLASER; TR= 2500ms; DS = 4; FOV = 1.76 x 1.76 cm^2, gridsize = 6.6 x 6.6 x 1 mm^3; Acquisition mode = weighted (k-space sampled symmetrically applying a Hanning window on a 13x13 imaging grid, 12 accumulations in the centre of k-space with a total of 512 scans), Npoints = 2048 ; SW = 13.34 ppm (4006.41 Hz); VAPOR water suppression and 10 mm thickness saturation slices positioned around the voxel to help reduce outer volume contamination.

3.4.3 MRSI studies in GB tumor (GL261) mouse

Consecutive 14 ms TE CSI-PRESS localization grids were acquired individually across the tumor, using as a reference T2w high resolution images. The first upper (dorsal) grid (Grid 1) (see also figure 1.6.2) had a matrix size of 10 × 10 followed by Grid 2 which was acquired 1 mm below Grid 1 with a matrix size of 12 × 12. This slice was followed by Grid 3 with the same matrix size of 12x12. Finally Grid 4 was acquired with a matrix size of 10x10. Each MRSI grid was shimmed individually and the grids were spatially located such that the volume of interest (VOI) included most of the tumoral mass as well as normal/peritumoral brain parenchyma. The same steps were followed for the Grids positioning using MRSI-semiLASER at TE=27ms. The other acquisition parameters were kept the same as in wt mouse studies.

3.4.4 Data Processing

The MRS acquired FID datasets for PRESS and SV-semiLASER were post processed by exporting to Bruker TOPSPIN 2.0 software and applying LB=4, phase correction and Fourier transformation to visualize the spectrum. This was further supported by a GUI based MATLAB script developed for post processing and quantitation of the results,

The MRSI acquired datasets were initially pre-processed at the MR workstation with ParaVision 5.1 (Bruker BioSpin), and then post-processed with 3D Interactive Chemical Shift Imaging (3DiCSI) software package version 1.9.17 (Courtesy of Truman Brown, Ph.D., Columbia University, New York, NY, USA) for line broadening adjustment (Lorentzian filter, LB, 4 Hz), zero and first order phase correction and exporting the data in ASCII format. The post processing pipeline was further supported by in house developed MATLAB scripts for post processing of MRS/MRSI datasets including, group delay correction, zero and first order phasing and exponential multiplication and line broadening. Quantitative results were also obtained using these scripts and the quantitation parameters used are described next.

3.5   QUANTIFYING PARAMETERS

The acquired MRS/MRSI datasets were analysed and quantified on the basis of specific quantifying parameters to investigate potential relationships between pulse sequences and the spectral patterns such as signal-to-noise ratio (SNR), linewidth, mean and standard deviation. The repeatability and reproducibility coefficients were also calculated and the results were summarized with the help of graphical representations, boxplots and histograms, Intensity and SNR maps and Bland Altmann plots. All these parameters are described next.

3.5.1 Signal to noise ratio (SNR)

The signal-to-noise ratio (SNR) is an important parameter used to describe the performance of a magnetic resonance imaging (MRI) system, and is frequently used for image evaluation, measurement of contrast enhancement, pulse sequence and radiofrequency (RF) coil comparison, and quality assurance [58]. SNR is a limiting factor in MRS/MRSI studies due to low metabolite concentration and sensitivity. The SNR of an MRS/MRSI spectrum is mainly governed by coil sensitivity, the effective voxel volume and the number of signal averages. The SNR between methods can be compared under similar scan times and parameters. The SNR of a spectral peak was calculated as the ratio of the height of the peak to the standard deviation of the noise in the baseline. The SNR as given by the equation 3.5.1;

$$\text{SNR} = \frac{|maximum\ peak\ intensity|}{standard\ deviation\ of\ noise} \qquad \text{[3.5.1]}$$

3.5.2 Linewidth

Linewidth is defined as the full-width at half-maximum (FWHM) of the resonance lineshape and is a primary factor affecting both spectral resolution and signal-to-noise ratio of NMR spectra [59]. NMR peaks were fitted to the Lorentzian lineshape. A Lorentzian line can be expressed mathematically (equation 3.5.2) and has three parameters amplitude, linewidth and peak position. Figure 3.5.1 shows the Lorentzian lineshape of an NMR peak.

$$Y = \frac{A\left(LW_{\frac{1}{2}}\right)^2}{\left(LW_{\frac{1}{2}}\right)^2 + 4(X_O - X)} \qquad \text{[3.5.2]}$$
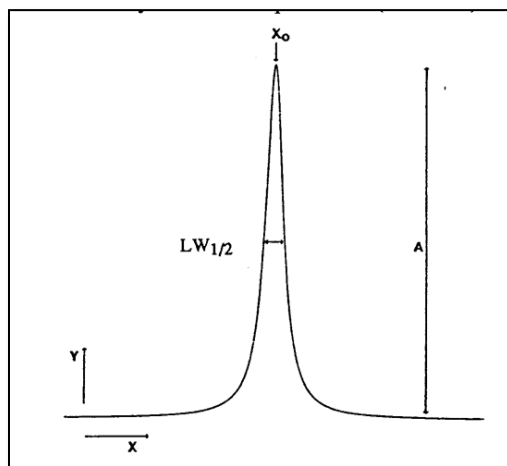
Figure 3.5.1 Lorentzian lineshape of an NMR peak [60]

Where   Y= area under the curve

A= amplitude/intensity

$LW_{1/2}$ /FWHM= full width at half maximum in Hz

x_o= peak position in Hz

The minimum obtainable peak width at half height is directly related to the spectral resolution of an instrument i.e. how close two peaks can be and still be distinguishable. The interpretation of correct linewidths and shapes allows to decide whether the sample was shimmed correctly.

3.5.3 Mean and Standard deviation

The Mean is defined as the mathematical average of a set of values. The Standard deviation is the square root of the variance of a data set. The calculation of mean and Standard deviation are standard statistical measures for analysis of spectra. The mean is calculated as shown in equation 3.5.3;

$$\bar{X} = \frac{sum\ of\ all\ values}{total\ number\ of\ values}$$ [3.5.3]

The mean of the means is a straight forward calculation. This is obtained by summing the means of all samples and dividing by the number of samples. The means of the means ($\mu_{\bar{x}}$) can be given by the equation 3.5.4;

$$\mu_{\bar{X}} = \frac{x_1 + x_2 + x_3\ + ...x_n}{n}$$ [3.5.4]

and the Standard deviation is given by equation 3.5.5.;

$$\sigma = \sqrt{\frac{\sum(x_i - \mu)^2}{N}}$$ [3.5.5]

Where σ= standard deviation

N= size of matrix
x_i= single value
μ =mean

The mean and Standard deviation was calculated using MATLAB.

3.5.4 Coefficient of Variation (CV)

The coefficient of Variation (CV) is a measure to determine the reliability of a method and is defined as the ratio of the standard deviation to the mean, with a smaller percentage indicating a more precise method. CV values below 5% are considered Good indicating high reliability of the tested method, and values between 5 and 10% are found to be in the acceptable range. The CV is given by the formula shown in equation 3.5.6;

$$CV= \frac{standard\ deviation\ (\sigma)}{mean(\mu)}$$ **[3.5.6]**

3.5.5 Repeatability and Reproducibility

The term repeatability refers to the variation in repeated measurements made on the same subject under identical conditions, whereas reproducibility covers many overlapping concepts. It is explicitly defined as the variation of the same measurement made on a subject under changing conditions, but in real-life practice it also includes changes in measurement method, observer, time frame, instrumentation, location, and/or environment [61]. Reliability is the magnitude of error between measurements. It is inevitable that there will be some degree of error in pre-clinical measurements, and the acceptable amount will depend on particular circumstances. The Coefficient of Variation (CV) , already described in equation 3.5.6, is a measure to determine reliability defined as the ratio of the standard deviation to the mean, where a smaller CV indicating a more precise method.

The repeatability and reproducibility can be quantitated by measuring the repeatability coefficient (RC) which is a number that, when two measurements of the same parameter are done under the same conditions, the difference between those two measurements will be less than the RC in 95% of cases [62] [63]. The smaller the repeatability coefficient is, the better the method.The formula for RC is given by equation 3.5.7:

$$\textbf{RC (repeatability coefficient)}=1.96 * \sqrt{2\sigma^2} =2.77\boldsymbol{\sigma}$$ **[3.5.7]**

Where σ^2 is the variability attributed to the measurement error, namely the variance of repeated measurements using the same acquisition method.

3.5.6 Intensity and SNR maps

For MRSI data, the maximum peak intensities and SNR of metabolites were spatially displayed as maps using MATLAB. Maps were plotted using the heatmap command with the jet colorscale, where red indicates highest and blue indicates lowest values for the variable plotted.

3.5.7 Boxplots and histograms

In descriptive statistics, a boxplot is a method for graphically demonstrating the locality, spread and skewness grouping of numerical data through their quartiles [64]. The boxplot display was used to visually compare the SNR differences between the implemented and stock Bruker sequences. On each box, the central mark is the median, the edges of the box are the 25th and 75th percentiles, the whiskers extend to the most extreme datapoints the algorithm considers to not be outliers, and the outliers are plotted separately.

Histograms are very commonly used graphical displays of data to show frequency distributions by using bars of different heights that fall within bins. The data plotted with a histogram is grouped into ranges and the height of each bar shows the number of data that fall within this range. Histogram plots were also used for SNR comparison of the implemented sequences since broader range histograms is an indication of higher heterogeneity.

3.5.8 Bland-Altman plots

The Bland-Altman plot, or difference plot, is a graphical method to compare two measurements techniques [65]. Using this method, we have plotted the differences between two techniques against the averages (mean) of the two techniques. Horizontal lines are drawn at the mean difference, and at the limits of agreement, which are defined as the mean difference plus and minus 1.96 times the standard deviation of the differences. The Bland Altman plots were calculated using Excel.

3.5.9 Statistical Analysis

A one-tailed student's t-test was conducted using excel to evaluate datasets for a one directional increase in SNR when comparing implemented sequences with stock Bruker sequences for compliance with a normal distribution . The significance level for all tests was kept as $p < 0.05$.

Chapter 4: PhD Experiments and Results

4.1 PRESS_Slice sequence implementation

4.1.1   Introduction

In this chapter we present the implementation of a localized spectroscopy method for slice selection called PRESS_Slice. This method was derived from the commercially available method PRESS **[16]** for single voxel spectroscopy studies. The PRESS method consists of a 90° excitation and a 180° refocusing pulse accompanied by slice-selective gradients in the slice thickness direction. The PRESS_Slice sequence was implemented on a 7T Bruker BioSpec 70/30 USR preclinical scanner using ParaVision 5.1 and the testing experiments were performed using phantoms. The results were compared using SNR vs slice thickness studies.

4.1.2   PRESS_Slice method implementation

A slice is a two-dimensional plane that is defined by its dimensions in x and y, and a thickness along the z-axis. The PRESS_Slice method was hence developed using the stock Bruker PRESS as departing sequence but modified such that the sampled NMR signal comes only from an excited slice. Figure 4.1.1 (A) shows the schematic of a simplified PRESS sequence and (B) shows a simplified PRESS_Slice sequence. For the Spin Echo condition to be fulfilled, it must hold that the intervals TE1 and TE2 are equal. The total echo time (TE) is given by equation 4.1;

$$TE= TE1+TE2 \qquad\qquad [4.1]$$

Where TE1 is the interval between half of 90° pulse to half of 180° pulse, and TE2 is the interval between second half of 180° pulse till acquisition (ACQ).

Note that in the PRESS_Slice sequence, the gradients (t1 shown in red) are applied along the same direction to localize only a two-dimensional plane i.e. a slice, whereas in the PRESS sequence, the gradients are applied in all three directions i.e. read, phase and slice to acquire a three-dimensional volume i.e. a voxel.
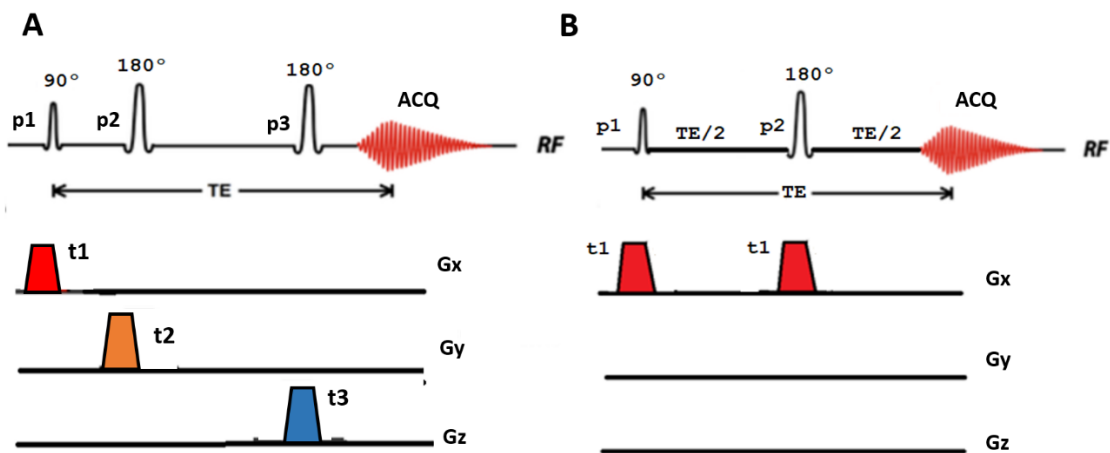
Figure 4.1.1 A) PRESS pulse sequence modified from [23] (B) PRESS_Slice pulse sequence. See text for further details.

Figure 4.1.2. shows the detailed pulse sequence diagram for the implemented PRESS_Slice sequence. The sequence was designed with minimum echo time of TE= 6ms using 700μs Hermite excitation and refocusing pulses. The modifications for the delays and gradients were introduced into the PRESS_Slice.ppg file. The delay calculations for the TE1(μs) and TE2(μs) intervals are shown in Figure 4.1.2.2 where p1 is the excitation pulse, p2 is the refocusing pulse, d6 is GradStabDelay, d4 is PVM_RISETIME, d8 is a fixed delay, and d7m1 and d9 are variable delays.
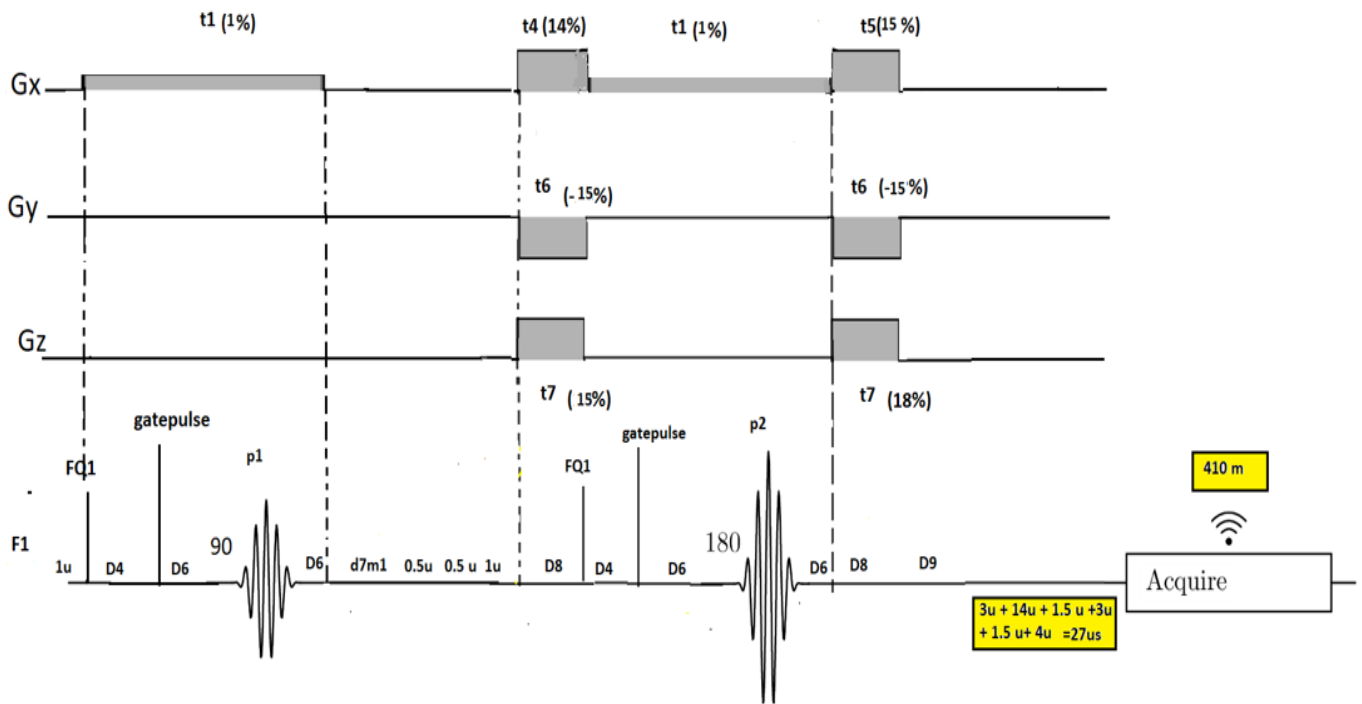
Figure 4.1.2 The detailed PRESS_Slice pulse sequence implemented on the 7T Bruker Biospec scanner at SeRMN

The Bruker method programming files for PRESS_Slice (parsrelations.c, baselevelrelations.c) were modified to adjust:

(1) the echo time intervals between the excitation and refocusing pulses to half the total echo time and

(2) the offset frequency for the slice thickness

4.1.3.   Checking increasing slice excitation direction setups

When a thicker slice is acquired, the signal from a bigger sample volume is averaged, which results in a higher signal-to-noise ratio (SNR). On the other hand, as the slice thickness is reduced, the SNR is reduced by a proportional amount **[66]**.

To test the performance of the implemented PRESS_Slice sequence depending on the expected outcomes of linear SNR increase with slice thickness, a phantom containing homogeneous $CuSO_4$ solution inside a spherical glass container (phantom 1) was used in the initial testing stage. Acquisitions were made using a surface mouse brain coil for reception in combination to a Transceiver [1]H 1000W 7.2 cm Inner diameter volume Coil for excitation. T2w MRI scans were taken, 25 coronal slices each 1.0mm thick and 25 axial slices each 2.0 mm in thickness to cover the entire FOV using a RARE sequence with a rare factor=8, TR=4200ms, TE= 12ms matrix size =

67

128 × 128, FOV = 1.92mm × 1.92mm. A waterline was acquired using the PRESS sequence (TR=2500ms TE=12ms, voxel size= (3mm)^3, NA=1,OVS=off, Npoints= 2048, SW= 13.3ppm, spoiler duration=1.5ms, spoiler strength=25%). The acquisition parameters were kept identical for acquisitions using the PRESS_Slice test method for the sake of comparisons. Although in the PRESS_Slice method setting a voxel size implies exciting a 3mm slice section along the assigned excitation direction.

The thickness parameter was varied by choosing different slices and slice orientations. The excitation direction was chosen orthogonal to the slice. Multiple permutations using different excitation orders, i.e. excitation directions, and slice thickness, were performed to record the effect of increasing slice thickness on the SNR. It was expected to see a linear increase in SNR only when the thickness was changing in the excitation direction. The effects of phase cycling were omitted by choosing DS=4 and Number of averages NA=1 The "patient orientation" was taken as Head first -SUPINE.

For the saggital slice, the excitation order was taken as RL-AP-HF such that RL direction is orthogonal to the saggital slice. The results for changing the slice thickness in the x direction i.e. (RL) red columns, y direction (AP) green columns and z direction (HF) blue columns are given in Figure 4.1.3(A). The SNR increased linearly only when the slice thickness was changed in the RL i.e. x direction.

For the axial slice, the orthogonal slice orientation was set as HF-RL-AP which means slice selection gradients were applied along the z direction. The results for changing the slice thickness in the z direction i.e. (HF) green columns, x direction (RL) red columns and y direction (AP) blue columns are given in Figure 4.1.3(B). The SNR increased linearly only when the slice thickness was changed in the HF i.e. z direction which was the excitation direction in this set of experiments.

Similarly, for the coronal slice, the orthogonal slice orientation was set as AP-RL-HF thus having y as excitation direction. The results for changing the slice thickness in the y direction i.e. (AP) blue columns, x direction (RL) red columns and z direction (HF) green columns are given in Figure 4.1.3 (C). The SNR increased linearly only when the slice thickness was changed in the AP i.e. y direction

Slice orientation	RL-AP-HF (mm)	SNR	Slice orientation	HF-RL-AP (mm)	SNR	Slice orientation	AP-RL-HF (mm)	SNR
Saggital slice	0.5 x 40 x 40	692.82	Axial slice	0.5 x 40 x 40	603.71	Coronal slice	0.5 x 40 x 40	586.87
	1 x 40 x 40	1224.24		1 x 40 x 40	1757.37		1 x 40 x 40	1324.66
	1.5 x 40 x 40	2127.78		1.5 x 40 x 40	2564.35		1.5 x 40 x 40	1796.30
	2 x 40 x 40	2737.24		2 x 40 x 40	2334.41		2 x 40 x 40	2501.89
	40 x 0.5 x 40	22765.61		40 x 0.5 x 40	24976.28		40 x 0.5 x 40	25341.36
	40 x 1 x 40	29143.14		40 x 1 x 40	25373.76		40 x 1 x 40	19879.16
	40 x 1.5 x 40	28954.63		40 x 1.5 x40	24604.67		40 x 1.5 x 40	17645.28
	40 x 2 x 40	21286.14		40 x 2 x 40	28151.74		40 x 2 x 40	22658.37
	40 x 40 x 0.5	26987.01		40 x 40 x 0.5	22913.15		40 x 40x 0.5	23046.19
	40 x 40 x 1	25904.36		40 x 40 x 1	18783.38		40 x 40 x 1	14948.69
	40 x 40 x 1.5	27543.68		40 x 40 x 1.5	23347.98		40 x 40 x 1.5	21990.83
	40 x 40 x 2	16230.27		40 x 40 x 2	18646.19		40 x 40 x 2	20639.67

Figure 4.1.3 (A) SNR values for saggital slice where the slice orientation is taken as RL-HF-AP (B) SNR values for axial slice where the slice orientation is taken as HF-RL-AP. (C) SNR values for coronal slice where the slice orientation is taken as AP-RL-H.F

Figure 4.1.4 graphically demonstrates the effects of increasing slice thickness vs SNR. The changing RL, HF and AP dimensions in the saggital, axial and coronal slice respectively have been plotted. The linear increase in SNR was visible as well as high values of correlation coefficient(R^2) for the fitted curve were obtained in all three slices. The R^2 values for the saggital slice was recorded as 0.9905 , for the axial slice 0.7817 and for the coronal slice 0.9934 indicating high correlation.
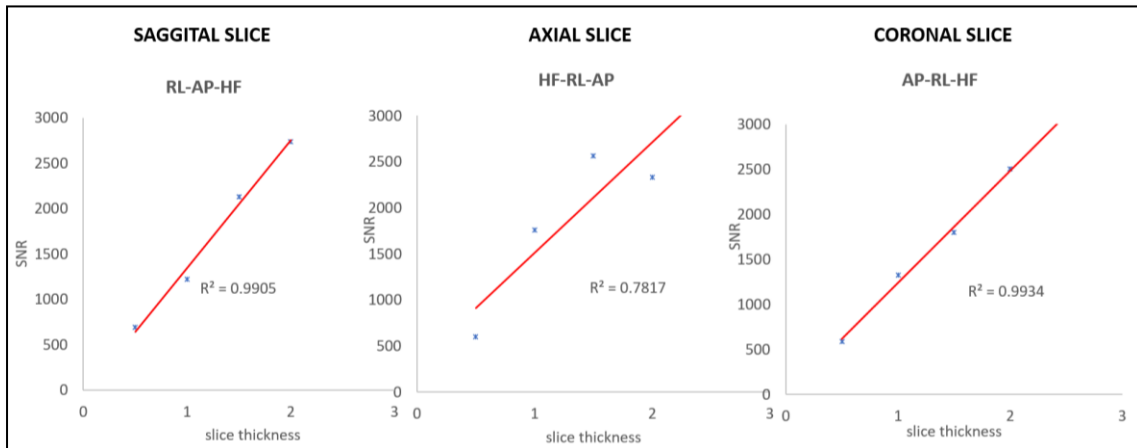
Figure 4.1.4 Plots of SNR vs slice thickness for the saggital, axial and coronal slice when changing the slice thickness in the RL, HF and AP directions respectively. The blue asteriks represent the data and the red line corresponds to the fit. The reslust show a linear increase in SNR vs increasing slice thickness. The coefficient of correlation was recorded as 0.9905 in the saggital slice, 0.7817 in the axial slice and 0.9934 in the coronal slice.

Since the results obtained matched our expectations, we decided to proceed with further experiments to verify the implemented PRESS_Slice sequence.

4.1.4 Single pulse vs Large thickness slice: a signal strength comparison

The purpose of this experiment was to compare the single pulse produced spectrum, to the one obtained from a large voxel with slice thickness of 35mm, while keeping gradient trim values off. The objective was to check whether the SNR obtained using the PRESS_Slice method was the same as the single pulse acquisition while keeping all the acquisition parameters such as the receiver gain (RG), Bandwidth, Npoints and Spectral frequency the same. The acquisition parameters for the single pulse were kept as follows: Npoints=4096, SW=10,000Hz, RG=5.0dB and the acquisition parameters for the PRESS_Slice were kept as follows; TE=6ms, Npoints = 4096, spoiler duration=1.5ms, OVS=off, SW =10,000Hz, RG=5.0dB. The results are shown in Figure 4.1.5. The SNR for the single pulse was recorded as 13681.87 and the SNR for the PRESS_Slice was recorded as 13515.72. The SNR of the single pulse acquisition, which excites the whole volume, was found similar to the SNR of PRESS_Slice when setting the slice thickness to 35mm which is much bigger than the diameter of the phantom, which also means that the whole phantom volume would be excited. It was hence concluded that no signal loses were produced by using the PRESS_Slice method with respect to a standard single pulse acquisition sequence.
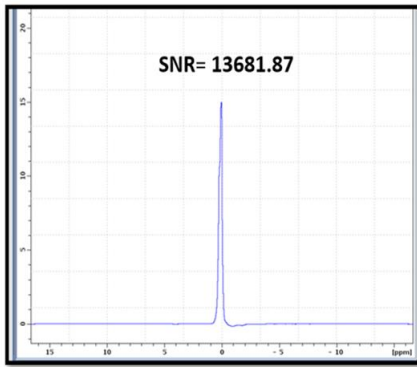
SINGLE PULSE
no of points= 4096, spectral width= 10000Hz, 33.3ppm,,
Receiver gain= 5.00, Basic frequency(BF1)= 300.326306
OF1= 0.0, (run with GOP)
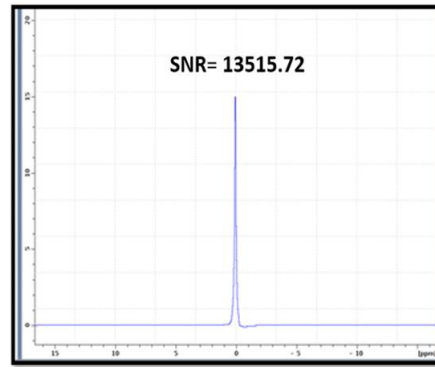
PRESS_SLICE (35mm)
TE= 6 ms, RG=5.0, BF1=300.3263172, TE
Calculation mode= minTE, Spoiler duration= 1.5
ms, Spoiler strength=21%, no of points=4096,
Spectral width=10000Hz, 33.3ppm, OVS=off,

Figure 4.1.5 Comparison of single pulse vs Large thickness slice spectrum acquired using the PRESS_Slice sequence

4.1.5 Testing slice localization

Next, the sequence was tested for adequate localization of the chosen slice using a two-compartment phantom (phantom 3 described in Chapter 3) (Figure 4.1.6 A). This phantom was used to check whether the tested method of slice selection selects slices in the different phantom compartments correctly. The phantom preparation was already described in Chapter 3.

Quantitative volumetric measurements were performed to verify the slice selection using the PRESS_Slice sequence in the two-compartment phantom. Due to the cylindrical shape of the phantom, a QuadTranceiver volume coil was used for excitation and reception. The water unsuppressed acquisition parameters were kept as follows; TE = 12ms, TR= 2500ms, DS= 4, Npoints = 2048, NA = 1, TE calculation mode = equalise, SW= 10 000 Hz (33.3 ppm), OVS= off.

Axial sections were acquired by placing the slice in the two compartments consecutively using PRESS_Slice sequence and the respective spectra were acquired as shown in Figure 4.1.6 B. The water and fat spectra were accurately localized at their respective resonance frequencies ca. 4.7 ppm and ca.1.3 (methylene groups) – 0.9 (methyl group) ppm as shown in Figure 4.1.6 (C and D).
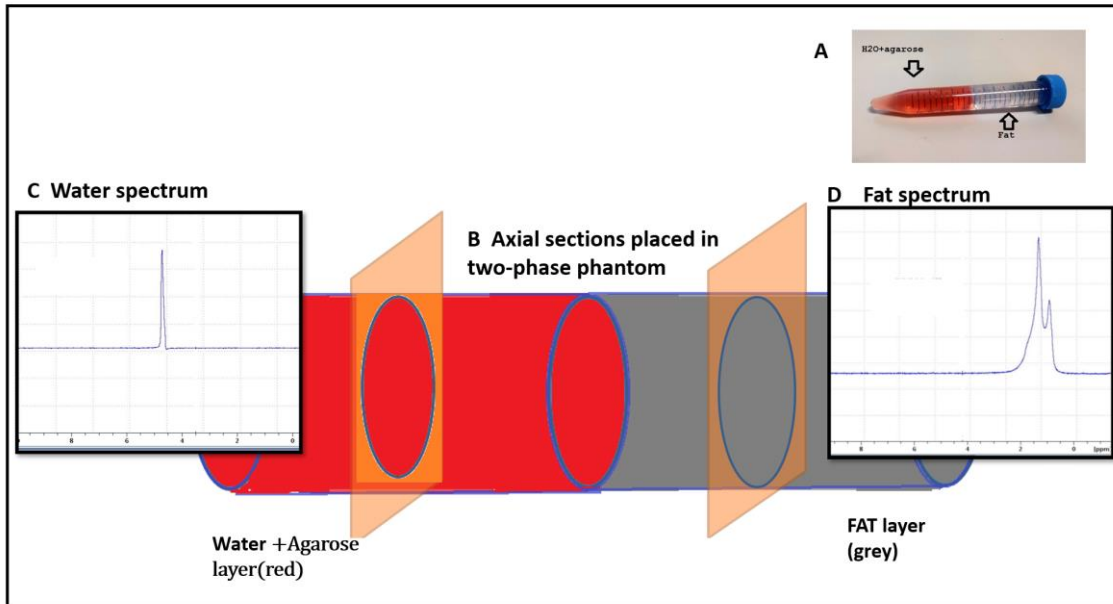
Figure 4.1.6 (A) Slice localization verification using a two-compartment phantom consisting of water in agarose (red) and fat laye (grey). (B) Two axial slices (orange) were acquired one after the other using the PRESS_Slice sequence by consecutively placing the slice in the water layer and fat layer, respectively. Spectra were obtained from each slice. Panel (C) showing water signal at 4.7 ppm and panel (D) showing major fat peaks at 1.3 – 0.9 ppm.

4.1.6 SNR versus slice thickness using the PRESS_Slice sequence

The performance of the PRESS_Slice sequence was further validated by acquiring water spectra at different slice thicknesses. The phantom and experimental parameters were kept the same as reported in section 4.1.5. The slice was positioned at the water layer and the experiments were repeated for n=4 for each slice thickness value to assess reproducibility. The slice thickness ranged from 0.5 mm to 12 mm. The SNR vs the increasing slice thickness (mm) was recorded for each experiment. Figure 4.1.7 shows the plot of linear increase in SNR vs slice thickness (mm) for four experiments.

Table 4.1 shows the values obtained for the mean SNR, standard deviation and the Coefficient of Variance (CV) for the experiments. As the slice thickness increased, the SNR and standard deviation also increased in a linear fashion up till 12 mm. This in turn also caused the Coefficient of Variance (CV) to show some increase, but always below 10%.

.
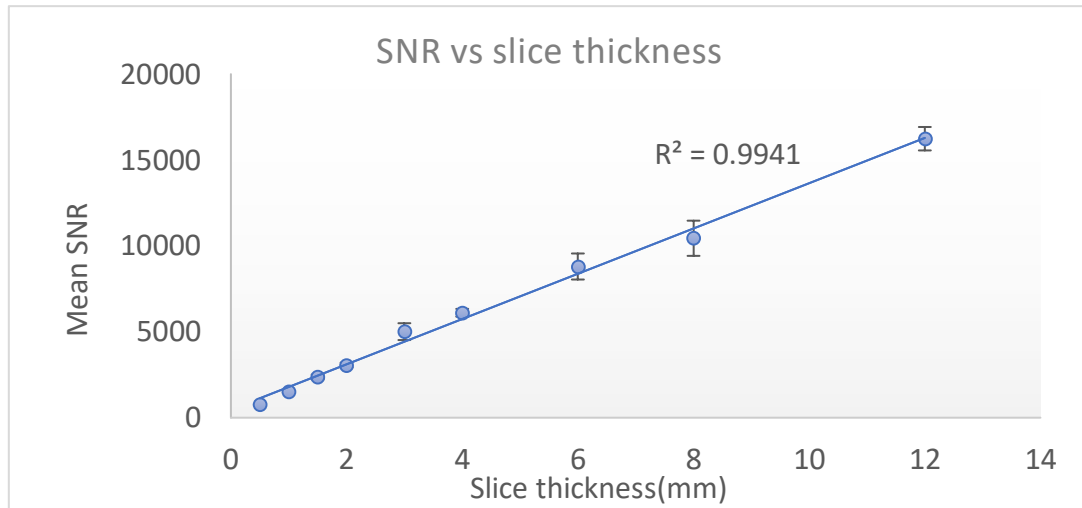
Figure 4.1.7 The mean SNR vs slice thickness (mm) for n=4 repeated experiments. The coefficient of correlationR² had a high value of 0.9941 indicating a linear dependency of the increase in SNR with the increase in slice thickness.

Table4.1 Mean SNR vs slice thickness (mm)

Slice thickness(mm)	Exp 1	Exp 2	Exp 3	Exp4	Mean SNR	standard deviation	CV
0.50	740.21	751.34	783.34	758.81	758.43	18.28	2.41
1.00	1579.00	1539.47	1459.53	1528.23	1526.56	49.71	3.26
1.50	2400.40	2191.15	2540.52	2331.53	2365.90	145.37	6.14
2.00	3003.40	2912.43	3060.48	3248.25	3056.14	141.84	4.64
3.00	5702.20	4888.04	4897.13	4548.86	5009.06	489.69	9.78
4.00	6041.40	6330.30	5821.87	6242.03	6108.90	226.34	3.71
6.00	9695.59	7904.48	9046.60	8557.49	8801.04	757.99	8.61
8.00	11484.90	9233.08	11071.88	9990.79	10445.16	1024.60	9.81
12.00	16170.48	16498.74	15337.57	16956.21	16240.75	682.91	4.20

The experiments were conducted in the water layer of the two-compartment phantom. The SNR for the water peak was recorded for four experiments (Exp1-Exp4) against increasing values of slice thickness. The mean SNR, standard deviation and Coefficient of Variance (CV) were calculated for the four experiments.

4.1.7 SNR comparison for increased number of accumulations (NA) using PRESS_Slice

The number of accumulations (NA), is an important determinant of SNR. SNR, in theory, is proportional to the square root of the number of accumulations as given by equation 4.2 **[67]**

$$SNR \propto \sqrt{NA}$$

[4.2]

Hence, when NA is increased 8-fold, the SNR should increase by 2.8-fold. This can be

appreciated in the PRESS_Slice acquired spectra obtained using the two-compartment phantom already described in the previous section. The acquisition parameters were kept the same while only changing the number of accumulations. Figure 4.1.8 shows the spectra obtained from the water and fat compartments using the PRESS_Slice sequence and the corresponding SNR values. Note that the peaks were sharper in the NA=8 spectrum for both water and fat regions compared to the NA = 1 spectrum using the PRESS_Slice sequence. The SNR increase for slices placed in water and fat regions using the PRESS_Slice sequence was calculated as follows;

Increase in SNR for water peak=$\frac{2211.85}{685.77}$ = 3.2-fold

Increase in SNR for fat peak at 1.3 ppm=$\frac{646.19}{249.92}$ = 3-fold

The increase in SNR with the PRESS_Slice sequence was in agreement with the expected results, and we obtained thinner spectral peaks. The spectra were also accurately localized in the corresponding regions. Hence, we concluded that the PRESS_Slice sequence had been implemented accurately.
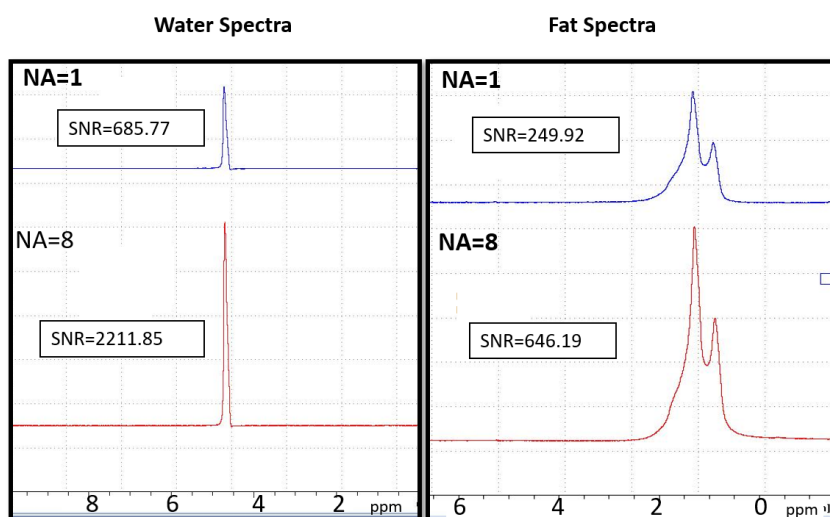
Figure 4.1.8 Comparison of water and fat spectra obtained using the PRESS_Slice sequence for NA=1 and NA=8

4.1.8 Conclusions

The implemented PRESS_Slice method exhibited accurate slice selection. The results were evaluated using signal-to-noise ratio (SNR) and lineshape comparisons. As expected, the SNR increased linearly with the increase in slice thickness. We hypothesized that in order to implement sophisticated high spatial and spectral resolution MRSI sequences, a deep knowledge of the Bruker pulse programming was required. The PRESS_Slice implementation performed was part of the learning process and proved to produce a reliable and accurate method for slice localized spectroscopy, giving reproducible results. The developed sequence could also be of interest in other SeRMN wprk, such hyperpolarization experiments, where slice selection spectroscopy is used but acquiring signal from ^{13}C instead of ^{1}H, and also for educational purposes.

The sequence development results were also accepted as an abstract entitled 'PRESS_Slice: SINGLE SLICE LOCALIZED 1H SPECTROSCOPY' and presented as digital poster at the *XVII Jornada*

Científica del Departament de Bioquímica i Biologia Molecular on 17th June 2021 at Universitat Autonoma de Barcelona (UAB).

4.2. Phantom tests using 300MHz High Resolution NMR spectrometer

4.2.1   Introduction

Phantoms designed to mimic specific in vivo features are essential in medical imaging and are employed in many MRI/MRSI applications [54]. Phantoms can be used to perform the validation of specific scan methodologies and can be used in the preparation of scan protocols. The purpose of this section of the PhD was to prepare reproducible and reliable phantoms, which can help validate in-vitro data acquisition sequences implemented during this PhD work. Two phantoms, namely **Phantom-A** (phantom 5) consisting of high concentration metabolites in a spherical glass container and **Phantom-B** (phantom 6) having low concentration metabolites in a cylindrical falcon tube were used in this study (phantom preparation described in Chapter 3). The purpose prepared phantom solutions were first examined using ^{1}H NMR acquired in a High-resolution Bruker Avance NEO 300MHz spectrometer to validate their content and concentrations. Once the purity and concentrations were evaluated, the prepared phantom solutions were tested using the Bruker stock PRESS localization sequence on a 7T Bruker BioSpec 70/30 USR spectrometer running ParaVision 5.1.

4.2.2   1D-^{1}H High resolution spectra acquisition on the Avance NEO 300MHz Bruker spectrometer for Phantom-A and Phantom-B solutions

All NMR experiments were performed on solutions contained in 5 mm NMR tubes at a field strength of 7 T with a Bruker Avance NEO 300 MHz console (300.16 MHz ^{1}H frequency) and a PA BBO 300S1 BBF-H-D-05 Z probe. 1D-^{1}H NMR spectra were acquired with a pulse-and-acquire experiment (pulse program = zg). The following acquisition parameters were used: 90 degree pulse (PW = 14 μs, pulse power = 8.91 W), NS = 32; DS = 2; SW = 15.715 ppm/4716.98 Hz; digitized with 16384 complex datapoints (TD = 32768); RG = 3.125dB ; prescan delay D1= 30 s and TAT = 10 min. Water supressed 1D-^{1}H NMR spectra were obtained by applying a low power presaturation pulse (pulse power = 0.069855 mW) during the prescan delay (pulse sequence = zgpr); all other acquisition parameters were the same as above. The resonance frequency of deuterium is monitored and used to correct for minor magnetic field strength variations during the experiment that would change the frequency of resonance of the phantom compounds and broaden their peaks. For that purpose, 600 μL of D_2O were added to the sample.

4.2.3   Single voxel spectroscopy acquisition on the Biospec 70/30 USR Bruker spectrometer for Phantom-A and Phantom-B

MR localized spectroscopy was performed using single voxel PRESS (Point Resolved Spectroscopy). The 7T Bruker BioSpec 70/30 USR spectrometer (Bruker BioSpin GmbH, Ettlingen, Germany) equipped with a mini-imaging gradient set (400 mT/m) was used for acquisitions. For Phantom A, the 72-mm inner diameter quadrature volume resonator was chosen as transmitter and receiver. For Phantom-B, a 72-mm inner-diameter linear volume coil was used as transmitter, and a dedicated mouse brain quadrature surface coil was used as receiver for MRS studies. The acquisition parameters of MRS studies were as follows: TR/TE = 2500/12 ms, NA = 128, DS = 4, VAPOR water suppression and OVS, voxel size = $(3mm)^3$, Npoints = 2048, SW = 13.34 ppm (4006.41 Hz),GRPDLY=67.98, spoiler strength = 25%, recycle time of D1 = 30 s and TAT = 5 min and 30 s.

4.2.4   Results

^{1}H NMR spectra of metabolite Phantom solutions were obtained with the help of a Bruker 300 MHz Avance High resolution spectrometer installed at the SeRMN, UAB. The spectra were acquired by taking small samples from the purpose prepared solutions for Phantom-A (phantom 5) and Phantom-B (phantom 6) having known metabolite concentrations (see chapter 3). Figure 4.2.1 shows a qualitative comparison of spectra obtained for samples (600 µL) of Phantom-A and Phantom-B solutions using the 300 MHz Avance spectrometer . The fairly long value of 30s for recycle time was chosen to ensure full relaxation of all signals from metabolites present in the phantom solutions. The difference in peak heights represents the difference in concentrations of the metabolites in the phantom solutions.
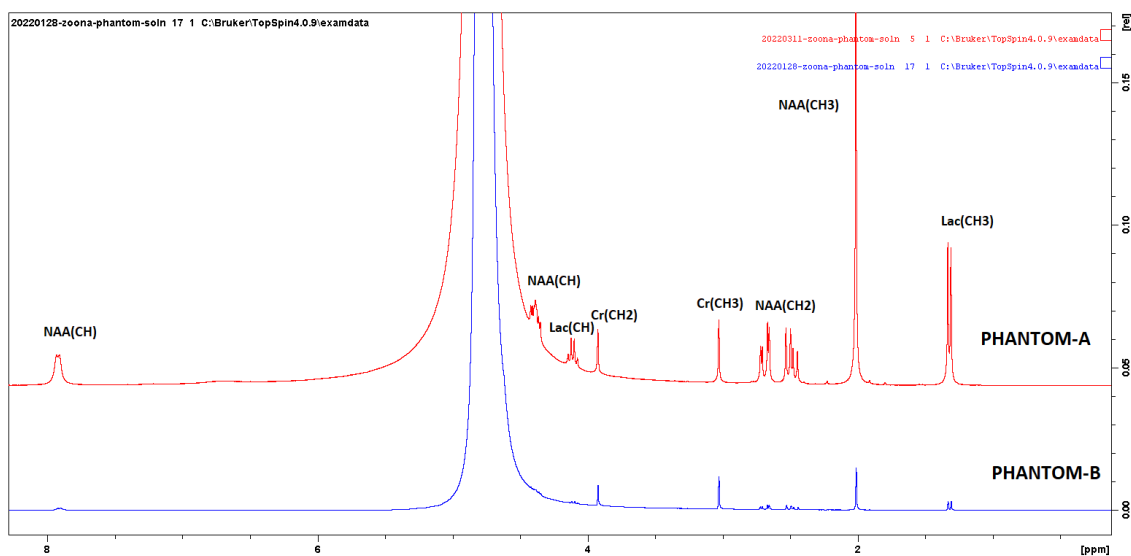
Figure 4.2.1 A qualitative metabolite peak comparison for Phantom-A and Phantom-B sample spectra acquired using the AVANCE 300MHz spectrometer. The concentrations of the individual metabolites can be visually compared by the difference in peak heights. For quantitative determination of relative concentrations, integrals were computed.

After the determination of the relative concentrations of the metabolites in Phantom-A and Phantom-B compared to the concentrations reported in Chapter 3, using the High-resolution spectrometer, the phantoms were also tested in the Bruker Biospec. Figure 4.22 shows the comparison of the spectra obtained using Phantom-A and Phantom-B in the Biospec scanner. It was observed that all expected major peaks were clearly visible in the acquired spectra using both phantoms.
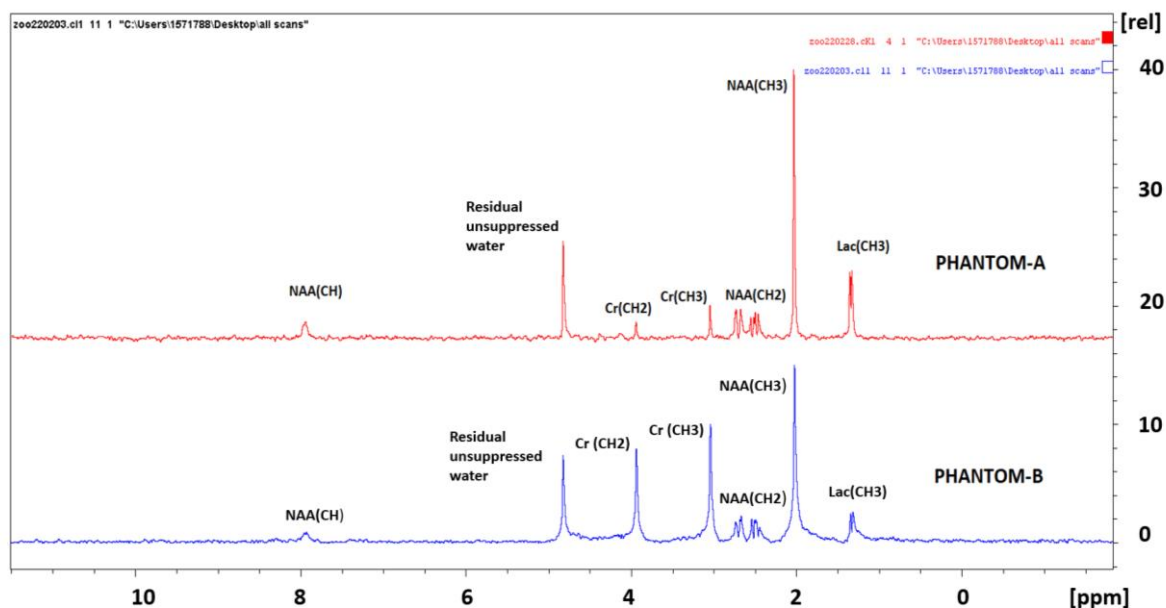
Figure 4.2.2 Bruker PRESS localized water suppressed spectra for Phantom-A (red) and Phantom-B (blue). The Phantom-A spectra was acquired with the quadrature volume coil setup while the Phantom-B spectra was acquired using a mouse brain surface coil setup.

We also wanted to quantitatively compare the relative concentrations determined for the metabolites using integrals of peaks of interest. By doing so, we aimed to measure accurate ratios of the different metabolites present in the phantom solution. The metabolite peaks of interest are plotted in Figure 4.23 for Phantom-A and Figure 4.2.4 for Phantom-B. The NAA (CH$_3$) peak was chosen as the reference for both phantoms and was assigned an expected value of the prepared concentration. For Phantom-A, the concentration for NAA (CH$_3$) was calculated as 125mM from the weighting and solution preparation process. The Cr (CH$_3$) measured area yielded a concentration of 26 mM while the Cr (CH$_2$) area yielded a concentration of 23mM. The Lactate (CH$_3$) peak area yielded a concentration of 56.3mM.

For Phantom-B, the NAA (CH$_3$) peak was assigned an expected value of 37.5mM. The Cr (CH$_3$) area produced a concentration of 9.29 mM and the Cr (CH$_2$) area produced a concentration of 8.95mM. The Lactate (CH$_3$) peak area produced a relative concentration of 5.1mM. The results are shown in Figures 4.2.3 & 4.24.

The difference between the experimental and calculated concentration values was also evaluated as a %age difference in the obtained concentrations using both phantoms. For phantom -A, the %age difference between experimental and calculated values was found as 0% for NAA, 30% for Cr and 13.2 % for Lac. For phantom B, the %age differences in concentrations were recorded as 0% for NAA, 10.5% for Cr and 2% fot Lac.
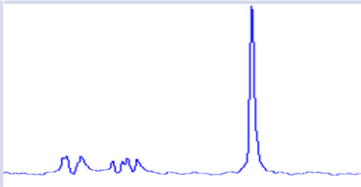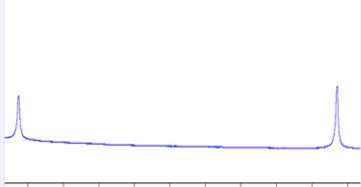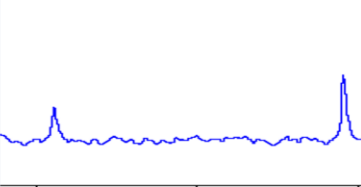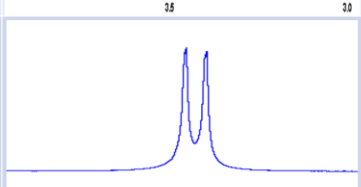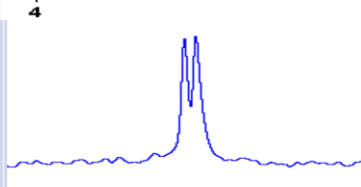
METABOLITE	AVANCE 300 MHz	BRUKER BIOSPEC 7T	CONCENTRATION
N-ACETYL ASPARTATE (NAA)			NAA CH$_3$ peak is 125 mM X 3 = **375** mM in protons
CREATINE (Cr) **CH3 &CH2**			Cr CH$_3$ = 80.1 mM in protons -> [Creatine] ~**26 mM** Cr CH$_2$ =46.9 mM in protons -[Creatine] ~ **23 mM**
LACTATE (Lac)			= 169.1 mM in protons -> [Lactate] ~ **54.33** mM

Figure 4.2.3 Metabolite peak quantitative comparison for Phantom-A spectra acquired using the AVANCE 300MHz spectrometer and the Biospec. The concentration values of individual metabolites are determined using integration of peaks using TOPSPIN.
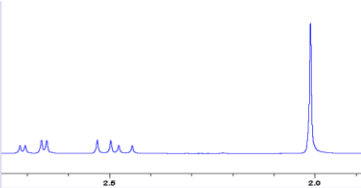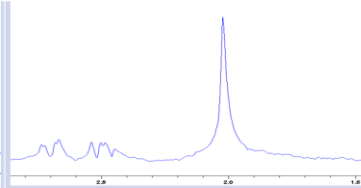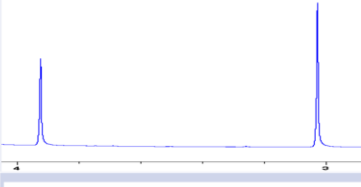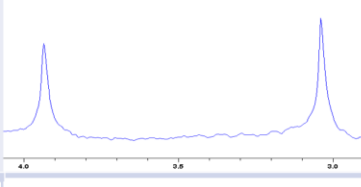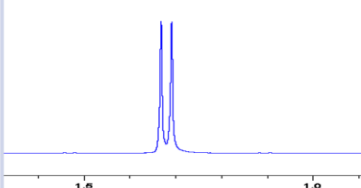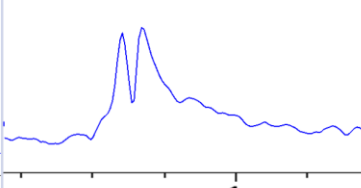
METABOLITE	AVANCE 300 MHz	BRUKER BIOSPEC 7T	CONCENTRATION
N-ACETYL ASPARTATE (NAA)			NAA CH$_3$ peak is 12.5 mM X 3 = **37.5** mM
CREATINE (Cr) **CH3 &CH2**			Cr CH$_3$ = 27.8231 mM in protons -> [Creatine] ~**9.293** mM Cr CH$_2$ = 17.7090 mM in protons -[Creatine] ~ **8.95** mM
LACTATE (Lac)			= 15.4 mM in protons -> [Lactate] ~ **5.1** mM

Figure 4.2.4 Metabolite peak quantitative comparison for Phantom-B spectra acquired using the AVANCE 300MHz spectrometer and the Biospec. The concentration values of individual metabolites are determined using integration of peaks using TOPSPIN.

78

4.2.5 Discussion

This study describes a qualitative and quantitative comparison of spectra acquired using two purpose prepared phantoms i.e. Phantom-A and Phantom-B. Since Phantom-A contains higher concentrations of the metabolites evaluated than Phantom-B, the acquired spectra were also qualitatively compared. It was observed (Figure 4.2.3) that at the same scale, the Phantom-A peaks appeared approximately 10-fold larger in intensity for NAA and Lac and 2-fold for Cr. This corresponds with the theoretical differences in the metabolite concentrations for Phantom-A and Phantom-B (Table 3.1 in chapter 3). Besides, the Biospec results shown in Figure 4.2.4. where all major peaks were visible for both Phantom A and Phantom B and no spurious signals were seen are reassuring. For quantitative purposes, the relative concentrations of the metabolites present in the phantoms were accurately determined using integration and the %age differences were calculated. The highest difference was recorded for the Cr peak at 3.03 ppm in the phantom A with a 30% difference in concentration compared to the actual calculatd values. The NAA and Lac concentrations were found to be more consistent based on the obtained %age differences.

4.2.6 Conclusion

The findings of this study suggest that the prepared Phantom-A and Phantom-B produce accurately recorded and reproducible spectra. The phantoms could also be replicated using the same preparation strategy, if needed. The phantoms were hence utilized for evaluating the performance of newly implemented MRS acquisition pulse sequences.

4.3 Single Voxel-semiLASER sequence Implementation

4.3.1 Introduction

In this chapter, the implementation of the single voxel semiLASER (SV-semiLASER) pulse sequence, which was developed on a 7T Bruker BioSpec 70/30 USR spectrometer running ParaVision 5.1, is discussed. The main goal of this sequence implementation is to facilitate the single voxel magnetic resonance spectroscopy acquisitions in mouse brain wild type (wt) and tumor models. The implemented sequence was first tested using phantom studies and later evaluated in-vivo in healthy and diseased tissue. The results were quantified by measuring metabolite signal-to-noise ratio (SNR) and half width at half maximum peak (HWHM) linewidth, and were compared to those obtained with state-of-the-art Bruker PRESS sequence. All studies involving animals were approved by the local ethics committee, according to regional and State legislations (protocol references CEA-OH-9685/CEEAH-3665).

4.3.2 Workflow of Single Voxel-semiLASER sequence implementation in PV5.1

Our goal was to implement the SV-semiLASER sequence on a Bruker scanner running ParaVision 5.1, which does not contain built-in blocks for SV-semiLASER sequence nor adiabatic pulses. The adiabatic pulses required for SV-semiLASER refocusing were generated using the TOPSPIN stdisp tool as already described in Chapter 1. The SV-semiLASER sequence was derived from the stock Bruker PRESS sequence in accordance with the steps discussed in Chapter 1 section 1.7.

The pulse program was written in the .ppg file of the new method entitled PRESS-semiLASER. The code in the localization module needed to be modified to implement the changes in the delays, gradient pulses and RF pulses. The sequence design was done in accordance with the minimum time requirements for a pulse and gradient turn on and off times. The sequence started with a VAPOR module (not shown in schematic) for water suppression.

4.3.2.1 Single Voxel semiLASER version 1: PRESS as starting sequence

The first test sequence entitled SV-semiLASER V1 incorporated only the delay changes required for the addition of two pairs of refocusing pulses in order to have spin-echo refocusing according to the condition in equation 4.3.1 [29]:

$$T1+ T3+ T5 = T2+ T4 \qquad\qquad [4.3.1]$$

Where the Minimum echo time (minTE) is given by;

$$minTE=T1 + T2+ T3+ T4+ T5 \qquad\qquad [4.3.2]$$

Figure 4.3.1 shows the pulse sequence diagram of the implemented SV-semiLASER V1 sequence. For the SV-semiLASER V1 sequence, the Hermite excitation pulse with Bandwidth 7714 Hz was

kept the same as in the PRESS sequence and the two Hermite refocusing pulses of 4885 Hz Bandwidth were replaced by four hyperbolic secant (sech) adiabatic refocusing pulses of 9003 Hz Bandwidth each and 180° flip angle.

The slice selective and rephasing gradients were kept the same as in the PRESS sequence with the small change of placing the rephasing gradient before the last refocusing pulse in the positive direction (shown in green in Fig. 4.3.2.1.1). The crusher gradients were not added. The minimum echo time feasible for this sequence implementation was TE=14ms. The implemented sequence was tested using a spherical phantom containing CuSO4 solution (phantom 1 described in Chapter 3) placed inside a volume resonator acting both as transmitter and receiver. The acquisition parameters for unsuppressed water acquisitions were kept as follows: TR/TE = 2500/20ms; NA = 1; DS = 0, VAPOR water suppression and OVS, voxel size = 3x3x3 (mm)^3, Npoints= 2048, SW = 13.34 ppm (4006.41 Hz), spoiler strength = 25%. The acquisition parameters remained the same for both sequences.
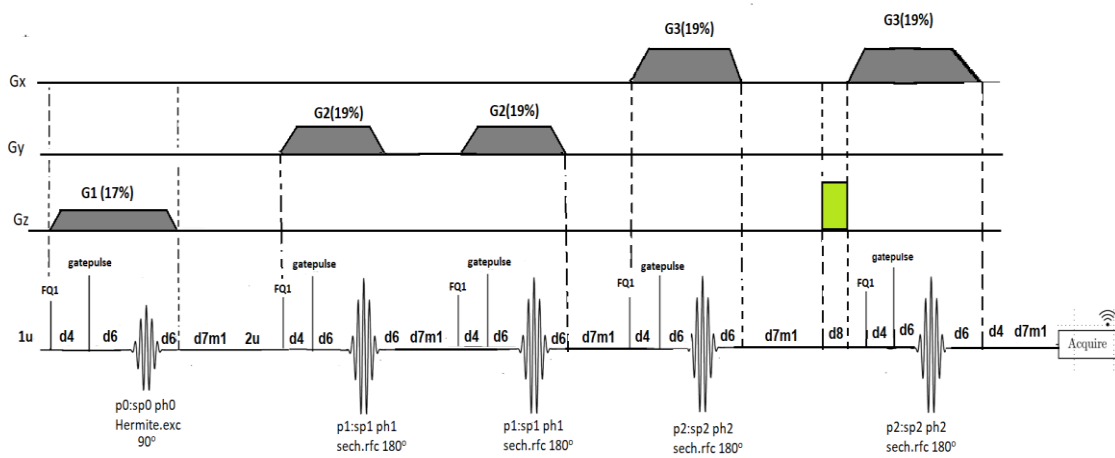
Figure 4.3.1 Implemented SV-semiLASER V1 pulse sequence diagram. See text for further details.

The results obtained for water unsuppressed spectra acquired using a (3 mm)^3 voxel placed at the isocentre inside a spherical phantom are shown in Figure 4.3.2. The PRESS spectrum (A) showed a narrow and symmetric peak corresponding to the water signal (localized at ca.4.7 ppm) whereas SV-semiLASER V1 (B) produced a distorted spectrum containing ripples in the baseline and bottom of the peak.

A. Unsuppressed water spectra Bruker PRESS   B. Unsuppressed water spectra SV-semiLASER V1
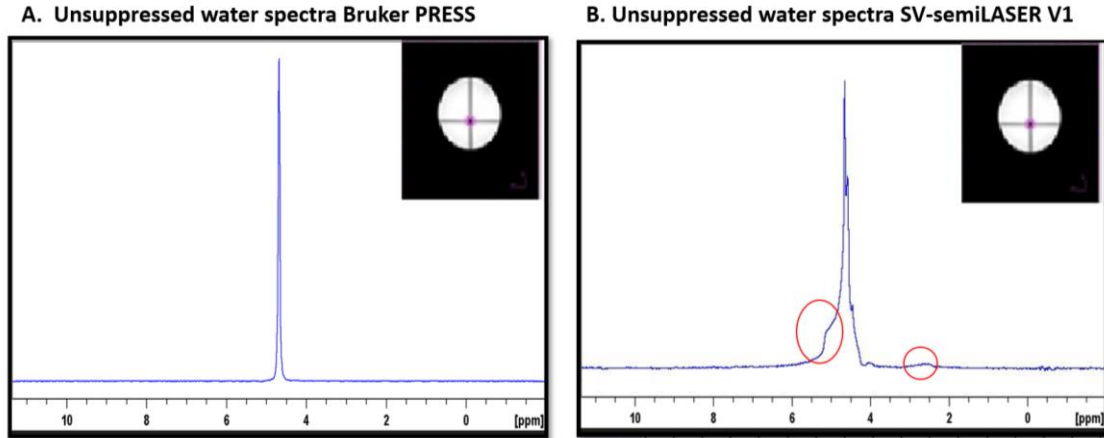
Figure 4.3.2 (A) Unsuppressed water spectrum for the PRESS sequence compared with (B) unsuppressed water spectrum for the implemented SV-semiLASER V1 sequence. Distortions in the water resonance and the baseline are encircled. The (3mm)³ voxel location inside the spherical phantom is shown in inset in pink.

The problems encountered using the SV-semiLASER V1 sequence pointed to spurious echo artefacts, which might be eliminated by the inclusion of crusher gradients to dephase unwanted coherences. Also, the slice selective and rephasing gradients had to be recalculated for an appropriate signal refocusing. These changes were implemented in version 2 and are explained in the next section.

4.3.2.2 Single Voxel-semiLASER version 2: Incorporation of rephasing gradients and crushers

The shortcomings of the SV-semiLASER V1 were solved to some extent in a new version called SV-semiLASER V2. The slice selective and rephasing gradients were recalculated for a $(3mm)^3$ voxel and crusher pairs were added next to the last refocusing pulse in all three planes (Figure 4.3.3).

The amplitude of the gradient ($(G)_z$) was calculated using equation [4.3.3];

$$G_z = \frac{RF\ bandwidth}{slice\ thickness} \qquad\qquad \textbf{[4.3.3]}$$

For the three slice selective gradients G1, G2 and G3 in the x, y and z planes respectively, the values can be calculated or directly obtained from the **PVM_VoxArrGradient** parameter in the method file which is a 3x1 matrix and contains the gradient values for the three slice selective gradients such that:

PVM_VoxArrGradient [0][0] = 17% (G1 gradient)
PVM_VoxArrGradient [0][1] = 19% (G2 gradient)
PVM_VoxArrGradient [0][2] = 19% (G3 gradient)

The PVM_ VoxArrGradient was defined in the **baselevelrelations.c** file under the function:

> **void SetGradientParameters (void)**

In Bruker ParaVision 5.1, the parameters that are used to calculate the gradient trim values for the **PVM_ VoxArrGradient** with changes in voxel size include **ACQ_grad_matrix**, **PVM_NVoxels** and **ACQ_trim[i][j].**

A calculated value of 8.1% according to the calculations described in appendix (C) was inserted in the pulse sequence as a fixed value (shown in green in Figure 4.3.3) as calculated for a $(3mm)^3$ voxel. The rephasing gradient is placed after the excitation pulse and before the first refocusing pulse thus having a negative amplitude to compensate for the dephasing introduced by the excitation gradient. Moreover, in SV-semiLASER version 2, the gradient orientation order for the slice excitation was changed to Bruker norm Gx-Gy-Gz (in SV-semiLASER version 1 the gradient orientation order was the reverse, Gz-Gy-Gx), and the slice direction order was set as RL-AP-HF (slice orientations described in Chapter 1).

Furthermore, equal crusher pairs were also added, along the three orthogonal directions, to the last refocusing pulse with a d8 minimum delay (shown in light yellow in Fig 4.3.3). To allow for crusher pair variation by user, three crusher variables were defined in the **parsdefinition.h** file. The crusher values were given a lower limit of 25% as the minimum crusher amplitude. The code was written in parsrelations.c file as:

Crusher_x= MAX_OF (Crusher_x, 25);
Crusher_y= MAX_OF (Crusher_y, 25);
Crusher_z= MAX_OF (Crusher_z, 25);

By the addition of crusher gradients and delays corresponding to crusher gradients, the minimum TE achieved with this sequence implementation increased to 19ms as a result of introducing additional delays to balance the equation 4.3.1.
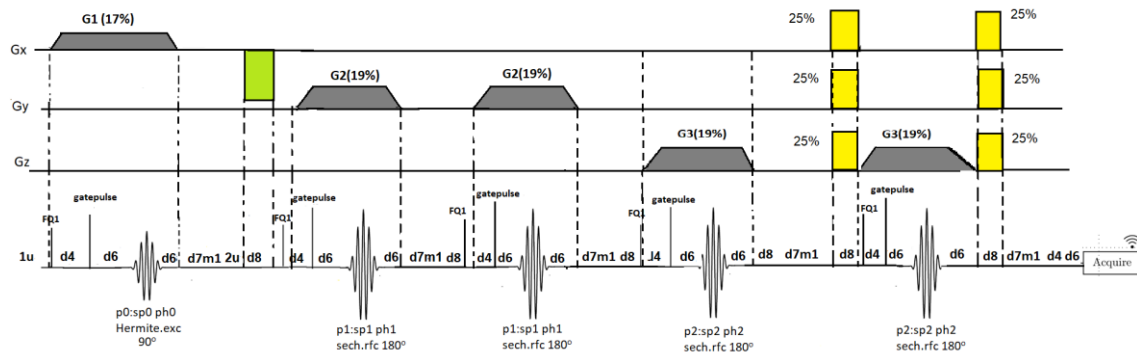
Figure 4.3.3 SV-semiLASER V2 pulse sequence diagram. See text for further details.

Moreover, for optimizing the crusher values in-vivo during acquisition, a crusher panel needed to be introduced in the ParaVision GUI. For this purpose, the geometry parameter in the method class was changed from PRESS to PRESS_semilaser for the SV-semiLASER V2 sequence to distinguish the method on the ParaVision GUI for the user. This was done by replacing the name of the method in the **parslayout.h** file. Figure 4.3.4 shows the method name changed from PRESS to PRESS-semilaser for the implemented SV-semiLASER V2 sequence in the ParaVision 5.1 GUI. Furthermore, the TE calculation Mode was also changed to the default settings for the SV-semiLASER V2 sequence in the ParaVision 5.1 GUI. As can be seen in Figure 4.3.5, in PRESS, the user can provide separate values of TE1 and TE2 based on internal calculation of echo time. TE calculation was redefined for the SV-semiLASER V2 and TE1 and TE2 were not used anymore,

hence they were removed from the panel. Another layout change made in this version was the introduction of a crusher panel in the GUI layout to facilitate the modification of the crusher values at runtime. Figure 4.3.6 shows the screenshot of the panel introduced on the ParaVision 5.1 GUI. The panel consists of three user defined crushers namely Crusher_x, Crusher_y and Crusher_z. The crushers were assigned a minimum value of 25% in the codes.
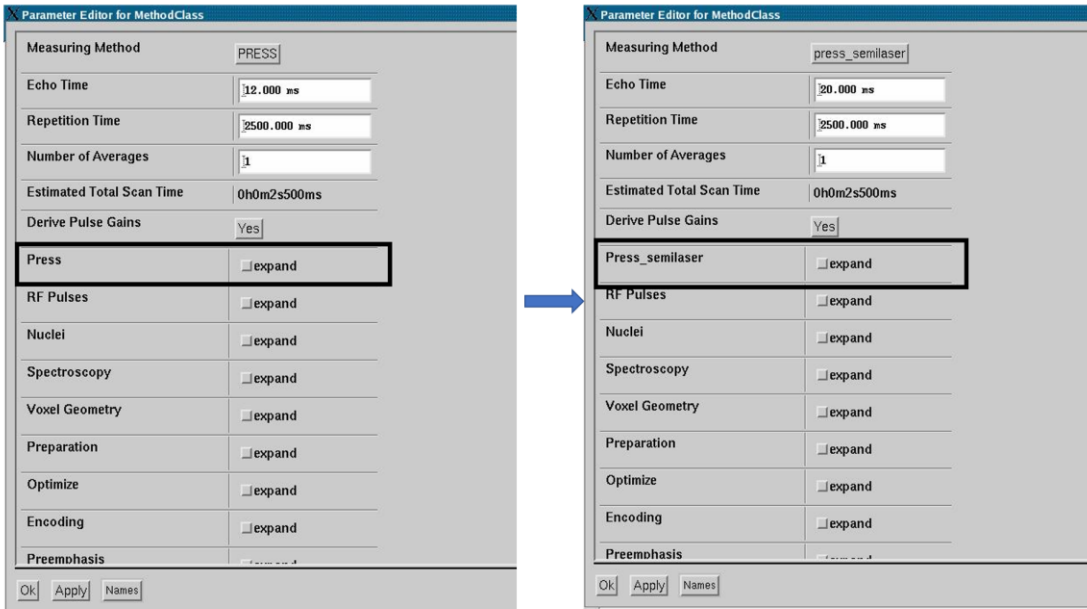
Figure 4.3.4 Screenshot of the Parameter Editor for Method Class Panel showing the method name changed from PRESS to PRESS-semilaser for the implemented SV-semiLASER sequence in the ParaVision 5.1 GUI.
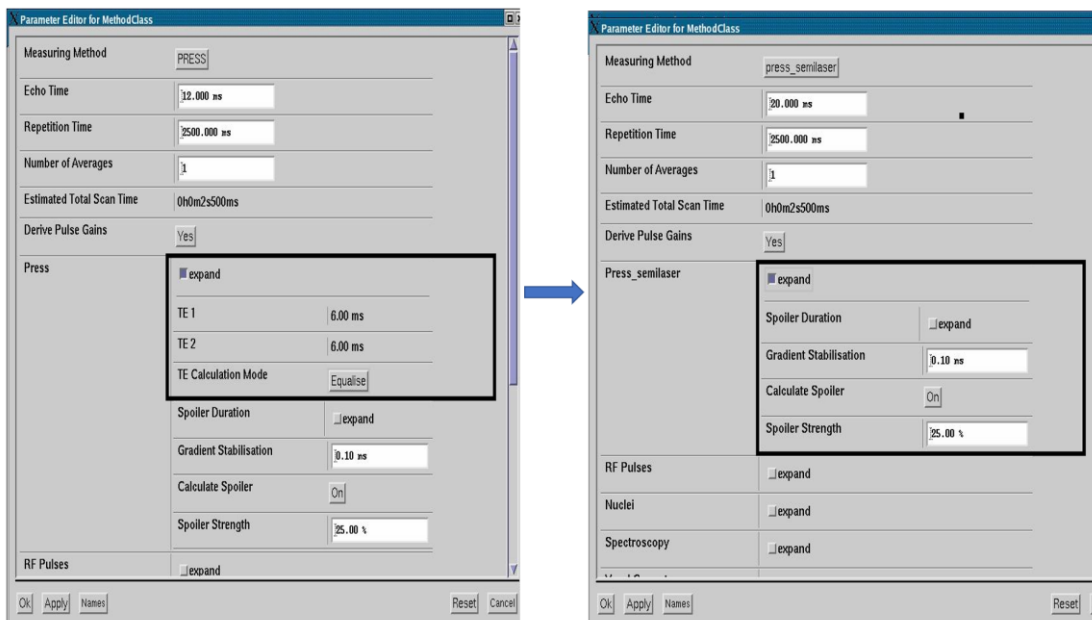
Figure 4.3.5 Screenshot of the Parameter Editor for Method Class Panel showing the TE Calculation Mode changed to the default settings for the PRESS_semilaser sequence in the ParaVision 5.1 GUI.
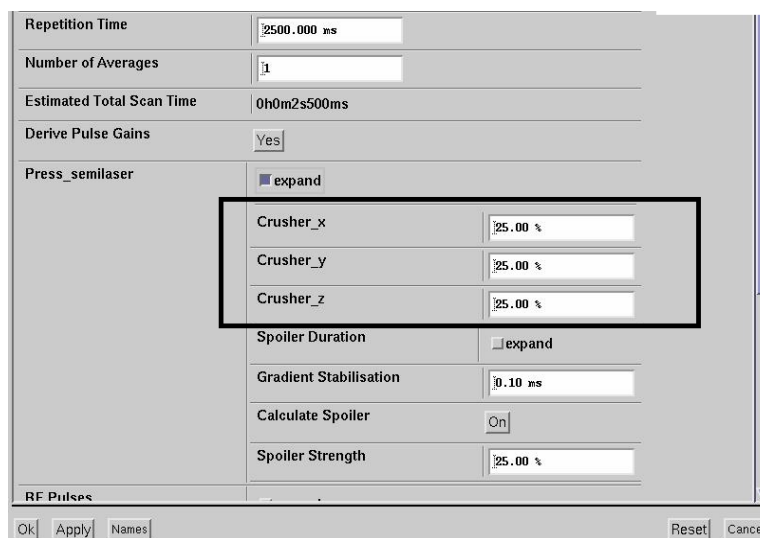
Figure 4.3.6 Screenshot of the Parameter Editor for Method Class Panel showing the crusher modification panel introduced in the ParaVision 5.1 GUI for the Press_semiLaser sequence.

The SV-semiLASER V2 sequence was first tested with the homogenous spherical phantom 1 as described in the previous section. Figure 4.3.7 A shows the corresponding acquired unsuppressed water spectra using the PRESS and SV-semiLASER V2 sequences. As can be seen, as a result of the addition of the appropriate rephasing gradient and the crushers, the lineshape of the unsuppressed water peak improved and the baseline imperfections were also fixed in the SV-semiLASER V2 spectra as compared to SV-semiLASER V1 spectra (Fig. 4.3.2.B). Moreover, it was observed that the SV-semiLASER V2 spectrum had higher SNR (2739.26) compared to PRESS (2236.47). The increase in SNR was expected as this has been previously described [68] .

To ensure that the sequence was performing effective localization of the voxel, experiments were then conducted with a two-compartment phantom (phantom 3) containing water and fat parts. Figure 4.3.7 B and C shows the water and fat spectra obtained using the PRESS and SV-semiLASER V2 sequences by positioning a $(3mm)^3$ voxel in the water compartment at the iso-center, followed by placing the voxel in the fat compartment, which was away from the iso-center. The top spectra correspond to the PRESS sequence and the bottom spectra correspond to the SV-semiLASER V2 sequence acquisitions. Water and fat peaks showed good lineshapes using the PRESS sequence. For SV-semiLASER V2, the water peak showed good lineshape as well, with better SNR compared to the PRESS sequence. However, the fat peak appeared distorted in the spectrum acquired with the SV-semiLASER V2 sequence. On the other hand, when placing the voxel within the fat compartment at the iso-center and the water voxel off-centered, it was the water signal which appeared distorted, displaying perfect lineshape for the fat signal (data not shown). Hence, it was deduced from the obtained results that there was a problem with the offset frequencies which were not accurately localizing the y and z planes, when away from the iso-center. This was later corroborated by comparing the O1 list with the PRESS one. To correct this problem, further literature reading was done to find an adequate solution.
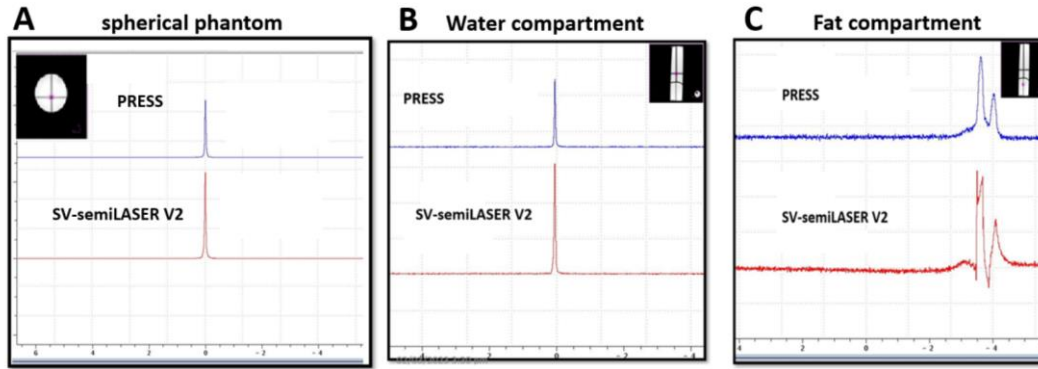
Figure 4.3.7 Representative spectra acquired with PRESS (top) and SV-semiLASER V2 (bottom) sequences. (A) Water spectra acquired from a voxel positioned at the iso-centre in the homogeneous water spherical phantom 1. Intersection of the greylines in the MRI image (inset), indicates the gradient iso-center where the voxel (red square) was located. (B) Water spectra acquired from a voxel positioned at the iso-center in the water compartment of a two-compartment cylindrical phantom. (C) fat spectra acquired by placing the voxel in the fat compartment, away from the iso-center. Inset in B shows coronal section through the two-compartment phantom with the $(3mm)^3$ voxel positioned at the iso-center in the water compartment in pink, while inset in C shows the $(3mm)^3$ voxel positioned away from iso-center in the fat compartment. The two compartment-phantom contained two separate parts, one containing water in agarose (upper compartment in inset image) and the other one containing fat from baby oil (lower compartment in inset image).

4.3.2.3 Single Voxel-semiLASER version 3: Off-center correction issues

SV-semiLASER V3 sequence (pulse sequence diagram shown in figure 4.3.8) focused mainly on correcting the offset frequency artifact described in section 4.3.2.2.

The ParaVision manual states that the **O1 list** in the **acqp** file of the method contains the offset frequency values for the different slice positions and the pulse programming command to give an increment in the offset list is the **FQ1: F1** command. This command is given before the RF pulse to increment the pointer of the O1 list to the next index. It is also put together with the gating command: **Gatepulse1.** The advantage of this command is to provide blanking pulses. It should be written before the pulse statement.

The simple removal of the fq1: f1 command before the second and fourth refocusing pulses to select the appropriate y and z planes fortunately solved the seemingly complex problem.
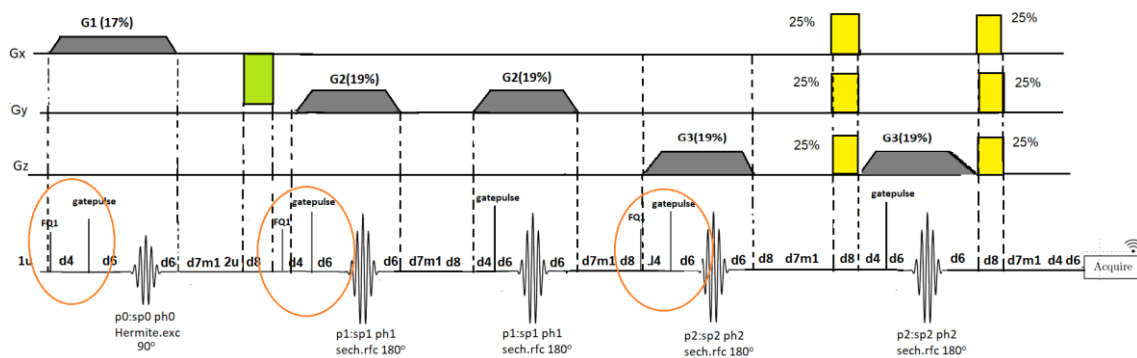
Figure 4.3.8 SV-semiLASER V3 pulse sequence diagram

Figure 4.3.9 shows the results obtained by acquiring a (3mm)^3 voxel in the two-compartment phantom with the SV-semiLASER V3 where (A) is the water peak accurately localized at the iso-center maintaining good lineshape and (B) is the fat two peak pattern (methylene and methyl) correctly localized at ca. 1.3 – 0.9 ppm using the voxel positioned away from the iso-center. These results confirmed that the implemented SV-semiLASER V3 sequence provided accurate localization of the water peak for a (3mm)^3 voxel.
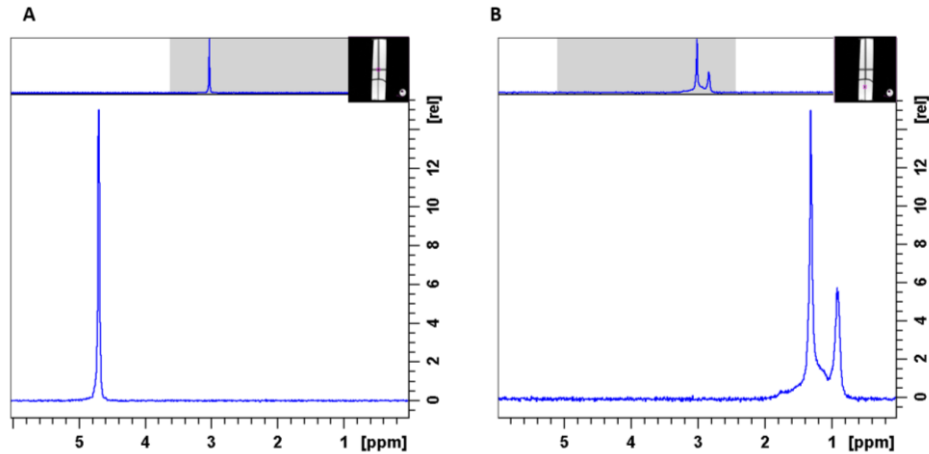
Figure 4.3.9 (A) Water peak at 4.7 ppm localized using the SV-semiLASER sequence by placing the (3mm)^3 voxel at the isocentre in the water compartment (shown in insert) (B) Fat peaks at 1.3 – 0.9 ppm localized using the SV-semiLASER sequence by placing the (3mm)^3 away from the iso-center in the fat compartment (shown in insert).

4.3.2.4 Single Voxel-semiLASER version 4: Variable voxel size and TE values

Upon obtaining satisfactory results for the voxel localization issues, our next goal was to fix the limitations of version 3. There were three main limitations identified in SV-semiLASER V3 including:

    I.   The sequence was designed only for a fixed voxel size of (3mm)^3
    II.   Only a fixed value of TE was possible
    III.   Crusher pairs were needed for all refocusing pulses to allow eliminating some residual spurious echoes

Therefore, the identified limitations were addressed in the SV-semiLASER V4. To be able to set variable voxel sizes, in this version, a variable named **tcomp** was declared and defined in the parsrelations.c file for a variable refocusing gradient (calculation discussed in appendix(C). Also, a user-defined variable delay **d7m1** was introduced to allow for a variable Echo time (TE). The minimum echo time achievable with the introduced modifications was 15.7ms. The delay interval calculations for the SV-semiLASER V4 implementation for minimum TE acquisition are given in Table 4.3.1. The five inter-pulse delays were 2.353 ms, 3.368 ms, 3.368 ms, 4.562 ms and 2.130 ms for Τ1 through Τ5, respectively. The minimum echo time, which is the sum of the delay intervals, can be calculated as follows in equation 4.3.2;

Minimum echo time (minTE)= Τ1 + Τ2+ Τ3+ Τ4+ Τ5

$$=2.35ms +3.37ms +3.37ms+4.56ms+2.13ms$$

$$\approx 15.7ms$$

Table 4.3.1 TE calculations for the SV-semiLASER sequence V4.

T1(ms)		T2(ms)		T3(ms)		T4(ms)		T5(ms)	
p1	0.35	p2	1	p3	1	p4	1	p5	1
d6	0.1	d6	0.1	d6	0.1	d6	0.1	d6	0.1
d7m1_mod	0.267	d4	0.267	d4	0.267	d4	0.267	d4	0.267
	0.002	d4	0.267	d4	0.267	d7m1_mod	0.267	d4	0.267
d4	0.267	d6	0.1	d6	0.1	d8	1.23	d6	0.1
d4	0.267	d4	0.267	d4	0.267	d4	0.267	d6	0.1
d6	0.1	d4	0.267	d4	0.267	d4	0.267	d6	0.1
p2	1	d6	0.1	d6	0.1	d6	0.1	d6	0.1
		p3	1	p4	1	p5	1	d6	0.1
Tau1(ms)	2.35	Tau2(ms)	3.37	Tau3(ms)	3.37	Tau4(ms)	4.56	Tau5(ms)	2.13

The five inter-pulse delay intervals are calculated as TAU1=2.35ms, TAU2=3.37ms, TAU3= 3.37ms, TAU4= 4.56ms and TAU5=2.13ms.

The minimum TE calculations (Table 4.3.2) were performed keeping in mind the placement of the **tcomp** gradient in the **tau4** interval and the placement of crusher gradients pairs along all refocusing pulses. The minimum delay added for a crusher was **d4=0.267ms** for a change in echo time. This variable delay was incorporated into the TAU1 and TAU4 intervals. The intervals were re-defined in the parsrelations.c file according to the new value for minimum TE=15.7ms.

Table 4.3.2: The interpulse delay intervals

Tau1(ms)	Tau2(ms)	Tau3(ms)	Tau4(ms)	Tau5(ms)
VoxPulse1.Length/2.0	VoxPulse2.Length/2.0	VoxPulse2.Length/2.0	VoxPulse3.Length/2.0	VoxPulse3.Length/2.0
+GradStabDelay	+ GradStabDelay	+ GradStabDelay	+GradStabDelay	+GradStabDelay
+PVM RiseTime	+PVM RiseTime	+PVM RiseTime	+PVM RiseTime	+PVM RiseTime
+0.02	+PVM RiseTime	+PVM RiseTime	+SpoilerDuration [1][0]	+PVM RiseTime
+PVM RiseTime	+ GradStabDelay	+ GradStabDelay	+PVM RiseTime	+GradStabDelay
+PVM RiseTime	+PVM RiseTime	+PVM RiseTime	+PVM RiseTime	+ GradStabDelay
+GradStabDelay	+PVM RiseTime	+PVM RiseTime	+ GradStabDelay	+ GradStabDelay
	+GradStabDelay	+GradStabDelay		+ GradStabDelay
				+GradStabDelay
+VoxPulse2.Length/2.0	+VoxPulse3.Length/2.0	+VoxPulse3.Length/2.0	+VoxPulse3.Length/2.0	+0.05

Where PVM RiseTime=d4, GradStabDelay=d6, Spoiler Duration=1.5, VoxPulse1.Length=0.7ms, Voxpulse2.Length= Voxpulse3.Length= 2ms.

Figure 4.3.101 shows the SV-semiLASER sequence V4 scheme. The added t_comp delay for a variable refocusing gradient is shown in green and, as can be seen, it was placed just before the final crusher pair. The delays incorporated into the Tau1 and Tau4 intervals for a variable echo time are the d7m1_mod delay and are indicated with a brown circle.

Figure 4.3.11 shows the water suppressed spectrum obtained for the implemented SV-semiLASER sequence tested for the first time on a wt mouse using our standard single voxel acquisition parameters of TR=2500ms; TE=20 in (both sequences for comparison); NA = 128; DS = 4, VAPOR water suppression and OVS, voxel size = 3x3x3 (mm)^3, Npoints = 2048, SW = 13.34 ppm (4006.41 Hz), spoiler strength = 25%; TAT = 5 min and 30 s. SV-semiLASER V4 provided a clean spectral profile, although the presence of a still strong residual water peak can be seen in

the SV-semiLASER V4 acquired spectrum as compared to PRESS, but it does not affect overall spectral quality. Well resolved signals from the different metabolites and a high SNR was also recorded for the NAA peaks in the SV-semiLASER V4 acquired spectrum. With these promising results obtained for the preliminary tests, the sequence evolution targeted fixing the problem of suboptimal water suppression.
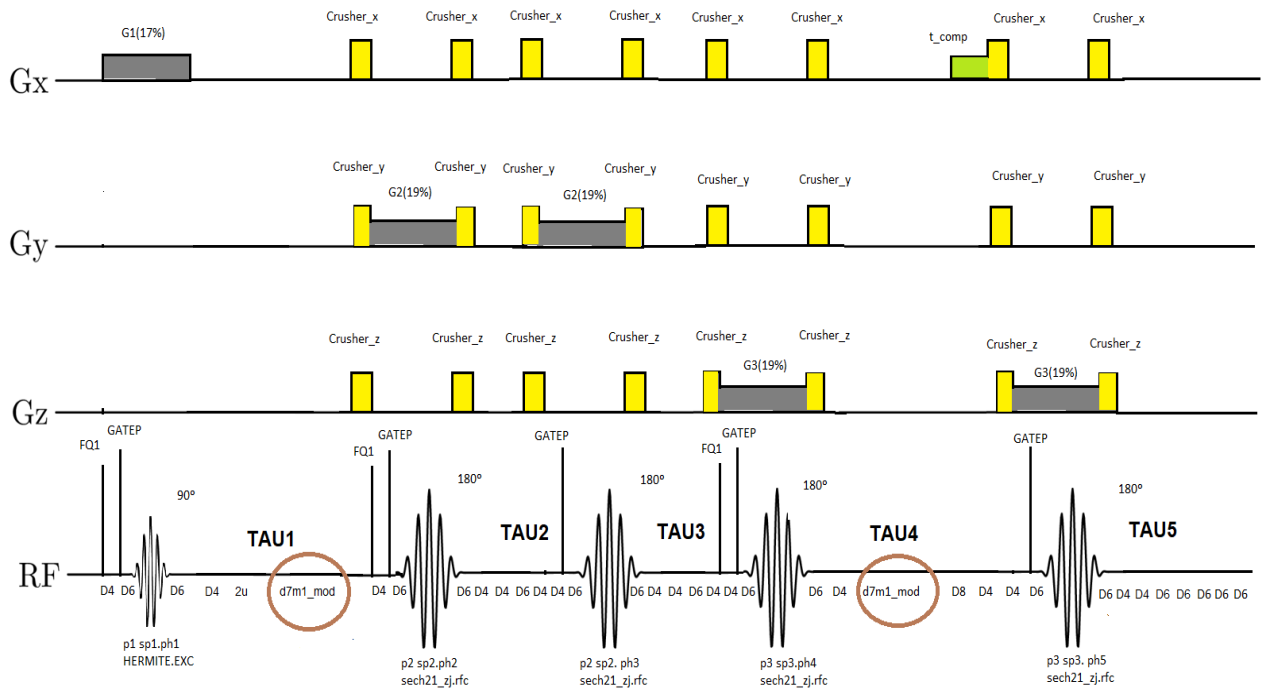
Figure 4.3.10 SV-semiLASER V4 pulse sequence diagram. The d7m1_mod user defined variable delay (encircled in red) was introduced in intervals TAU1 and TAU4 to allow variable echo time.
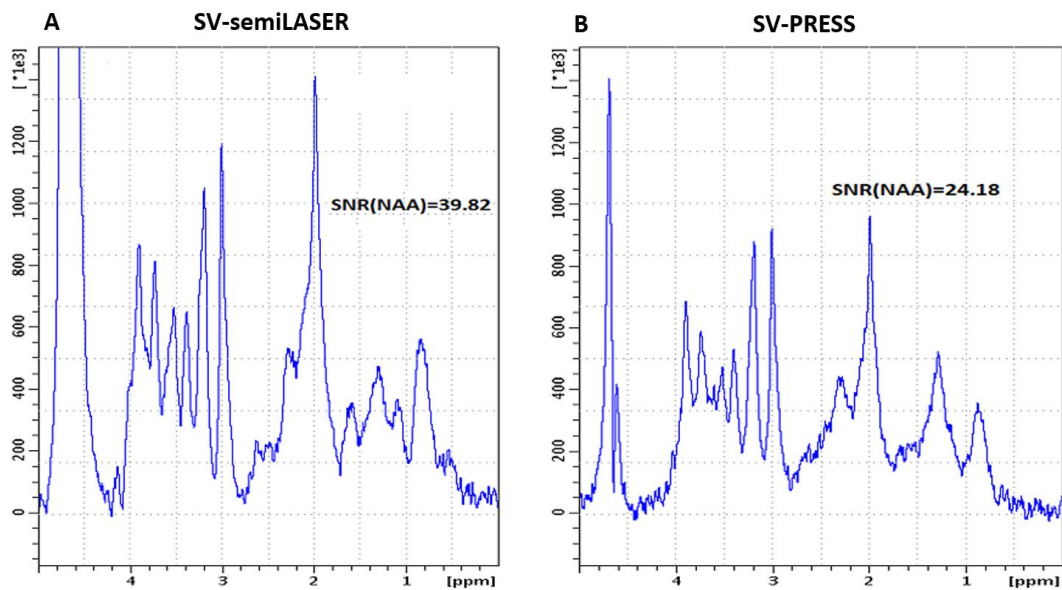
Figure 4.3.11 Localized water suppressed spectra acquired in-vivo in wild type mouse using (A) SV-semiLASER (B) Bruker PRESS.

Then, the acquisition protocol was optimized while fixing the problem of high residual water peak by fine tuning acquisition parameters such as the *Gap to Voxel and OVS slice thickness*. Figure 4.3.12 shows the results obtained from the further optimized SV-semiLASER sequence in a wt mouse and compared with the PRESS sequence. Notice the improvement in water suppression with a thin residual peak visible in the SV-semiLASER spectrum, which is similar to the residual water peak in the PRESS spectrum. This final optimised protocol is the current implementation on the 7T BioSpec scanner at UAB and was used for the additional experimental results.
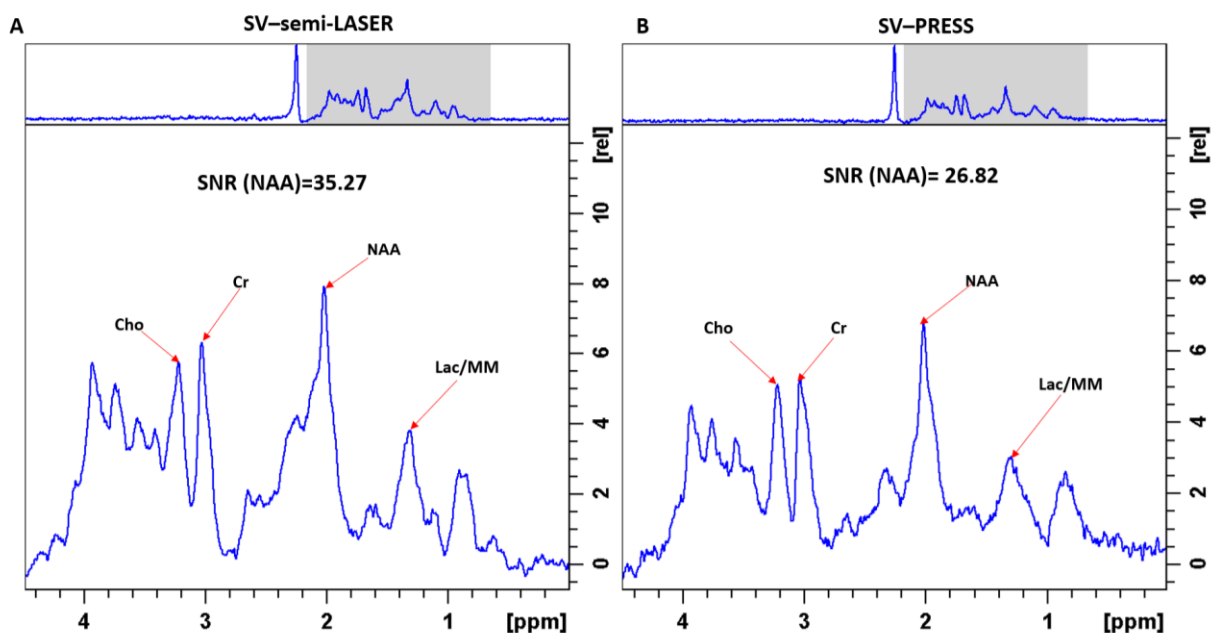
Figure 4.3.12 Localized water suppressed spectra acquired in-vivo in wild type using (A)SV-semiLASER sequence after water suppression optimization (B)SV-PRESS sequence.

The implemented SV-semiLASER V4 sequence exhibited good performance on the basis of quality evaluation standards defined in literature [69] [27] such as SNR, spectral quality, artefacts etc. The hyperbolic secant adiabatic refocusing pulses perform uniform refocusing of the spins both in the center and near the edges of the slice resulting in an increase in the amount of signal sampled by the sequence and higher signal-to-noise ratio than standard PRESS. Also, the minimum echo time achieved with this sequence, by efficient placement of crushers and delay calculations, was as low as 15.6ms which is highly suitable for data acquisition at high magnetic field. The SV-semiLASER V4 sequence will be referred to as the implemented SV-semiLASER sequence from here onwards.

4.3.3 Single Voxel-semiLASER vs PRESS

4.3.3.1   Volume excitation validation

90

By inspecting our SV-semiLASER sequence implementation results, we consistently obtained higher SNR values for the SV-semiLASER sequence as compared to PRESS. Although a similar increase in SNR has been previously reported [68], before moving on to longitudinal experiments with living animals we wanted to verify that the excited volumes in the phantom using both PRESS and SV-semiLASER sequences were the adequate ones. To do so, we designed a set of experiments in which the excited prescribed volume was progressively decreasing. In this manner, when exciting volumes bigger than the diameter of the phantom, the NMR signal detected should not vary, and we would expect to measure a progressive decrease in sampled signal when the size of the voxel goes below the dimensions of the phantom. Thus, in case the SV-semiLASER was exciting bigger volumes than the theoretically prescribed ones, we would not have a match between the phantom diameter and the prescribed voxel size at which we start detecting a decrease in signal.

For these studies we decided to use as phantom a cylindrical glass NMR tube with outer diameter 10 mm (inner diameter 8.9 mm) containing water with $CuSO_4$ solution and acquired non-isotropic voxels by changing only the Y dimension and keeping the X and Z dimensions equal to 15 mm (greater than the phantom diameter). Figure 4.3.13 shows the cross-section of the cylindrical phantom and axial slices of changing thickness in blue (15mmx1mmx15mm), red (15mmx5mmx15mm), green (15mmx8mmx15mm) and yellow (bigger than phantom diameter).
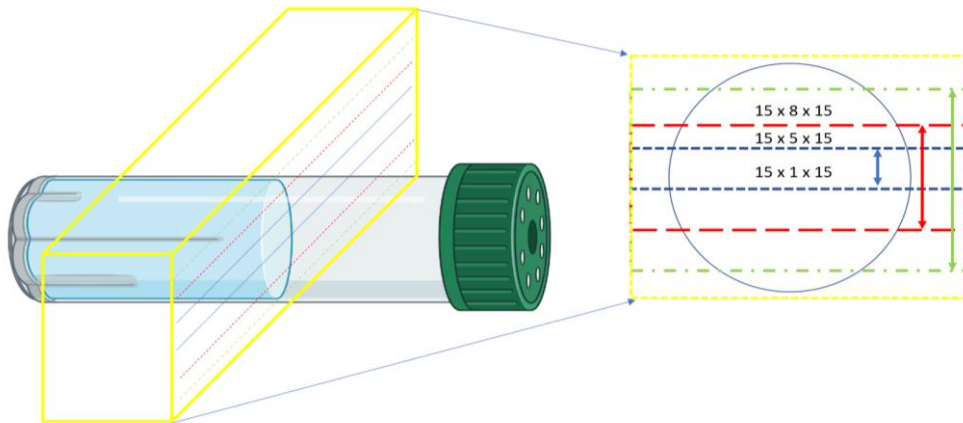
Figure 4.3.13 Cross-sectional representation through the cylindrical glass NMR tube phantom filled with buffered CuSO4 in water and axial sections (at left) of variable voxel thickness.

When the prescribed voxel size is bigger than the phantom inner diameter,

$$\text{Excited sample Volume} = \boldsymbol{L * \pi R^2}$$ where L is the excited dimension along z direction i.e. the length of the excited tube.

When the prescribed voxel size is smaller than the phantom inner diameter (Y<8.9mm), the excited sample volume should be equal to the length multiplied by the partial excited area of

the circle (purple dashed area in Fig 4.3.14). This purple area was calculated by subtracting the blue areas from the area of the circle.

d=y/2   **R**= radius (4.45 mm)   **L**= Z dim (15mm)

$\theta = 2 * \arccos\frac{d}{R}$

Area of blue regions= $(\frac{R^2}{2}(\theta - \sin\theta))*2$

Area of excited region= πR^2- Area of blue regions

Volume of excited region= Area of excited region * **L**
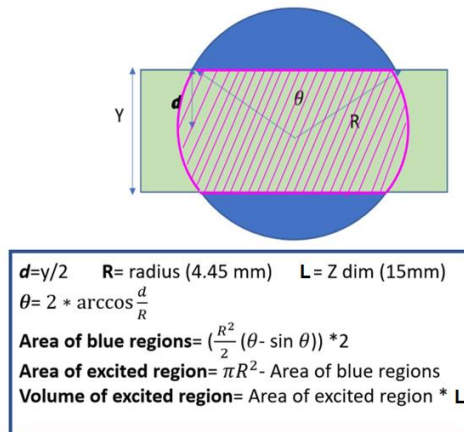
Figure 4.3.14 Graphical representation of the volume excitation calculation: the purple shaded region shows the excited volume inside the phantom. The blue regions are the remaining phantom area outside the volume of excitation but inside the phantom where d is half height of the voxel, Y is voxel dimension and ϑ is angle at the center of the phantom

The relationship between the theoretically excited volume measured in (mm)^3 inside the phantom vs the Y-voxel prescribed dimension in (mm) is shown in Figure 4.3.15. Beyond the diameter of the phantom i.e. 8.9mm, the excited volume should remain constant. To evaluate this experimentally, SNR was measured for the PRESS and SV-semiLASER sequences when varying the y dimension of the voxel size at short and long echo times. Figure 4.3.16 shows plots for SNR vs Y dimension using PRESS and SV-semiLASER sequences at TE=20ms (A) and TE=136ms (B). The fact that the theoretical trend of varying SNR vs voxel size was followed, and was similar for PRESS and SV-semiLASER, indicated that there was no apparent problem with the excited voxel dimensions possibly being larger for SV-semiLASER with respect to PRESS. Moreover, it was consistently observed that the SV-semiLASER sequence provided higher SNR for the same excitation volume.

Y dim (mm)	excited volume inside phantom (mm)3
30	933.29
25	933.29
20	933.29
15	933.29
10	933.29
8	771.99
7	589.71
6	465.64
5	322.49
4	252.73
3	141.04
1	41.47
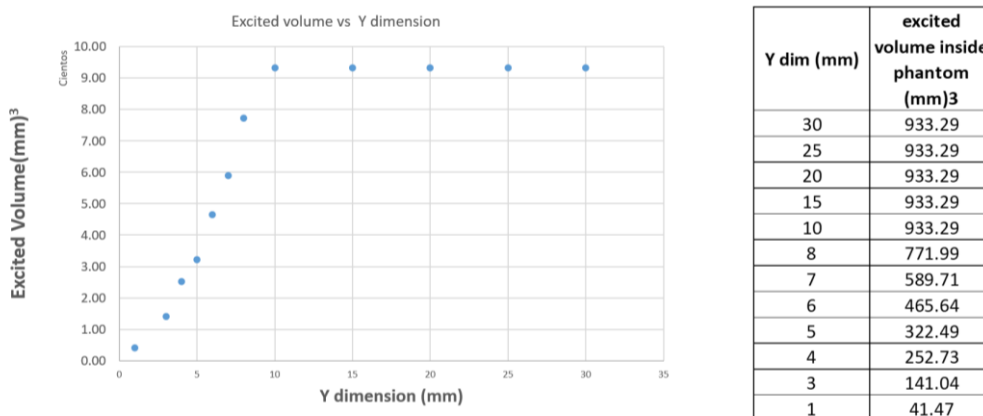
Figure 4.3.15 : Plot for the theoretical excited Volume (mm)³ inside the phantom vs Y dimension (mm). Beyond 8.9 mm, which is the inner diameter of the phantom, the excited volume remains constant.
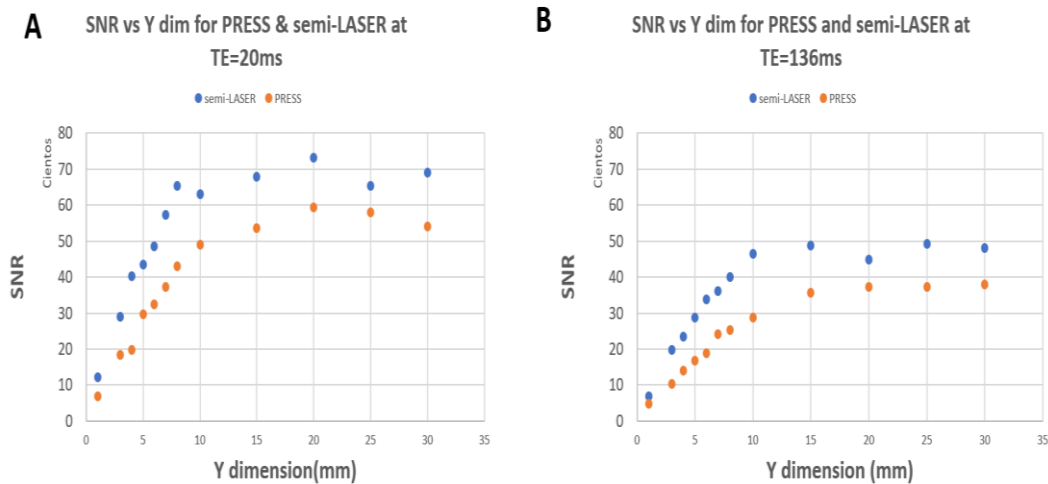
Figure 4.3.16 (A) Plots for SNR vs Y dim (mm) using PRESS and SV-semiLASER sequences at TE=20ms and (B) TE=136 ms.

4.3.3.2 Comparison at standard TE=20ms using a volume transceiver coil

To test the SV-semiLASER implemented sequence under homogeneous conditions, the experiments were first performed using a transmit-receive volume coil which produces a homogenous signal reception throughout a larger area than surface coils [70]. The Bruker Biospec scanner at UAB is equipped with a QuadTranceiver ^{1}H 1000 W 7.2 cm inner diameter volume coil for excitation and reception which was used for this initial comparison.

The SV-semiLASER sequence was tested by placing a $(3mm)^3$ voxel at the magnet iso-center (to ensure maximum SNR) of the highly concentrated spherical phantom 5 (described in Chapter 3 section 3.2) containing 125mM N-Acetyl Aspartate (NAA), 20mM Creatine (Cr), 50mM Lactate and distilled water. Water suppressed spectra were acquired using the PRESS and SV-semiLASER sequences with acquisition parameters TR=2500ms TE=20ms, NA=128, OVS=on, Npoints= 2048, SW= 13.3ppm, spoiler duration=1.5ms, spoiler strength=25%. FASTMAP shimming was done with voxel size $(3mm)^3$ at the iso-center. The acquisition parameters were kept identical for acquisitions using PRESS and SV-semiLASER methods for the sake of comparisons.

The spectra were evaluated for spectral linewidth, SNR, efficiency of water suppression and presence of unwanted coherences. It has been previously proposed that the residual suppressed water signal should preferably be of the same height or lower than the largest metabolite peak [27].

SV-semiLaser and PRESS acquired spectra are displayed in Figure 4.3.17 and showed accurately resolved metabolite peaks including N-Acetyl Aspartate (NAA) at ca.2.01ppm and ppm, Phosphocreatine (Cr) at ca. 3.02ppm and 3.9ppm, Lactate at ca. 1.3ppm and the residual water at ca. 4.7ppm. The SNR of NAA peak for the SV-semiLASER sequence was calculated as 392.64, for the Cr peak was 49.5 and for the Lactate peak was 94.39. Whereas the SNR for the NAA peak in the PRESS spectrum was 175.51, for the Cr peak was 22.32 and for the Lactate peak was 43.5. The results show a 2.3x SNR increase in NAA, 2.2x SNR increase in Cr and 1.13x SNR increase in Lactate for the SV-semiLASER sequence compared to PRESS sequence. These high SNR values were obtained as a result of using highly concentrated metabolites

For the SV-semiLASER spectrum, the linewidth obtained by fitting the NAA peak to a Lorentzian was 4.97 Hz and for the PRESS spectrum the linewidth was recorded as 7.83 Hz. The reduction of linewidth indicates narrower peaks in the SV-semiLASER spectrum which is a measure of higher spectral quality. Both the SV-semiLASER and PRESS spectrum displayed sufficient water suppression. No evidence of spurious echoes was seen in the SV-semiLASER acquired spectrum.
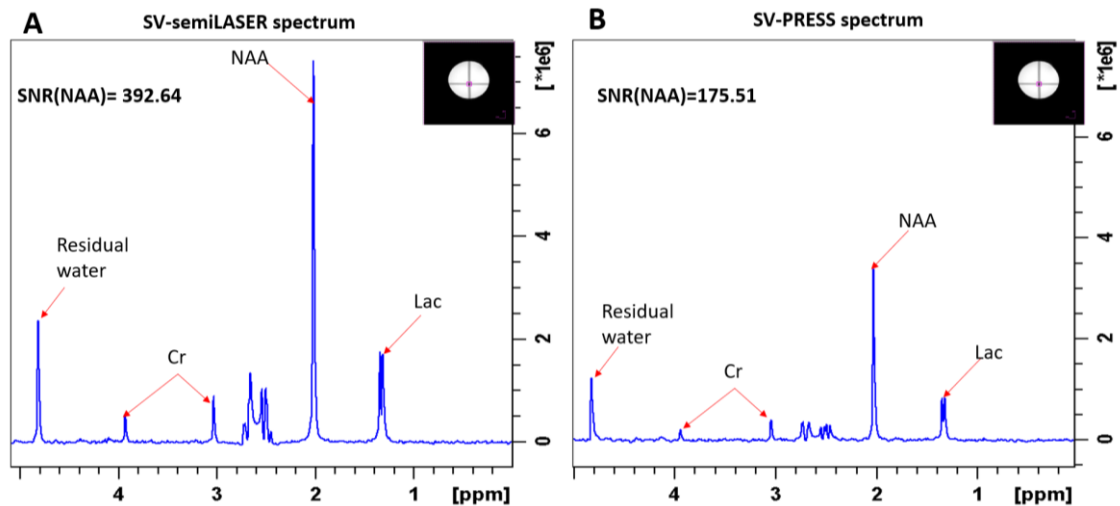
Figure 4.3.17 Water suppressed spectrum at TE=20ms using the volume coil for Tx/Rx acquired from the cylindrical phantom-A with SV-semiLASER (A) and SV-PRESS (B).

4.3.3.3 Comparison at standard TE=20ms using a surface coil receiver

Surface coil receivers can also be used for reception. The advantage of positioning the surface coil immediately above or in direct contact with the surface of the phantom ensures high SNR because of the proximity of the coil to the sample [70]**.** To test the sequence in conditions mimicking the mouse brain acquisitions and in order to obtain a more realistic SNR comparison, we used the same coil set up used in our mouse brain studies (a surface coil receiver and a volume coil transmitter) and phantom-B (phantom 6) which mimics physiological metabolite concentrations. Phantom-B, which consists of a 15mL cylindrical Falcon tube filled with low concentration metabolites solution consisting of 12.5mM N-Acetyl Aspartate (NAA), 10mM Creatine (Cr), 5mM Lactate and 1mM tetra deutero-propionic acid (TSP) (as chemical shift reference) was used.

The acquisitions were made using a Linear [1]H 1000 W 7.2 cm inner diameter volume coil for excitation and a dedicated mouse brain surface coil as receiver. Water suppressed spectra were acquired using PRESS and SV-semiLASER sequences with TR=2500 ms, TE=20 ms, voxel size= $(3mm)^3$, NA=128, OVS=on, Npoints= 2048, SW= 13.3 ppm, spoiler duration=1.5 ms, spoiler strength=25%, DS=4, with VAPOR water suppression and OVS. FASTMAP shimming was performed over a $(4mm)^3$ volume.

Figure 4.3.18 shows the comparison of water suppressed spectra for SV-semiLASER vs PRESS sequences. All metabolites (NAA, Cr and Lac) are properly detected at their expected frequency of resonance for both the SV-semiLASER and PRESS sequences at the same TE=20ms. The linewidth for the NAA peak in the SV-semiLASER was 4.27 Hz and for the PRESS sequence it was 4.75Hz. The slightly narrower linewidth obtained with the SV-semiLASER sequence could be due to the relative insensitivity of the adiabatic refocusing pulses to B1 inhomogeneities and resonance offsets [18]. The SNR values recorded for the SV-semiLASER sequence were 196.25 for the NAA peak, 130.81 for the Cr peak and 37.17 for the Lactate whereas for the PRESS sequence the SNR was recorded as 137.82 for NAA, 92.51 for Cr and 28.85 for Lactate. The increase in SNR was 1.4-fold for the NAA peak, 1.4-fold for the Cr peak and 1.3-fold for Lactate. Hence, we can conclude that the SV-semiLASER sequence provides an overall 1.4-fold increase in SNR as compared to the PRESS sequence.

The increase in SNR and the reduction in linewidth produced by the SV-semiLASER sequence were consistent with our previous findings in section 4.3.3.2. Hence, we concluded that at the same TE=20ms, the SV-semiLASER sequence gives superior performance in comparison to PRESS.
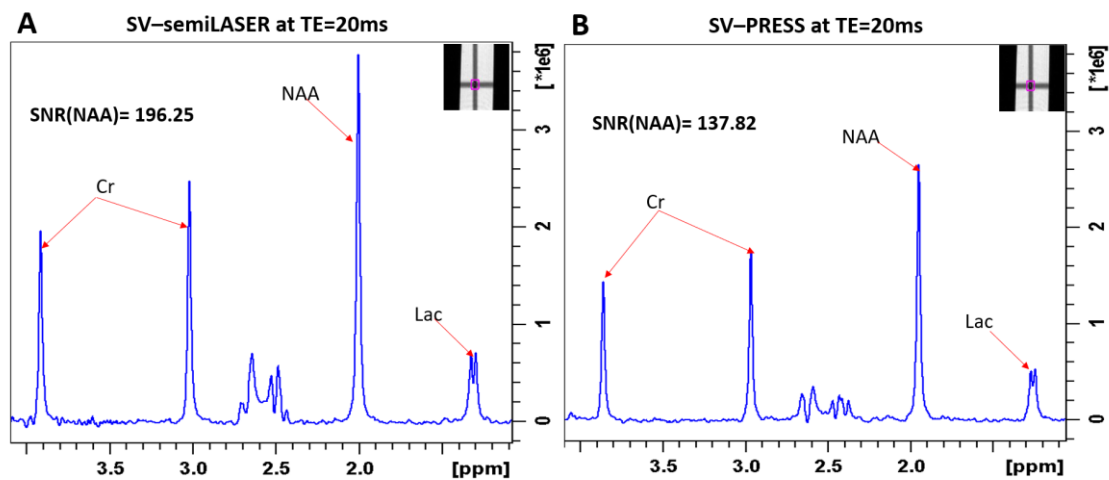
Figure 4.3.18 SV-semiLASER water suppressed spectrum in phantom B at 20ms TE. (B) PRESS water suppressed spectrum of phantom at 20ms TE. The voxel is positioned at the magnet iso-center in both sequences

4.3.3.4   Comparison at minimum achievable TE

To compare the spectra properties at the minimum achievable echo time for each sequence, the experiments were repeated using the same settings as described in section 4.3.3.3, only changing the used TE for both sequences. The minimum TE values were TE=16 ms for the SV-semiLASER sequence and TE=12 ms for the PRESS sequence. All other acquisition parameters were kept the same as reported in section 4.3.3.3.

Figure 4.3.3.4 shows the SV-semiLASER spectrum acquired at TE=16ms and the PRESS spectrum acquired at TE=12ms. The SNR for the SV-semiLASER sequence using the NAA peak was recorded at 205.6 for the NAA peak, 140.6 for the Cr peak and 33.26 for Lactate. For the PRESS sequence, the SNR recorded for the NAA peak was 144.72, for the Cr peak was 98.33 and for Lactate was 23.77. The increase in SNR was 1.4-fold for the NAA peak, 1.4-fold for the Cr peak and 1.4-fold for Lactate.

The water peak was adequately suppressed (below the metabolite peaks) in both spectra. However, the presence of some spurious signals close to the baseline noise level were seen in the SV-semiLASER spectrum in Figure 4.3.19 (encircled, red oval). These signals could be produced as a result of unwanted unfiltered coherence pathways and/or imperfect RF pulse profiles [71] or they could be due to Eddy currents which cause broadened resonances and/or distorted line shapes, especially in short TE experiments. These effects get more pronounced at shorter echo times and therefore a longer echo time may be advisable to obtain an artefact free spectrum. Hence, we concluded that even with a higher minimum echo time, the SV-semiLASER sequence achieved selection of a voxel in the phantom at the iso-center with an adequately suppressed water peak and higher SNR for the NAA peak as compared to the conventional PRESS sequence. We also decided to maintain an echo time of TE=20ms for the rest of SV-semiLASER studies to minimize the observed spurious signals.
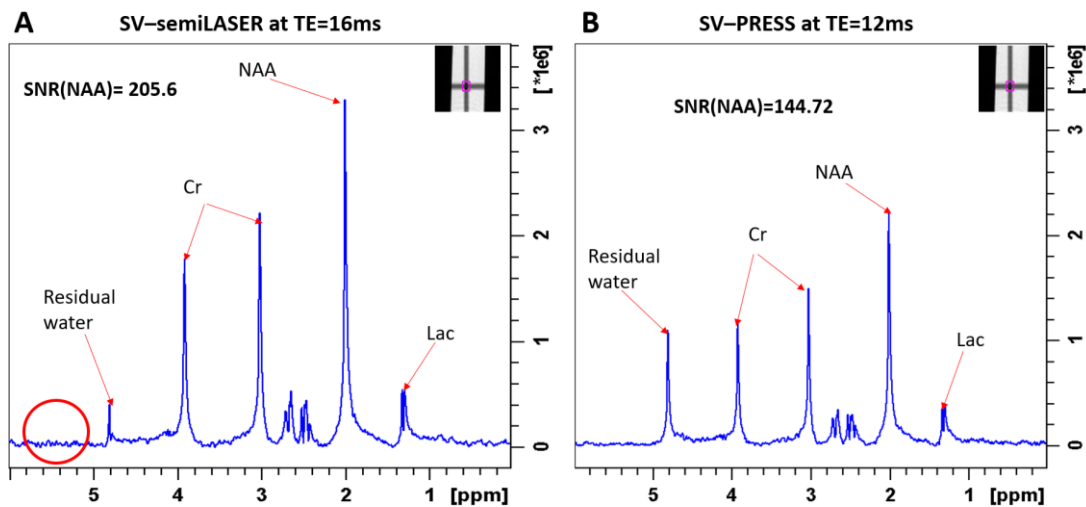
Figure 4.3.19 SV-semiLASER water suppressed spectrum from phantom-B at TE=16ms. (B) PRESS water suppressed spectrum in phantom at TE=12ms. The presence of some spurious signals close to the baseline noise level were seen in the SV-semiLASER spectrum encircled with red oval

4.3.3.5   Comparison of sequences performance in wild-type and tumor harbouring mice.

MRS sequences are also used for monitoring the molecular properties and metabolic heterogeneity of brain tumors in preclinical settings [72]. The main differences between normal

brain parenchyma and tumor areas include higher choline/creatine (Cho, 3.21/Cr, 3.03 ppm) ratios, higher NMR visible mobile lipids (ML, 0.9 and 1.3 ppm) and lactate (Lac, 1.3 ppm and 4.1 ppm) peak intensities in tumor areas [73] [74], as well as lower N-acetyl-aspartate/N-acetyl containing compounds (NAA/NAc, 2.02 ppm) signal [75].

Single voxel (SV ^{1}H-MRS) data were acquired in-vivo using wild type (wt) C57/BL6 normal mice and GL261 tumor bearing mice.Single voxel spectra acquired from wt and tumor bearing mice brain using SV-semiLASER and SV-PRESS sequences for a (3 mm)[3] voxel placed in the striatum/equivalent tumour position are compared in Figure 4.3.20. In the wt mouse dataset, an SNR increase of 1.3 times was obtained for the NAA peak with the SV-semiLASER, whereas in the tumor mouse a slightly lower 1.1 times increase was recorded for the Lac/MLpeak. The comparisons were made at the same TE=20ms. The drop in the overall SNR increase in tumor mouse using the SV-semiLASER sequence was dependent on the metabolite chosen as well as the shimming of the voxel. The greater inhomogeneity of the tumor areas also influences the SNR increase. Placement of the voxel in a low grade or frankly malignant or necrotic region of the tumor may yield distinctly different MR spectroscopy results [76] [77].

WT mouse
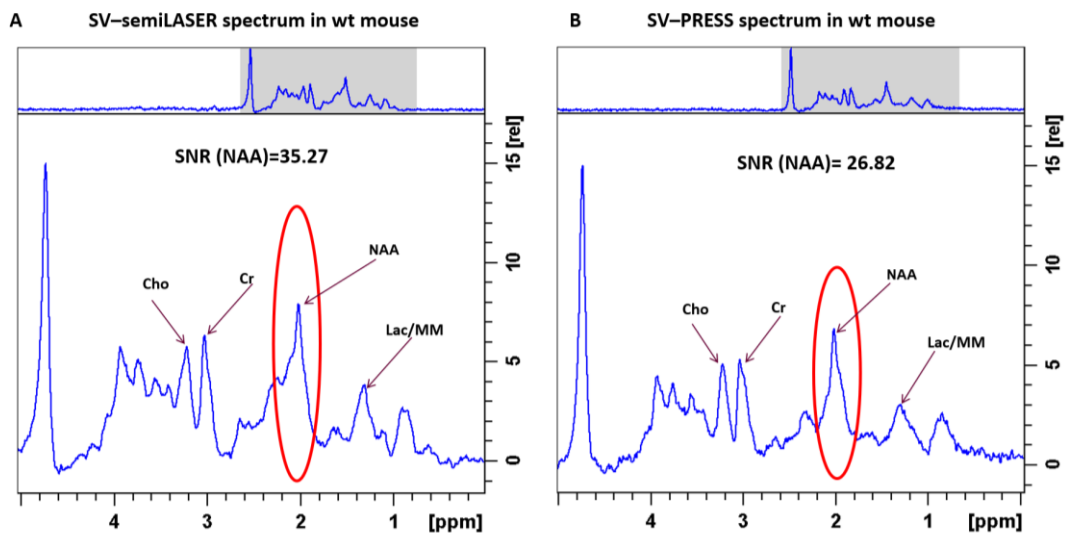
Tumor mouse
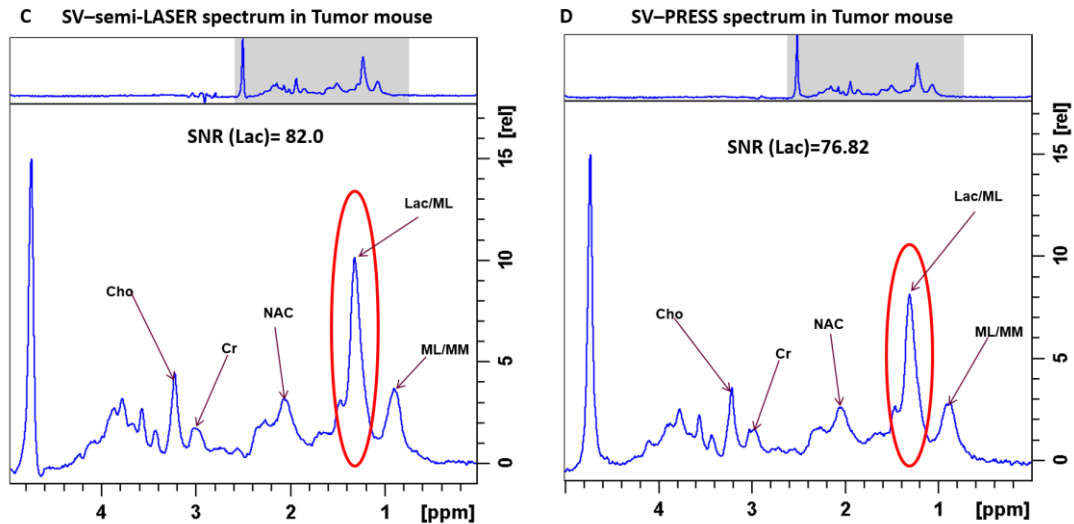
Figure 4.3.20 Mouse brain spectra acquired at TE=20ms with SV-semiLASER (A,C) and SV-PRESS (B,D) from wild type (A,B) and tumor(C,D) mice. The NAA peaks in wt mouse and the Lactate/ML peaks in tumor mosue are encircled in red.

4.3.3.6   Repeatability and Reproducibility tests

As already described in Chapter 3, repeated measurements made on the same subject under identical conditions determine the repeatability of a method whereas the reproducibility can be defined as the variation of the same measurement made on a subject under other potentially changing conditions. To check the reliability of the implemented SV-semiLASER sequence under similar and potentially changing conditions, intraday and interday experiments were performed where intraday refers to repeated acquisitions (n=3 minimum) without changing any parameter and with the same adjustments, while interday refers to the same experiments performed on three consecutive days changing external factors such as shimming, receiver gain etc. The repeatability coefficient (RC) and the coefficient of variation (CV) were computed to quantify the repeatability and reproducibility tests. Phantom B was used in all experiments and the acquisition parameters were kept the same as described in section 4.3.3.3.

Figure 4.3.21 shows the comparison of single voxel spectra acquired using SV-semiLASER and PRESS sequences for three "cloned" scans which were run one after the other to obtain Intraday experiments and were labelled 1.1, 1.2 and 1.3 respectively.
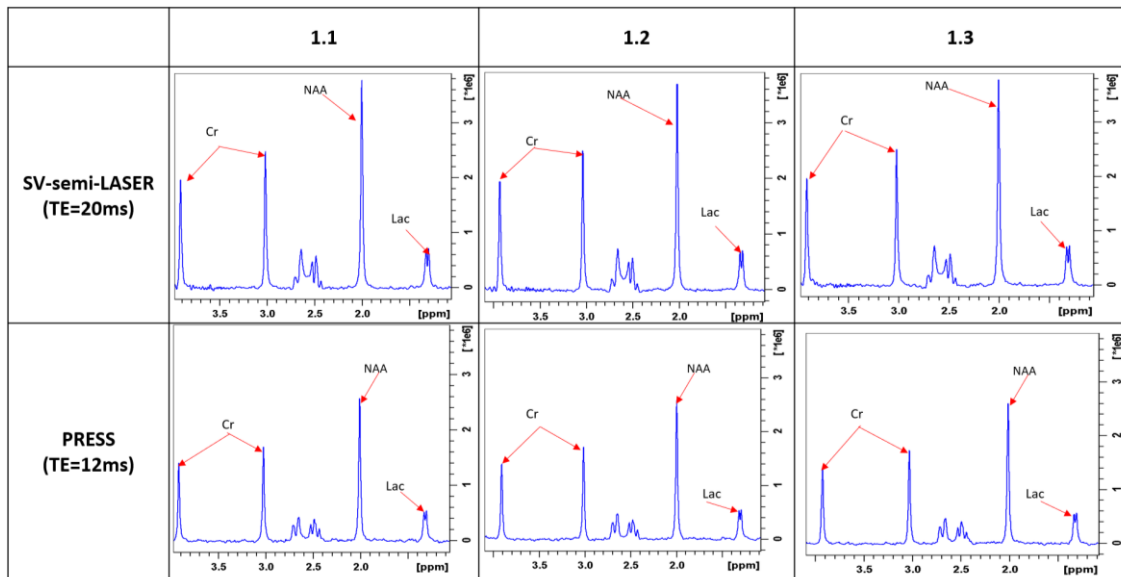
Figure 4.3.21 Spectra acquired from phantom B using SV-semiLASER and PRESS sequences for 3 repeat experiments 1.1, 1.2 and 1.3. SV-semiLASER sequence used TE=20ms and the PRESS sequence TE=12ms.

The mean SNR and standard deviation, coefficient of Variation (CV) and repeatability coefficient (RC) are recorded in Table 4.3.3. Mean SNR values are plotted in Figure 4.3.22 for the metabolites NAA, Cr and Lac. From the results obtained, it was observed that for intraday tests, the SV-semiLASER sequence provided a higher mean SNR and smaller standard deviation for all three metabolites as compared to SV-PRESS. The CV was also smaller (less than 5% showing good method performance) for the SV-semiLASER sequence and hence the reliability of results for the NAA peak was CVs: 2%, Cr 4% and Lac 3% indicating greater precision in comparison to PRESS sequence where the reliability of results for the NAA peak were CVs: 5%, Cr 6% and Lac 6%. The RC's calculated for the SV-semiLASER sequence were also smaller than the PRESS sequence suggesting better repeatability intraday.

Table 4.3.3 Intraday repeatability results for mean SNR of metabolites using SV-semiLASER and SV-PRESS sequences in phantom B studies.

SV-semi-LASER				PRESS			
exp	NAA SNR	CrSNR	LacSNR	exp	NAA SNR	CrSNR	LacSNR
1.1	196.25	130.81	37.16	1.1	126.09	84.35	27.42
1.2	201.84	138.91	37.94	1.2	138.19	94	30.9
1.3	193.57	129.66	36.01	1.3	133.2	91.39	29.42
SNR±std	197.22±4.22	133.13±5.04	37.04±0.97	SNR ±std	132.49±6.08	89.91±4.99	29.25±1.75
CV	0.02	0.04	0.03	CV	0.05	0.06	0.06
RC	11.69	13.96	2.69	RC	16.84	13.83	4.84

The mean SNR is expressed as mean ± std. The coefficient of variation (CV) and repeatability constant (RC) are also calculated for both methods for NAA, Cr and Lac signals.
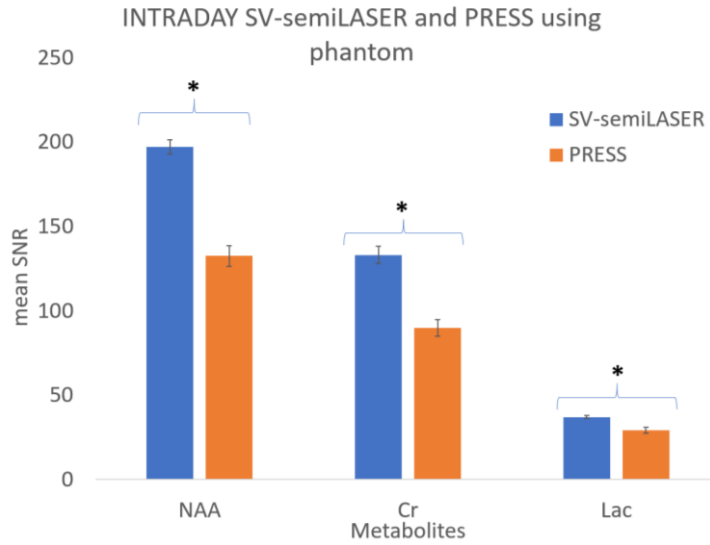
*Figure 4.3.22 Intraday repeatability results for mean SNR of metabolites NAA (N-Acetyl Aspartate), Cr (Creatine) and Lac (Lactate) using SV-semiLASER (blue) and PRESS (orange) in phantom B studies. *represents a statistically significant one tailed student's t-test result (P ≤ 0.05).*

The experiments were also repeated (interday) on three consecutive days (day1, day2 and day3) to verify the reproducibility of the implemented sequence. In interday experiments, although the sequence parameters were maintained the same, experimental conditions might change due to small differences in sample positioning with respect to coil, tuning or shimming adjustments. The acquired spectra using the two sequences in comparison are plotted in Figure 4.3.23 and the calculated data including mean SNR and standard deviation, coefficient of variance and repeatability coefficient are tabulated in Table 4.3.4 and plotted in Figure 4.3.24. The mean SNR was consistently higher and the standard deviation was consistently lower in SV-semiLASER results obtained for all three metabolites in comparison to the PRESS sequence. Similar to intraday results, the SV-semiLASER sequence gives a smaller coefficient of variation for all three metabolites for interday results. The reliability of results in the SV-semiLASER sequence for the metabolites was, CVs: NAA 3%, Cr 2% and Lac 2%. For the PRESS sequence, the reliability of CVs was: NAA 10%, Cr 11% and Lac 9% suggesting a better reliability of the implemented SV- semiLASER sequence. The RC's calculated for the SV-semiLASER sequence are also smaller than the PRESS sequence suggesting better reproducibility in interday experiments.
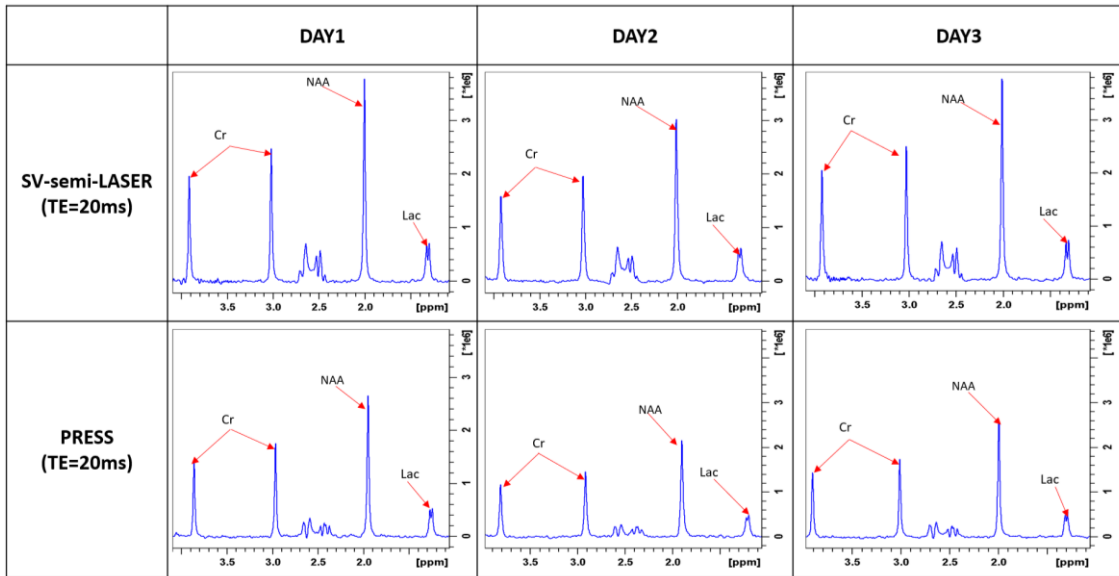
Figure 4.3.23 : Spectra acquired from phantom B using SV-semiLASER and SV-PRESS sequences for experiments conducted on three consecutive days i.e. day1, day2 and day3. TE was kept the same at TE=20ms for both the SV-semiLASER sequence and the SV-PRESS sequence.

Table 4.3.4 Interday repeatability results for mean SNR of metabolites using SV-semiLASER and SV-PRESS sequences in phantom studies.

SV-semi-LASER				PRESS			
exp	NAA SNR	CrSNR	LacSNR	exp	NAA SNR	CrSNR	LacSNR
DAY1	196.25	130.81	37.17	DAY1	137.82	92.51	28.85
DAY2	188	126.8	36.3	DAY2	130.08	90.11	28.11
DAY3	187.66	125.59	37.87	DAY3	112.55	75.6	24.41
SNR±std	190.64±4.86	127.73±2.73	37.11±0.79	SNR±std	126.82±12.95	86.07±9.15	27.12±2.38
CV	0.03	0.02	0.02	CV	0.10	0.11	0.09
RC	13.47	7.57	2.18	RC	35.86	25.35	6.59

The mean SNR is expressed as mean ± std. The coefficient of variation (CV) and repeatability constant (RC) are also calculated for both methods for NAA, Cr and Lac signals.

101
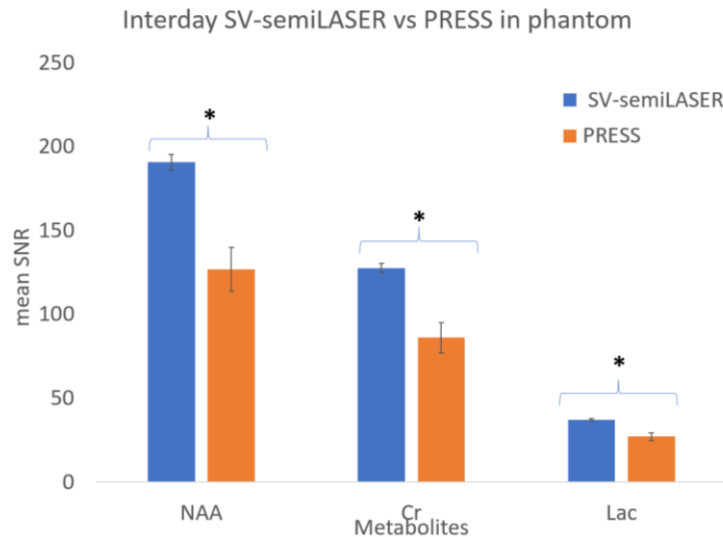
*Figure 4.3.24 Interday repeatability results for mean SNR of metabolites NAA (N-Acetyl Aspartate), Cr (Creatine) and Lac (Lactate) using SV-semiLASER (blue) and SV-PRESS (orange) in phantom studies. * represents a statistically significant one tailed student's t- test result (P ≤ 0.05).*

The implemented SV-semiLASER sequence was further tested for reproducibility in-vivo in wt mice using single voxel acquisitions performed on the same wt mouse for three consecutive days. The obtained spectra are plotted for comparison in Figure 4.3.25. The Echo time was kept the same at TE=20 ms for both the SV-semiLASER and the SV-PRESS sequence. Similar to results obtained with phantom B, SV-semiLASER spectra gave a visually higher peak intensity as compared to the SV-PRESS sequence in wt mouse for metabolites NAA, Cr and Lac. The calculated data including mean SNR and standard deviation, coefficient of variation and repeatability coefficient are tabulated in Table 4.3.5 and plotted in Figure 4.3.26. The SV-semiLASER sequence gives a smaller coefficient of variation for all three metabolites. For the SV-semiLASER sequence, the reliability of results was, CVs: 5% for the NAA peak, Cr 7% and Lac 11%. For the SV-PRESS sequence, the reliability was CVs: 14% for the NAA peak, Cr 12% and Lac 22% again suggesting a better reliability of the implemented SV-semiLASER sequence. The RC's calculated for the SV-semiLASER sequence were also smaller than the PRESS sequence suggesting better reproducibility in interday experiments.
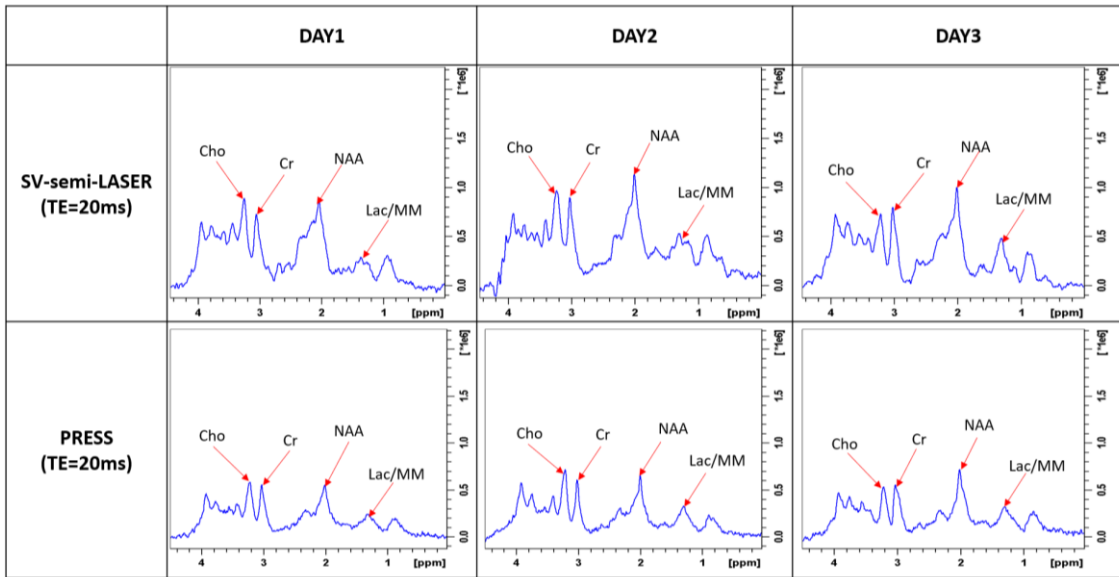
Figure 4.3.25 : Spectra acquired using SV-semiLASER and SV-PRESS sequences for experiments conducted on 3 consecutive days i.e. day1, day2 and day3 on a wt mouse. The Echo time was kept the same at TE=20ms for both the SV-semiLASER and the SV-PRESS sequence. Similar to results obtained in phantom B, SV-semiLASER spectra give a visually higher peak intensity as compared to the PRESS sequence in wt mouse for metabolites NAA, Cr and Lac/MM

Table 4.3.5 Interday repeatability results for mean SNR of metabolites using SV-semiLASER and SV-PRESS sequences in-vivo in wt mice studies.

SV-semi-LASER				PRESS			
exp	NAA SNR	Cr SNR	Lac SNR	exp	NAA SNR	Cr SNR	Lac SNR
DAY1	31.76	26.7	16.92	DAY1	18.62	18.98	11.79
DAY2	28.87	23.33	15.93	DAY2	24.38	22.84	18
DAY3	31.38	24.28	19.62	DAY3	23.66	18.64	13.89
mean SNR±std	30.67±1.57	24.77±1.74	17.49±1.91	mean SNR±std	22.22±3.14	20.15±2.33	14.56±3.16
CV	0.05	0.07	0.11	CV	0.14	0.12	0.22
RC	4.35	4.82	5.29	RC	8.70	6.45	8.75

The mean SNR is expressed as mean ± std. The coefficient of variation (CV) and repeatability constant (RC) are also calculated for both methods for NAA, Cr and Lac signals.
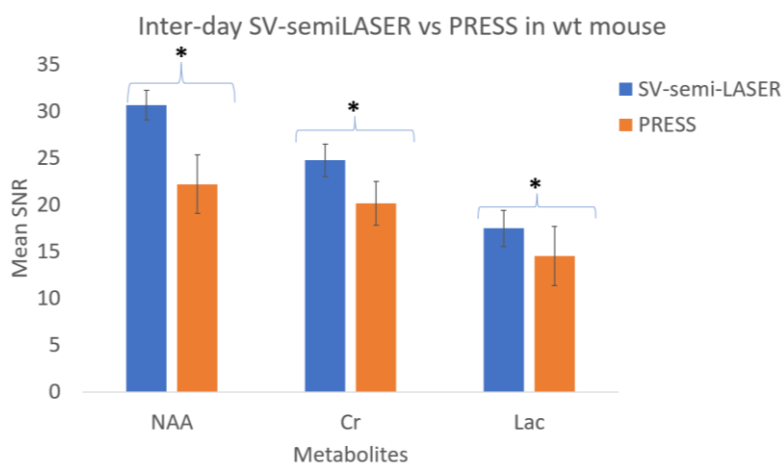
*Figure 4.3.26 Interday repeatability results for mean SNR of metabolites NAA (N-Acetyl Aspartate), Cr (Creatine) and Lac (Lactate) using SV-semiLASER (blue) and SV-PRESS (orange) in-vivo in wt mouse studies. * represents a statistically significant one tailed student's t-test result (P ≤ 0.05).*

4.3.4   Conclusions

The presented implementation of SV-semiLASER sequence with high-bandwidth adiabatic refocusing RF pulses and well-balanced and concurrently optimized crusher gradients and delays resulted in a minimum Echo Time of TE=15.7ms. The sequence was tested using various phantoms as well as wt and tumor mouse models on a 7T Bruker Biospec scanner. The results consistently provided higher SNR for the implemented SV-semiLASER sequence. The ca. 1.3-fold increase in SNR should be advantageous for quantitation of metabolites as well as monitoring changes in the content of those metabolite over time and in various regions of the normal as well as tumor brain. The test-retest repeatability and reproducibility and the reliability of the SV-semiLASER sequence in phantoms as well as in mouse models in vivo was also established, showing improved performance with respect to the standard SV-PRESS sequence. This SV-semiLASER sequence could provide added value in pre-clinical diagnostics and research and substantially increase the data quality achievable by MRS and thereby contribute to the wider utility and use of the technology. Furthermore, the increased SNR offered by our SV-semiLASER implementation opens the door to new possibilities in studies of mouse brain diseases such as reduction in voxel size and hence minimization of partial volume effects while maintaining sufficient SNR. The higher SNR achieved could also help reduce the overall scan time of the experiment by acquiring a reduced number of accumulations (averages per scan) while preserving acquisition quality. The reduction in scan time could be a major game changer in overcoming the inherent long scan time limitation of in vivo MRS studies.

4.4 MRSI semiLASER sequence implementation

In this chapter we present the implementation of the multi-voxel MRSI-semiLASER sequence on the 7T Bruker Biospec scanner with the aim to improve higher resolution multi-voxel spectroscopic data acquisition in mouse brain wild type (wt) and tumour models as well as in phantom studies and incorporate it as an additional tool to the Bruker stock CSI-PRESS sequence.

The MRSI-semiLASER sequence consists of a combination of conventional non-adiabatic slice-selective excitation of the proton spins, together with double slice-selective refocusing of the spins by two pairs of adiabatic full-passage (AFP) pulses [78]. This produces a spin echo in a volume of interest (VOI) while the adiabatic nature of the higher bandwidth hyperbolic secant refocusing pulses provides insensitivity to B1 inhomogeneities as well as sharp selection profiles and a smaller chemical shift displacement error (CSDE) than standard CSI-PRESS acquisition [79]. The CSDE occurs when there is an imperfect magnetic field homogeneity within the NMR sample. Ideally, the magnetic field should be uniform across the sample, but in reality, there can be variations and distortions due to imperfections in the magnet or the sample itself. These variations in the magnetic field can cause the resonant frequency of the nuclei to be shifted, leading to errors in the measured chemical shifts. Figure 4.4.1 illustrates the chemical shift displacement error (CSDE) in mouse brain MRSI. The frequency offset Δf excites slightly different regions (shown in red) than the initial grid planned for a certain frequency of resonance. This results in the excited volume of interest (VOI) being shifted from VOI1 to VOI2 and hence signals with different chemical shifts experience different slice selections leading to CSDE errors.
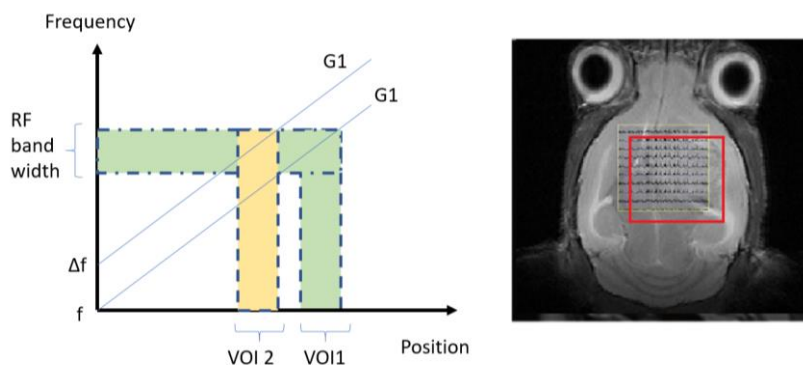
Figure 4.4.1 Illustration of the chemical shift displacement error (CSDE) in mouse brain MRSI. The frequency offset Δf excites a slightly different region (shown in red) than the initially planned grid. This results in the excited volume of interest (VOI) being shifted from VOI1 to VOI2. Figure adapted from [20].

The MRSI-semiLASER sequence helps in combating this CSDE by utilizing voxels closer to the edge of the VOI. In addition, the MRSI-semiLASER sequence provides more homogeneous voxels which helps in reducing the partial volume effects that causes increased variability in spectra. One disadvantage of the MRSI-semiLASER sequence is the longer minimal echo time in comparison to the CSI-PRESS sequence, due to the higher bandwidth of the refocusing pulses.

The results reported in the current chapter summarize the comparisons of using the newly implemented MRSI-semiLASER sequence over the commercially available CSI-PRESS sequence when tested in phantoms and in healthy and tumor mouse brain. The analysis was also extended by incorporating k-space sampling strategies using multiple acquisition modes and increased spatial resolution by reducing slice thickness in the implemented MRSI-semiLASER sequence.

The results showed improved homogeneity of the voxels and reduction in chemical shift displacement error (CSDE).

4.4.1 MRSI-semiLASER sequence implementation

For the ParaVision 5.1 implementation, the MRSI-semiLASER sequence, was derived from the stock CSI-PRESS sequence following the same logic as the Single Voxel-semiLASER sequence implementation already discussed in section 4.3.

For the MRSI-semiLASER sequence, the shortest echo time (TE) was achieved through a combination of optimally chosen RF pulses, crusher gradient and delay lengths. The excitation pulse for the MRSI-semiLASER sequence consisted of a 600μs, 9000Hz conventional Hermite shape (Figure 4.4.2). This was identical to the Bruker CSI-PRESS sequence. The refocusing pulses in the MRSI-semiLASER sequence consisted of 2000 μs and 9003Hz bandwidth Hyperbolic secant (HS) adiabatic pulses. Whereas, the Bruker CSI-PRESS sequence consisted of 600μs, 5700 Hz conventional Hermite refocusing pulses. The flip angles and voxel dimensions were kept the same in both sequences. Adiabatic refocusing requires slightly larger gradient strengths in the y and z directions due to longer RF pulse lengths and bandwidths. The echo time calculations for the implemented MRSI-semiLASER sequence are described in more detail in appendix (C).

The rephasing gradient in the MRSI-semiLASER sequence was applied just after the excitation gradient. Additionally, phase encoding gradients were introduced in the x and y planes to spatially encode the signal from different locations within the sample. By applying a series of gradients with varying strength and duration, the signal from each location can be assigned a unique phase, which is then used to reconstruct an image of the metabolites in the sample. Additionally, equal crusher pairs were also added before all refocusing pulses (not shown in the pulse sequence diagram) to avoid spurious signal. The gradient order was kept as Gz-Gy-Gx following the gradient order in the Bruker CSI-PRESS sequence. VAPOR water suppression and OVS were also applied prior to the localisation module as shown in Figure 4.4.2, to avoid signal contamination from outside the MRSI grid.

To calculate the minimum echo time, as previously described in chapter 4.3, the spin echo condition must hold such that(equation 4.4.1):

$$T1 + T3 + T5 = T2 + T4 \qquad\qquad [4.4.1]$$

The five inter-pulse delays of 3.73 ms, 5.80 ms, 5.80 ms, 7.50 ms and 3.90 ms for T1 through T5, respectively were chosen. The minimum echo time was then equivalent to:

Minimum echo time (TE) = T1 + T2 + T3 + T4 + T5 $\qquad\qquad$ **[4.4.2]**

$$= 3.73 \text{ ms} + 5.8 \text{ ms} + 5.8 \text{ ms} + 7.50 \text{ ms} + 3.90 \text{ ms}$$

$$= 26.71 \text{ ms}$$

The CSDE was defined as the difference in slice position between the water (4.7 ppm) and lipid-CH_3 (1.3 ppm) resonances, and was calculated using equation 4.4.3:

$$\text{CSDE (\% of voxel size)} = \frac{Frequency\ difference\ between\ 2\ resonances\ (Hz)}{Bandwidth\ of\ frequency\ selective\ pulse(Hz)} \qquad \textbf{[4.4.3]}$$

The CSDE calculations showed reduction in chemical shift displacement using the MRSI-semiLASER sequence. For CSI-PRESS the CSDE was = 9%, 14.2% and 14.2% in the x, y and z planes and for MRSI-semiLASER the CSDE was = 9%, 8.9% and 8.9% in the x, y and z planes.
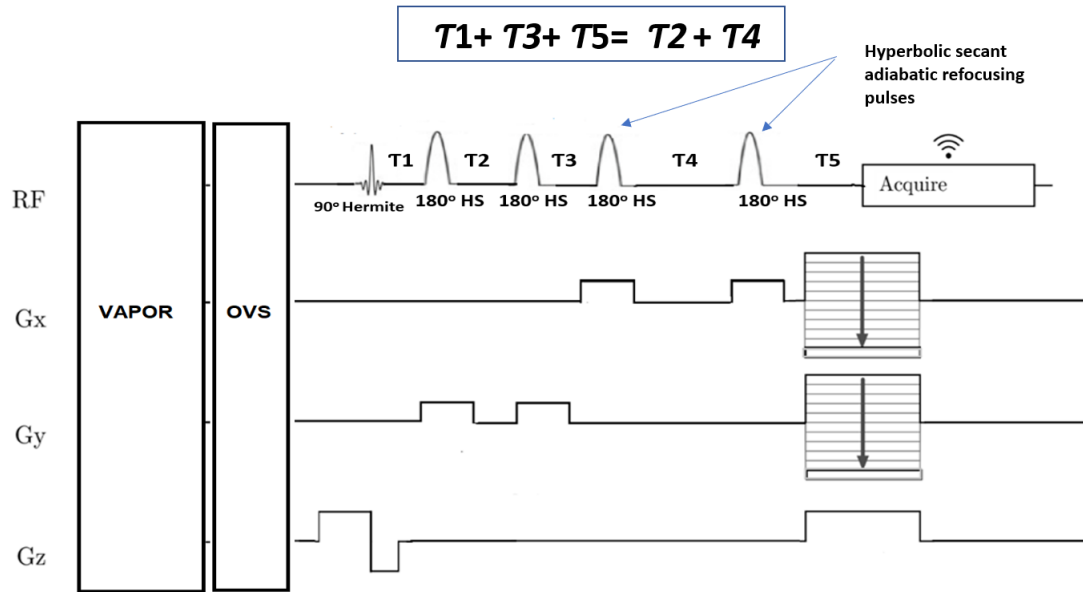
Figure 4.4.2 The simplified sequence diagram of the implemented MRSI-semiLASER sequence [80]. See text and abbreviations list for further details.

Figure 4.4.3 (A) shows the complete timing diagram, (B) and (C) contains the breakdown of the timing diagram into different sections to better visualize the delays and intervals. The code written corresponding to each section is also displayed on the left.

A
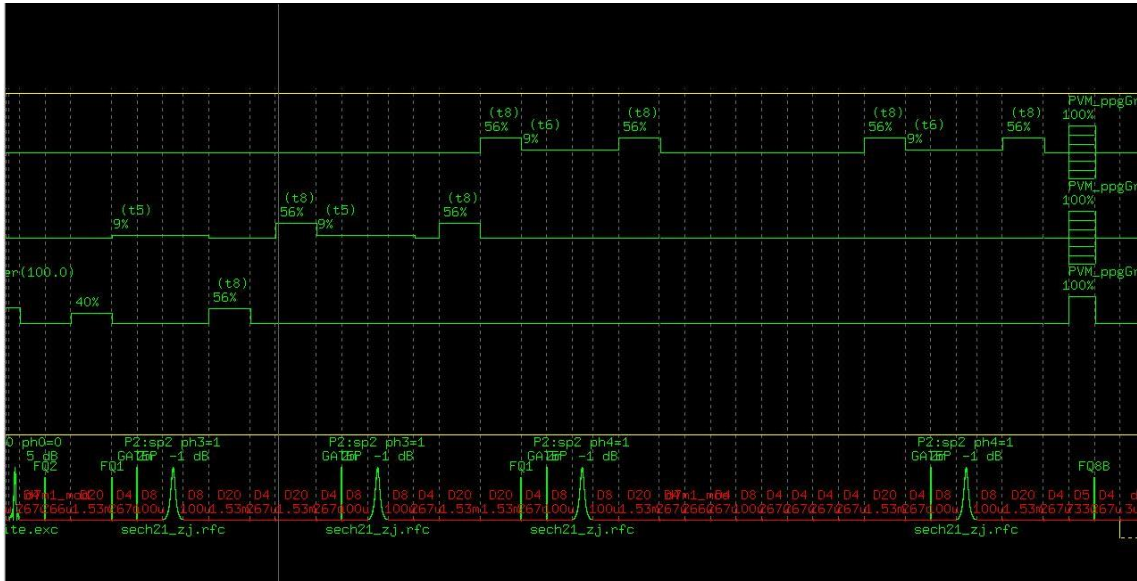
B

```
10u  fq1:f1
d4      grad{(0)|(0)|(t0)}          ; slice gradient on
d8 gatepulse 1
p0:sp0  ph0                         ; excitation pulse
d4  groff
```

```
d7m1_mod  groff  fq2:f1
d20    grad{(0)|(0)|(t8)+(t1)}            ;spoiler
d4    grad{(0)|(t5)|(0)} fq1:f1      ;second slice
d8      gatepulse 1
p2:sp2  ph3
d8
d20    grad{(0)|(0)|(t8)}
d4    groff
d20    grad{(0)|(t8)|(0)}
d4    grad{(0)|(t5)|(0)}
d8  gatepulse 1
p2:sp2  ph3
d8
d4    groff
d20    grad{(0)|(t8)|(0)}
d20    grad{(t8)|(0)|(0)}
d4    grad{(t6)|(0)|(0)} fq1:f1
d8      gatepulse 1
```
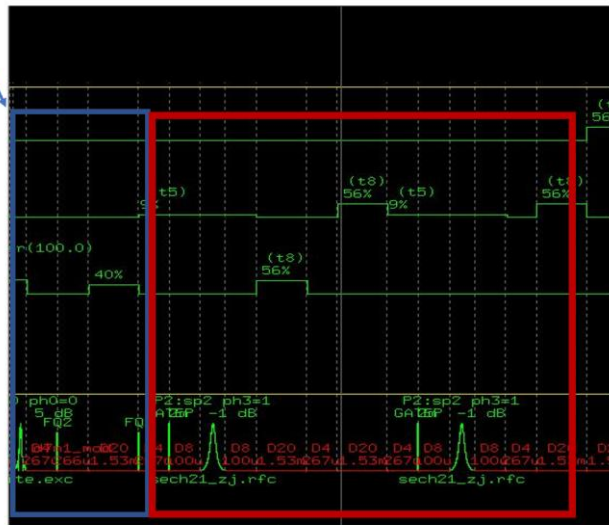
C
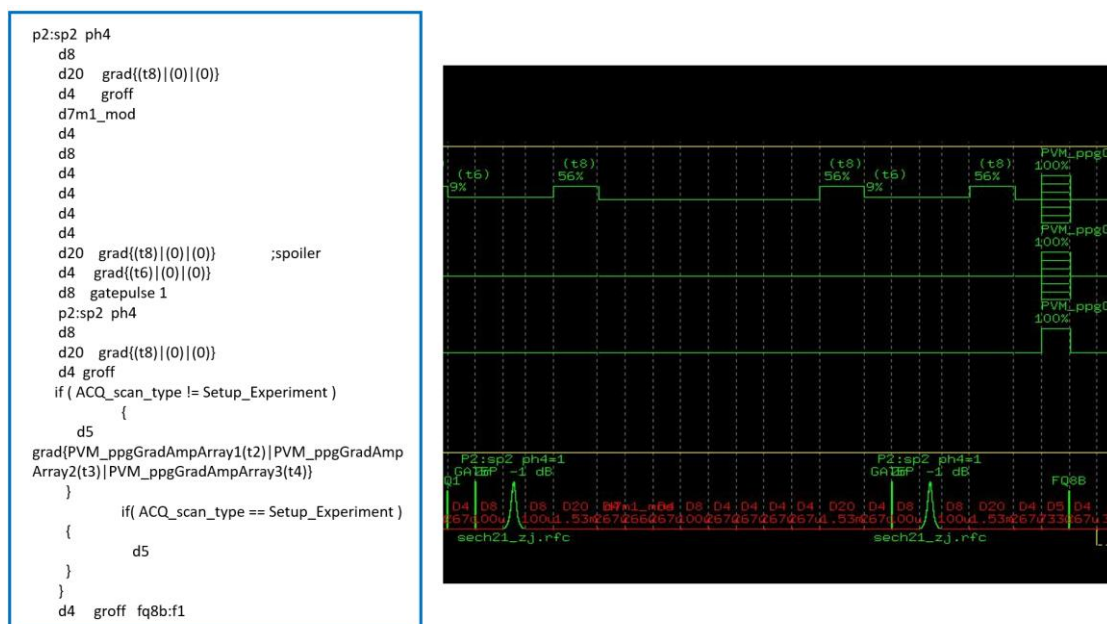
Figure 4.4.3 Bruker ParaVision 5.1 version screenshots of the pulse sequence timing diagrams represented in graphical format for the implemented MRSI-semiLASER sequence and the corresponding code in pulse program file on the left. (A)Complete localization module in the pulse timing diagram (B) sub-interval from excitation pulse where the rephasing lobe is merged with the first crusher having amplitude 40% and the first pair of refocusing pulses, (C) sub-interval between the second pair of refocusing pulses and the remaining interval till acquisition.

To post process the acquired MRSI datasets using the MRSI-semiLASER sequence, the Bruker **csidash.tcl** macro [51] was also modified to **csidash_v3_zoo.tcl** for compatibility purposes with the implemented MRSI-semiLASER sequence. The modified files included the csiproc.tcl and csiacqu.tcl. This macro creates three post processed data folders in the ParaVision GUI using the TOPSPIN spectroscopic tools to process the spectrum of each voxel of the CSI image with functions such as baseline correction**,** exponential multiplication with line broadening constant, zero filling etc. The phase correction values PHC0 and PHC1 are among the useful parameters which are stored in the output folders obtained from the macro post processing. The modification of this macro completed the MRSI-semiLASER sequence implementation and hence we moved forward with sequence testing under different chosen conditions.

In the next sub sections, we compiled and presented the experimental results for testing the implemented MRSI-semiLASER sequence. The common objectives of all experiments performed were two-fold; first to see whether the implemented sequence provided accurate localization of the metabolite resonances without producing any frequency drift or artefacts in the acquired MRSI grid; and second to compare the intensity and SNR of the metabolites in the acquired spectra between the implemented and the stock Bruker sequence to evaluate the performance of the newly implemented sequence. In vivo mouse brain PRESS CSI and MRSI-semiLASER were acquired with similar experimental parameters for a direct comparison.

4.4.2 Validation of implemented MRSI-semiLASER sequence using a volume transceiver coil

4.4.2.1 MRSI-semiLASER vs CSI-PRESS at same TE using an ethanol in water phantom

To test the implemented sequence under homogeneous conditions, the experiments were first performed using a volume transmit-receive QuadTranceiver [1]H 1000 W 7.2 cm inner diameter volume coil for more homogeneous excitation and reception. A spherical glass phantom (phantom 2) containing water and ethanol in 3:1 ratio was used to for MRSI acquisitions at the same echo time. The acquisition parameters were kept as follows: TE = 27 ms, TR = 2500 ms, VAPOR water suppression, FOV= $(17.6mm)^2$, slice thickness = 1 mm, voxel size = $(6.6 mm)^2$, SW = 4006.41 Hz; NA = 512, acquisition mode = weighted , OVS = on and TAT= 21 min.

The MRSI inner grid is a 12x12 matrix consisting of 144 sub-spectra ranging from voxels 11 to 22. Each of the sub-spectra may act as an individual spectral vector and contributes towards the overall homogeneity of the MRSI grid. The mean SNR maps for the CH_3 peak at 1.26 ppm are plotted and compared for the (A) MRSI-semiLASER and (B) CSI-PRESS sequences in Figure 4.4.4. The mean SNR of the inner grid voxels for the MRSI-semiLASER sequence was recorded as 1.78 x 10^3 and the mean SNR for the CSI-PRESS sequence as 1.40 x 10^3. This indicated a 1.3-fold increase in SNR for the MRSI-semiLASER sequence under equal conditions. The mean spectra obtained using the two sequences were also compared for lineshape and are plotted in panels C and D (Figure 4.4.4). The MRSI-semiLASER spectrum produced visually similar lineshape to the CSI-PRESS spectrum and the ethanol resonances were accurately observed including CH_3 at 1.26 ppm and CH_2 at 3.72 ppm. The SNR maps also showed visual improvement in homogeneity of the MRSI grid with the implemented sequence.
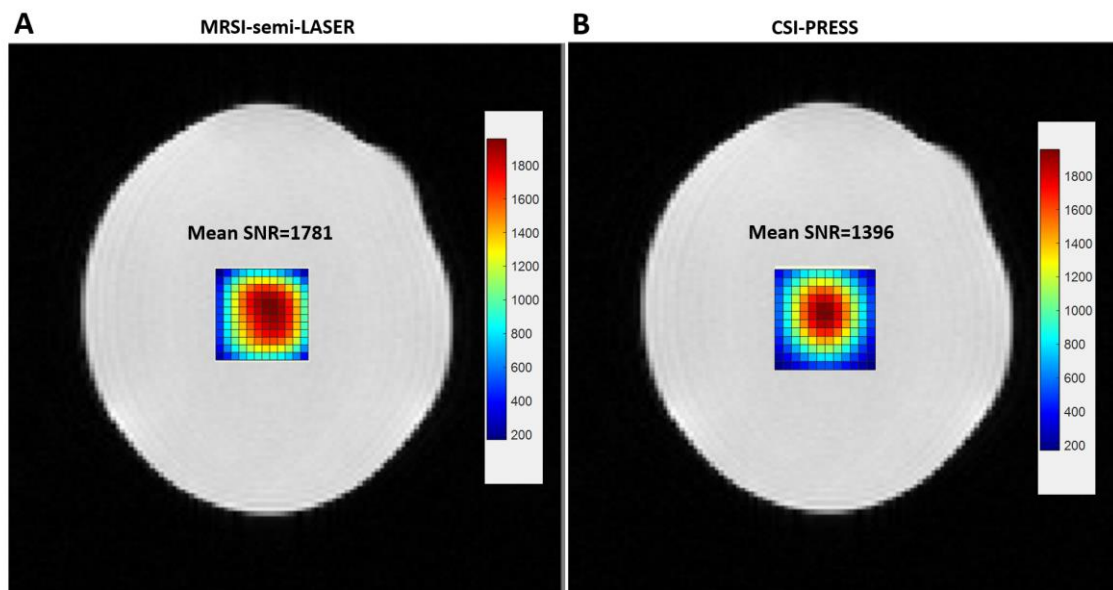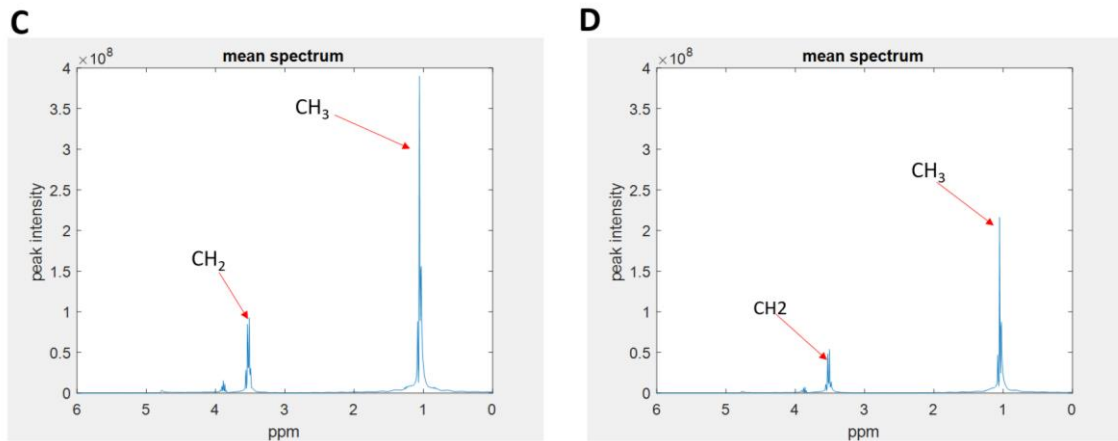
Figure 4.4.4 (A) MRSI-semiLASER, (B) CSI-PRESS intensity maps for ethanol (CH₃) peak acquired at TE = 27ms for comparison purposes.The maps are overlaid on T2 weighted images. (C) Mean water suppressed spectrum for MRSI-semiLASER and (D) Mean water suppressed spectrum for CSI-PRESS acquisitions.

4.4.2.2 Comparison with CSI-PRESS at same TE using metabolite phantom A

To see whether brain-like metabolite resonances could be correctly recorded using the implemented MRSI-semiLASER sequence in the volume coil setup, additional experiments were performed using the high concentration metabolite phantom (phantom A) as described in section 3.2. All acquisition parameters were kept the same as reported in the previous section 4.4.2.1 experiments. The SNR maps were plotted for the NAA peak, which is the most abundant metabolite in phantom A. The map for the MRSI-semiLASER sequence (Figure 4.4.5 (A)) appeared more homogeneous across the grid compared to the CSI-PRESS at (B). The MRSI-semiLASER sequence recorded produced a mean SNR of 40.79 for the NAA peak at ca. 2.01 ppm, 29.97 for the Cr peak at ca. 3.02 ppm and 7.81 for the Lac peak at 1.3 ppm. On the other hand, the CSI-PRESS sequence (Figure 4.4.5 (B)) resulted in a mean SNR of 23.73 for the NAA peak, 18.48 for the Cr peak and 6.24 for the Lac peak. This indicated a 1.7-fold increase in SNR for the NAA peak, 1.6-fold for the Cr peak and 1.3-fold for the Lac peak when using the MRSI-semiLASER sequence. Figure 4.4.5 C&D shows the mean spectra for the MRSI-semiLASER and CSI-PRESS sequences, where the blue line indicates the mean over all spectra, whereas the grey patch indicates the standard deviation, to demonstrate variability among spectral patterns. All metabolites were localized correctly including NAA at 2.01ppm, Creatine and 3.02 and 3.9ppm and Lactate at 1.3ppm. The NAA (CH_2) peaks were also visible for the MRSI-semiLASER spectrum whereas the CSI-PRESS spectrum failed to allow the visualization of the NAA aspartate peaks at ca. 2.48 ppm and ca. 2.67 ppm. For all the experiments conducted the results provided significantly higher SNR using the MRSI-semiLASER sequence in addition to more homogenous SNR maps. Hence, we proceeded to further test the implemented sequence using the standard mouse brain acquisition configurations i.e. a surface coil receiver.
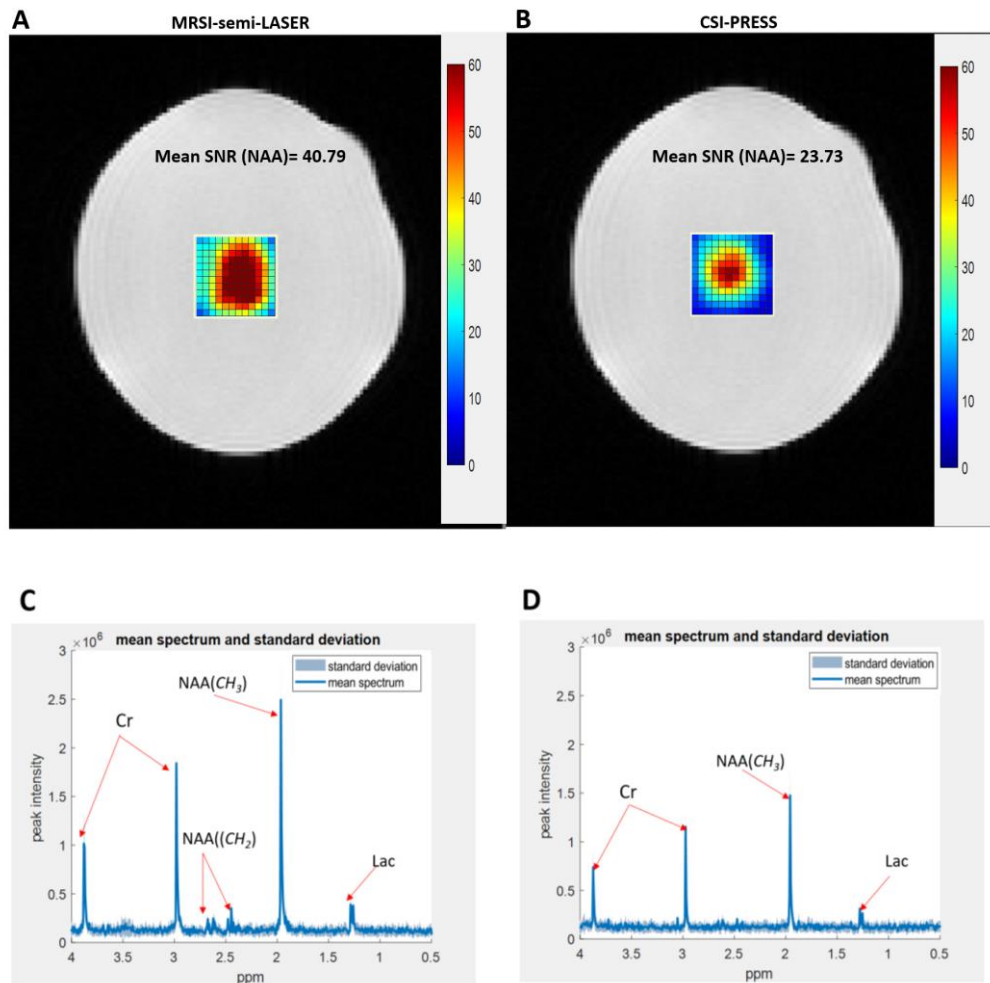
Figure 4.4.5 (A) NAA intensity map using MRSI-semiLASER, (B) NAA intensity map using CSI-PRESS maps overlaid on the corresponding T2w image of phantom A (C) mean spectrum and standard deviation for MRSI-semiLASER with zoomed panel to compare standard deviation with (D) mean spectrum and standard deviation for CSI-PRESS.

4.4.3 Validation of the implemented MRSI-semiLASER sequence using a surface receiver coil

After obtaining satisfactory results using the volume coil setup, the implemented MRSI-semiLASER sequence was evaluated initially with Phantom B) using a volume coil transmitter and a surface coil receiver setup, which is the standard configuration for mouse brain acquisitions, and later tested in-vivo.

4.4.3.1 MRSI-semiLASER vs CSI-PRESS in-vitro in phantoms B at equal TE

To prove that the implemented MRSI-semiLASER sequence produced similar results to the ones obtained using the more homogeneous volume coil setup presented in section 4.4.2, experiments were repeated comparing MRSI-semiLASER and CSI-PRESS performance using

phantom B. The echo time value chosen was TE = 27ms. The other acquisition parameters were kept as follows: TR = 2500ms, VAPOR water suppression, FOV= (17.6mm)^2, slice thickness = 1 mm, voxel size = (6.6mm)^2, SW = 4006.41 Hz; NA=512, acquisition mode = weighted and TAT = 21 min.

The NAA intensity maps overlaid on T2w images and inner grid mean spectra from voxels 11 to 22 are plotted in Figure 4.4.6 A and B. The MRSI-semiLASER sequence produces an improved homogeneity of the inner grid which is indicated by more homogeneous across the grid NAA SNR maps obtained. The mean SNR for the MRSI-semiLASER acquired dataset calculated from the 144 grid (12x12) voxels was recorded at 55.26 for NAA, 35.14 for Cr and 6.92 for Lac. For the CSI-PRESS sequence the SNR was recorded at 39.54 for NAA, 30.73 for Cr and 6.38 for Lac. The results indicated a 1.4-fold increase in SNR for the NAA peak, 1.1-fold for the Cr peak and 1.1-fold for the Lac peak, using the MRSI-semiLASER sequence.SNR values higher than those obtained with volume coil configuration were recorded, owing to the fact that surface coils are much smaller than the volume coils and give higher SNR because they sample noise only from nearby regions [81]. The mean spectrum and standard deviation for the MRSI-semiLASER and CSI-PRESS sequences are shown respectively in Figure 4.4.6 C and D. Similar to our results for experiments with the volume coil, all metabolites were detected correctly including NAA at 2.01ppm, Creatine and 3.02 and 3.9ppm and Lactate at 1.3ppm. The standard deviation was found to be visually comparable in both sequences.

Our results produced consistent improvement for the MRSI-semiLASER sequence compared to CSI-PRESS at equal TE. Hence, our next goal was to compare the sequence performance under the minimum achievable echo time condition for each sequence.
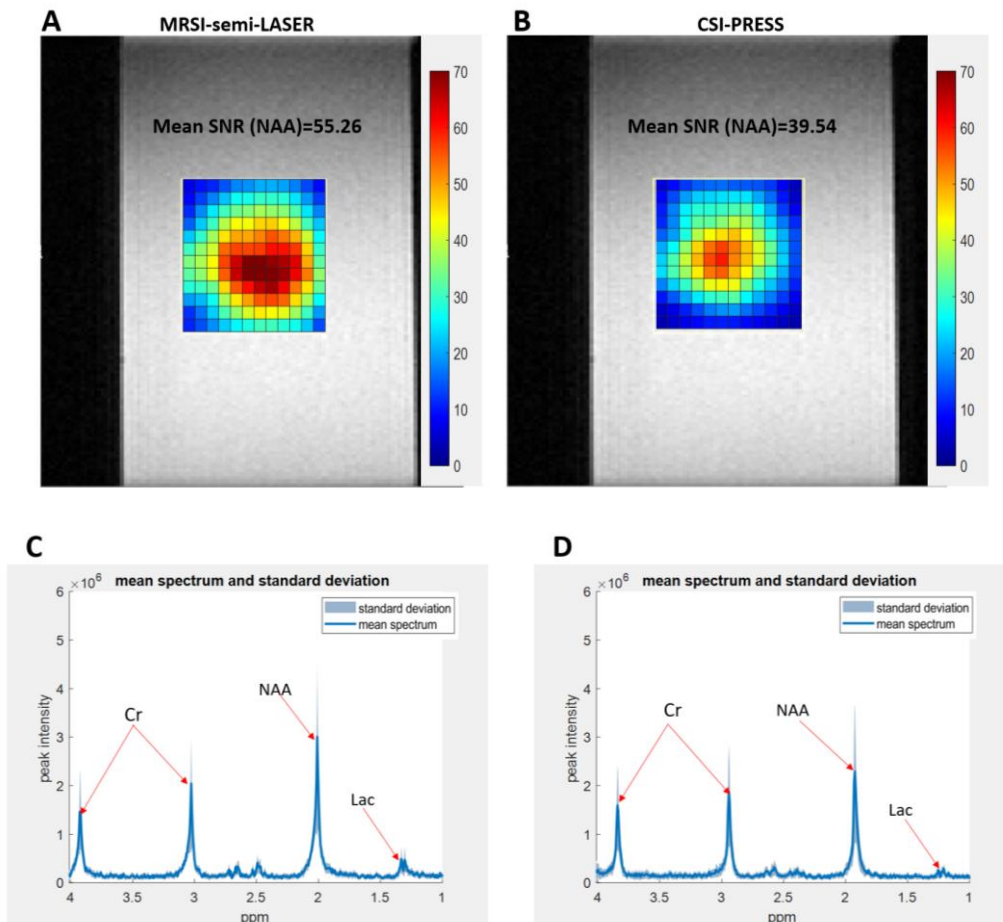
Figure 4.4.6 A-NAA intensity map using MRSI-semiLASER, B- NAA intensity map using CSI-PRESS, C- mean spectrum for MRSI-semiLASER and D- mean spectrum for CSI-PRESS at TE = 27 ms

4.4.3.2 MRSI-semiLASER vs CSI-PRESS in-vitro from phantom B at minimum achievable TE

The CSI-PRESS protocol had a minimum achievable echo time of TE = 14ms while the implemented MRSI-semiLASER had minimum echo time TE = 27ms. The comparisons were hence made between the two sequences at different echo time to prove the efficacy of the sequences at their best possible acquisition conditions performance. In such TE comparisons it is also important to consider the TE effects on metabolites that display J-coupling dependent fast evolution or have short T2 relaxation times e.g. Lactate, etc. For metabolite patterns that are composed of singlets or which have spectra dominated by a large singlet, the TE effect is much less substantial e.g. NAA etc. Thus, to avoid TE influences on metabolite relaxation and SNR evaluation, comparisons were made for the more stable NAA singlet at 2.01ppm.

The phantom B and all other acquisition parameters except TE were kept the same as reported in section 4.4.3.1. The SNR map comparison for the NAA peak is given in Figure 4.4.3.2 A and B and in panels C and D the mean spectra are shown. All metabolite peaks were detected properly. The mean SNR for the MRSI-semiLASER sequence calculated from the 144 voxels was 53.18 for NAA, 36.49 for Cr and 10.98 for Lac. For the CSI-PRESS sequence the SNR was 44.77 for NAA, 32.02 for Cr and 10.21 for Lac. The obtained results suggested a 1.2-fold increase in SNR for the

NAA peak at ca. 2.01ppm, 1.1-fold for the Cr peak at ca. 3.02 ppm and 1.1-fold for the Lac peak at ca. 1.3 ppm. These results showed that even at a longer TE, the MRSI-semiLASER sequence reported an increase in SNR over the CSI-PRESS sequence for NAA.

Figure 4.4.3.2 C and D represent the mean spectra and standard deviation for the MRSI-semiLASER and CSI-PRESS sequences. The standard deviation was similar for both MRSI-semiLASER and CSI-PRESS on visual inspection..

Hence, we concluded that even at a longer TE, the MRSI-semiLASER sequence performance was superior to the stock Bruker PRESS sequence. This paved the way to test the sequence for the first time in-vivo in wild type mice.
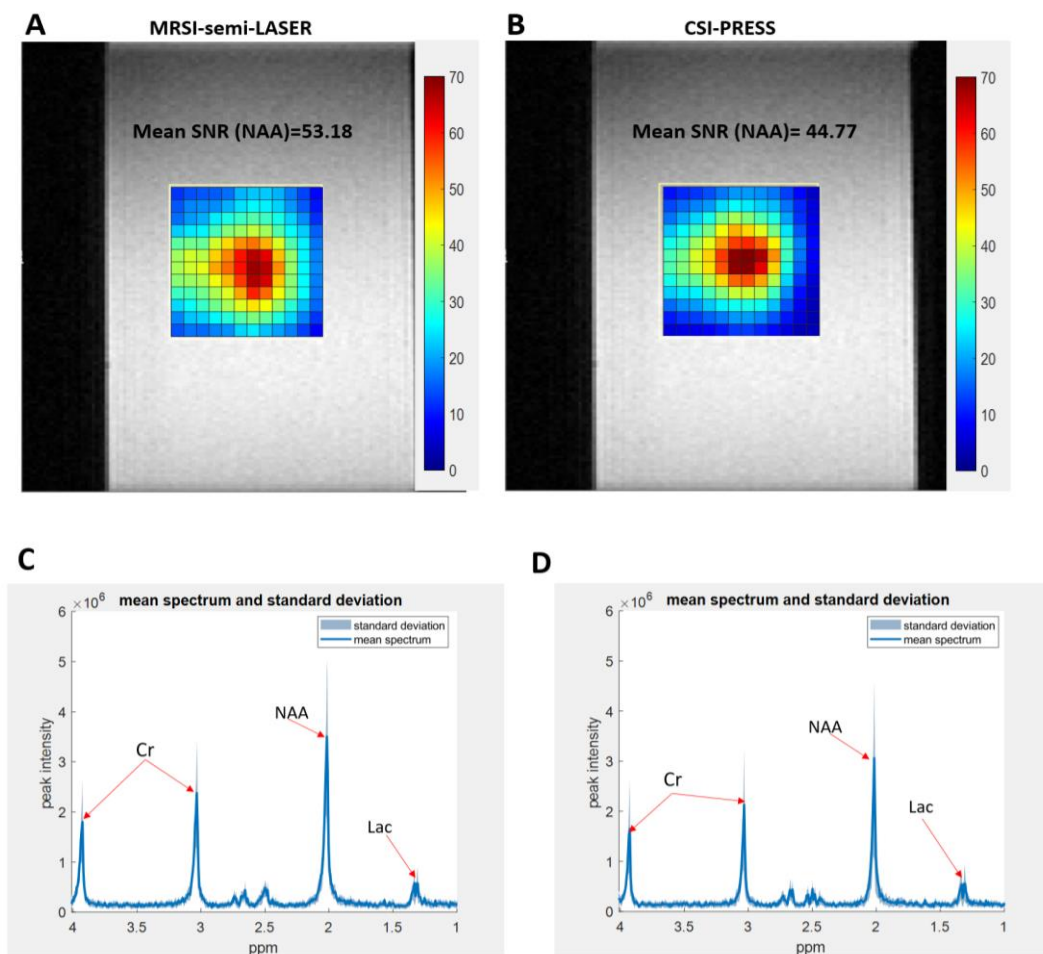
Figure 4.4.7 A-NAA SNR map for MRSI-semiLASER, B-NAA SNR map for CSI-PRESS, C and D represent the mean spectrum and standard deviation for MRSI-semiLASER and CSI-PRESS respectively at minimum TE for each sequence. See text for further details.

Figure 4.4.3.2 A-NAA SNR map for MRSI-semiLASER, B-NAA SNR map for CSI-PRESS, C and D represent the mean spectrum and standard deviation for MRSI-semiLASER and CSI-PRESS respectively at minimum TE for each sequence. See text for further details.

4.4.3.3 MRSI-semiLASER vs CSI-PRESS in-vivo in wt mouse at equal TE

Once the results with the phantom experiments proved to be consistent with our previous findings, we moved forward to test the sequence using animal models since the main objective of this sequence implementation was to provide an alternative acquisition scheme for high resolution MRSI studies in mice brain with further applications in treatment response to therapy in glioma models.

The first experiments measured the unsuppressed water spectra obtained from MRSI-semiLASER and CSI-PRESS acquisitions in a healthy mouse brain. The acquisition parameters for the unsuppressed acquisition were chosen as TE = 20ms, TR = 2500ms, VAPOR water suppression = off, FOV = $(17.6mm)^2$, slice thickness = 1 mm, voxel size = $(6.6mm)^2$, SW = 4006.41 Hz. As a standard procedure, saturation slices were also placed around the VOI to suppress the contribution of unwanted signal from the scalp. The saturation slices were applied in all in-vivo MRSI experiments reported in this thesis. Figure 4.4.8 A and B show the comparison of representative water unsuppressed spectra obtained for the MRSI-semiLASER and CSI-PRESS sequences. The representative spectra were selected from the same voxel position in the MRSI grid of the two sequences. The waterline for the MRSI-semiLASER sequence shows a reduction in the linewidth of the spectrum i.e. the CSI-PRESS spectrum has a linewidth of 33.78 Hz whereas the MRSI-semiLASER spectrum produce a slightly narrower linewidth of 31.95 Hz. This reduction in linewidth indicated improved homogeneity of the MRSI acquisitions with the implemented sequence.

The water suppressed spectra was then acquired in-vivo in mouse brain using the MRSI-semiLASER and CSI-PRESS sequences with the following acquisition parameters; TE = 27ms, TR = 2500ms, VAPOR water suppression, FOV = $(17.6mm)^2$, slice thickness = 1 mm, voxel size = (6.6mm)2, SW = 4006.41 Hz; NA=512, acquisition mode = weighted and TAT=21 min. Figure 4.4.8 C and D show representative spectra comparison for water suppressed MRSI acquisitions in-vivo in mouse brain from the same voxel location. While keeping the same TE, the MRSI-semiLASER spectra visually showed higher metabolite intensities compared to CSI-PRESS and all the different metabolites such as N-Acetyl Aspartate (NAA), Creatine (Cr), Choline (Cho) and others were detected properly. These results were consistent with our findings in phantom studies as well.
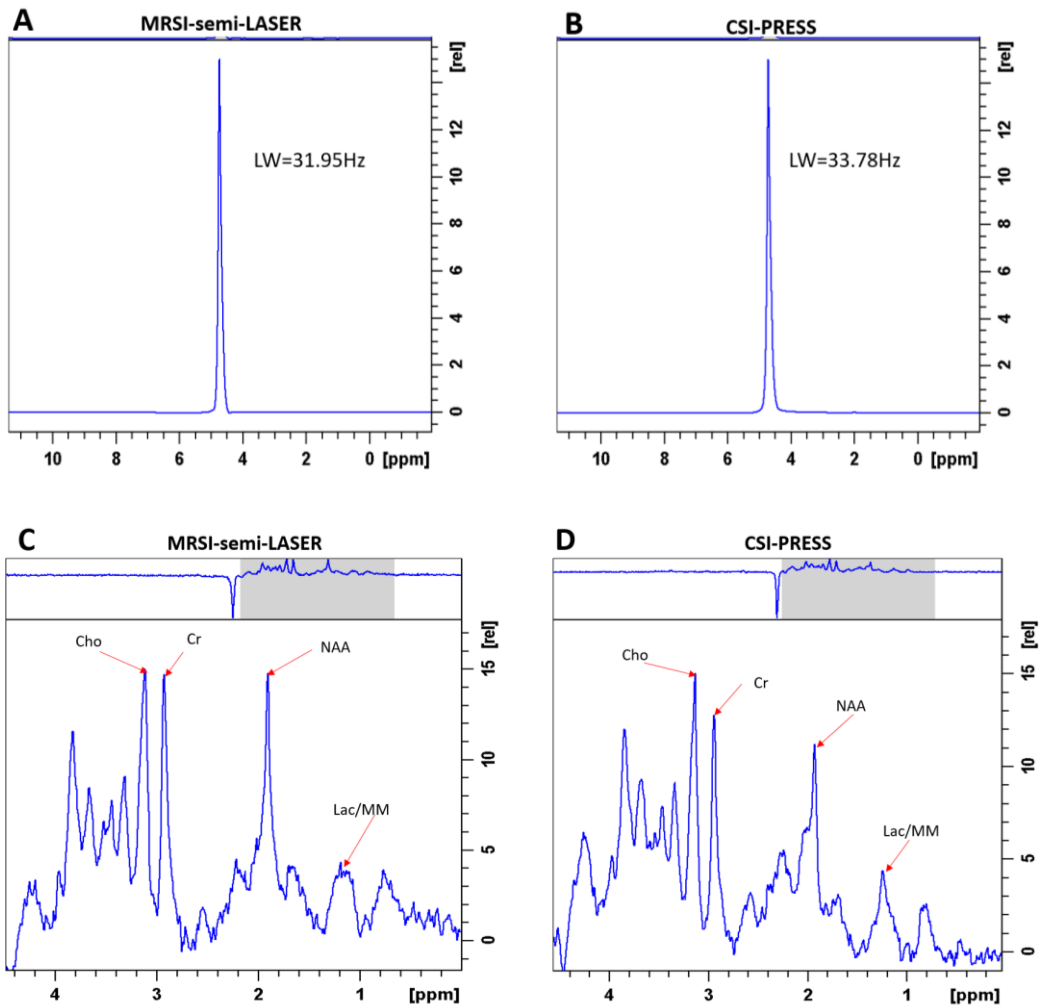
Figure 4.4.8 A and B unsuppressed water spectra comparison in wt mouse using MRSI-semiLASER and CSI-PRESS. C and D represent the single spectrum comparison from inner grid) for the MRSI-semiLASER and CSI-PRESS sequences respectively. The increase in apparent metabolite intensity in C can be observed by visually comparing the peak heights in both spectra with respect to noise below 0.5 ppm.

MRSI grids overlaid on T2-weighted images of the mouse brain for CSI-PRESS and MRSI-semiLASER are shown in Figure 4.4.9 panels A and B respectively. The mean SNR for the MRSI-semiLASER sequence was recorded as 15.7±3.3 for the NAA peak and 11.9±3.5 for the CSI-PRESS. This indicated a 1.3x increase in mean SNR for the MRSI-semiLASER sequence over CSI-PRESS at the same TE. Moreover, the MRSI-semiLASER showed a more homogeneous metabolic profile as interpreted from the NAA SNR map compared to the CSI-PRESS sequence seen in Figure 4.49 A and B. For further comparison, the mean spectra and the standard deviation are plotted for the MRSI-semiLASER and CSI-PRESS sequences in Figure 4.4.9 C-D where C represents the MRSI-semiLASER and D represents the CSI-PRESS sequence. The standard deviation was comparable in both sequences.
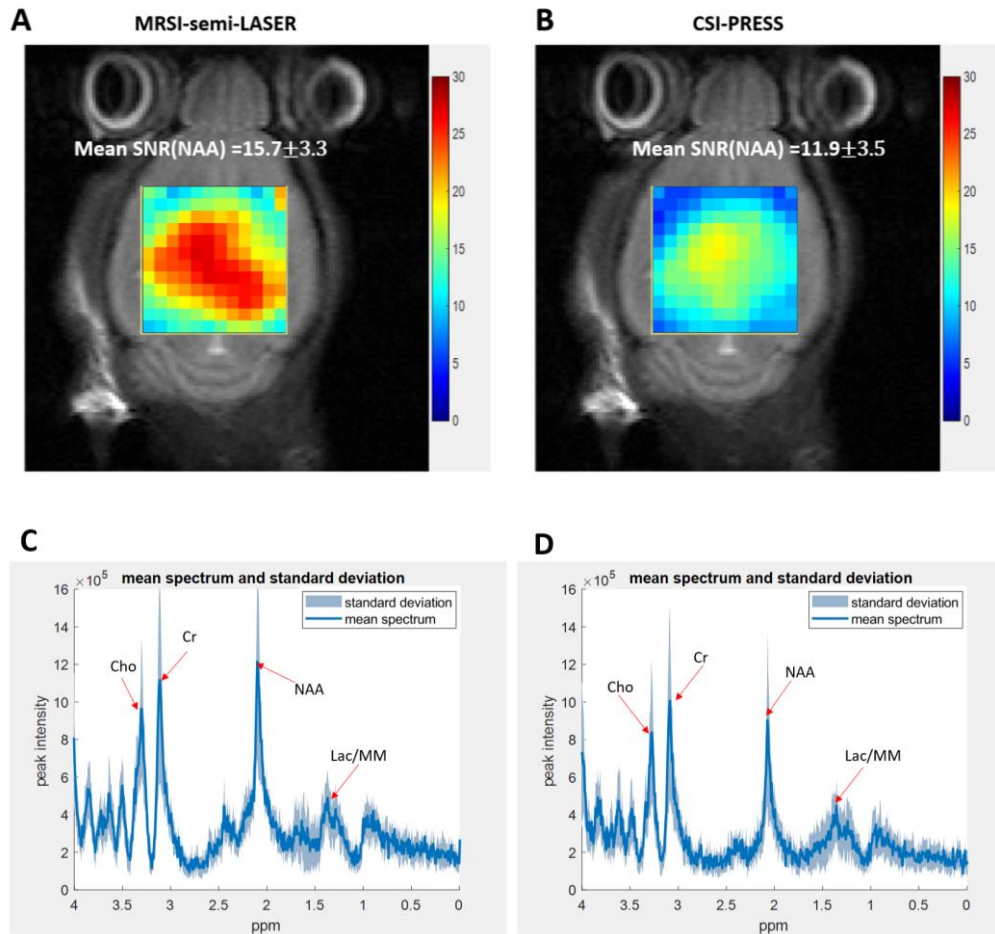
Figure 4.4.9 wt mouse and MRSI-semiLASER (A) and (B) CSI-PRESS NAA intensity maps respectively overlaid on their corresponding T2w image of the investigated mouse (C) and (D) mean and standard deviation spectra for MRSI-semiLASER and CSI-PRESS sequences respectively at equal TE.

4.4.3.4 MRSI-semiLASER vs CSI-PRESS in-vivo in wt mouse at minimum achievable TE

Since we had already observed in phantom studies, the effect of reducing the echo time for CSI-PRESS sequence, we conducted the same experiments in wt mouse to evaluate the sequence behaviour in-vivo. Figure 4.4.10shows the results obtained in-vivo in wt mouse using individual sequences where the minimum echo time used was TE = 27ms for the MRSI-semiLASER sequence and TE = 14ms for the CSI-PRESS sequence. The MRSI-semiLASER SNR map for NAA in Figure 4.4.10 A visually appears more homogeneous as compared to the CSI-PRESS NAA SNR map in Figure 4.4.3.4 B. The mean SNR for the NAA peak was recorded at 16.6$\pm$6.1 for the NAA peak with the MRSI-semiLASER and 13.6±5.4 for the CSI-PRESS sequence. This indicated an SNR increase of 1.2-fold for the MRSI-semiLASER sequence over the CSI-PRESS at minimum possible TE for each sequence. For further comparison, the mean spectra and the standard deviation are plotted for the MRSI-semiLASER and CSI-PRESS sequences in Figure 4.4.10 C-D where C represents the MRSI-semiLASER and D represents the CSI-PRESS sequence. The standard deviation of SNR values within the MRSI grid was comparable for both sequences.
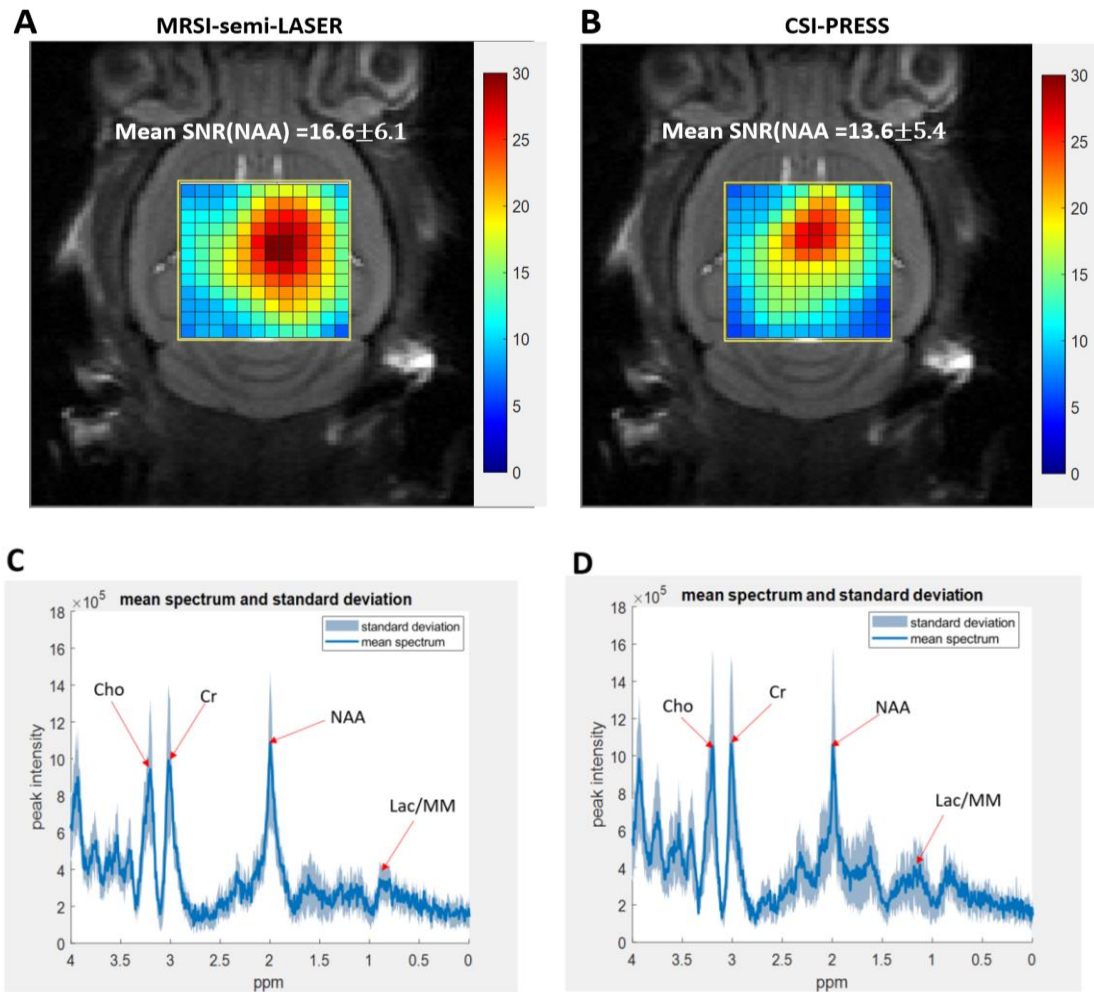
Figure 4.4.10 wt mouse (A) and (B)MRSI-semiLASER and CSI-PRESS NAA SNR maps respectively overlaid on corresponding T2w image of the mouse (C)and (D) mean and standard deviation spectra for MRSI-semiLASER and CSI-PRESS sequences respectively at minimum achievable TE.

Based on our results from experiments conducted in both, phantoms, and in-vivo in wt mouse at similar and minimum echo times, we were able to conclude that the implemented MRSI-semiLASER sequence always provided higher SNR (1.1-1.7-fold) and greater homogeneity of the grid in comparison to the CSI-PRESS. To better visualize the spatial homogeneity of the grid, sub-spectra inside the inner grid were further compared in-vitro and in-vivo.

4.4.3.5 Spatial homogeneity comparing individual spectra of the inner grids of MRSI-semiLASER vs CSI-PRESS in phantoms B and in-vivo in wt mouse

The main problem with MRSI acquisitions is that not all spectra have the same quality especially near the edges where the spectra lose their SNR due to RF pulse imperfections and B1 inhomogeneities. To investigate the MRSI-semiLASER inner grid spectra in further detail, we compared spectra in selected sections of the grid for the MRSI-semiLASER and CSI-PRESS acquisitions in-vitro as well as in vivo.

On visual comparison of the 12x12 inner grids acquired using the CSI-PRESS (A) and MRSI-semiLASER (B) sequences as shown in Figure 4.4.11, we found the MRSI-semiLASER grid more homogeneous, with visually lower number of sub-spectra (yellow) with low signal intensities as compared to the number of sub-spectra (blue) having low intensities in CSI-PRESS grid.

A- CSI-PRESS

B- MRSI-semiLASER

Figure 4.4.11 Visual comparison of 12x12 inner grid sub-spectra acquired using CSI-PRESS (A) and MRSI-semiLASER (B) sequences. The visually chosen (eye inspection) high intensity sub-spectra are shown in red in the CSI-PRESS grid and the low intensity sub-spectra are shown in blue. For the MRSI-semiLASER grid, the high intensity sub-spectra are shown in purple and the low intensity sub-spectra are shown in yellow. The MRSI-semiLASER grid contains fewer yellow sub-spectra as compared to the blue sub-spectra in the CSI-PRESS grid.

Furthermore, the inner grid spectra were compared in three sub-sections of the acquired MRSI grid. These datasets were acquired using phantom B with the standard MRSI acquisition setup of volume Tx and surface Rx coils. The acquisition parameters were kept the same as used for in-vivo MRSI

acquisitions. Figure 4.4.12 shows the sub-sections obtained, where (A) and (E) show the position of the MRSI grid in the phantom, (B) and (F) show the 25 spectra subsections acquired from the top left corner of the MRSI grid, (C) and (G) show the 25 spectra subsections at the center of the grid and, (D) and (H) show the 16 spectra subsections from the bottom right corner of the MRSI grid using MRSI-semiLASER and CSI-PRESS, respectively.

On visual inspection of the acquired spectra in the three sub-sections, the MRSI-semiLASER sub-sections B and D in Figure 4.4.12 were found to contain more high SNR spectra as compared to the sub-sections F and H obtained using the CSI-PRESS sequence. The center sub-section appeared with visually good SNR for both MRSI-semiLASER and CSI-PRESS, as shown by sub-sections B and D, respectively.
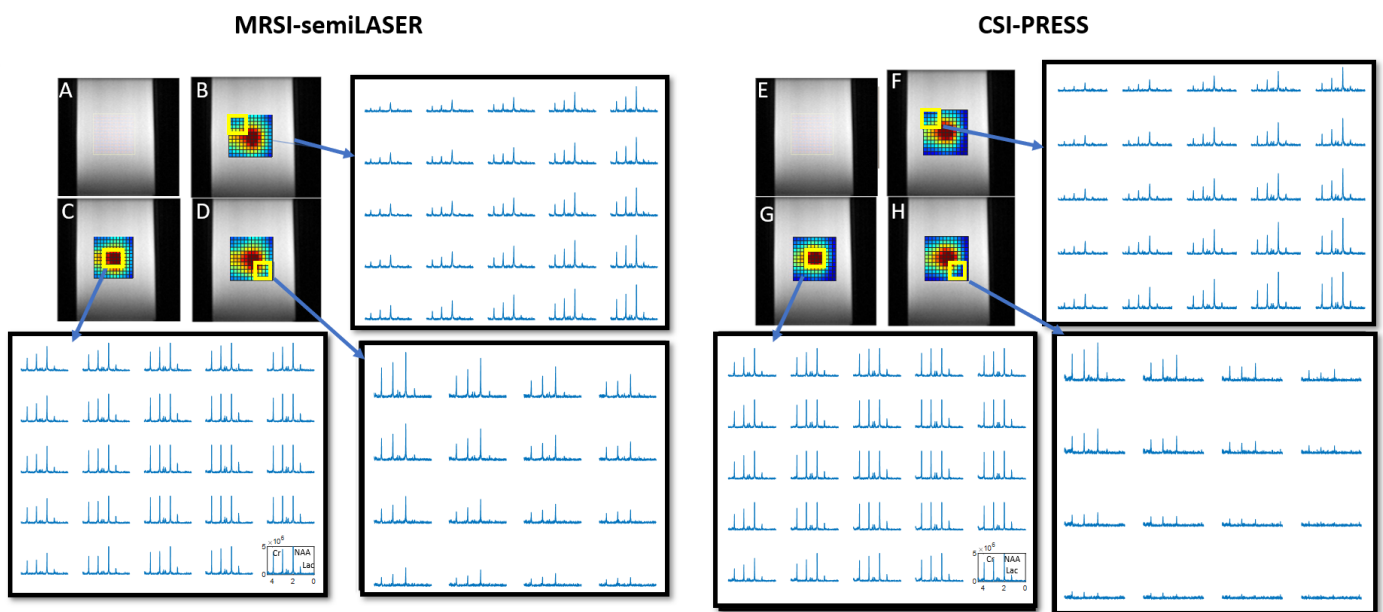
*Figure 4.4.12 **MRSI-semiLASER obtained from phantom B***(A) Position of the MRSI inner grid in phantom B in-vitro, (B) 25 spectra subsection acquired near the top left corner of the MRSI grid as shown in the insert, (C) 25 spectra subsection acquired from the center voxels of the MRSI grid (D) 16 spectra subsection acquired from the bottom right corner of the MRSI grid. **CSI-PRESS obtained from phantom B** (E) Position of the MRSI inner grid in phantom B in-vitro, (F) 25 spectra subsection acquired near the top left corner voxels of the MRSI grid , (G) 25 spectra subsection acquired from the center voxels of the MRSI grid and (H) 16 spectra subsection acquired from the bottom right corner of the MRSI grid.*

To further validate our observations obtained in phantom studies, this analysis was repeated in-vivo for wt mouse. The comparisons were repeated in the same three subsections as already demonstrated in phantom studies. Figure 4.4.13 shows the sub-sections obtained, where (A) and (E) show the position of the MRSI grid in the mouse brain, (B) and (F) show the 25 spectra subsection acquired from the left frontal part of the MRSI grid, (C) and (G) show the 25 spectra subsection at the center of the grid and, (D) and (H) show the 16 spectra subsection from the cortical right side of the MRSI grid using MRSI-semiLASER and CSI-PRESS respectively. The visual comparison of the MRSI spectra in the sub-sections was consistent with our phantom results, and the sections B and D in the MRSI-semiLASER sequence appeared more homogeneous with better spectral profiles/higher SNR than sections F and H in CSI-PRESS. The central subsections C and D appeared more homogeneous than peripheral voxels for both acquisition sequences.

MRSI-semiLASER   **CSI-PRESS**
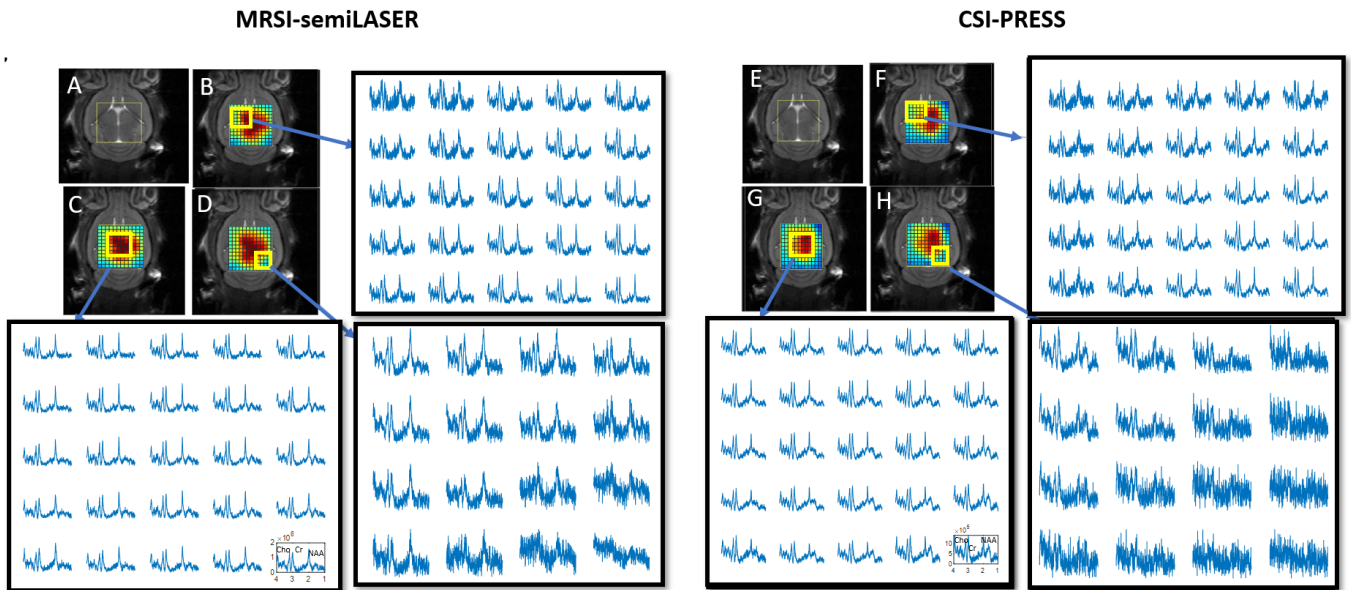
*Figure 4.4.13 **MRSI-semiLASER acquisition from wt mouse brain** (A)Position of the MRSI inner grid in-vivo in wt mouse brain, (B) 25 spectra subsection acquired near the top left corner of the MRSI grid as shown in the insert, (C) 25 spectra subsection acquired from the center voxels of the MRSI grid (D) 16 spectra subsection acquired in the bottom right corner of the MRSI grid. **CSI-PRESS acquisition from wt mouse brain** (E) Position of the MRSI inner grid in-vivo in wt mouse brain, (F) 25 spectra subsection acquired near the left frontal voxels of the MRSI grid , (G) 25 spectra subsection acquired from the center voxels of the MRSI grid and (H) 16 spectra subsection acquired from the cortical right corner of the MRSI grid.*

On the basis of the improved spatial and spectral homogeneity in the MRSI grids using the MRSI-semiLASER sequence, we concluded that this improved homogeneity could contribute towards reducing the partial volume effects thereby improving the quantification of metabolites as well as the diagnostic performance in mouse brain studies.

4.4.4 Chemical shift displacement effect tests

One of the inherent advantages of the adiabatic refocusing pulses is to reduce the CSD error or CSDE, which refers to the spatial shifts in the excited volume for metabolites resonating at different frequencies. The chemical shift artefact is caused by the frequency-selective RF localization pulses exciting slightly different locations for different metabolite peaks. For singlets, this results only in a positional shift of the voxel, however for coupled metabolites such as lactate, it results in a positional shift as well as changes in phase and amplitude at the edges of the voxel (J-modulation). Hence, this can be corrected by using larger bandwidth pulses such as the hyperbolic secant refocusing pulses [82].

To verify whether the MRSI-semiLASER sequence was producing any mis-mapping or misregistration of the metabolite resonances outside the VOI, we prepared a two-chamber cylindrical phantom (phantom 4, full description in chapter 3.2) filled with two different metabolite solutions (Figure 4.4.14 A). Multislice acquisitions with the slice orientation set perpendicular to the long axis of the phantom were performed using the vendor CSI-PRESS sequence and the implemented MRSI-semiLASER sequence (Figure 4.414 B). Our hypothesis in

this experiment was to observe that the implemented MRSI-semiLASER sequence did not produce any metabolite misregistration outside the boundaries of the chamber in which each metabolite was contained. Metabolite peak intensity maps for the NAA peak at 2.01 ppm and the Cr peak at ca. 3.9ppm were obtained using 3D Interactive Chemical Shift Imaging (3DiCSI) external software.
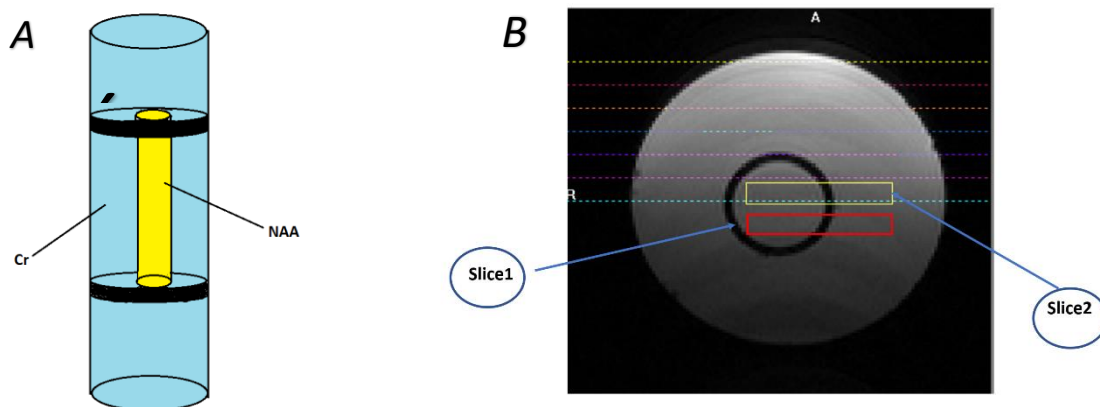
Figure 4.4.14 (A) The inhouse prepared two-chamber cylindrical phantom 4 (B) Prescription of two coronal MRSI grids (yellow and red) over the axial T2w image of the two-chamber cylindrical phantom.

Two slices were acquired using the prepared two-chamber cylindrical phantom for three sets of measurements (n=3). In each measurement, the VOI was defined corresponding to positions of slice1 and slice2 depicted in Figure 4.4.14 B. A 72-mm inner-diameter linear volume coil was used as transmitter, and a dedicated mouse brain quadrature surface coil was used as receiver for MRSI studies. The acquisition parameters for MRSI studies were as follows: TR/TE = 2500/27 ms ; NA = 512; DS = 4, VAPOR water suppression and OVS, voxel size = 6mm x 6mm x 1mm, FOV = 1.76 x 1.76 cm^2 , resolution = 2.2 mm, SW = 13.34 ppm (4006.41 Hz) and TAT = 21min. After FASTMAP shimming, the resultant line width of water was obtained at ca. 4.6 Hz which corresponds to a very good shimming. MRSI acquisitions were performed using vendor sequence CSI-PRESS and implemented sequence MRSI-semiLASER.

The intensity maps for the selected metabolite were obtained for slice 1 and slice 2 and repeated for all three experiments. Figure 4.4.15 shows the intensity maps for NAA and Cr, from the voxels selected in slice 1 and slice 2 using the MRSI-semiLASER and CSI-PRESS sequences in one experiment (Exp3).

The results obtained in this study were consistent with our initial goal where we aimed to evaluate any misregistration of metabolite resonances by the MRSI-semiLASER sequence. In all three experiments, the MRSI-semiLASER sequence produced more homogeneous maps of the selected metabolite within the chosen slice compared to peak maps using the CSI-PRESS sequence without any visible potential contamination of signal from outside the VOI. The CSDE between the NAA and Cr peaks was calculated as 0% in the x, y and z directions using the MRSI-semiLASER sequence. Hence, it was concluded that the implemented MRSI-semiLASER sequence successfully acquired spectra from two independent VOIs containing different metabolite solutions with minimal CSDE.
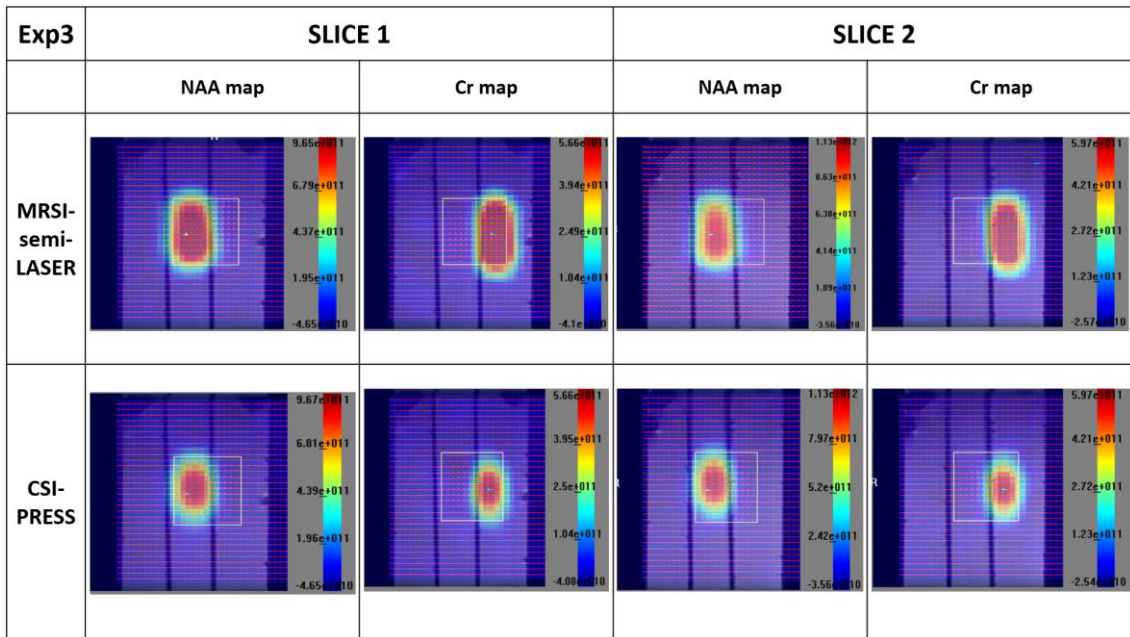
Figure 4.4.15 (Exp 3) NAA and Cr intensity maps from slice 1 and slice 2 using CSI-PRESS and MRSI-semiLASER sequences in experiment 3. The maps appeared more homogeneous for the MRSI-semiLASER sequence in both slice 1 and slice 2 without any visible potential contamination of signal from outside the VOI.

4.4.5 Repeatability and Reproducibility in phantom and in-vivo on wt mice

4.4.5.1 MRSI-semiLASER vs CSI-PRESS using intraday and interday experiments in phantoms

The concepts of repeatability and reproducibility have already been described briefly in Chapter 3 and experiments reported in section 4.3. To ensure consistency with our previous studies and investigating test-retest repeatability for the implemented MRSI-semiLASER sequence, the intraday (concept explained in chapter 4.3) tests were performed on phantoms using three repeated measurements on the same day while keeping the same receiver gain and B_0 homogeneity (FASTMAP shimming). Multiple interday experiments were also performed and repeated for n=3 on three consecutive days, also using phantoms.

The intraday experiments were performed using phantom B (described in Chapter 3). The TE values were chosen as TE = 14 ms for CSI-PRESS and TE = 27ms for MRSI-semiLASER sequences for comparison at the minimum possible echo time. All other acquisition parameters were kept the same as previously reported. The results obtained were post processed using an inhouse made MATLAB based routine for manual phase correction of the spectra.

The mean spectra and standard deviation of the Intraday (1.1, 1.2 and 1.3) MRSI-semiLASER and CSI-PRESS experiments using various metabolites in phantom studies are summarized in Figure 4.4.16. All metabolites were accurately detected at the expected resonance frequencies, such as NAA at ca. 2.01 ppm, Cr at ca. 3.02 and 3.9 ppm and Lactate at ca. 1.3ppm. The calculated values for the mean of the means ($\mu_{\bar{x}}$) SNR and standard deviation (std) are recorded in Table 4.4.1. The MRSI-semiLASER sequence showed an SNR increase of 1.3-fold for the NAA peak, 1.2-fold times increase in SNR for the Cr peak and around 1.1-fold increase in SNR for the Lactate

peak. The increase in SNR observed is expected since it was also recorded in the preceding experiments in section 4.4.3.4. The intraday experiments should not be affected by external noise or error sources due to changes in receiver gain, etc. Hence the standard deviation of the SNR values was lower in both the MRSI-semiLASER and the CSI-PRESS results. The coefficient of variation (CV) were also smaller for the MRSI-semiLASER sequence and hence the reliability of results for the NAA peak was 1%, Cr 4% and Lac 3%, indicating greater precision in comparison to the CSI-PRESS sequence where the reliability of results for the NAA peak was 10%, Cr 9% and Lac 2%. The RC's calculated for the MRSI-semiLASER sequence were also smaller than the CSI-PRESS sequence suggesting better repeatability intraday. Figure 4.4.17 provides a graphical representation of the mean SNR and standard deviation for the intraday experiments using MRSI-semiLASER and CSI-PRESS. MRSI-semiLASER mesn SNR was statistically significantly higher than CSI-PRESS mean SNR for all the metabolites analysed with a one tailed student's t- test result (p ≤ 0.05). In conclusion, for all the intraday experiments, the NAA SNR was consistently recorded higher in the MRSI-semiLASER acquisitions as compared to the CSI-PRESS results. The SNR maps also visually appeared more homogeneous for the MRSI-semiLASER acquisitions, similar to our previous observations.
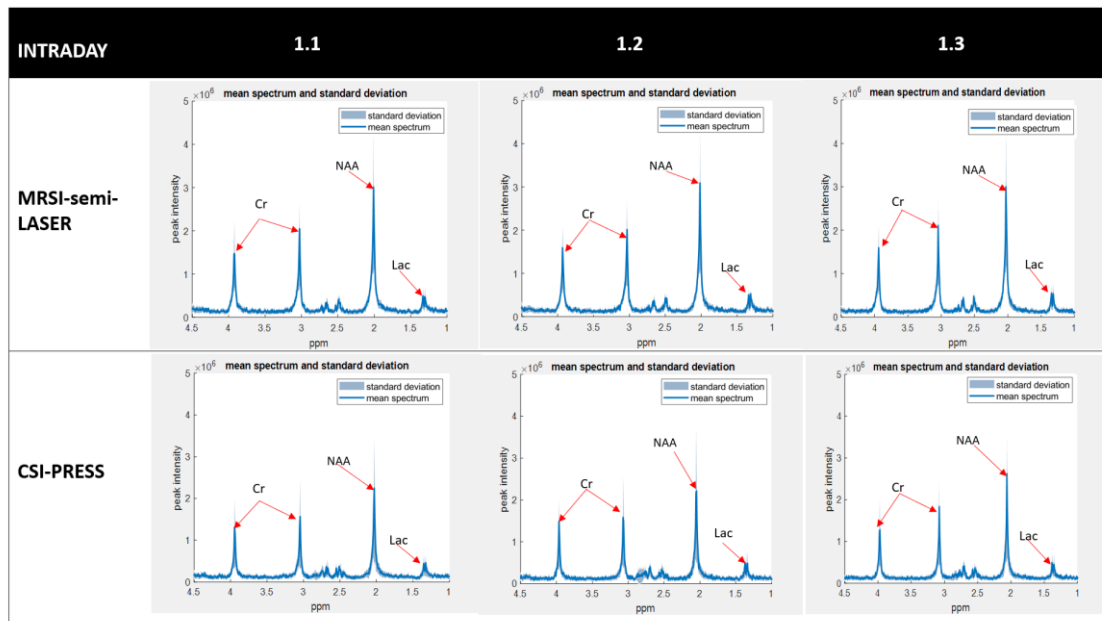
Figure 4.4.16 Mean spectra and standard deviation for interday experiments using MRSI-semiLASER and CSI-PRESS in phantom B.

Table 4.4.1: SNR values from intraday MRSI-semiLASER vs CSI-PRESS experiments in phantom B

MRSI-semi-LASER

exp name	NAA(2.01ppm)	Cr (3.03 ppm)	Lac (1.3ppm)
1.1	52.37	35.05	10.01
1.2	51.32	33.00	10.60
1.3	51.16	35.46	10.54
$\mu_{\bar{x}}\pm$ std	51.62 $\pm$0.66	34.50$\pm$1.32	10.38 $\pm$ 0.32
CV	0.01	0.04	0.03
RC	1.83	3.66	0.89

CSI-PRESS

exp name	NAA(2.01ppm)	Cr (3.03 ppm)	Lac (1.3ppm)
1.1	39.38	26.98	9.76
1.2	36.44	26.84	9.52
1.3	44.49	31.39	9.93
$\mu_{\bar{x}}\pm$ std	40.10$\pm$4.07	28.40 $\pm$ 2.59	9.74 $\pm$ 0.21
CV	0.10	0.09	0.02
RC	11.27	7.17	0.58

The mean of the means SNR is expressed as $\mu_{\bar{x}}\pm$ std. The coefficient of variation (CV) and repeatability constant (RC) were also calculated for both methods for NAA, Cr and Lac signals. The MRSI-semiLASER sequence shows an SNR increase of 1.3-fold for the NAA peak, 1.2-fold times increase in SNR for the Cr peak and approximately 1.1-fold increase in SNR for the Lactate peak.
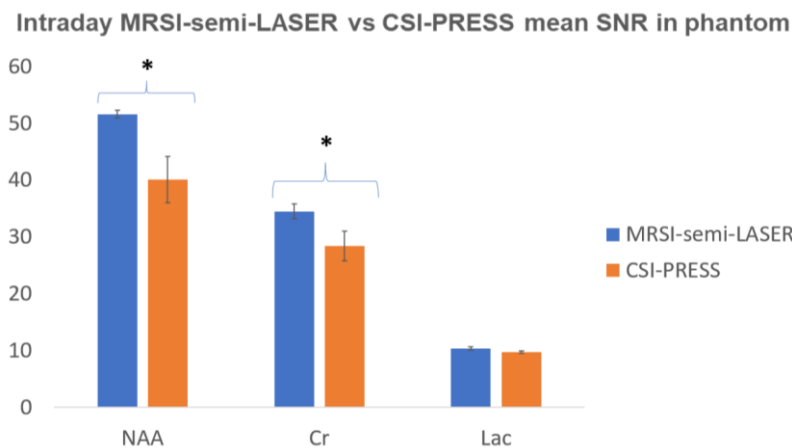
Figure 4.4.17 Intraday MRSI-semiLASER vs CSI-PRESS in phantom B, mean of means SNR and standard deviation. * represents a statistically significant one tailed student's t- test result (p ≤ 0.05).

The tests were further conducted on three consecutive days to obtain interday repeatability of the results. Variations of receiver gain and B_0 homogeneity changes could be additional factors influencing the overall values in mean SNR and on standard deviation. Figure 4.4.18 shows the mean spectra comparison for the interday experiments using MRSI-semiLASER and CSI-PRESS sequences in phantom B. The MRSI-semiLASER sequence showed an SNR increase of 1.2-fold for the NAA peak, 1.2-fold increase in SNR for the Cr peak and a 1-fold increase in SNR for the Lactate peak. Table 4.4.2 shows the comparison of mean of means SNR ($\mu_{\bar{x}}$) and standard deviation (std), coefficient of variation (CV) and repeatability coefficient (RC) for the interday experiments. Similar to our findings in the intraday experiments, the coefficient of variation (CV) were smaller for the MRSI-semiLASER sequence and hence the reliability of results for the NAA peak was

recorded at 5%, Cr 4% and Lac 3% indicating greater precision in comparison to the CSI-PRESS sequence where the reliability of results for the NAA peak was 10%, Cr 9% and Lac 4%. The RC's calculated for the MRSI-semiLASER sequence were also smaller than the CSI-PRESS sequence suggesting better repeatability interday as well. Figure 4.4.19 graphically summarizes the results for SNR comparison between metabolites using the two sequences. The results obtained produced a statistically significant student t-test result (p ≤ 0.05).
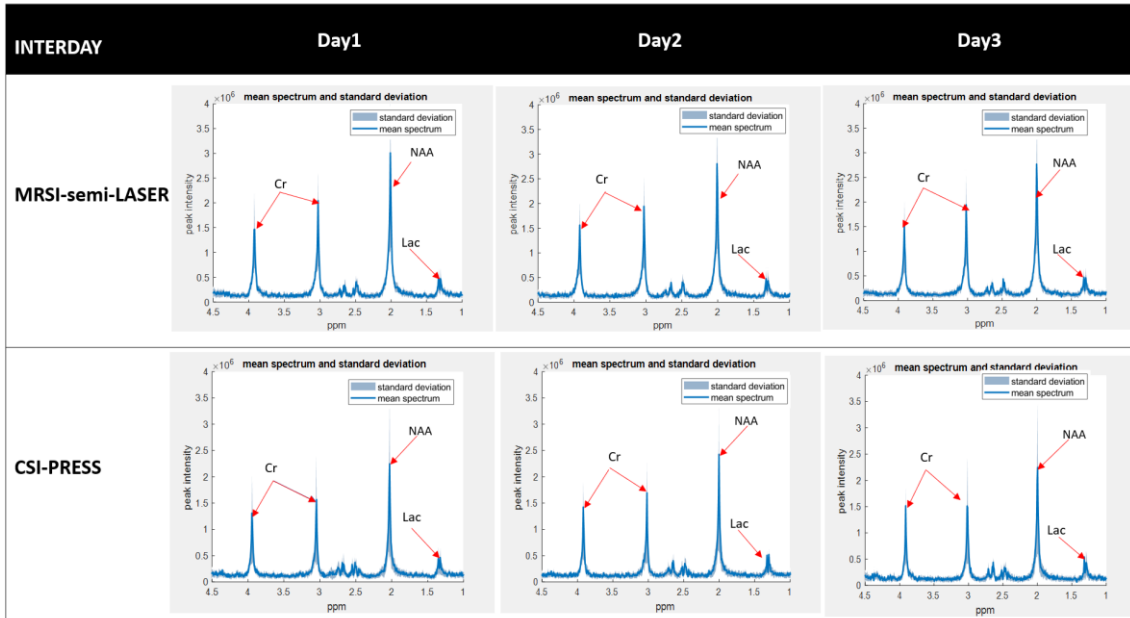
Figure 4.4.18 Mean and standard deviation for interday experiments spectra using MRSI-semiLASER and CSI-PRESS on phantom B.

Table 4.4.2 SNR values for interday MRSI-semiLASER vs CSI-PRESS experiments in phantom B

INTER-DAY MRSI-semi-LASER vs CSI-PRESS using phantom

MRSI-Semi-LASER

exp name	NAA(2.01ppm)	Cr (3.03 ppm)	Lac (1.3ppm)
Day 1	51.14	35.00	10.67
Day 2	46.65	32.41	10.01
Day 3	46.99	33.15	10.19
$\mu_{\bar{x}} \pm$ std	48.3±2.50	33.5±1.33	10.3±0.34
CV	0.05	0.04	0.03
RC	6.92	3.70	0.95

CSI-PRESS

exp name	NAA(2.01ppm)	Cr (3.03 ppm)	Lac (1.3ppm)
Day 1	46.22	31.72	10.25
Day 2	40.57	28.14	9.99
Day 3	37.89	26.79	9.46
$\mu_{\bar{x}} \pm$ std	41.6±4.25	28.9±2.55	9.9 ±0.40
CV	0.10	0.09	0.04
RC	11.78	7.06	1.12

The mean of means SNR is expressed as $\mu_{\bar{x}} \pm$ std. The coefficient of variance (CV) and repeatability constant (RC) are also calculated for both methods for NAA, Cr and Lac signals.
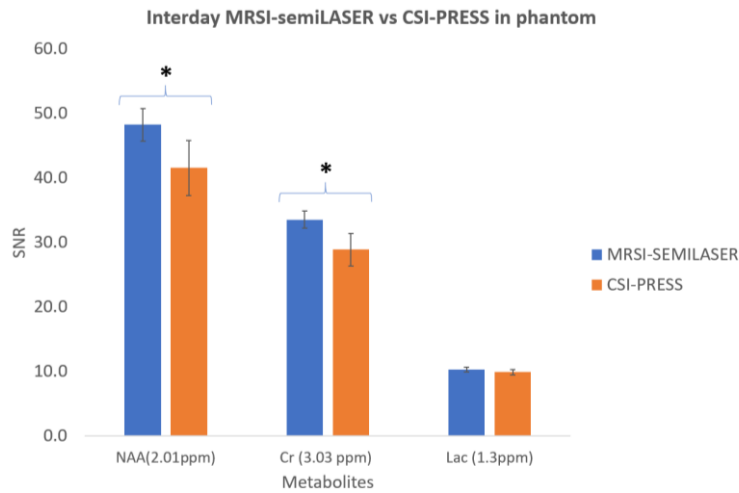
Figure 4.4.19 Graphical representation for SNR comparison of metabolites using the MRSI-semiLASER and CSI-PRESS sequences in phantoms. * represents a statistically significant one tailed student's t-test result (p ≤ 0.05).

The boxplot and histogram comparison for all intraday and interday experiments analysing NAA SNR are demonstrated in Figure 4.4.20. The MRSI-semiLASER sequence provided superior SNR for all acquisitions. The histograms plotted for the intraday and interday experiments in the bottom row also displayed the higher SNR distribution for a larger number of voxels and hence are an indicative measure of better homogeneity of the MRSI grid in the MRSI-semiLASER sequence.
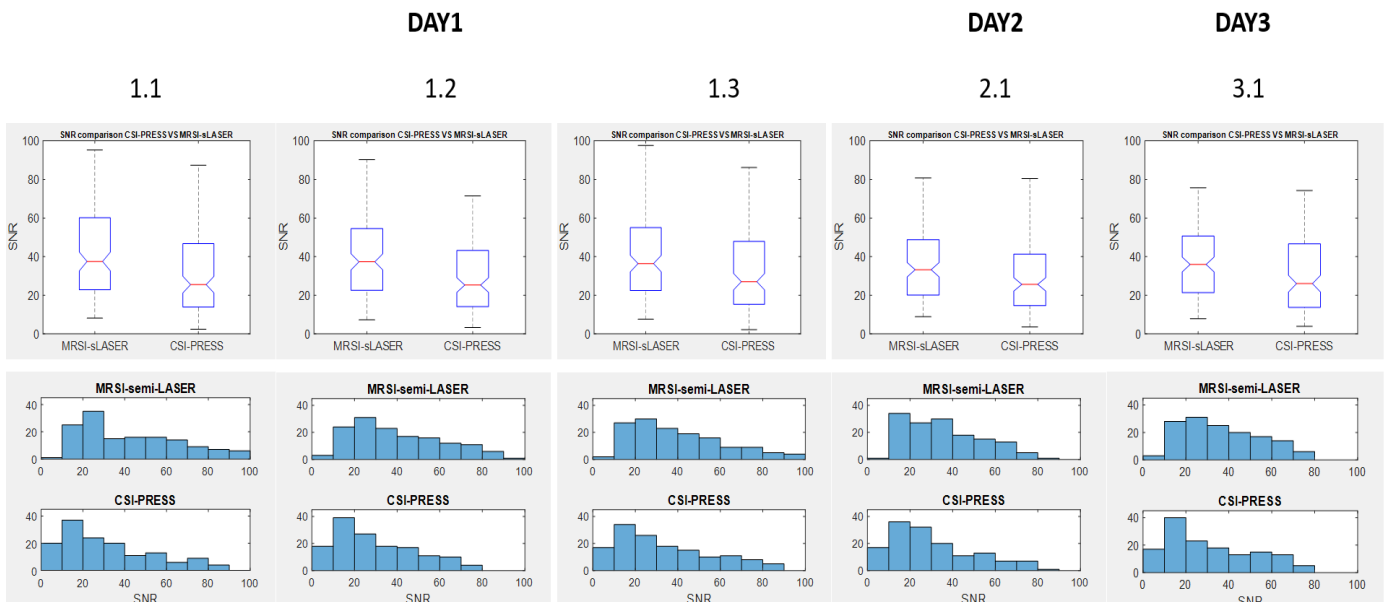
Figure 4.4.20 NAA SNR boxplot and histogram comparison for intraday and interday experiments using MRSI-semiLASER and CSI-PRESS sequences in phantoms.

The reproducibility was further analysed by the Bland Altman plots for the intraday and interday experiments in phantoms using MRSI-semiLASER and CSI-PRESS sequences. Figure 4.4.21 shows

the intraday and Figure 4.4.22 shows the interday Bland Altman plots for NAA SNR. The plots were computed for the 144 sub-voxel NAA SNR values where each point indicates the NAA SNR for a sub spectrum and were compared between two datasets acquired by the same sequence to check data reproducibility. The upper and lower limits of agreement,(UOA) and (LOA) respectively, denoted by dotted yellow lines were defined using the bias (mean of the SNR values) and the standard deviation (std).

In the intraday experiments, the MRSI-semiLASER lies within the limits of the LOA and UOA while the Bruker PRESS sequence results diverge from the UOA for instance in comparing experiments 1.2 and 1.3. Overall, the MRSI-semiLASER experiments demonstrated good reproducibility between intraday experiments. The interday results indicated more variation between the compared datasets and the plots diverged outside the LOA and UOA for both the MRSI-semiLASER and CSI-PRESS sequences. Hence, we deduced that the interday reproducibility is lower as compared to intraday results for both sequences.
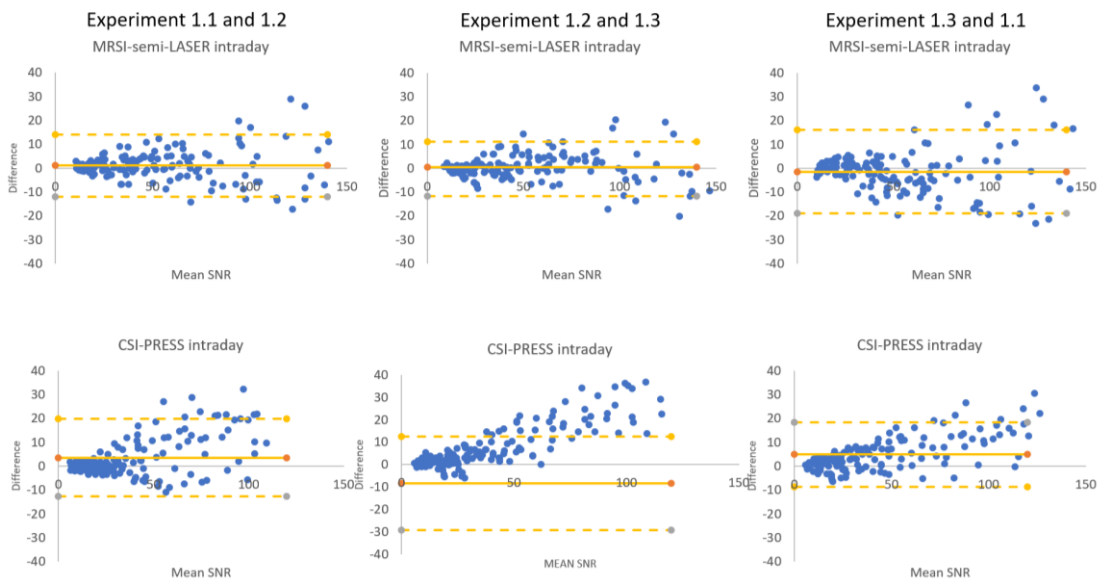
Figure 4.4.21 Intraday experiments using MRSI-semiLASER and CSI-PRESS in phantom B. The upper and lower limits of agreement, (UOA) and (LOA) respectively, denoted by dotted yellow lines and the the bias (mean of the SNR values) and the standard deviation (std) is denoted by the solid yellow line.

129
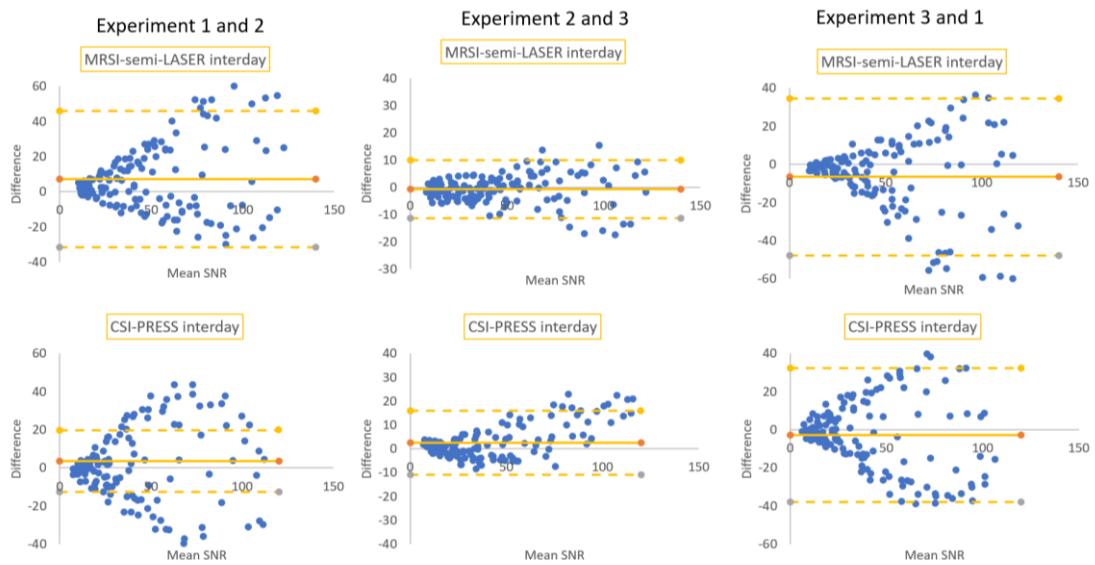
Figure 4.4.22 Interday experiments using MRSI-semiLASER and CSI-PRESS in phantom B. See figure 4.4.21legend for further details.

4.4.5.2 MRSI-semiLASER vs CSI-PRESS interday experiments using wt mouse

To further verify the repeatability of results in in-vivo studies using wt mice, the implemented sequence was also tested interday on three consecutive days i.e. day1, day2 and day3, respectively.

The interday experiments were performed in-vivo on wt mouse and water suppressed spectra were obtained. The acquisition parameters and coil configurations were kept the same as already reported in section 4.4.4. Figure 4.4.23 shows day1, day2 and day3 NAA SNR maps obtained for the MRSI-semiLASER vs CSI-PRESS acquisitions in-vivo in the same wt mouse.

Higher SNR for the NAA peaks (1.1-fold) was recorded by the MRSI-semiLASER sequence for all three days as compared to the CSI-PRESS sequence. This result was consistent with our interday tests in phantom B. The maps also showed visually increased homogeneity of the MRSI-semiLASER grids.
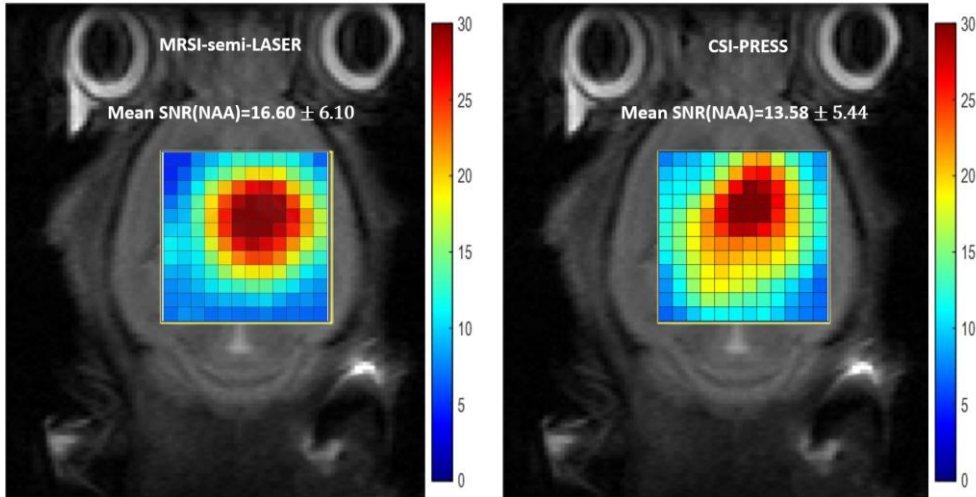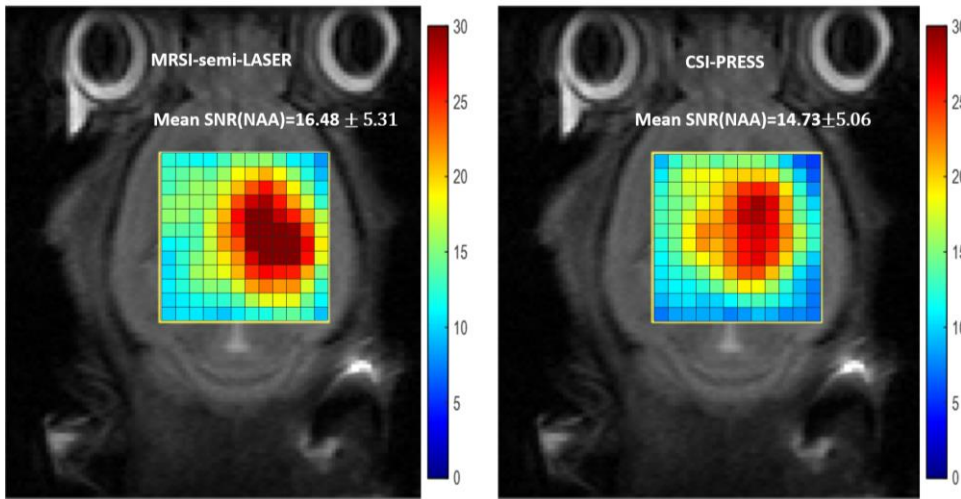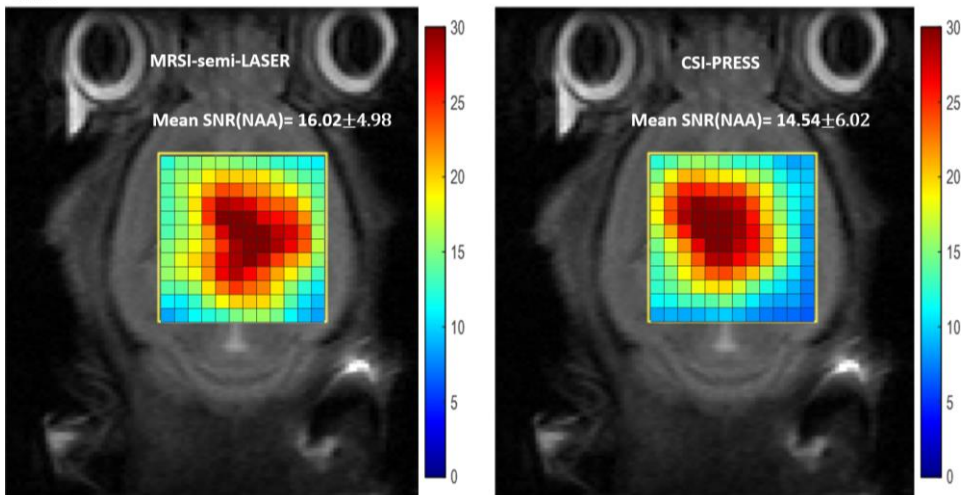
Figure 4.4.23 NAA SNR maps for interday tests using MRSI-semiLASER and CSI-PRESS sequences in-vivo on wt mouse for day1, day2 and day3.

The mean spectra and standard deviation for the in-vivo experiments performed is compared in Figure 4.4.24. The high SNR metabolites labeled include N-Acetyl Aspartate (NAA) at 2.01ppm, Total creatine (phosphocreatine+creatine) (Cr) at 3.02ppm and Choline (Cho) at 3.9ppm. The spectra displayed good repeatability of the results and improvement in mean SNR for MRSI-semiLASER. The standard deviation is also visibly smaller in the case of MRSI-semiLASER spectra. The quantitative results are reported in Table 4.4.3 and graphically represented in Figure 4.4.25.

In accordance with the interday tests conducted in phantom B, the coefficient of variation (CV) were found smaller for the MRSI-semiLASER sequence in wt mouse as well and hence the reliability of results for the NAA peak was recorded at 2%, Cr 1% and Lac 5% indicating greater precision in comparison to the CSI-PRESS sequence where the reliability of results for the NAA peak was 4%, Cr 5% and Lac 6%. The RC's calculated for the MRSI-semiLASER sequence were also smaller than the CSI-PRESS sequence suggesting better repeatability interday in-vivo as well.
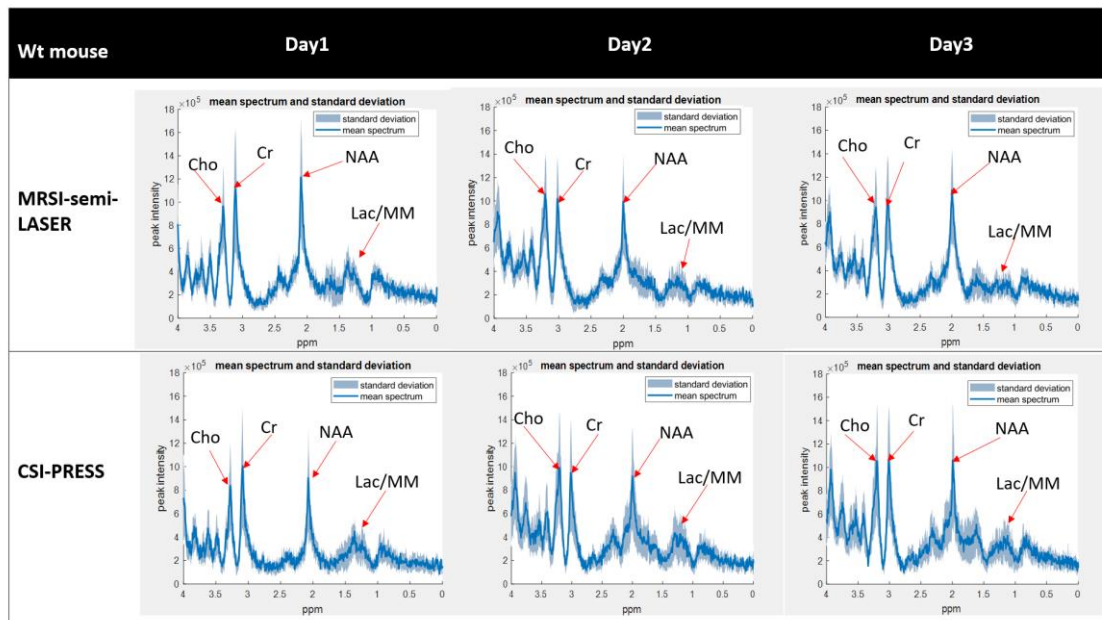
Figure 4.4.24 Mean spectra and Standard deviation for interday tests in-vivo on wt mouse. The high SNR metabolites labeled include N-Acetyl Aspartate (NAA) at 2.01 ppm, total creatine (phosphocreatine+creatine) (Cr) at 3.02 ppm and Choline (Cho) at 3.9ppm.

Table 4.4.3 SNR for interday MRSI-semiLASER vs CSI-PRESS experiments in-vivo in wt mouse.

MRSI-Semi-LASER

exp name	NAA(2.01ppm)	Cr (3.03 ppm)	Cho(3.2 ppm)
Day 1	16.60	15.59	16.03
Day 2	16.48	15.82	16.26
Day 3	16.02	15.64	14.76
Mean SNR ± St.Dev	16.37±0.31	15.68±0.12	15.68±0.81
CV	0.02	0.01	0.05
RC	0.85	0.34	2.24

CSI-PRESS

exp name	NAA(2.01ppm)	Cr (3.03 ppm)	Cho (3.2 ppm)
Day 1	13.58	15.18	13.50
Day 2	14.73	14.03	14.90
Day 3	14.54	15.50	15.07
Mean SNR ± St.Dev	14.28±0.62	14.90±0.77	14.49 ±0.86
CV	0.04	0.05	0.06
RC	1.71	2.14	2.39

The mean SNR is expressed as mean ± SD. The coefficient of variation (CV) and repeatability constant (RC) are also calculated for both methods for N-Acetyl Aspartate (NAA), Phosphocreatine (Cr) and Choline (Cho) signals.
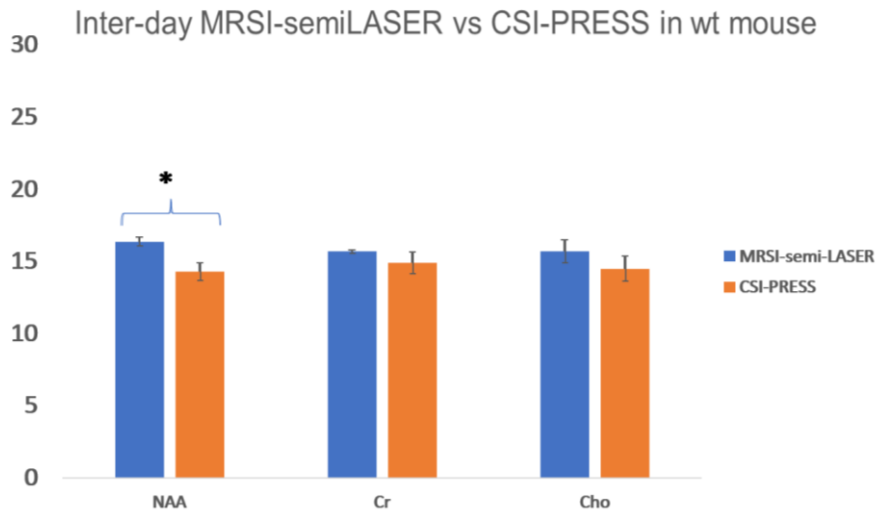
*Figure 4.4.25 Graphical representation of the mean SNR and standard deviation for interday scans using MRSI-semiLASER and CSI-PRESS in-vivo in wt mouse. * represents a statistically significant one tailed student's t-test result (p ≤ 0.05).*

With these results, we concluded our repeatability and reproducibility tests with the conclusion that the implemented MRSI-semiLASER sequence provides good repeatability as well as reproducibility for the intraday as well as interday experiments, resulting in superior quality spectra, improved homogeneity and higher SNR thereby leading towards higher spatial resolution under homogeneous conditions such as phantoms as well as in-vivo in wt mouse. Our next goal was to test the sequence using more heterogenous conditions such as tumor mouse models.

4.4.6 Mouse brain tumor acquisitions

As already explained in Chapter 1, MRSI studies have proven benefitial in providing information about the molecular properties and metabolic heterogeneity of tumor tissue. Hence, the implemented MRSI-semiLASER sequence was also used to evaluate brain GB tumors in mice to challenge its performance in more heterogeneous environments.

4.4.6.1. Comparison between MRSI-semiLASER vs CSI-PRESS in-vivo in brain GB mice at equal TE (27 ms).

The purpose of this section was to evaluate the performance of the implemented MRSI-semiLASER sequence in-vivo using a mouse brain GB tumor model and to assess the quality of the acquisitions on the basis of spectral profiles and SNR in comparison to the CSI-PRESS sequence. A GL261 GB tumor harbouring C57/BL6 mouse with a tumor volume of 55 mm^3 and a body weight of 17.9 g was used in this experiment (mouse C1692). The acquisitions were performed at the same echo time of TE= 27 ms and Lactate/ML was chosen as the main resonance for comparisons. Any potential variability due to Lactate T_2 relaxation was avoided by keeping the acquisition TE constant. Other acquisition parameters were: TR=2500ms, VAPOR water suppression, FOV= (17.6mm)^2, slice thickness= 1 mm, voxel size = (6.6mm)^2, SW= 4006.41 Hz; NA=512 and TAT= 21 min.

The mean spectra and standard deviation are plotted in Figure 4.4.26 A and B and the SNR maps for the Lactate/ML peak at ca. 1.3 ppm are shown in Figure 4.4.26 C and D. The MRSI-semiLASER recorded a ca. 1.4-fold higher SNR than the CSI-PRESS sequence for the lactate peak in the tumor mouse at the same echo time. These results indicated the ability of the implemented sequence to produce higher SNR tha CSI-PRESS even under more heterogeneous conditions.
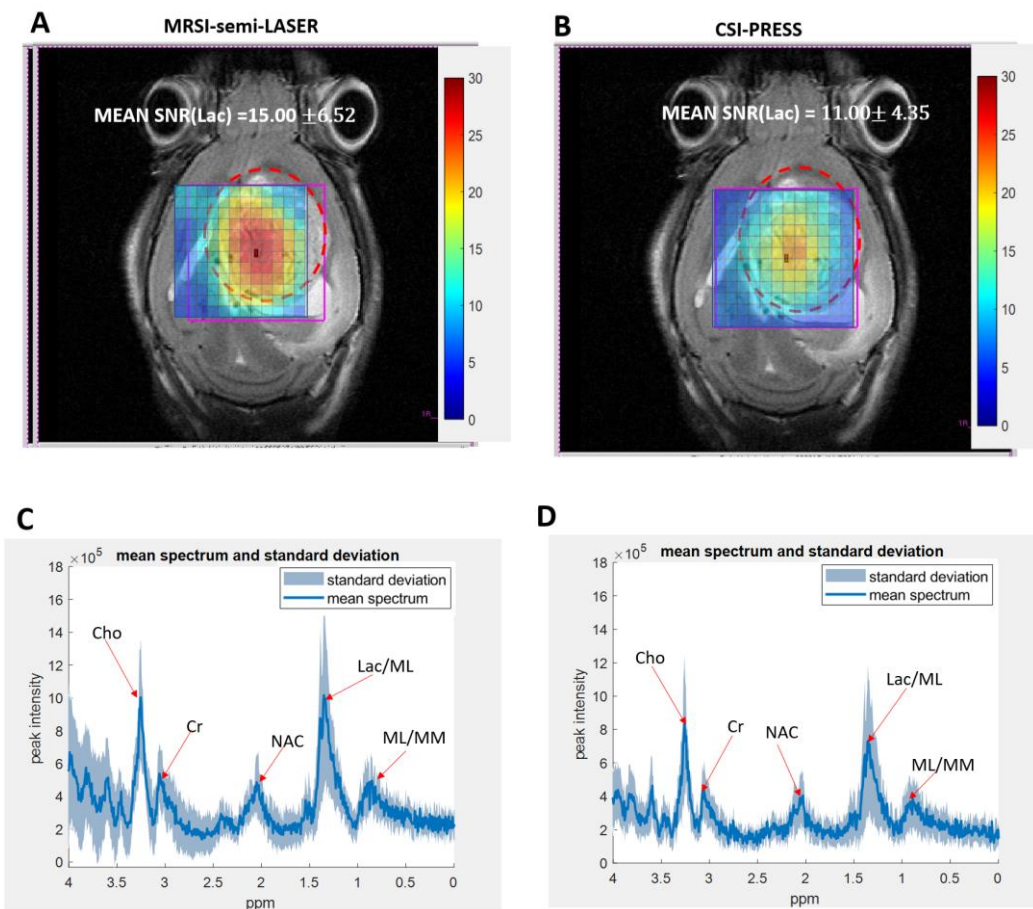
Figure 4.4.26 Mean Spectra and standard deviation for A-MRSI-semiLASER and B-CSI-PRESS at same TE = 27 ms in-vivo in the GL261 GB mouse C1692, followed by Lactate SNR maps for C-MRSI-semiLASER vs D- CSI-PRESS. The T2w assessable tumor mass is encircled with red dotted line. The MRSI-semiLASER shows a 1.4-fold increase in SNR at equal TE.

4.4.6.2. Comparison between MRSI-semiLASER vs CSI-PRESS in-vivo in brain GB mice at the minimum possible TE for each sequence.

Since the utility of the sequence was already established in our previous findings, our next step was to compare the MRSI-semiLASER performance with the gold standard CSI-PRESS sequence at a minimum echo time of TE = 14 ms to ensure optimum performance. The testing was done using a GL261 GB tumor mouse model (C1836) on day 15 post inoculation with a tumor volume of 32.5mm^3. The TE for the MRSI-semiLASER sequence was maintained at 27ms. The mean spectra and standard deviation are plotted in in Figure 4.4.27 A and B and the SNR map comparisons for the Lactate/ML peak at ca. 1.3 ppm are shown in Figure 4.4.27 C and D. Despite tumor inhomogeneities, the MRSI-semiLASER recorded a 1.2-fold higher SNR than the CSI-PRESS sequence for the lactate/ML peak even at the minimum possible echo time used.
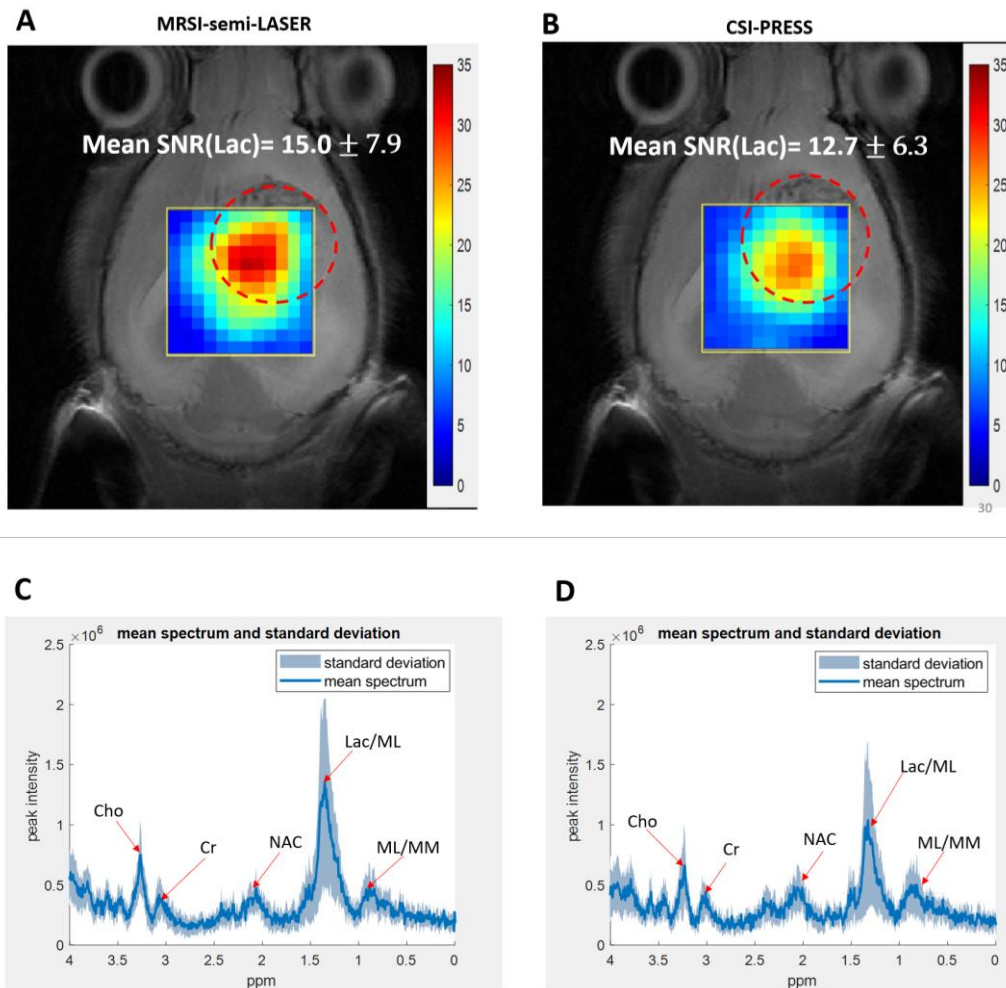
Figure 4.4.27 Mean Spectra and standard deviation for A-MRSI-semiLASER and B-CSI-PRESS at minimum achievable TE in-vivo from GB tumor mouse C1836 followed by Lactate/ML SNR maps for C-MRSI-semiLASER vs D- CSI-PRESS. The T2w assessable tumor mass is encircled with a red dotted line. The MRSI-semiLASER shows a 1.2-fold increase in SNR at the minimal TE possible.

In general terms, the performance of the implemented MRSI-semiLASER sequence in-vivo in normal and tumor mouse was superior to the CSI-PRESS sequence in terms of spatial homogeneity and SNR demonstrated both at same TE as well as at the minimum TE possible for each sequence. These results were also in agreement with our previous studies using phantoms. Hence, we concluded that the implemented MRSI-semiLASER sequence provides superior performance to CSI-PRES in-vitro as well as in in-vivo studies.

4.4.6.3 Comparison of SV-semiLASER vs MRSI-semiLASER in-vivo in brain GB mice

To extend the SVS vs MRSI comparison already mentioned in Chapter 1 to our implemented semiLASER sequences, we compared the SV-semiLASER and MRSI-semiLASER acquisitions in the GB tumor mouse model. The objective of this comparison was to qualitatively visualize and compare the improved spatial and spectral resolution using the implemented semiLASER sequences in-vivo in the GL261 tumor mouse. The acquisition parameters for the single voxel acquisitions were kept as follows: TR=2500ms TE = 20 ms, voxel size= (3mm)^3, NA=128, RG=1.0,

OVS=on, Npoints = 2048, SW = 13.3 ppm, spoiler duration = 1.5ms, spoiler strength = 25%, DS = 4, with VAPOR water suppression, OVS and FASTMAP shimming was performed over a $(4mm)^3$ volume. The acquisition parameters for Multi-voxel acquisitions were kept as follows: TR = 2500ms,TE = 27ms, VAPOR water suppression, FOV= $(17.6mm)^2$, slice thickness = 1 mm, voxel size = $(6.6mm)^2$, SW = 4006.41 Hz; NA =512 and TAT= 21 min.

Figure 4.4.28 shows the comparison of spectra acquired using single and multi-voxel semiLASER sequences in a GL261 tumor-bearing mouse (C1768).. The visual inspection of the SV-semiLASER spectrum and MRSI-semiLASER representative spectra showed a higher spatial resolution for the MRSI-semiLASER which in turn seem to improve the spectral resolution. The main metabolites identified in the SV-semiLASER pattern were Lactate and mobile lipids (Lac/ML) at ca. 1.3 ppm, N-acetyl containing compounds (NAC) [75] at ca. 2.01ppm, Total Creatine (phosphocreatine+creatine) (Cre) at 3.03 and 3.9 ppm, total choline (mostly Phosphocholine+Free choline+Glycerophosphocholine) (Cho) at 3.2 ppm and myoinositol and Glycine (Mi/Gly) at 3.57 and Mi at 3.61 ppm. With the MRSI-semiLASER spectrum, due to the higher spatial resolution with less averaging blurring, additional metabolites can be more confidently identified. Among those we have Taurine (Tau) at 3.42 ppm, Alanine (Ala) at 1.47ppm and Glutamate+glutamine (Glx) at 3.75ppm. The peaks appeared better resolved in the MRSI spectrum and even some splittings (Lac doublet at ca. 1.3 ppm) hinted. The MRSI-semiLASER technique hence provided a higher spatial resolution compared to SV-semiLASER and could provide additional information about metabolic pattern changes within tumor brain.
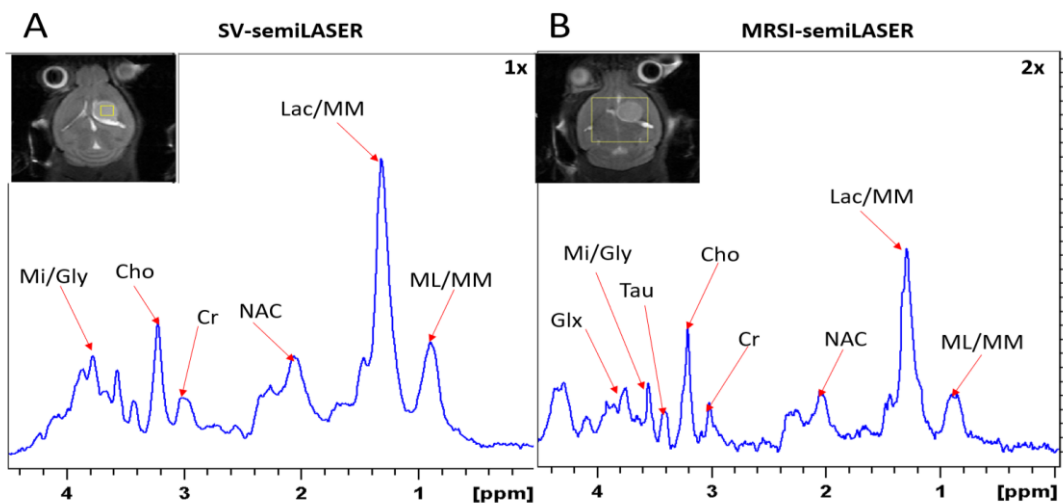
Figure 4.4.28 Single voxel semiLASER spectrum at 1x and single spectrum from Multi-voxel MRSI-semiLASER grid zoomed 2x plotted to the same scale acquired in a GL261 tumor-bearing mouse (C1768). The voxel and grid locations are specified in the insets containing the T2 weighted images. The spectra are plotted in the range 0-4.5 ppm where ML= Mobile lipids, Lac= lactate, Ala= alanine, NAc= N-acetyl containing compounds, Cre= Total creatine (phosphocreatine+creatine), Cho= choline containing compounds, Tau = taurine, Mi= Myo-inositol, Gly= glycine, Glx= glutamate+glutamine (probably also alanine signals).

The results obtained also confirmed the increase in SNR and spatial resolution of the MRSI-semiLASER acquired grids. Hence the MRSI-semiLASER sequence, with higher signal to-noise

ratio (SNR) and spatial resolution, may allow us to better detect functional metabolic changes, helping to understand morphological and physiological changes occurring in tumour tissue and surrounding brain parenchyma.

4.4.6.4 Towards achieving higher spatial resolution by reducing slice thickness in brain GB mice

In multi-slice MRSI acquisitions, the thickness of the slices that are acquired determines the spatial resolution of the resulting spectra. In an effort to optimize the multi-slice 2D-MRSI acquisitions obtained with the current protocol and the validation of the implemented MRSI-semiLASER sequence to improve the spatial resolution, we studied the effects of reduced slice thickness by acquiring an extra slice within the same tumor volume. For this purpose, five consecutive 0.8 mm slice thickness grids were able to be satisfactorily acquired individually across the GB tumor in GL261 Tumor-bearing mice. These five slices covered the same volume as the four 1mm slices that would be acquired with our previous protocol.

Figure 4.4.29 presents the high resolution MRSI-semiLASER grids in a GL261 tumor-bearing mouse for a multi-slice acquisition consisting of five contiguous 0.8mm slices. Slices were prescribed across the mouse brain, covering the tumor and avoiding scalp by using the T2w axial images as reference (at left in the figure 4.4.29). Each MRSI grid was shimmed individually. Six saturation slices (ST, 10 mm; sech-shaped pulses: 1.0ms/20250 Hz) were positioned around the VOI to minimize OV contamination. The MRSI grids are shown graphically superimposed to the T2w image for each slice (middle). On the right, Lactate/mobile lipid/macromolecules (Lac/ML/MM) maps, at ca. 1.3 ppm, were overlaid on corresponding T_2w images.

A Comparison of 1 mm versus 0.8 mm slice thickness MRSI-semiLASER with weighted k-space acquisitions is shown in Figure 4.4.30, where representative spectra from brain peritumoral parenchyma and tumor regions are displayed. The linewidth for (Lac/ML/MM) peak (outlined in yellow) was calculated by fitting to a Lorentzian peak. The shimming over the thinner 0.8 mm slices resulted in improved B0 homogeneity with respect to 1 mm slices, hence peaks appear narrower and more intense, and their SNR is larger than expected. Table 4.4.4 shows mean SNR values of the whole grid for several metabolites, reflecting less than the expected 20% SNR decrease in the 0.8 mm slice grid compared to 1 mm.

Hence we concluded that with our in-house implementation of the MRSI-semiLASER sequence, a 20% slice thickness reduction can be achieved without losing relevant spectral quality and thereby producing higher spatial resolution acquisitions.
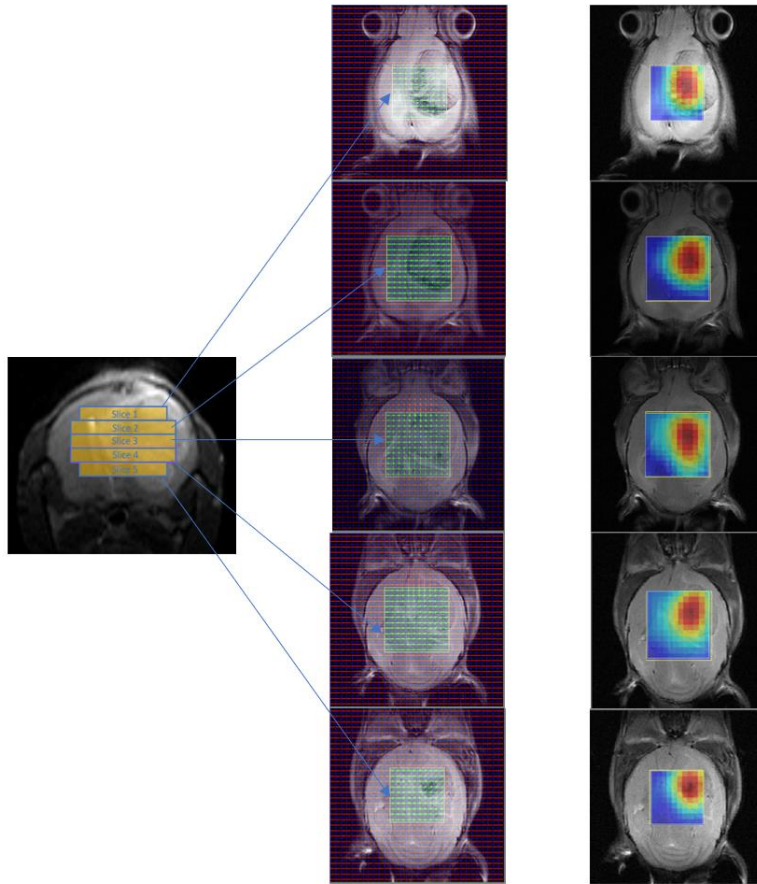
Figure 4.4.29 High resolution MRSI-semiLASER grids in a GL261 tumor-bearing mouse (C1768). T₂w axial images shown as reference (left), five contiguous 0.8 mm coronal slices were prescribed across the mouse brain, covering the tumor and avoiding scalp. Each MRSI grid was shimmed individually. Six saturation slices (ST, 10 mm; sech-shaped pulses: 1.0 ms/20250 Hz) were positioned around the VOI to minimize OV contamination. The MRSI grids are shown graphically superimposed to the T2w image for each slice (middle). On the right, Lac/ML/MM maps, at ca. 1.3 ppm, were overlaid on the corresponding T2w images.
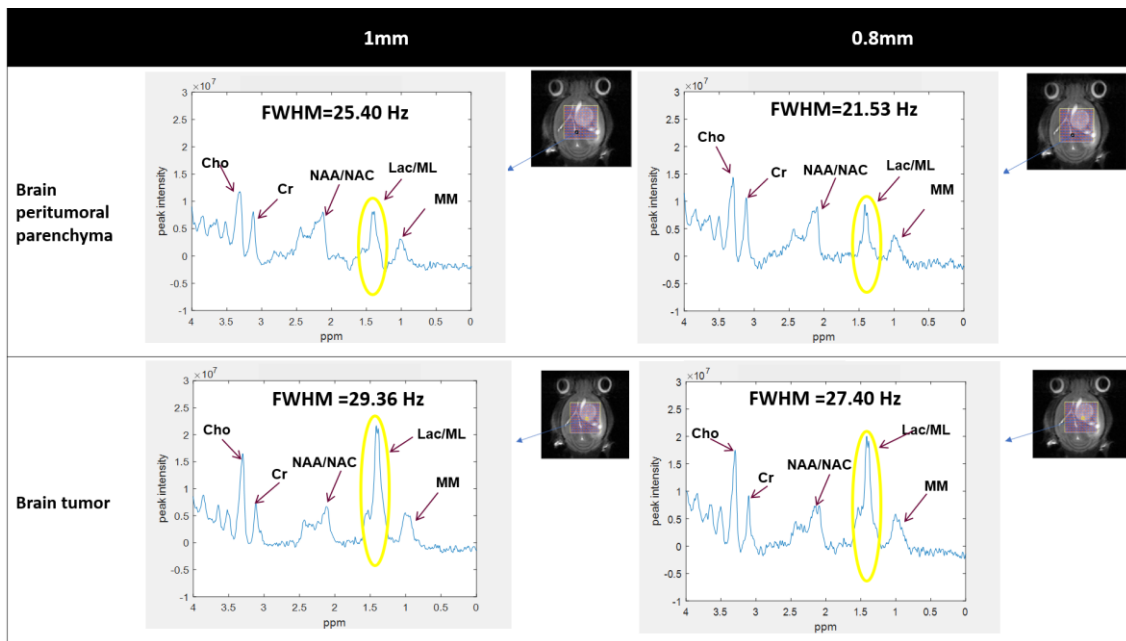
Figure 4.4.30 Comparison of 1 mm versus 0.8 mm slice thickness MRSI-semiLASER acquisitions with representative spectra from brain peritumoral parenchyma and tumor regions. The linewidth for Lactate/mobile lipid/macromolecules (Lac/ML/MM) peak (outlined with yellow ovals) was calculated by fitting to a Lorentzian peak. The shimming over the thinner 0.8 mm slices resulted in improved B0 homogeneity with respect to 1 mm slices, hence peaks appear narrower and more intense, and their SNR is larger than the one obtained for 1 mm slices.

Table 4.4.4: Mean SNR values of the entire grid for Lactate (Lac/ML/MM), NAA, Creatine and Choline signals in MRSI-semiLASER acquisitions with slice thickness of 1 mm versus 0.8 mm.

	SNR 1mm	SNR 0.8mm	%SNR reduction
LACTATE	12.35±6.47	11.25±6.00	9.00
NAA	9.36±1.62	8.94±1.63	4.50
CREATINE	9.42±2.81	9.12±3.16	3.20
CHOLINE	13.53±4.43	11.98±3.50	11.46

The SNR obtained for the various metabolites at 0.8 mm is higher than the 20% expected reduction based on volume reduction.

4.4.6.5 Nosological Images

As described in Chapter 1, the nosological images based on Magnetic Resonance Imaging and Magnetic Resonance Spectroscopic Imaging (MRSI) can be used to characterize tumor tissue. The approach is useful in assisting glioma diagnosis, where several tissue patterns such as normal, proliferating tumor, and necrotic tissue are present in the same region of interest. The semi-supervised Spectra Classifier was developed within a previous project using machine learning approaches and trained using sources from spectra acquired using the Bruker stock CSI-PRESS sequence in GL261 bearing mouse brains [83] [43].

To see whether the available classifier could generate nosological maps for the acquisitions using the implemented MRSI-semiLASER sequence, the acquisitions using this one and the stock

Bruker CSI-PRESS sequence, acquired at the same TE, were post processed using spectra classifier [44] . Figure 4.4.31 presents the nosological maps, spectra comparison and TRI calculation for MRSI-semiLASER vs CSI-PRESS for a single slice in tumor brain where (A) is the MRSI-semiLASER nosological map with a TRI of 0% and (C) is the representative spectrum for MRSI-semiLASER at TE=27ms, (B) is CSI-PRESS nosological map with a TRI of 0% and (D) representative spectrum for CSI-PRESS at TE=27ms. Red color labels proliferating tumor, blue color labels normal brain parenchyma and green color labels responding brain tumor. The maps were accurately generated and the same Tumor Response Index (TRI) [2] of TRI=0% represented untreated tumor tissue for both MRSI-semiLASER and CSI-PRESS spectra calculated using equation 1.6 described in Chapter 1.
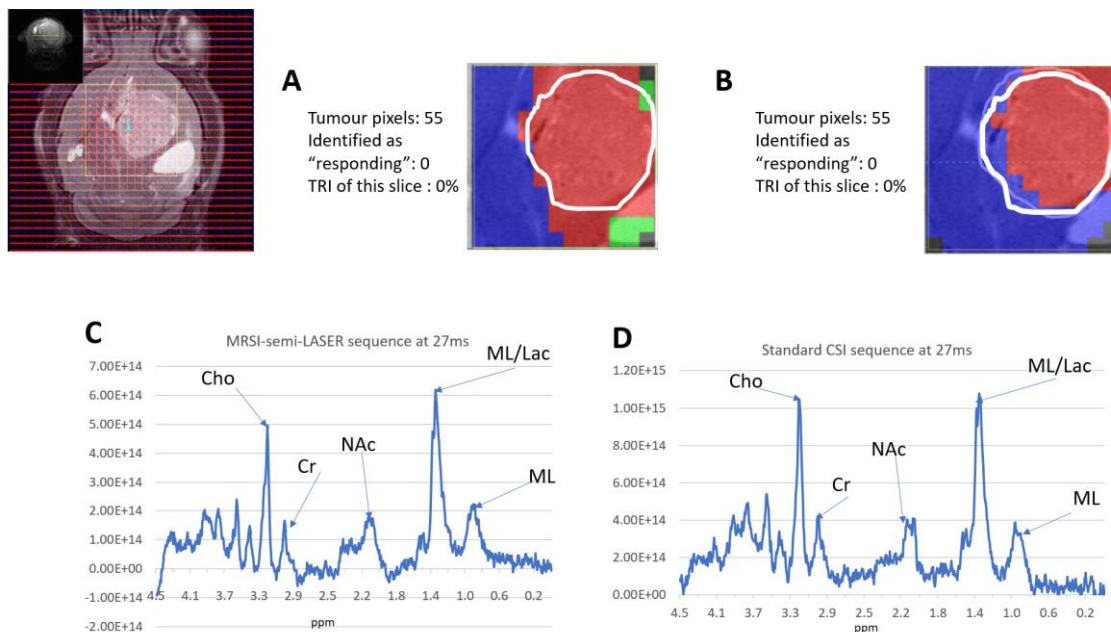
Figure 4.4.31 Nosological maps, spectra comparison and TRI calculation for MRSI-semiLASER vs CSI-PRESS for a single slice in tumor brain where (A) MRSI-semiLASER nosological map with a TRI of 0% and (C) representative spectrum for MRSI-semiLASER at TE=27ms, (B) CSI-PRESS nosological map with a TRI of 0% and (D) representative spectrum for CSI-PRESS at TE=27ms. Red color labels proliferating tumor, blue color labels normal brain parenchyma and green color labels responding brain tumor.

Nonetheless, the results for the minimum TE acquisitions did not meet our expectations in some tested cases. The classification results may be affected by the spectral differences in baseline and echo time between the sources that were used to train the spectra classifier and the MRSI-semiLASER test spectra.MRSI-semiLASER and CSI-PRESS acquired datasets acquired at the minimum TE possible for each sequence, were used to obtain additional nosological images for three GL261 tumor bearing mice, which included case C1836 at day 15 p.i. with a tumor volume of 32.5 mm^3, case C1828 at day 18 p.i. with a tumor volume of 59 mm^3 and case C1831 at day 18 p.i. with a tumor volume of 55.3 mm^3. Figure 4.4.32 represents the nosological maps and spectra obtained using case C1836 at day 15 p.i. One of our observations included that the nosological maps showed accurate correlation in some cases while in others the spectra classifier derived nosologicval image did not prescribe the tumor as expected for both MRSI-semiLASER as well as CSI-PRESS spectra. We also repeated the experiments with a different glioma model CT-2A which has been described to be intrinsically less immunogenic than GL261 [84] and are closer to GB's after treatment [85]. The results obtained were similar to GL261

tumors (data not shown). Further retraining may make the classifier robust enough to also recognize properly CT-2A tumors [86].
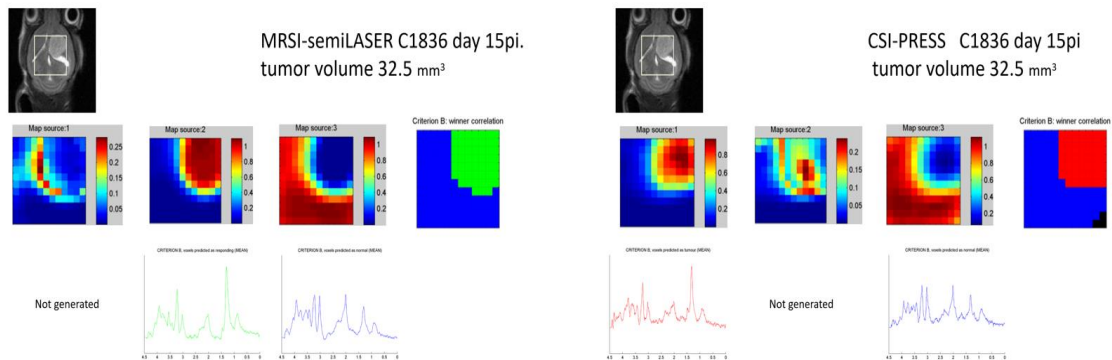
Figure 4.4.32 Nosological maps for MRSI-semiLASER and CSI-PRESS sequences on additional GL261 bearing tumors. The tumor mass was differentially recognized (criterion B winner correlation) from brain parenchyma in both cases but in C1836 acquired with MRSI-semiLASER the classifier decided the tumour was responding to therapy (green colour coding) while in this case, no treatment had been applied yet.

We hence concluded that the spectra classifier nossological images predictor may require retraining using data from both the MRSI-semiLASER and CSI-PRESS sequences in future studies to improve robustness of tumor mass evaluation when the new MRSI-semiLASER sequence is used for acquisition.

4.4.7 k-space sampling strategies using multiple acquisition modes

In the MRSI acquisitions, several different weighting schemes can be selected via the parameter Experiment mode, such as: Standard, Elliptical and Weighted [51]. These modes govern the scheme with which the phase encoding gradients are applied and can serve to improve the localization or to reduce the overall scan time. These sampling schemes must always be reported, according to the consensus paper on minimum reporting guidelines for MRSI acquisitions [87].

The Standard mode consists of a conventional MRSI-experiment, in which a constant number of phase encoding steps is performed in every spatial dimension and averaged NA times. In such an experiment, a rectangular fraction of the k-space is sampled uniformly. The resulting spatial response function looks like a sinc-function (Figure 4.4.33 A).

The Weighted mode performs a variable number of averages for each phase encoding step, according to its position in k-space. The number of times a certain phase encoding step is averaged is determined by the Hanning function. The data is interpolated into a larger image matrix size for analysis, using "Fourier interpolation" to obtain the same spatial resolution with a Hanning-weighted sequence as with standard MRSI. This type of weighting is superior in the sense that it allows a suppression of sidebands caused by the spatial response function(SRF) by

multiplying with a weighting function i.e. the Hanning function. (Figure 4.4.33 B). The number of times a certain phase encoding step is averaged is also determined by the Hanning function.

In the Elliptical acquisition mode, to reduce measurement time, it is possible to skip the phase encoding steps in the corners of the k-space, sampling a spherical fraction of kspace. This makes the spatial response function also look more spherical, but also a bit broader (Figure 4.4.33 C). This yields a higher SNR, but also a lower spatial resolution. To obtain the same spatial resolution as in a standard CSI experiment, a higher number of phase encoding steps in each direction has to be performed. The missing data points are filled with zeros, so the resulting data files contain a rectangular data matrix.

The spatial resolution of a normal MRSI experiment is exactly equal to the FOV divided by the number of phase encoding steps. With the increase in the number of phase encoding steps the elliptical mode may provide the same resolution as the weighted acquisition mode and hence the increase in SNR may be an additional advantage. No significant increase in the overall scan time of the experiment is expected with the elliptical acquisition mode.

Additionally, in ParaVision 5.1, a pipeline filter is used that controls the averaging and also zero-fills the suppressed signals in both the Elliptical and Weighted experiment modes.
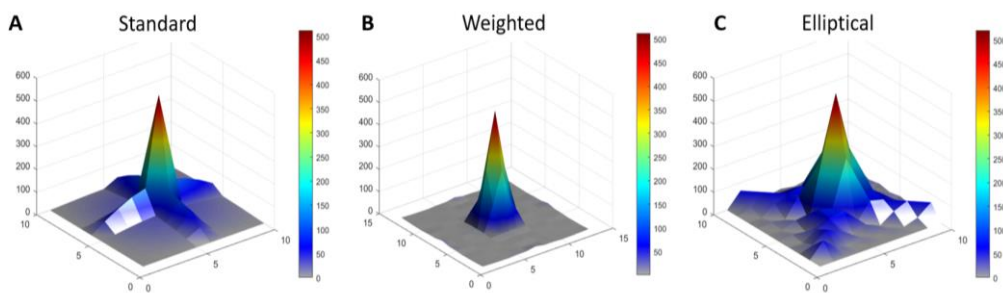
Figure 4.4.33 Point spread functions for the MRSI-semiLASER acquisition modes: standard, weighted, and elliptical [51]. The standard mode yields the lowest SNR. The weighted mode has better spatial response profile due to Hanning filtering and yields intermediate SNR. The elliptical weighting scheme skips the phase encoding steps in the corners of k-space. The missing data points are zero-filled and a higher number of phase encoding steps in each direction are acquired, within the same acquisition time, which causes broadening of the spatial response function but also increases the SNR [88].

Our goal was to test and compare the performance of the implemented MRSI-semiLASER sequence using the elliptical phase encoding mode, although the established protocol for PRESS-CSI was set as weighted because of the theoretical benefits reported in literature. The implementation of sampling k-space elliptically to obtain proton MR spectroscopic Imaging (MRSI), with PRESS localization, pattern in a preclinical study with phantoms and the GL261 GB mouse model of glioma on a 7T preclinical scanner are described herein. This method offers a fast and robust data acquisition with high spatial resolution and increased signal to noise ratio resulting in high quality spectroscopic maps.

For MRSI-semiLASER the acquisition parameters were kept as: TE = 27ms; TR = 2500ms; VAPOR water suppression; FOV = 17.6 x 17.6 mm ; slice thickness = 1 mm or 0.8 mm; voxel size = 6.6 x 6.6 mm (middle grids) and 5.5 x 5.5 mm (outer grids); acquisition matrix size of 8x8 interpolated to 32 x 32, thus resulting in a voxel matrix size of 12 x 12 and 10 x 10 in middle and outer grids, respectively; SW = 4006.41 Hz; NA = 512 (standard and weighted), 520 (elliptical); TAT= 21 min per grid. SNR values were estimated as maximum signal intensity divided by standard deviation

of the noise. Figure 4.4.34 summarizes the acquisition parameters for MRSI-semiLASER (A) and CSI-PRESS (B) sequences.

A

Acquisition modes	STANDARD	ELLIPTICAL	WEIGHTED
TE(ms)	27	27	27
TR(ms)	2500	2500	2500
Number of acquisitions	512	520	512
Number of encoding steps	8	13	12
Dummy scans (DS)	4	4	4
Slice dimensions	6mm x 6mm x1mm	6mm x 6mm x1mm	6mm x 6mm x1mm
Acquisition time	21 min 30 s	21m 50s	21m 30 s
Spectral width	13.34	13.34	13.34
FOV(mm)	17.6	17.6	17.6
Resolution(mm)	2.2	2.2	2.2

B

Acquisition modes	STANDARD	ELLIPTICAL	WEIGHTED
TE(ms)	14	14	14
TR(ms)	2500	2500	2500
Number of acquisitions	512	520	512
Number of encoding steps	8	13	12
Dummy scans (DS)	4	4	4
Slice dimensions	6mm x 6mm x1mm	6mm x 6mm x1mm	6mm x 6mm x1mm
Acquisition time	21 min 30 s	21m 50s	21m 30 s
Spectral width	13.34	13.34	13.34
FOV(mm)	17.6	17.6	17.6
Resolution(mm)	2.2	2.2	2.2

Figure 4.4.34 A, acquisition parameters for the MRSI-semiLASER sequence using different k-space acquisition modes. B,the acquisition parameters for the CSI-PRESS sequence using different k-space acquisition modes.

4.4.7.1   Multiple acquisition modes in phantoms

Experiments were conducted with the low concentration cylindrical phantom B used in previous experiments. The MRSI-semiLASER and CSI-PRESS spectra were acquired in all three k-space acquisition modes. A comparison of the acquired mean spectra and standard deviation in phantom studies is shown in Figure 4.4.35. The spectra showed visually greater peak intensity in the elliptical acquisition mode for both MRSI-semiLASER and CSI-PRESS in comparison to the standard and weighted mode. The weighted mode provides intermediate peak intensities. The standard deviation is comparable in both sequences due to the homogenous phantom characteristics. Figure 4.4.36 shows the comparison of the NAA SNR maps using the MRSI-semiLASER and CSI-PRESS sequences with the different acquisition modes. The metabolite maps obtained for the MRSI-semiLASER sequence in the elliptical acquisition modes visually show a more homogenous MRSI grid. The SNR values obtained are also plotted in the Figure 4.4.36.
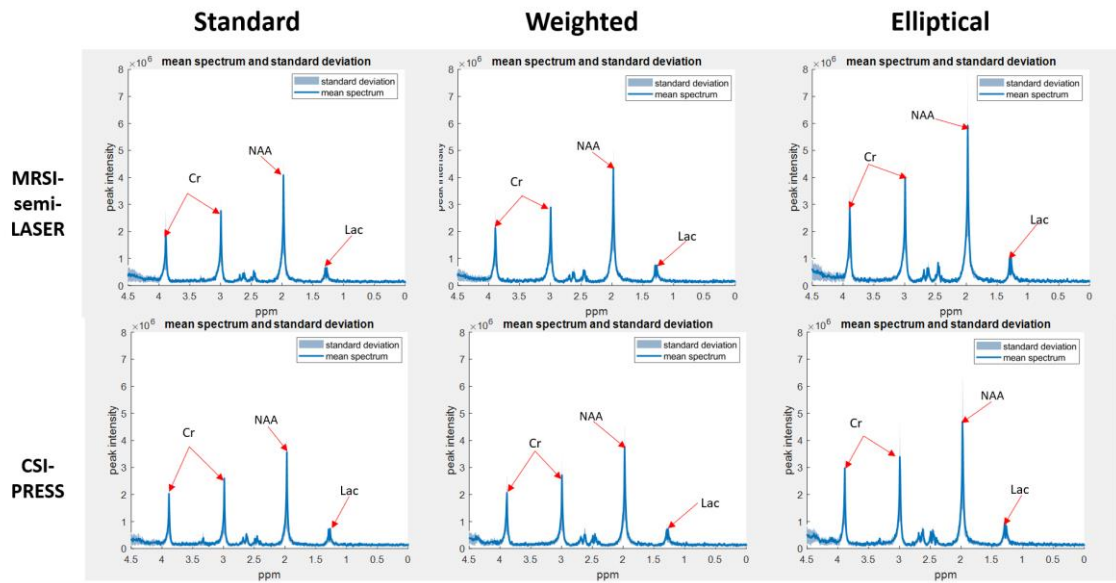
Figure 4.4.35 Comparison of mean spectra and standard deviation obtained with MRSI-semiLASER and CSI-PRESS sequences in different acquisition modes using phantom B. The highest peak intensities are recorded with the MRSI-semiLASER sequence in the elliptical acquisition mode. The weighted mode provides intermediate values while the standard has the lowest SNR.
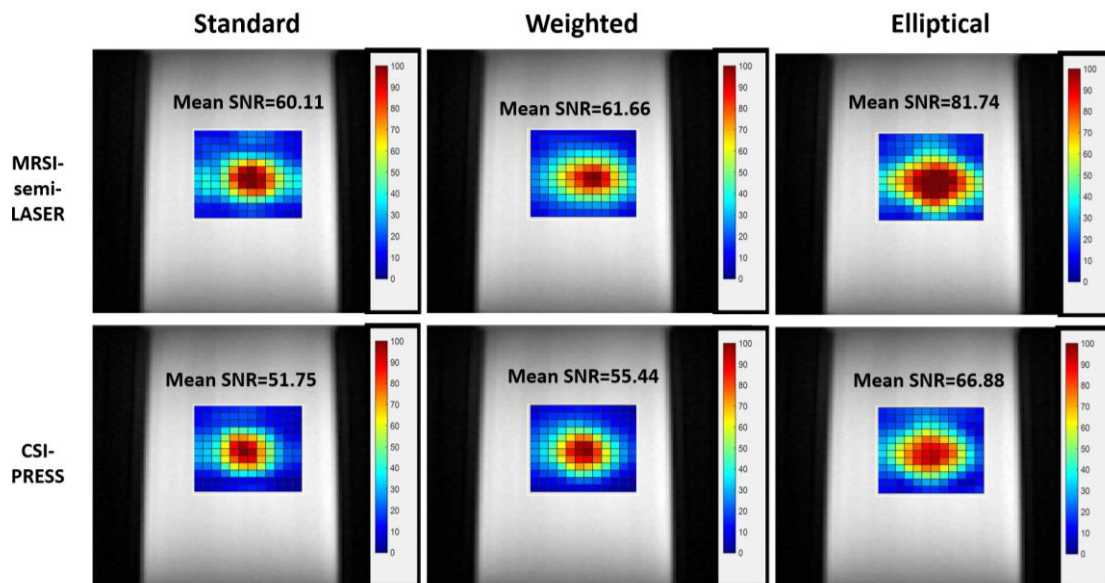
Figure 4.4.36 Comparison of SNR maps for the NAA peak using MRSI-semiLASER and CSI-PRESS sequences using phantom B. The mean SNR is also reported for the metabolite peak in the inner grid. The highest SNR value is obtained for the MRSI-semiLASER acquisition in the elliptical experiment mode. The weighted and standard acquisition modes provide comparable SNR values.

4.4.7.2   Elliptical mode test using a two-cylinder phantom

The elliptical acquisition mode was further tested with the MRSI-semiLASER sequence and the CSI-PRESS sequence with the two-chamber phantom (phantom 4 described in section 3.2) to investigate chemical shift displacement. No visible spatial shifts in the excited volume for metabolites resonating at different frequencies was observed. Figure 4.4.37 exhibits the map plotted for the NAA peak at 2.01 ppm, which was seen in the inner cylinder only, while the map for the Cr peak at 3.9ppm was visible in the outer cylinder only.
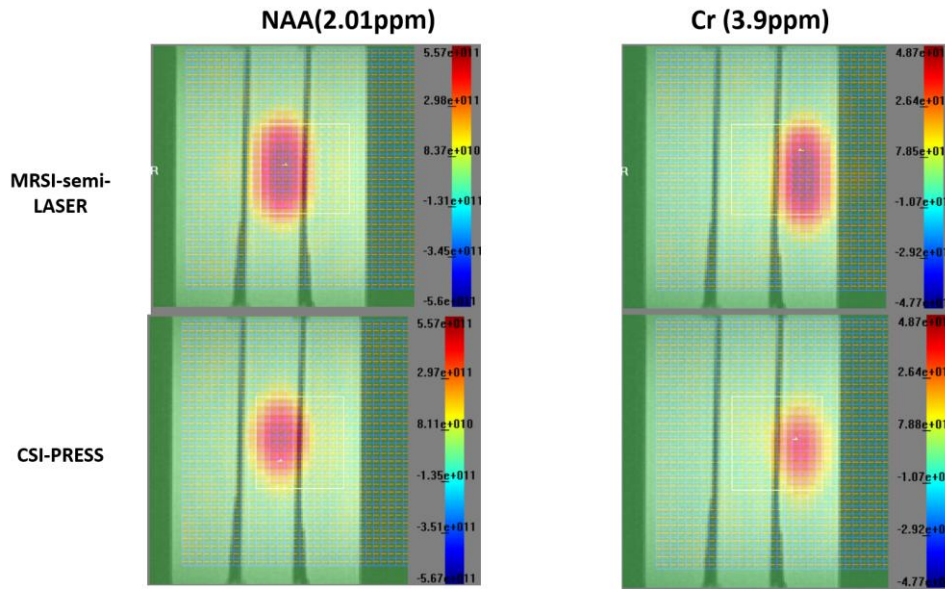
Figure 4.4.37 Elliptical acquisition mode visually tested for chemical shift displacement in the two-cylinder phantom using MRSI-semiLASER and CSI-PRESS sequences.

.

4.4.7.3 Multiple acquisition modes in-vivo in wt and tumor mouse using the implemented MRSI-semiLASER sequence

To obtain the comparison for multiple acquisition modes in-vivo in wt as well as tumor mouse models, experiments were conducted using the multiple semiLASER sequence.

Since the benefits of the implemented MRSI-semiLASER sequence have already been established, we moved forward by evaluating the sequence performance in terms of spectra quality and SNR in wt as well as tumor mouse using the multiple acquisition modes. Figure 4.4.38 gives a comparison of the mean spectra obtained for the MRSI-semiLASER sequence using wt and GB tumor mice.

Consistent with our phantom B results, we found that for the wt mouse, the elliptical mode produced the highest SNR recorded for the NAA peak using both the MRSI-semiLASER and CSI-PRESS sequences. The SNR for the NAA peak in the elliptical acquisition mode using MRSI-semiLASER was obtained at 18.8±8.0. The SNR for the NAA peak in the weighted mode produced intermediate values at 15.7±5.5. Lastly, the lowest SNR was obtained for the NAA peak in the standard mode where the SNR was recorded at 14.8±5.1. These results were similar to our observations in phantoms and further proved that superior SNR could be obtained by combining the elliptical acquisition scheme with the implemented MRSI-semiLASER sequence.

The mean spectra obtained using MRSI-semiLASER sequence for the tumor mouse using all three acquisition modes showed the presence of increased lactate and reduced NAA/NAC along with an increase in Choline, which is representative of tumors. The mean SNR recorded for the Lactate peak in elliptical mode was 14. 8 ± 7.3, in weighted was 12.4 ± 6.5 and in the standard mode was 12.7 ± 7.1. The results are summarized in table 4.4.5.

As already demonstrated with our phantom results, the highest SNR for the chosen metabolite peak was recorded in the elliptical acquisition mode for both the wt and tumor mouse using the implemented MRSI-semiLASER sequence. In the light of the obtained results, we find the elliptical weighting mode superior in terms of SNR and metabolite peak intensities for our wt mouse and brain tumor applications. We did not observe any artefact contamination in the obtained spectra. The significance of the weighted mode cannot be ignored since the spatial resolution of the MRSI experiment depends on the width of the spatial response function (SRF) and the acquisition weighting improves the shape of the SRF. However, for spectroscopic uses, we recommend using the elliptical weighting for higher SNR.
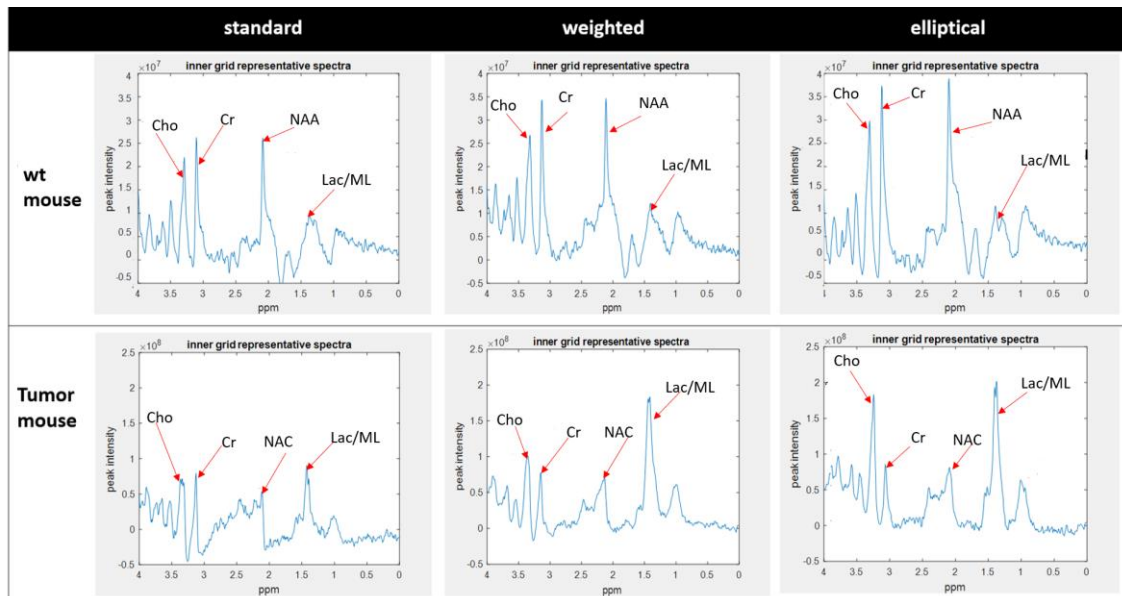
Figure 4.4.38 MRSI-semiLASER acquisition scheme comparison for mean spectra acquired using a wild-type mouse and a GL261 tumor-bearing mouse, C1768. Spectra were acquired in the standard, weighted and elliptical modes respectively.

Table 4.4.5 Acquisition mode SNR comparison in-vivo in wt vs the C1768 tumor mouse using MRSI-semiLASER.

	Standard	Weighted	Elliptical
WT mouse (NAA SNR)	14.8 ± 5.1	15.7 ± 5.5	18.8 ± 8.0
Tumor mouse (Lac SNR)	12.7 ± 7.1	12.4 ± 6.5	14.8 ± 7.3

The NAA SNR values ate reported in the wt mouse and Lac SNR values are reported for the C1768 tumor mouse.

4.4.8 Discussion and Conclusions

This work describes an improved multi-voxel spectroscopic imaging pulse sequence (MRSI-semiLASER) that uses the semiLASER localization approach. The Bruker CSI sequence containing the PRESS localization block (CSI-PRESS) was modified by replacing the aforementioned PRESS block with a semiLASER one, resulting in an MRSI-semiLASER sequence. This work was developed on a 7T Bruker BioSpec 70/30 USR spectrometer running ParaVision5.1 which does not contain either built-in blocks for semiLASER sequence or adiabatic pulses. The sequence was tested in phantoms, wt C57/BL6 mice and GB tumor mouse brain and compared with the stock CSI-PRESS sequence. The results show improved homogeneity and reduction in chemical shift displacement error (CSDE) in the phase encoding direction going down from 14.2% in CSI-PRESS to 8.9% in MRSI-semiLASER

Also, due to the 1.2-fold/1.4-fold increase in SNR measured from tumor brain, increased spatial resolution was achieved using MRSI-semiLASER applied to GL261 tumor-bearing mice, which allowed to acquire an extra slice within the same tumor volume. When decreasing the slice thickness from 1 mm to 0.8 mm, we expected to see a 20% reduction in SNR, however, SNR was maintained above the expected level. Narrower water peak widths at half height were observed in spectra acquired at 0.8 mm indicating better B0 homogeneity in thinner slices, which results in narrower and more intense peaks with SNR larger than predicted based on volume differences.

Moreover, different k-space sampling strategies were evaluated showing significant SNR increase with elliptical sampling, which may allow to further increase the spatial resolution or a reduction in the total experimental time. Scheenen et al. have already shown reduction in scan time by combining the semi-LASER sequence with elliptical k-space sampling for ^{1}H-MRSI of the human brain at 7T [89]. With elliptical phase encoding, where corners of k-space are skipped, a higher number of phase encoding steps in each direction can be acquired within the same acquisition time, as compared to standard or weighted acquisition. This causes broadening of the spatial response function but also increases the SNR. Jiani Hu et al. have also shown the utility of the elliptical k-space sampling scheme to achieve high spatial resolution and reduce scan time for ^{1}H MRSI of human breast cancer in a clinical setting at 3T [90].

 The weighted mode had been used by default in our previous studies because its known improved PSF as compared to standard or elliptical acquisition modes. Nonetheless, elliptical acquisition provided good quality spectra with no apparent artefactual signals and a 16.7 % SNR increase with respect to weighted acquisitions.

In this study we have shown the added value of using the fully adiabatic localization in MRSI-semiLASER. Moreover, the increased SNR obtained with elliptical phase encoding may also improve spectral pattern analysis of our murine brain tumor models.

4.5 MATLAB processing and post processing tools

Common post-processing techniques of MRS spectra includes multiplication with a filter in the time domain, zero-filling, Fourier transform (FT), phasing, and baseline correction, similar to post-processing of high-resolution NMR data.

In this chapter, MATLAB based post-processing scripts developed in-house for the phase correction of single and multi-voxel NMR spectra are presented. The single voxel script was also supported by a Graphical User Interface (GUI) for the convenience of users. The tools further provided signal-to-noise (SNR) ratio and linewidth (LW) estimation for a resonance of interest in the phase corrected spectra selected by the user, and generated SNR maps and boxplots for SNR representation. The tools were implemented in MATLAB R2019b and were tested using single voxel magnetic resonance spectroscopy phantom datasets acquired on a 7T Bruker Biospec preclinical scanner running ParaVision 5.1 as well as with MRSI datasets acquired using phantoms and in-vivo data.

4.5.1 Phase Correction

Phasing is an NMR spectral adjustment process that is intended to maximize the absorptive character and the symmetry of all NMR peaks over all regions of an NMR spectrum. Phasing is one of the most important steps in spectral processing as even small phasing errors can lead to significant problems that will ripple down through all remaining spectral processing and post-processing steps [91]**.** As beautifully explained by Chen et al in their article "An efficient algorithm for automatic phase correction of NMR spectra based on entropy minimization" [92].

> "zero-order and first-order phase corrections are required for Fourier transform NMR spectra in order to obtain the desired appearance of the real part of the spectra. The zero-order phase mis-adjustment arises from the phase difference between the reference phase and the receiver detector phase. The first-order phase mis-adjustment arises from the time delay between excitation and detection, flip-angle variation across the spectrum, and phase shifts from the filter employed to reduce noise outside the spectral bandwidth [...]. Zero-order phase correction is frequency-independent, while first-order phase correction is frequency dependent."

The phasing is also important for careful testing of implemented pulse sequence's performance, to ensure that any undetected or phase-distorting pulse-sequence errors will not propagate into the NMR spectra [91].

We had the need to automatize the existing post processing pipeline used by our group to process MRSI datasets. Hence, we proposed to implement tools to perform phase correction of NMR spectra acquired for single and multi-voxel spectroscopy. MATLAB based postprocessing scripts were developed using manual and pre-defined phase correction approaches to replace the 3D Interactive Chemical Shift Imaging (3DiCSI) software and to convert ParaVision MRSI

datasets into an ASCII format suitable for the Dynamic MRSI Processing Module (DMPM, a MATLAB tool) [93] that prepares those datasets for the pattern recognition software we use for assessing response to therapy in murine glioblastoma This work was not planned initially but due to due to the unsuitability of the 3DiCSI software with ParaVision MRSI outputs beyond the 5.1 version, there was an urgent need to work towards an alternative.

4.5.2 Single voxel phase correction and LB

The single voxel spectral processing can be achieved through several data post-processing steps including, group delay correction, zero and first order phasing and exponential multiplication and line broadening. The effects of single voxel phase correction are inspected using a semiLASER acquired spectrum for the spherical phantom B containing NAA, Cr and Lactate (phantom description in chapter 3).

 A shift in the time domain data is equivalent to the application of a frequency-dependent, linear phase shift in the frequency domain. This problem can be solved by applying a circular shift to move the early distorted points of the FID to the end. This shift was obtained by reading the GRPDLY parameter stored in the acqu file at the time of acquisitions. The GRPDLY parameter shows the group delay (in units of fractional points) of the digital filter processing and is needed for spectroscopic processing of data within TOPSPIN. The decimation rate DECIM was chosen such that the chosen sweep width SW (or SWH) is as close as possible to the setting determined by the dwell time (DWOV) and DECIM. The factor DECIM was stored as an acquisition status parameter and is necessary to calculate a suitable baseline correction of a scan and the 1st order phase correction during FT. The DSPFVS is a documenting parameter and contains the number of the used firmware version. This parameter was automatically set at the start of an acquisition. The acquisition parameters DECIM, DSPFVS, and GRPDLY were read and extracted from the 'acqu' file. These three parameters specify the way in which digital filtering was used with this dataset and were used to compensate for the group delay which digital filtering introduces [51].

The value for DSPFVS was checked. If it is < 20 the pipeline exits because the correction method for that case is not implemented yet. However, such a situation did not arise in our experiments. The GRPDLY value was also checked and if it is -1, the program exits to avoid running into computation errors (not a frequent error). The 'fid' file was read and stored as a vector of complex data points and Fast Fourier transform (FFT) was applied to the FID to obtain a (complex data points) spectrum distorted by the digital filter group delay (Figure 4.5.1). The GRPDLY value (grpdly=67.984) was used to calculate the 1st order phase correction factor needed to compensate the digital filter effect by shifting the initial distorted points to the end of the FID. The fid and spectrum obtained after this digital filter correction are plotted in (Figure 4.5.2).

(a) original FID

(b) original unphased spectra
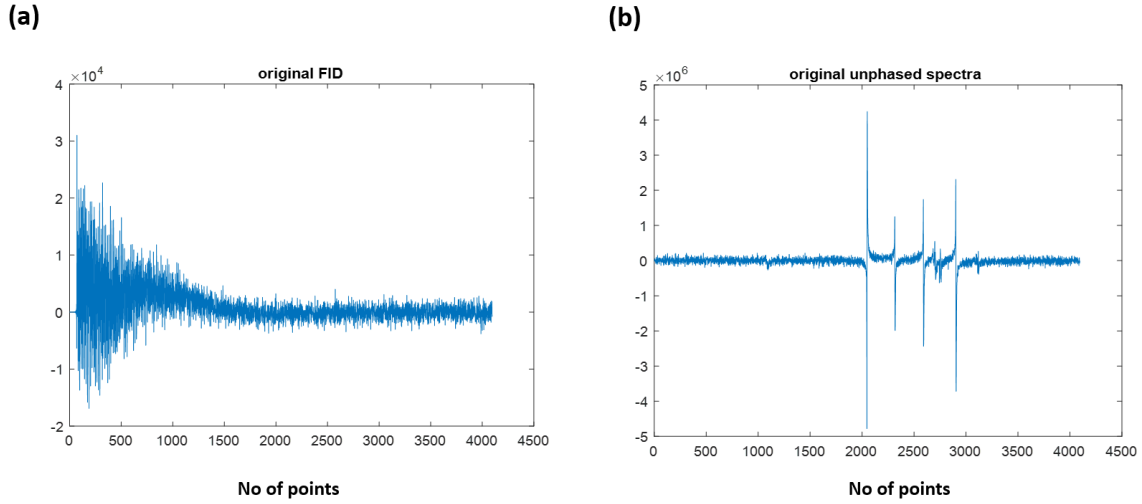
Figure 4.5.1 (a) The original FID acquired using SV-semiLASER sequence in a homogeneous phantom B with acquisition parameters already defined in section 4.3.3.3 (b)the unphased Fourier transformed spectrum.

(a) Fid after digital filter correction

(b) spectra after digital filter correction
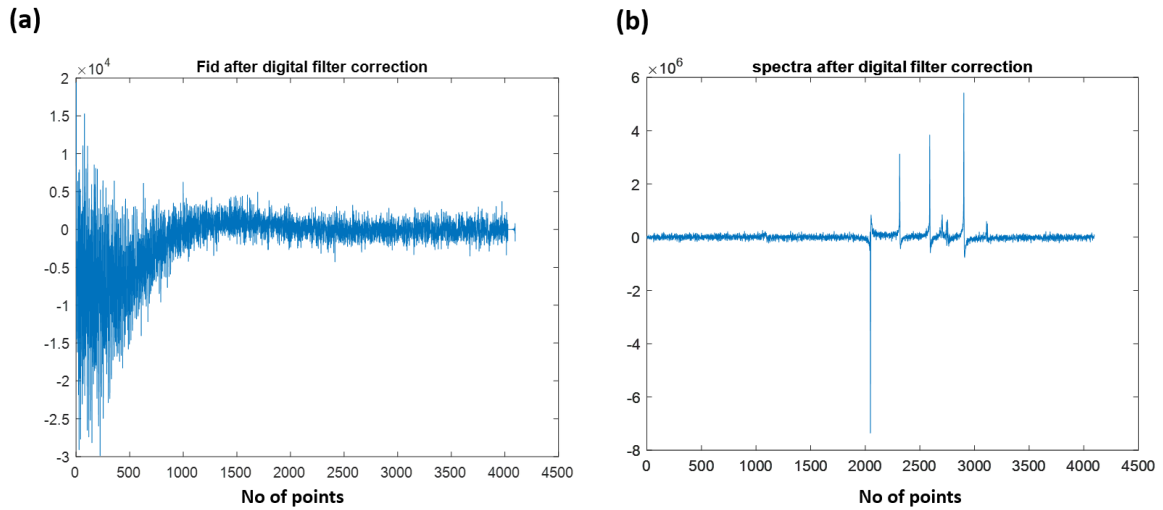
Figure 4.5.2 (a) The FID for phantom B aquisition after applying the digital filter correction (b) The Fourier transformed spectrum after applying the digital filter correction.

Although the group delay correction also adjusts the phase of the spectrum to some extent as can be seen in Figure 4.5.2 (b), additional zero and first order phase corrections are needed to fully correct the phase of the phantom B peaks in the spectrum. The PHC0 and PHC1 parameters correspond to the zero and first order phase correction set by user in TopSpin at the time of acquisition. The values of these parameters were read from the 'procs' file. The zero and First order phase correction vectors are applied on each spectrum datapoint using a Bruker accessible equation. The data, consisting of real points R(i) and imaginary points I(i) were phase corrected according to the equations 4.5.1, 4.5.2 and 4.5.3:

$$R0(i) = R(i)cosa(i) - I(i)sina(i) \qquad [4.5.1]$$

$$I0(i) = I(i)\cos a(i) + R(i)\sin a(i) \qquad [4.5.2]$$

where: $\qquad a(i) = PHC0 + (i-1) PHC1 \qquad [4.5.3]$

Where i > 0, R0 and I0 represent the corrected values and PHC0 and PHC1 are phase correction values read from the datasets. The phase correction was then applied to the distorted spectrum and the corrected spectrum was saved. Figure 4.5.3 represents the FID and the fully phased spectrum after applying the zero and first order phase corrections.
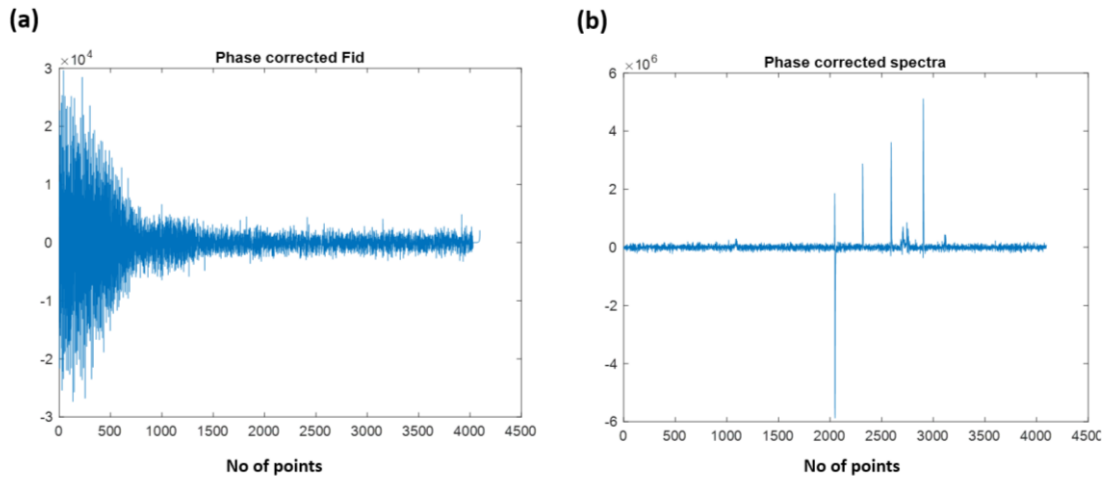
Figure 4.5.3 (a) The phase corrected FID for phantom B (b) The Fourier transformed spectrum after zero and first order phase correction.

Apodisation or line broadening (LB) was also applied to the phased spectra to smooth out the noise and improve the SNR. This is a very common data processing technique where the FID is multiplied by a decaying exponential function (the Fourier transform of which is a Lorentzian line with a full width at half height of LB). The larger LB, the faster the decay of the exponential. The product of the FID with the exponentially decaying function is Fourier transformed to give the NMR spectrum.

To apply line broadening the phase corrected spectrum was converted back to time domain using inverse Fourier transform (ifft). Exponential multiplication and line broadening (LB) entered by the user were applied to the time domain fid signal using the formula given by equation 4.5.4;

$$\text{exponential multiplication=} \ e^{\left(\frac{-(i-1).LB.\pi}{2.SWH}\right)} \qquad [4.5.4]$$

where SWH is the spectral width in Hertz (SWH=4006.410 Hz)

The FID was then converted back to Fourier domain for visualization and further processing. Figure 4.5.4(a) show the FID after line broadening and (b) shows a nicely phased spectrum obtained with a line broadening value of LB = 4 Hz. Applying the LB on the FID and spectrum can improve the signal-to-noise ratio by reducing the impact of noise or baseline distortions. It effectively narrows down the contributions from high-frequency noise and increases the prominence of the signal components.

(a)

FID after exponential multiplication

(b)

PHASED SPECTRA AFTER LINE BROADENING

No of points

No of points
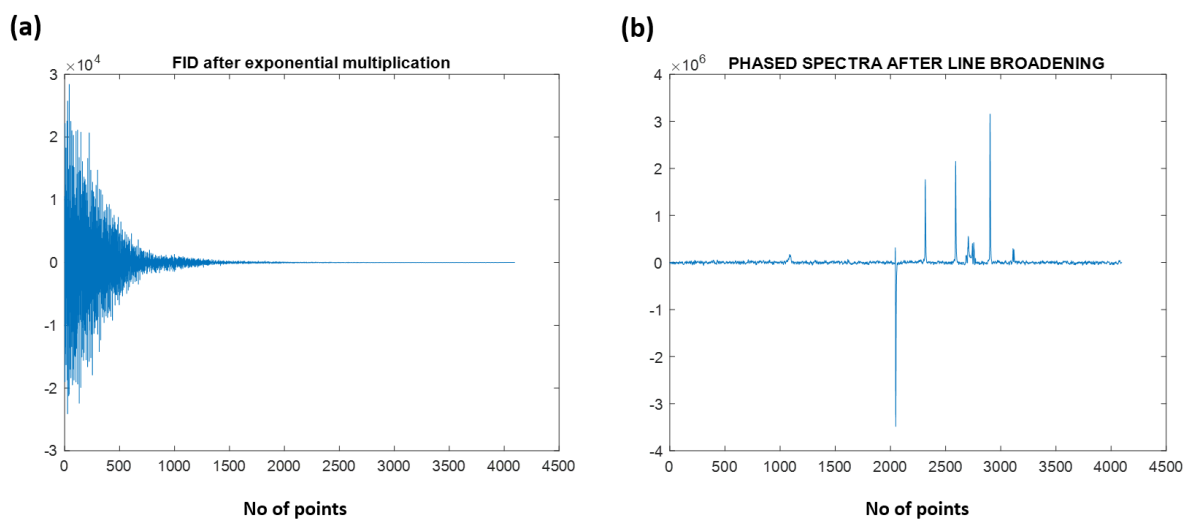
Figure 4.5.4 (a) The phase corrected FID for phantom B after line broadening and exponential multiplication by 4 Hz (b) Fourier transformed spectra after line broadening and exponential multiplication.

This approach was found to be sufficiently suitable for phase correcting single voxel datasets. Once the spectrum is fully adjusted, it can then be used for quantitation analysis.

4.5.3 Binning and peak picking

The first step to obtain quantitative results using the phase corrected spectrum is to apply binning to separate metabolite peaks. Binning can be a very simple method, not even requiring alignment, to extract peak intensities from multiple NMR spectra prior to performing multivariate statistical analysis. Binning involves dividing NMR spectra into small regions which are sufficiently wide to include one or more NMR peaks. The binning method was derived from the FID pipeline [94] [95]. The intensity of each bin was determined by calculating the area under the curve. Peak selection was done by assigning the starting and ending chemical shifts (peakppmmin, and peakppmmax) corresponding to the range of chemical compound of interest. Next the maximum intensity value of the peak in the selected chemical shift range was recorded.

Similarly, to calculate the noise, the region (noiseppmmin, noiseppmmax) was chosen corresponding to chemical shifts where no metabolite signal was expected and the standard deviation of maximum signal intensity for noise in the selected region was obtained.

In the chosen dataset, consisting of NAA (2.01 ppm), Cr (3.03 ppm and 3.9 ppm) and Lac (1.3 ppm) resonances, the NAA peak at 2.01ppm was selected to compute quantitative results Figure 4.5.5(a) shows the phased spectra plotted into ppm scale (ppm scale conversion code in appendix A) and (b) shows the NAA peak extracted between the range 1.5 ppm and 2.2 ppm and the noise signal extracted between -1 ppm and 0 ppm.
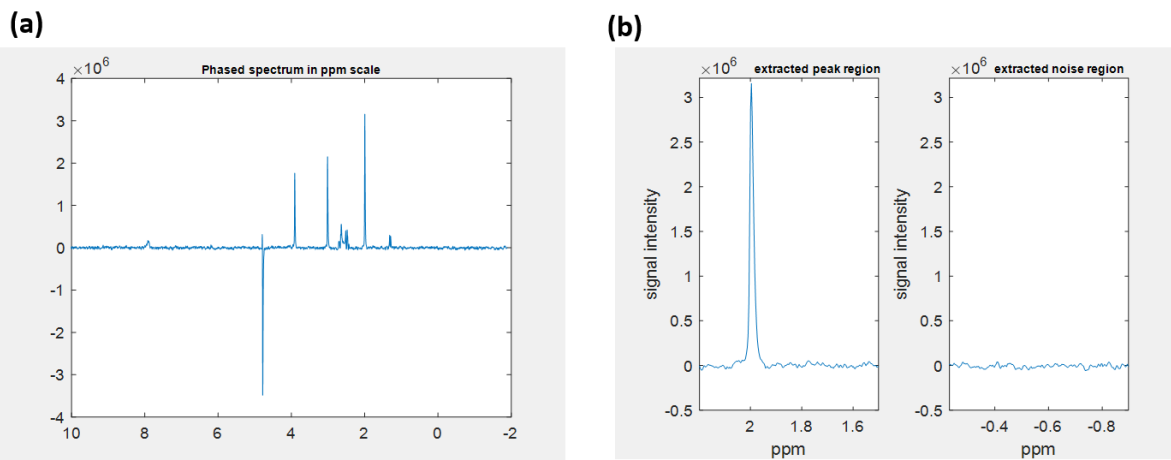
Figure 4.5.5 (a)The phased spectrum from phantom B plotted in ppm scale (b) The extracted NAA peak at 2.01 ppm and noise region.

Once the required peak has been selected, different statistical parameters such as maximum intensity, SNR, linewidth etc can be calculated to analyse the metabolite signals quantitatively.

4.5.4 SNR and Linewidth calculation

As is already known, SNR is measured as the ratio of the peak height over the root-mean-square deviation (RMSD or standard deviation) value of the noise floor. Good SNR is typically > 10, especially for publication purposes. Higher line-broadening increases SNR but too much line broadening pushes the intensities into the base which makes the base intensity difficult to integrate, hence leading to errors [96] and the signal overlap decreases spectral resolution. The single voxel phase correction pipeline also allowed for the direct computation of SNR and linewidths of a selected resonance within the phase corrected spectra.

The maximum peak intensities from the extracted peak and noise region were used to calculate the Signal-to-noise ratio (SNR) which was obtained by using the formula in equation 4.5.5**:**

$$SNR = \frac{maxpeak}{\sigma}$$ **[4.5.5]**

Where σ is the standard deviation of the intensities in the noise region. It was calculated using formula in equation 4.5.6;

$$\sigma = \sqrt{\left(\frac{1}{N}\sum_{n=1}^{N} \left| x_n{}^2 \right| \right)}$$ **[4.5.6]**

 In this example, the calculated SNR value for the NAA peak was measured to be equal to 113.2.

In the implemented pipeline, the linewidth of the extracted peak was calculated by integrating the function op_getLW from the FID-A pipeline [94] [95] [97]**.** This function helped to estimate the linewidth of a reference peak in the spectrum. By default, the reference peak is set at water, between 4.4 and 5.0 ppm. Two methods were used to estimate the linewidth as defined in the

FID-A pipeline: 1. Full width at half maximum (FWHM) was measured by taking the full width at half maximum of the reference peak. 2. The FWHM was measured by fitting the reference peak to a Lorentzian lineshape and determining the FWHM of the best fit (Figure 4.5.6).

In this example, the first method calculated the linewidth of the NAA peak at ca. 3.91 Hz. The linewidth obtained by fitting the spectra to the Lorentzian peak was measured as ca. 4.25 Hz. The output FWHM was given by the average of these two measures and was equal to ca. 4.08 Hz.
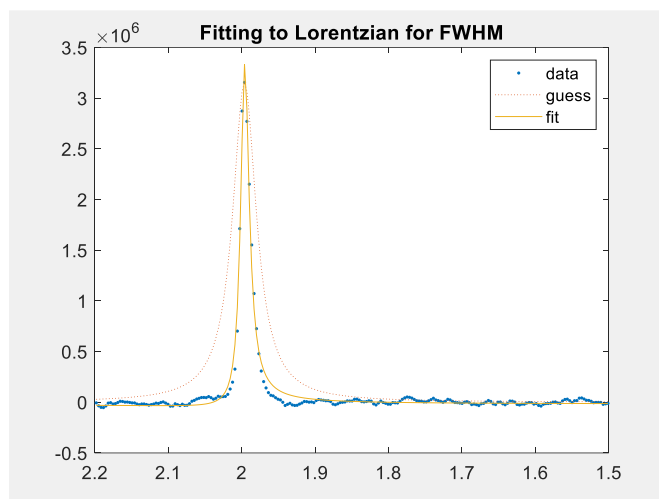
Figure 4.5.6 The extracted NAA peak in phantom B fitted to a Lorentzian peak for linewidth calculation.

4.5.5 Graphical User Interface (GUI) for single voxel phase correction and analysis

A Graphical User Interface (GUI) for single voxel phase correction, named svspipeline (Figure 4.5.5.1) was implemented in the MATLAB using guide to provide a tool which combines all the steps required for phase correction automatically, and facilitates the user adequate interaction for easy analysis of single voxel datasets. To begin with, the user needs to provide the full pathname for the dataset to be loaded into the GUI. The single voxel spectra can then be displayed using the load spectra tab. The original spectrum will be loaded into the top grid.

To phase correct the spectrum automatically, the user can press the 'phase correction` push button. The phase corrected spectra will be displayed in the adjacent grid in the top row. If the spectrum appears inverted, a 180° phase shift can be manually applied on the phase corrected spectra.

The line broadening can then be entered by the user in the edit box next to the push button labelled "line broadening". The resulting phased spectra is displayed in the first grid in the bottom row. For a further expansion of the spectra phasing, the zoom icon is provided on top of the GUI.

To obtain quantitative results, the user first needs to enter the maximum and minimum limits labelled as "ppmmin" and "ppmmax" to define the peak region for the resonance of choice. The

peak region can be selected using the slider icons. The noise region has been pre-defined between -1 to 0 ppm in the codes. The estimated SNR will be automatically generated by pushing the button labelled "SNR". The selected peak will also be displayed in the second grid on the bottom row. The method to calculate the Linewidth was the same as described in the previous section and will be visible on clicking the push button labelled "linewidth". The compiler generates a check if the fitting is optimal to the spectra "-are you satisfied with fit? y/n". If the response is "y" the calculated value is generated in the text box and the fitted peak overlaps the extracted peak in the bottom grid. If the response is "n", the process is repeated. For the selected dataset, phantom B, the SNR calculated for the NAA peak is equal to 113.2 and the linewidth for the NAA peak is calculated as 4.10 Hz. These results are displayed in the GUI layout in Figure 4.5.7.
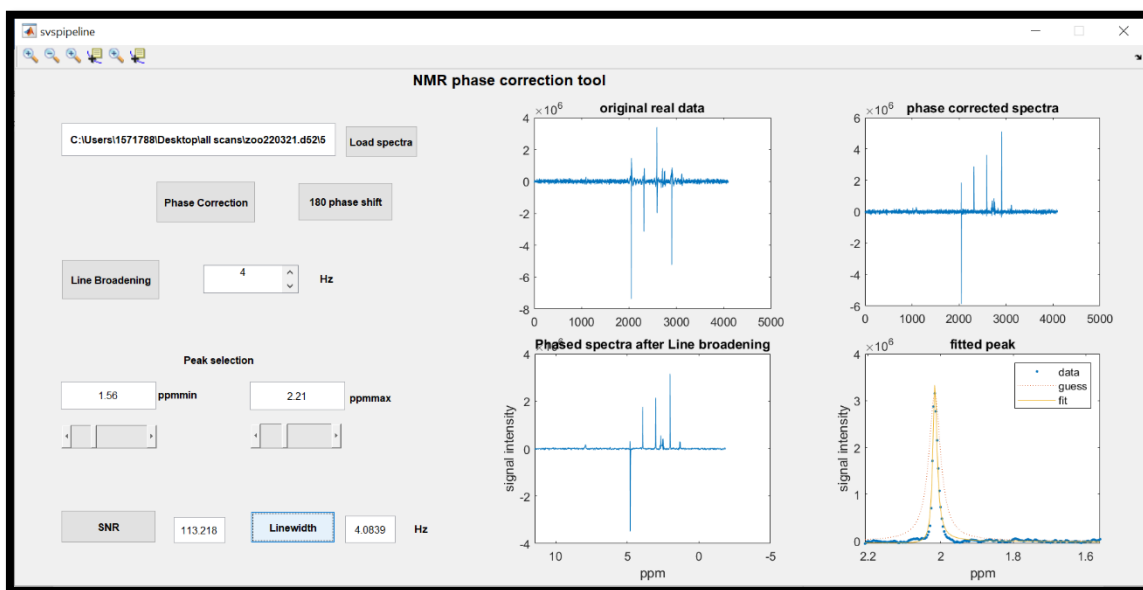
Figure 4.5.7 Screenshot of the GUI Layout for svspipeline.

4.5.6   Importing TopSpin processed spectra for automatic SNR and Linewidth computation

A MATLAB script entitled '**singlevoxel_topspin**' was developed to read the phase corrected intensity values directly from the Bruker acquired dataset by reading the 1r and 1i files obtained using TopSpin post-processing. It is general practice to export the acquisition to TOPSPIN and perform line broadening using the LB command and exponential multiplication, Fourier transform and phase correction using the efp command, to visualize the acquired spectrum. The TOPSPIN processing creates two files (1r, 1i) in the same directory as the original acquisition which contains the phased real and imaginary intensity values.

Processing in Topspin performs calculations in double precision floating point but stores the result in 32-bit integer values. During double to integer conversion, the data are scaled up or down such that the highest intensity of the spectrum lies between 228 and 229. This means the 32-bit resolution is not entirely used. This allows for the highest intensity to be increased, for example during phase correction, without causing data overflow. NC_proc shows the amount of scaling that was done, for example: – NC_proc = -3 means the data were scaled up (multiplied by 2) three times and NC_proc = 4 means the data were scaled down (divided by 2) four times [98].

It is hence important to recognize that the 1r and 1i files are intensity scaled by TopSpin according to the intensity scaling factor Nc_proc which is stored in the procs file after processing with TopSpin.

The real and imaginary components can hence be combined to obtain a complex valued matrix. This matrix is then plotted to the ppm scale and the SNR and linewidth are calculated using the same approach as defined in section 4.5.4.

The same dataset described in the previous subsection was tested using this script. The results obtained are plotted in Figure 4.5.8. (A) shows the phase corrected spectrum plotted to ppm scale, (B) shows the extracted NAA peak and noise plotted to the same scale, while (C) shows the NAA peak fitted to the Lorentzian lineshape. The maximum intensities are higher than those plotted in the GUI due to scaling of the intensities by Topspin. The SNR for the NAA peak was 107.8 which is slightly lower than the SNR obtained using the svspipeline and the line width of the NAA peak was 5.37Hz which is slightly higher, compared to the svspipeline results.
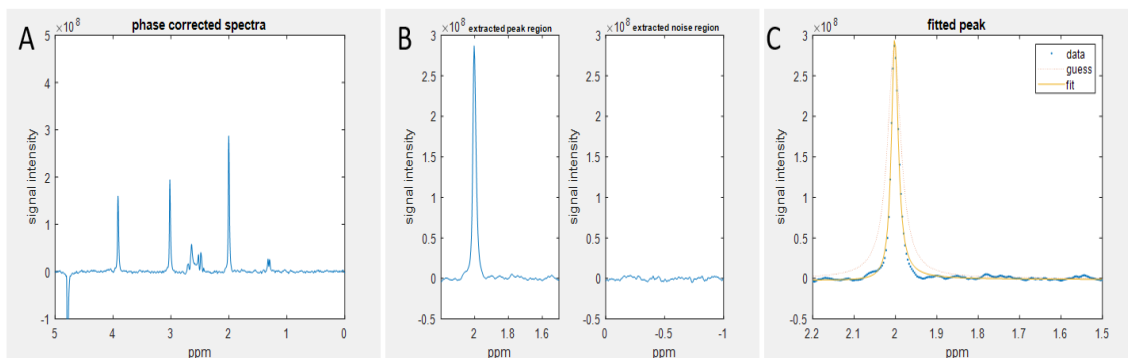
Figure 4.5.8 (A) The imported TOPSPIN processed spectrum from phantom B plotted to ppm scale, (B) The extracted NAA peak and noise regions plotted to the same scale, while (C) Fitted NAA peak to the Lorentzian lineshape.

4.5.7 MRSI phase correction

In this section, we discuss some of the automatic and manual phase correction tools developed during this study using the phase correction algorithm applied on a single voxel spectra. The purpose to develop these tools was to enable the user with fast and easy post processing of complex MRSI datasets. The tools were shown to work well on both phantom and normal brain datasets and sufficient phasing of the spectra was obtained within the selected volume.

2D MRSI produces large amounts of data, and robust automated data-processing schemes to generate metabolite maps are helpful to facilitate spectra interpretation. Algorithms used in practice by many spectroscopy groups process spectra on a voxel by voxel basis to find phase corrections which impose symmetry upon a reference peak in the spectrum and minimize the negative baseline deviations on either side of the peak [99]. Also, to quantify in vivo MRSI data, the variations in the spectral line-shape, peak location, and baseline among the sub-voxels in the MRSI grid need to be accounted for.

A manual MRSI phase correction tool was hence also developed on MATLAB to facilitate the post processing of MRSI datasets for the user. The steps incorporated for the manual phase correction are listed as follows:

1. The 2dseq image file is read in MATLAB script.
2. The parameter file visu_pars are read to record the visu parameters required to read the image.
3. The file acqus is used to read the grpdelay parameter
4. The phase correction values PHC0 and PHC1 are also read from the procs file. Nonetheless, the script will prompt the user to enter a phase value. The applied phase value can be of user's choice or the PHC0/PHC1 values can be used.
5. The phase correction is then applied on the full 32 x32 matrix followed by line broadening using exponential multiplication
6. The phased inner grid 12 x12 spectra are then extracted from the full matrix
7. The grid is then exported to DMPM format text file. This code to export to DMPM was also exclusively developed in this PhD project
8. Also, the phased inner grid can then be used to obtain quantitative results for SNR using maps, mean spectrum, standard deviation and boxplots.

The scripts were first tested with spherical phantom B dataset containing NAA, Cr and Lac using the CSI-PRESS sequence for empirically chosen phase values of PHC0=-10 and PHC1=0 (Figure 4.5.9) where panel (A-F) show the 12x12 manually phase corrected spectra, extracted metabolite peak and noise mean spectrum, mean and standard deviation spectrum, Metabolite SNR map and SNR boxplot respectively. All metabolite peaks were correctly phased and the NAA peaks were extracted correctly. The mean SNR for NAA was found to be equal to 30.95.
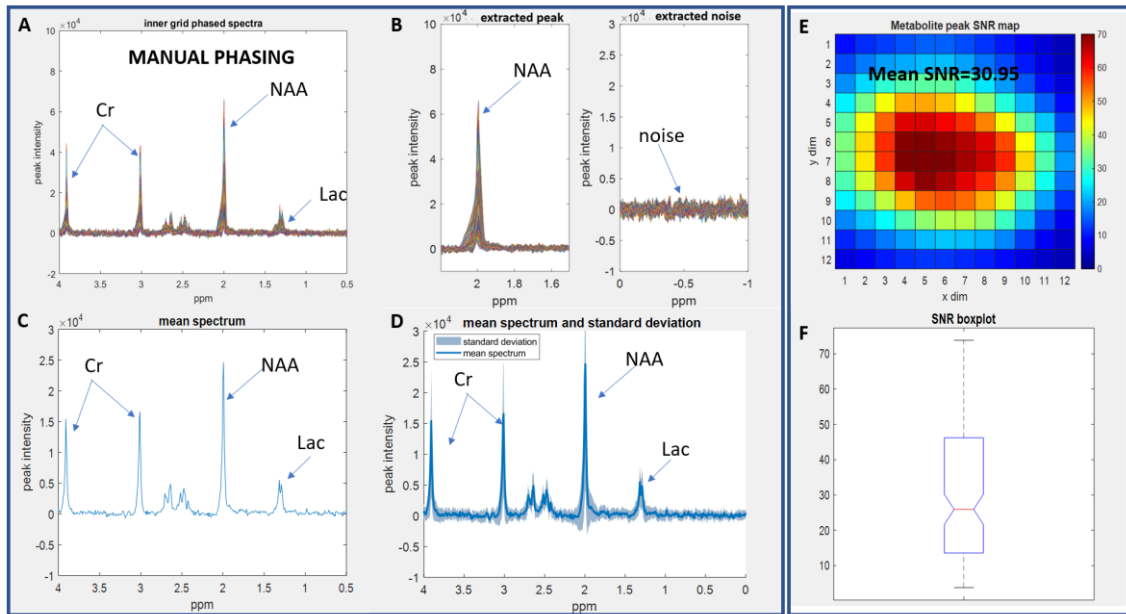
Figure 4.5.9 (A) Manually phase corrected spectra (B) extracted NAA metabolite peak and noise (C) mean spectrum (D) mean and standard deviation (E) Metabolite SNR map (F) SNR boxplot for NAA using a dataset acquired from Phantom B.

The exported data file was read into DMPM software correctly as shown in Figure 4.5.10 which is the DMPM screenshot of the loaded spectra. The spectra in blue are the loaded spectra visually comparable to spectra plotted in Figure 4.5.9 (A) and the spectra in red are the first aligned spectra which by default takes the resonance of the total choline peak (Cho) as reference.
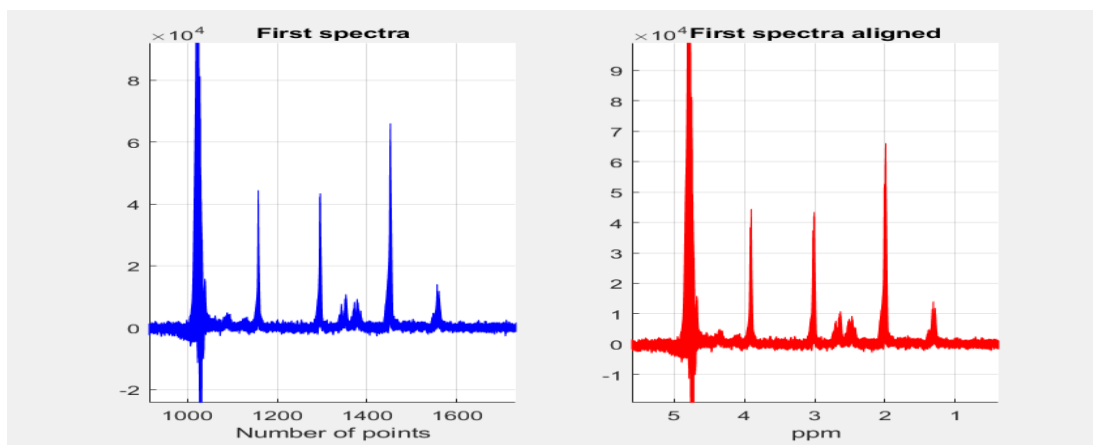
Figure 4.5.10 First and second aligned spectra obtained using DMPM.

Figure 4.5.11 shows the manual phasing results for an in-vivo wt mouse brain dataset acquired with the MRSI-semiLASER sequence. The panel description is the same as in Figure 4.5.9. The NAA peaks at ca. 2.01 ppm are binned forall 144 spectra in the inner grid and displayed. The mean spectrum and standard deviation can also be accurately visualized. The SNR map for the metabolite peaks provides evidence of the homogeneity of the grid and the corresponding mean SNR of the 144 grid elements is displayed. The statistical box plot representation can also be computed with the help of this script.
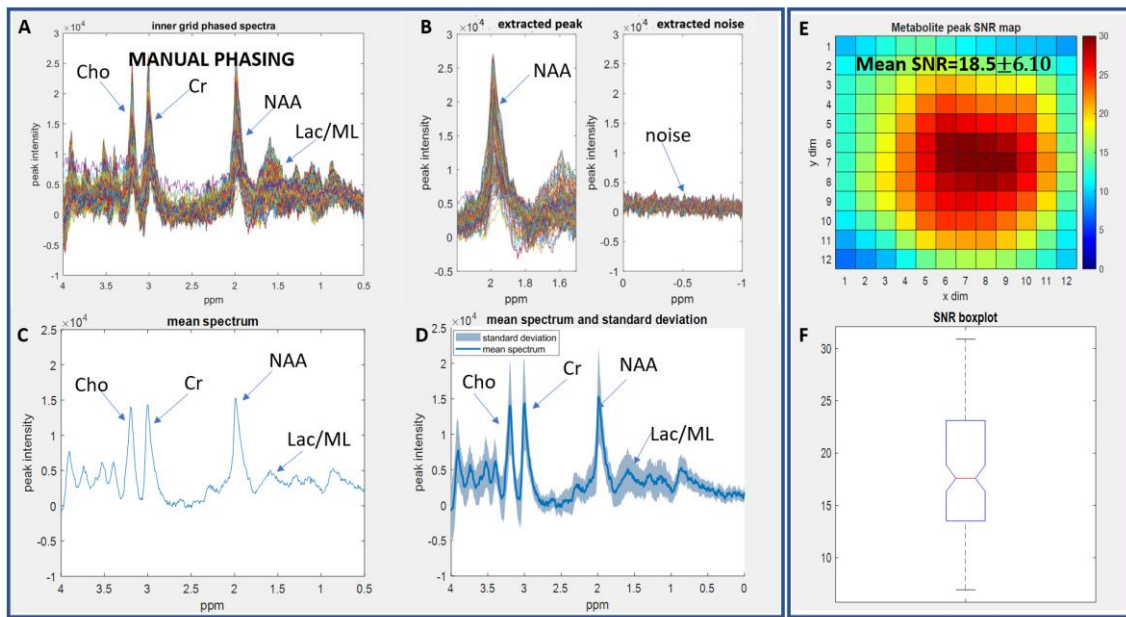
Figure 4.5.11 (A) Manually phase corrected spectra (B) extracted metabolite peak and noise (C) mean spectrum (D) mean and standard deviation (E) Metabolite SNR map (F) SNR boxplot for dataset from in-vivo wt mouse brain.

An alternative approach: Similar to single voxel phase processing, the multi-voxel datasets also contain processed datasets obtained using post-processing with the Bruker macro CSIdash. The phase corrected single spectrum is stored in the folder expno+e2 as a ser file. The 2rr and 2ii files contain the complex valued column intensities of the phase corrected spectrum also stored in procs folder expno+e2. The PCH0 and PCH1 phase coefficients are also saved in the same folder.

The important differences between the Bruker csidash processed file and raw data include;

1. The spectra are zero filled with a factor of 1 to a matrix dimension of 12x12 in the csidash macro.
2. The spectra are intensity scaled according to the NC_proc parameter stored in procs file. This intensity scaling is performed when the spectra is processed in TOPSPIN by the csidash macros.

The scaled intensity column vectors can thus be combined in a complex form using the equation 4.5.7:

$$spec=real\_spec+1i*imag\_spec \qquad [4.5.7]$$

where real_spec=2rr and imag_spec=2ii

and the inner grid consisting of 12x12 matrix i.e. 144 spectra (spec3) is then extracted from the data set:

$$spec2=reshape(spec,[2048\ 32\ 32]) \qquad [4.5.8]$$

$$spec3=spec2(:,11:22,11:22) \qquad [4.5.9]$$

The inner grid spectra can then be directly exported to DMPM and used to obtain quantitation results without any further processing. The phantom results obtained with this script are shown in Figure 4.5.12 where A contains the TopSpin phase corrected spectra, B extracted metabolite peak and noise, C mean spectrum, D mean and standard deviation, E Metabolite SNR map and F SNR boxplot. The mean SNR for the NAA peak recorded using this method was 33.88 which is higher than the SNR calculated using the manual phasing. The results for the exported text file to DMPM are shown in Figure 4.5.13.

,
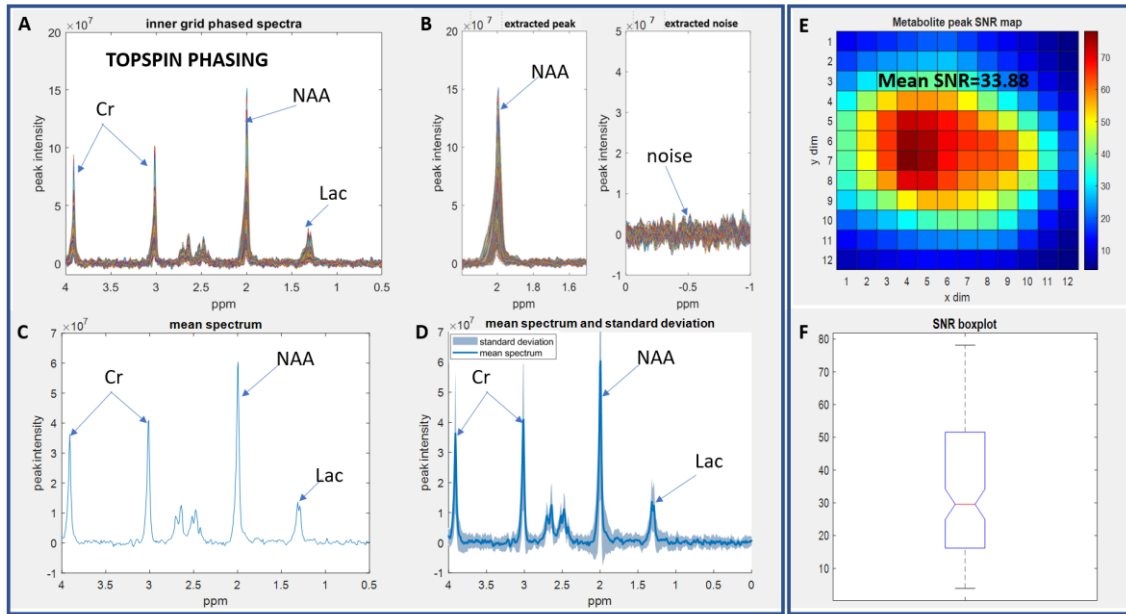
Figure 4.5.12 (A) TopSpin phase corrected imported spectra from phsntom B (B) extracted NAA metabolite peak and noise (C) mean spectrum, (D) mean and standard deviation (E) NAA metabolite SNR map (F) SNR boxplot using the same dataset as already shown in Figure 4.5.9.
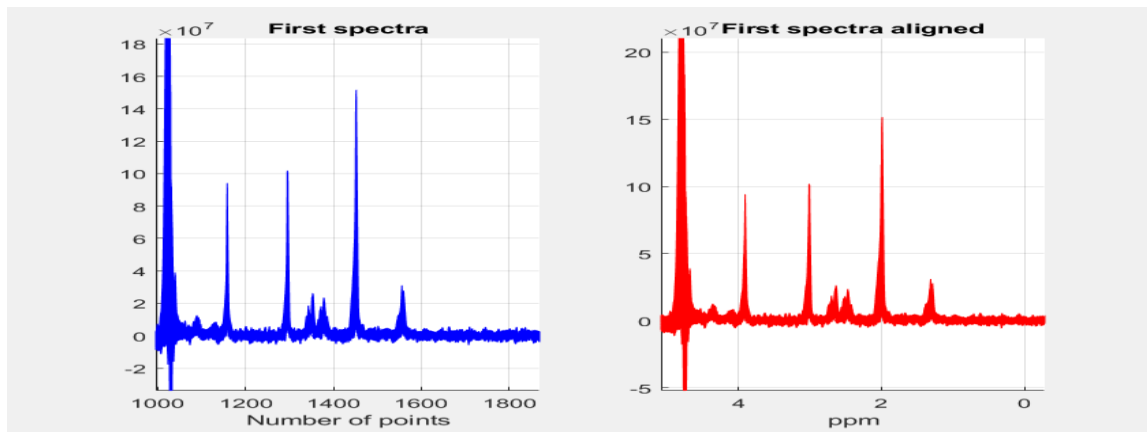
Figure 4.5.13 First and second aligned spectra obtained using DMPM.

Similar to manual phasing , the in-vivo data set was also tested using the TopSpin phasing script. The results of an in vivo dataset acquired using the MRSI-semiLASER sequence in wt mouse are given in Figure 4.5.14 where panel (A) shows the TopSpin phase corrected spectra, panel (B) shows the extracted metabolite peak and noise, panel (C) shows the mean spectrum , panel (D) shows the mean and standard deviation, panel (E) shows the NAA metabolite SNR map and

panel (F) shows the SNR boxplot. The mean SNR for NAA was recorded as 23.48 which was also higher than with the manual phasing because of intensity scaling, which improves the SNR.
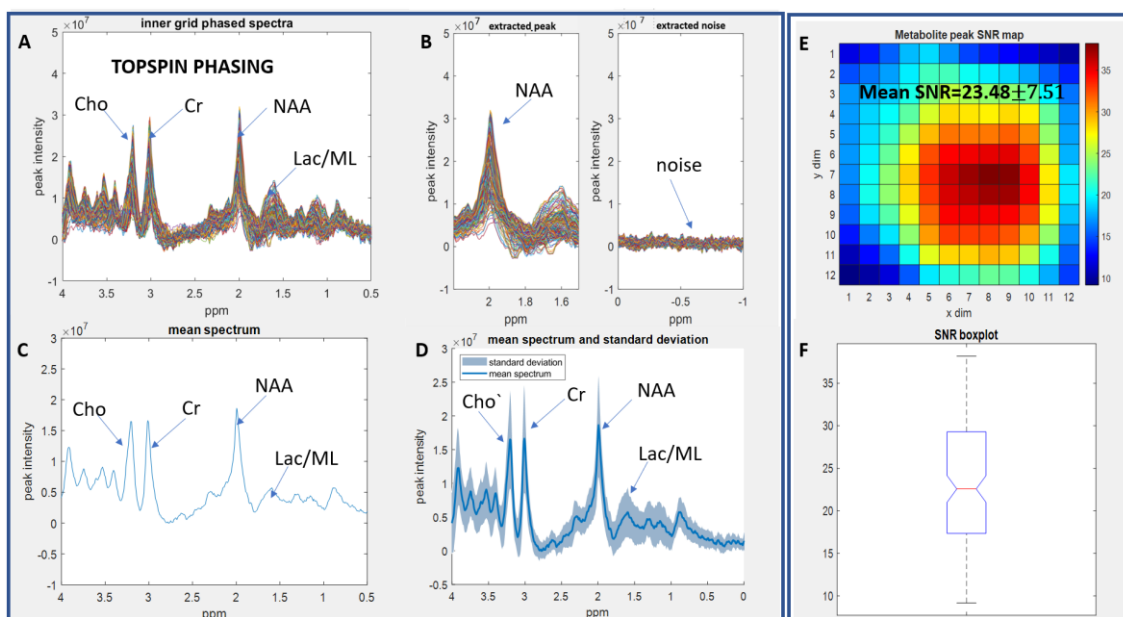
Figure 4.5.14 (A) TopSpin phase corrected spectra for a wt mouse (B) NAA extracted metabolite peak and noise (C) mean spectrum (D) mean and standard deviation (E) NAA metabolite SNR map (F) SNR boxplot.

4.5.8   Proposed pipeline to reduce post-processing time

In a further effort to improve the current post processing pipeline used by our group in the mouse brain diagnostic studies, an alternate pipeline was proposed, aiming to reduce the overall processing time and hence speed up the entire process in a reproducible manner. Additionally, the aim was to develop an alternative to the 3DiCSI software provided by Qi Zhao at Columbia University which is unmaintained and posed several problems with data acquired with later versions of ParaVision 5.1.

Figure 4.5.15 shows the work flow of the current and proposed post processing pipeline. In the current processing protocol, (bottom) the raw data (2dseq) file is taken from the CSI DASH macro resulting files and all the steps such as line broadening and phase correction had to be repeated by the user in the 3DiCSI software before exporting the inner grid voxels as text file readable by DMPM. The data processed by the CSIDASH macro was only used on-site for visual inspection at acquisition time and hence not utilized later on for data analysis resulting in additional time being consumed in repeating the needed steps.

The proposed pipeline (top) consists of a MATLAB script developed to directly read the processed data from the Bruker CSIDASH macro. The 2rr/2ii files contain the complex intensities. The phase correction and Line broadening (LB) values are stored in the procs file of the same folder. Using this processed dataset, the MATLAB script exports the dataset to a DMPM readable format text file. The proposed pipeline hence reduces the overall required postprocessing time.

An additional benefit of using the 2rr/2ii files is that intensity scaling increases the intensity range for display purposes and hence the spectra can be visualized better. Also, the averaging combined with scaling helps in increasing the SNR [100]. The difference in SNR was already visualized between the manual and pre-defined phase corrected results. This was also suggested in [91] to be used as an essential post processing step. The scaling also removes the bias created from highly concentrated values which can make a small number of metabolites dominate the outcomes for statistical analysis and hence makes those analysis more reliable.
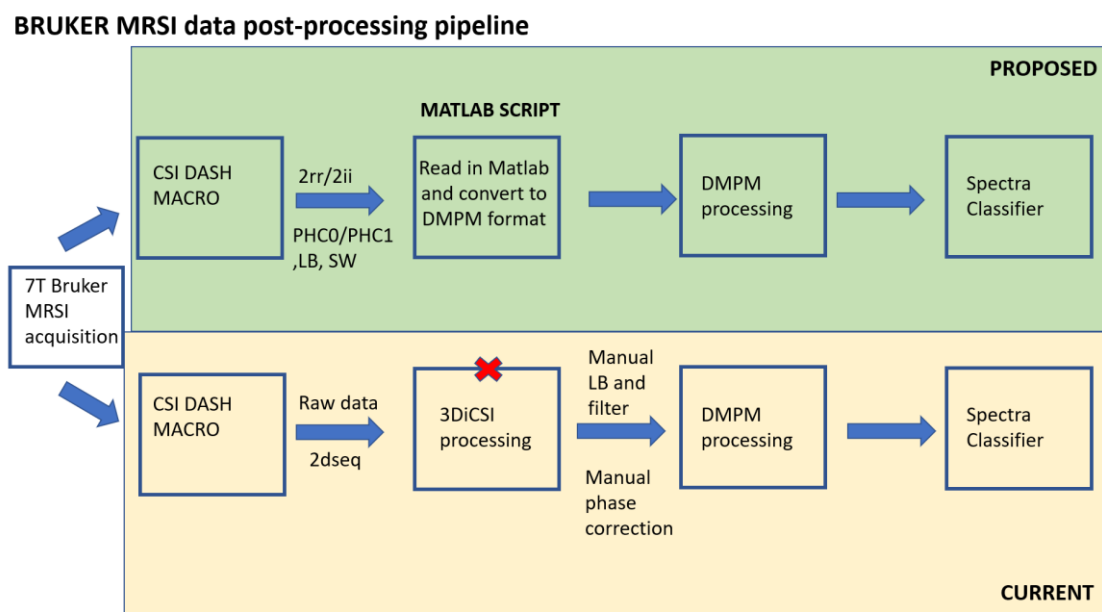
Figure 4.5.15 MRSI post processing current and proposed data processing pipelines.

4.5.9   Discussion and Conclusions

Phasing NMR spectra is extremely important to precondition the data for further numerical analysis such as the Spectraclassifier-related strategies. Manual and TopSpin phasing approaches have been discussed and their results were compared for both single and multi-voxel datasets. For single voxel datasets, both scripts work well providing comparable results. For MRSI datasets, the manual phasing script has the advantage that it uses raw 2dseq file and hence can be post processed anytime even away from the scanner. It also gives more freedom to the user to manually phase correct. The disadvantages of this script include longer processing time, lower SNR and requiring a proficient user. On the contrary, the Topspin phasing script does not require repetitive processing of the data and hence is more efficient in terms of total processing time required. The disadvantage of this method is the requirement of pre-processed data in Topspin. The proposed pipeline using the Topspin phased MATLAB script in place of the 3DiCSI software can act as an useful alternative for MRSI data post-processing.

Several algorithms for automated phase correction of NMR spectra have already been published in literature such as entropy minimization based phase correction discussed by Chen et al. in

[92]. In the FID-A routine , Near et al. [95] have presented MATLAB based phase correction routines for 1D NMR spectra . Deep learning based methods are also currently in the market for automated phase and baseline correction of MRS spectra [101]. To the best of our knowledge, phase correction routines for Bruker MRSI in-vivo datasets are less readily available and hence we contributed towards development of MATLAB based scripts which proved to be fundamental for the data analysis done during this PhD project.

4.6   NMR-SCOPE B simulations

In this section, we describe the NMR-SCOPE B simulation results obtained from the INSPiRE-MED associated secondment which took place at the Department of Magnetic Resonance and Cryogenics, Institute of Scientific Instruments of the Czech Academy of Sciences, under the supervision of Dr Zenon Starčuk and Dr Jana Starčukova in Brno (Czech Republic) from 9th to 21st October 2022, and associated virtual supervision-related work. The goal of this secondment was to understand the intrincacies of the NMRScopeB plugin to jMRUI use. This plug-in contains functions to support the development of methods for MR spectroscopic imaging. Under the guidance of Dr Zenon Starčuk, the simulations on NMRSCOPE-B for spin echo pulse sequences such as PRESS and semiLASER sequences was accomplished. The sequence simulations were also tested for test situations such as unbalanced crushers, delay changes etc.

4.6.1 Introduction to NMRSCOPE-B (jMRUI plug-in)

NMRScopeB version 2.0 is a plugin of the program jMRUI version 6.0 (discussed in chapter 3) (http://www.jmrui.eu/) and is accessible either from the jMRUI wizard or from the jMRUI's menu item "Custom" by selecting the item "NMRScopeB". This plugin provides the useful functionality for the simulation of coupled spin systems during the NMR experiment and can be also used for simulation of metabolites basis sets. In the simulation, such properties as chemical shifts, spin-spin coupling, relaxation, spatial and/or spectral excitation selectivity, and customized pulse sequences are accounted for. The primary target was to support the simulation of metabolite FIDs in biomedical MR spectroscopy, as needed for spectroscopic quantitation, but many functions are meant to support the development of methods for MR spectroscopic imaging [102].

The NMRSCOPE-B contains a dedicated panel, shown in Figure 4.6.1 where the user defines the pulse sequence that describes the way the spectrometer controls the evolution of the spin system(s) which are predefined in the Physics panel. The simulation is started by one of the Launch buttons present in this panel. The pulse sequence can be either loaded from a .nsq file and modified as needed, or designed from scratch, or loaded with a protocol. Any modified sequence can be saved for further use in a new .nsq file, and visualized by clicking the "Draw Sequence" button.
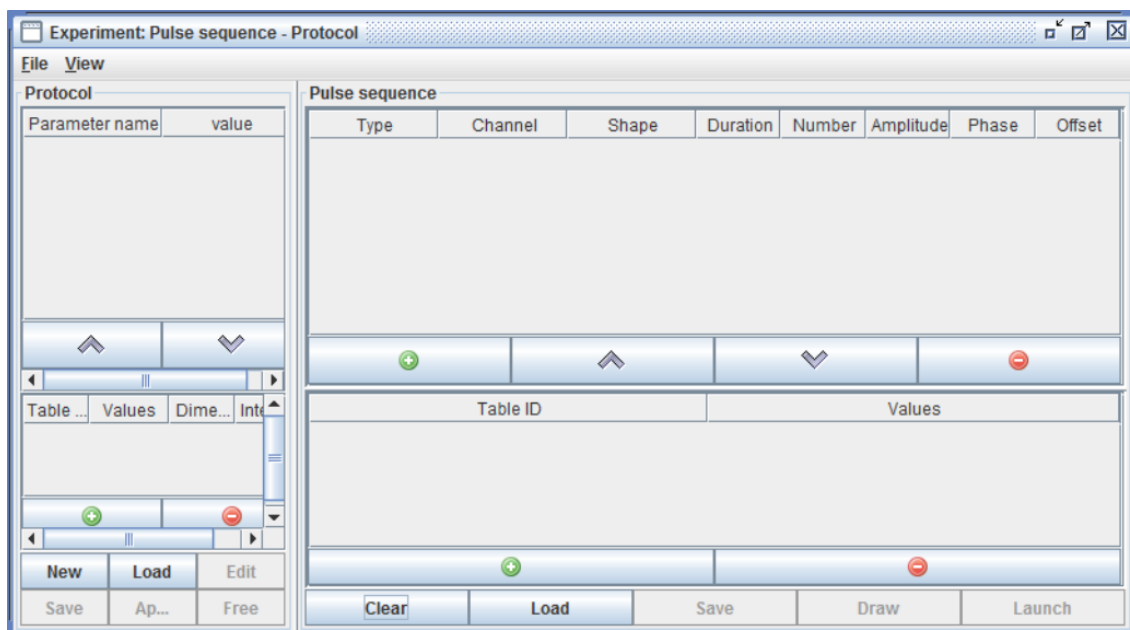
Figure 4.6.1 Pulse sequence protocol panel for NMRSCOPE B v2.

4.6.2 SV-PRESS sequence simulation

The sequence simulation was obtained through the predefined protocol (MEGA-)PRESS as pattern for own pulse sequence development. The new PRESS was hence derived from an existing protocol by removing the MEGA pulses and inserting time delays and pulses. Besides phase cycling, an efficient task-adjustable coherence-transfer-pathway selection mechanism is ensured by Fourier-based implementation of crushers. The results can be exported to MATLAB.

Figure 4.6.2 shows the Bruker PRESS pulse sequence simulated using NMRSCOPE B. The sequence consists of a 90° Hermite excitation pulse, pulse length (Tp)= 700 ms and two 180 ° Hermite refocussing pulses (Tp) = 700 ms shown in the bottom panel entitled 1H_re/im. The RF pulses were accompanied by slice-selective gradients in the top panel where gx (red) is the slice selective gradient in the x direction along the excitation pulse. The compensation / rephasing part of gx is also shown in red in the opposite direction to gx. The y and z gradients i.e. gy (green) and gz (blue) accompany the refocusing pulses.

The trick panel shows the crusher pairs used in this simulation. The crusher pairs are simulated as trick operations and model a perfect crusher pair under a perfectly homogenous B1 field. The trick observation is a simple and theoretically perfect model substitute for an event that would be impractical to be modelled in a regular way, such as setting the spin system to the Boltzmann equilibrium – full relaxation (Init_M), or the performance of an ideal crusher – irreversible zeroing all coherences except populations (Null_Mxy), or full saturation – all magnetization components set to zero (Null_Mz & Null_Mxy) [102].

The spectrum was simulated for water and three metabolites namely, N-Acetyl Aspartate, Creatine and Lactate with concentrations matching those contained in the spherical phantom A. The RF pulses were chosen the same as in the Bruker PRESS sequence which consists of a Hermite excitation pulse with Bandwidth 7714 Hz and 90° flip angle and two Hermite refocusing pulses of 4885 Hz Bandwidth and 180° flip angle. The acquisition parameters were set as follows: TE =

15.7ms, TR = 2500ms, Voxel = 3(mm)^3 for a spherical phantom distribution. Figure 4.6.3 shows the simulated spectrum for the Bruker Press sequence. The localized peaks include Lac (CH$_3$) at 1.3 ppm and (αCH) at 4.1 ppm, NAA CH$_3$ peak at 2.01 ppm, βCH$_2$ at 2.48 ppm+2.67 ppm, αCH at 4.47 ppm, Creatine CH$_3$ at 3.03 ppm, CH$_2$ at 3.9ppm, and water at 4.7ppm.
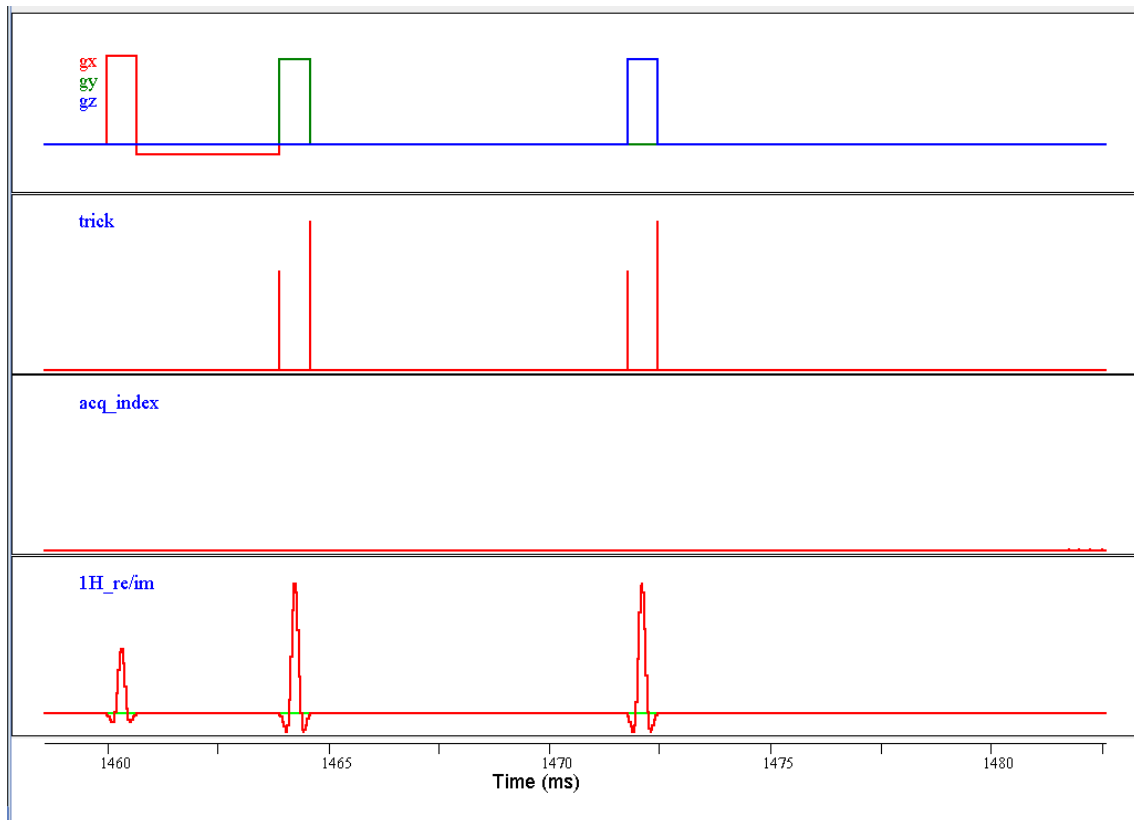
Figure 4.6.2 Simulated Bruker SV-PRESS pulse sequence.
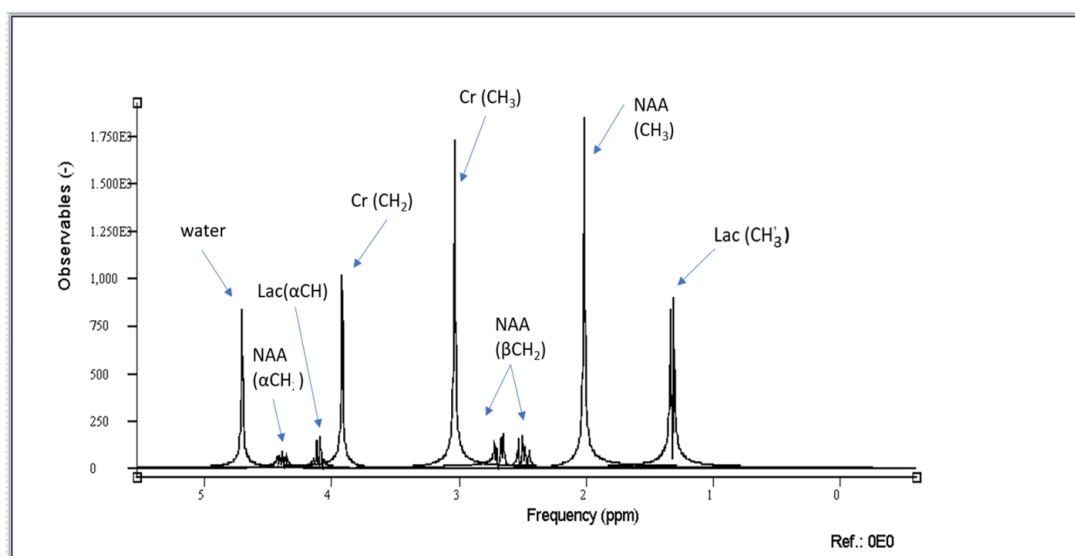
Figure 4.6.3 Single voxel PRESS spectra from simulated Bruker PRESS sequence localized peaks including Lac (CH₃) at 1.3 ppm and (αCH) 4.1 ppm, NAA CH₃ peak at 2.01 ppm, 6CH₂ at 2.48 ppm+2.67 ppm, αCH at 4.47 ppm, Creatine CH₃ at 3.03ppm and CH₂ at 3.9 ppm and water at 4.7 ppm.

4.6.3 SV-semiLASER sequence simulation

The semiLASER sequence already implemented in NMR-SCOPE B was modified according to our implementation of the SV-semiLASER sequence on the 7T Bruker scanner as already described in section 4.3. . To do so, the program codes were modified by introducing user defined delay intervals, D1, D2, D3 ,D4 and D5 to set the delay values manually. The delay intervals were chosen such that the relationships D2=D3 and D1+D3+D4 = D2+D5 were maintained. The values of the intervals were kept as D1 = 1003 ms, D2 = 1368 ms, D3 = 1368 ms, D4 = 2498 ms and D5 = 1519 ms. Figure 4.6.4 shows the simulated SV-semiLASER sequence.

The sequence, similar to what was done for the simulation of the PRESS spectrum, was simulated for water and three metabolites, namely, N-Acetyl Aspartate, Creatine and Lactate, contained in a spherical phantom. The RF pulses chosen were kept the same as the SV-semiLASER V1 sequence which uses the Hermite excitation pulse with Bandwidth 7714 Hz and 90° flip angle and four hyperbolic secant (sech) adiabatic refocusing pulses of 9003 Hz Bandwidth each, and 180° flip angle. The acquisition parameters were set as follows: TE = 15.7 ms, TR = 2500 ms, Voxel = 3(mm)³, Hermite excitation pulse, pulse length (Tp)= 700 ms, flip angle (FA) = 90° , hyperbolic secant refocussing pulses (Tp) = 2000ms, FA = 180°, Npoints = 4096, SW_Hz = 4000 Hz. Figure 4.6.5 shows the simulated spectrum for the SV-semiLASER sequence. The localized peaks include Lac (CH₃) at 1.3 ppm and (αCH) 4.1ppm, NAA CH₃ peak at 2.01 ppm, βCH₂ at 2.48 ppm+2.67 ppm and αCH at 4.47 ppm, and Creatine CH₃ at 3.03 ppm and CH₂ at 3.9 ppm, and water at 4.7 ppm. The semiLASER spectrum was similar to the PRESS simulated spectrum but the metabolite peaks showed higher intensity by visual inspection indicating an increase in SNR, as already demonstrated by our real acquisition experiments.
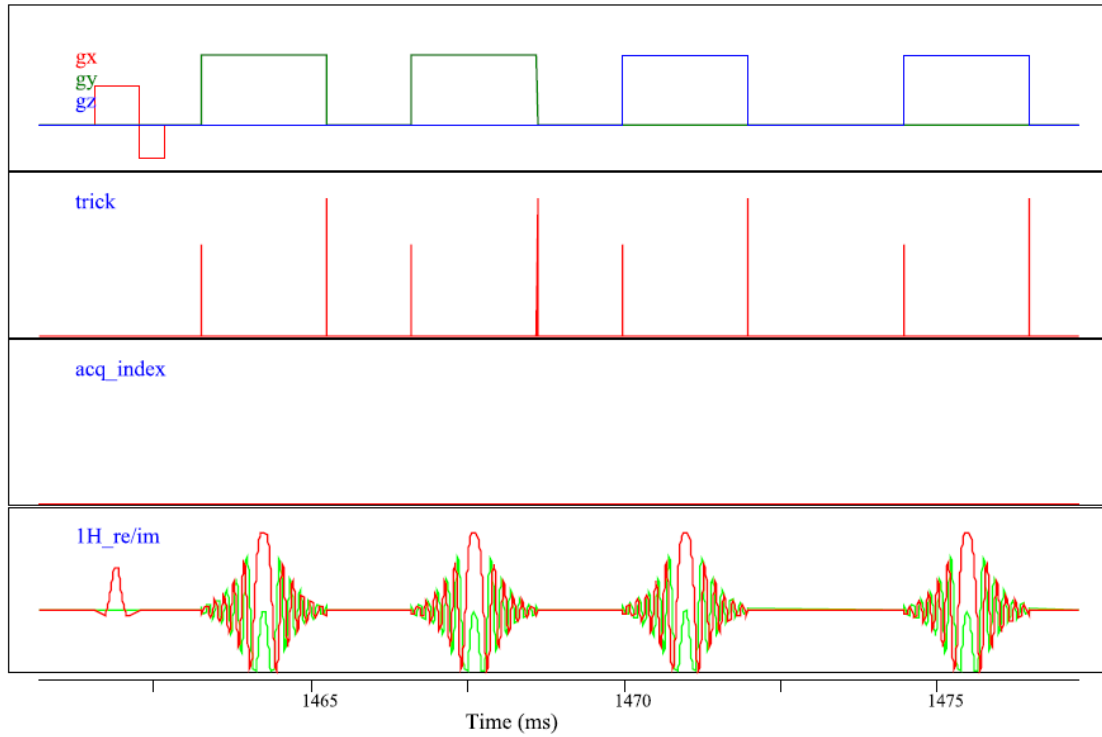
Figure 4.6.4 SV-semiLASER simulated pulse sequence.

.
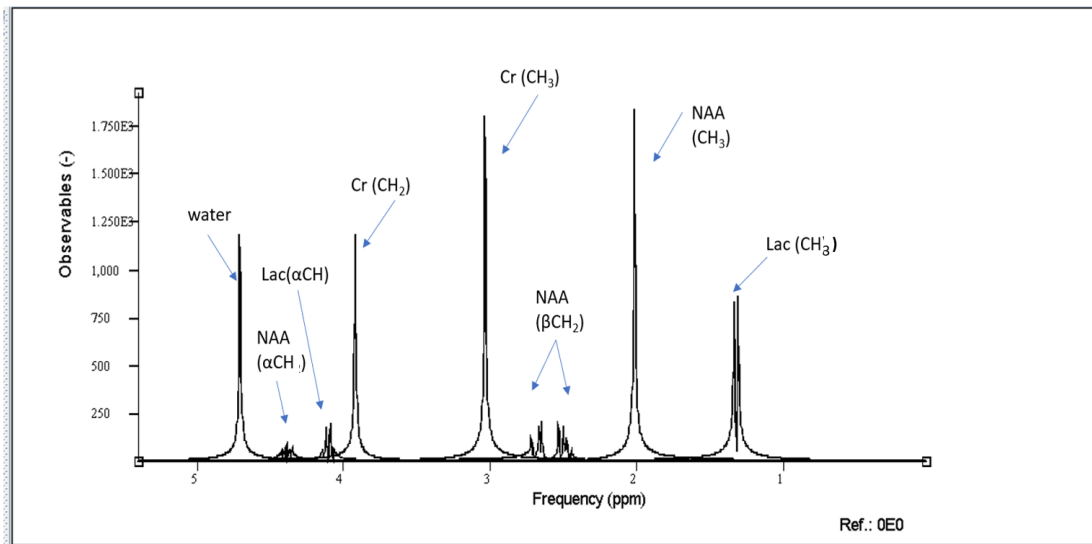
Figure 4.6.5 Single voxel spectra simulated using the SV-semiLASER sequence for the metabolites Lac (CH₃) at 1.3 ppm and (αCH) 4.1ppm, NAA CH₃ peak at 2.01ppm, βCH2 at 2.48ppm+2.67 ppm and αCH at 4.47ppm and Phosphocreatine CH3 at 3.03 ppm and CH₂ at 3.9 ppm and water at 4.7 ppm.

169

4.6.4 Simulating the effects of unbalanced delays and gradients

The goal of this task was to assess how sensitive was the pulse sequence to mismatched delays causing the spin echo condition (described in section 4.3) for the semiLASER sequence to fail. We expected to see a small difference, in the order of 5% to 10%, affecting only one of the tau intervals. However, J-coupling is identical in the spectral coverage band and at the iso-center, all magnetization is rotated identically. Also, the simulated pulse profiles are perfect. Hence small changes in delay interval did not affect the spectra, even marginally. However, introducing a large change in the delay values was different, for instance in the example shown in figure 4.6.6 (A) the D1 delay was increased from 1003 ms to 5000 ms in the modified semiLASER pulse sequence. This change violated the spin echo condition and hence all resonances did not appear equally affected, for instance the Cr peak at 3.01 ppm was suppressed but visible at 3.9ppm (Figure 4.6.6 (B)). The encircled resonances between 2 ppm and 3 ppm (red oval) could not be identified correctly due to the violation of the spin echo condition and reduced peak intensities.
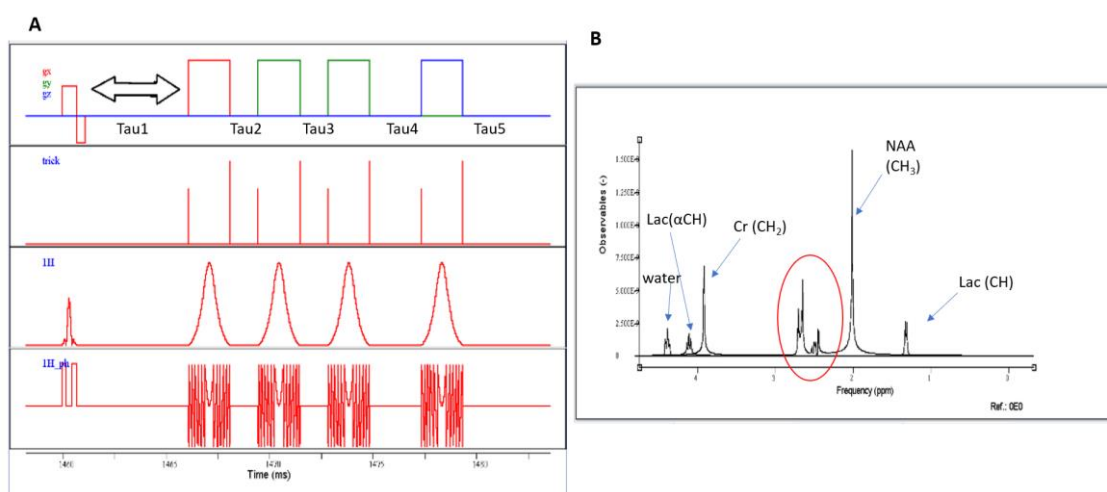
Figure 4.6.6 (A) Simulated semiLASER pulse sequence with the TAU1 interval increased to violate the spin echo condition (B) The resulting semiLASER simulated spectrum showing distorted profiles (red oval). The relationship between signal intensities was not maintained and the resonance at 3.01 ppm disappeared.

When the gradient between the refocusing pulses p3 and p4 were not balanced at the end of the p3pulse, the spin phases become more or less randomly distributed. In such a situation, spins with opposite phases cancel each other out, so the measured signal is smaller than in the case of coherent motion [103]. To visualize these effects of signal attenuation, the delay duration for the z gradient was reduced for p4 and p5 using the modified SV-semiLASER pulse sequence, encircled (black ovals) in Figure 4.6.7 (A), hence creating a mismatch between the delay duration of refocusing pulses. Introducing this change lead to partial suppression of some resonances such as the NAA (CH$_3$) peak and Lac (CH$_3$) shown in (Figure 4.6.7(B)).
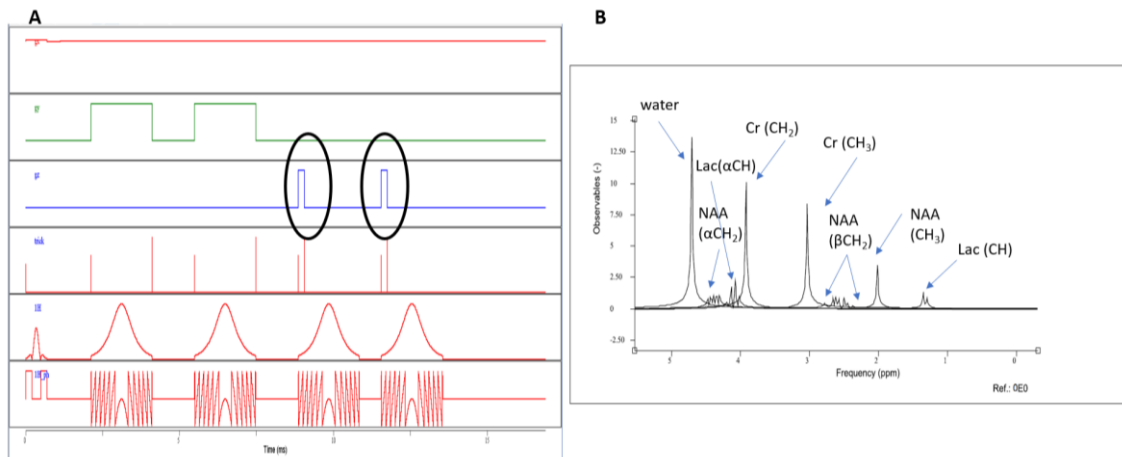
Figure 4.6.7 (A)Simulated semiLASER spectrum showing unbalanced gradients (B) Resulting semiLASER simulated spectrum after gradient imbalance.

4.6.5 CONCLUSIONS

The NMRSCOPE B serves as an efficient tool to predict the behaviour of implemented sequences and also to check test conditions and recognize the behaviour of the signals based on spin system physics. The simulated single voxel results for PRESS and semiLASER sequences and the test conditions were consistent with our findings using the Bruker Biospec 7T scanner. In future, further work can be done to develop MRSI sequences which currently do not exist with the NMRSCOPE -B simulator as an evaluation prior step before real bench lab work.

Chapter 5: General Discussion

5.1 Applications of SV-semiLASER in phantom studies and in-vivo in wt mouse

The main finding of this PhD work has been that the SV-semiLASER sequence is a powerful tool for studying brain metabolic changes and has a great potential in preclinical research on Bruker systems equipped with Paravision 5.1 software. This claim was supported by our actual experiments performed using the implemented SV-semiLASER sequence first in benchmarking in vitro tests and later on for in-vivo applications. The spectral patterns obtained were found to be similar to PRESS spectra and on several occasions better resolved than the normal PRESS spectra. The sequence produced best performance at an optimal short echo time (TE = 20ms). The overall 1.3-fold-1.4-fold improvement in SNR in phantoms and 1.2-fold-1.3-fold improvement in SNR for in-vivo mouse subjects provided by the SV-semiLASER sequence in comparison to the stock Bruker PRESS sequence is an added advantage of the developed SV-semiLASER sequence, since it may allow to decrease the number of accumulations and also reduced voxel volumes as compared to SV-PRESS. Furthermore, our findings were also consistent with previous reports of improved SNR and spectral quality with semiLASER.

The use of adiabatic refocusing pulses for improved MRSI has already been established and several authors have used different types of adiabatic pulses such as Shinnar-Le Roux to demonstrate better refocusing performance in clinical settings [104]. Furthermore, Landheer et al, [29] have shown the clinical utility of an implemented single voxel semi-LASER sequence that is capable of acquiring artefact-free data with an echo time (TE) of 20.1 ms on a standard clinical 3T scanner. The sequence was proven to obtain high quality spectra when evaluated with Cramer Rao Lower Bounds (CRLBs) in relation to individual resonances. In our SV-semiLASER implementation we have targeted the pre-clinical utility of this sequence and have reached a minimum echo time (TE) of 15.7ms which in the best of our knowledge is the lowest possible echo time achieved. Landheer et al, used 20 kHz bandwidth Gradient offset independent adiabatic (GOIA) pulses for refocusing in their implemented sequence while we have utilised the hyperbolic secant (sech) pulses for our SV-semiLASER implementation. The GOIA pulses are suitable for clincal usage since they provide very precise spatial localization whereas for our preclinical implementation, the sech pulses proved to be adequate. Landheer et al have also reported the increase in SNR in terms of reduced Cramér-Rao lower bound(CRLB's) whereas in our experiments, we have presented a direct evaluation of the SNR improvement using the implemented SV-semiLASER sequence compared to stock Bruker PRESS sequence.

In the future, our implementation of the SV-semiLASER may be further optimised by introducing phase cycling schemes similar to what was used in [29] to avoid the formation of spurious artefacts that may be visible in the acquired spectra at minimum echo time.

5.2 Application of MRSI-semiLASER in phantom studies and in-vivo in wt mouse

We observed increased SNR in all phantom and in-vivo wt mouse studies for the implemented MRSI-semiLASER sequence. The SNR maps obtained using the MRSI-semiLASER for different metabolites such as NAA were also visually more homogeneous than the maps for the stock CSI-PRESS sequence as a result of better excitation profile of the adiabatic refocusing pulses and the reduction in chemical shift displacement errors. With sharp selection profiles and a small CSDE,

voxels closer to the edge of the VOI are suitable for the evaluation, which does not stand true in the case of CSI-PRESS. Furthermore, the relative insensitivity to B1 inhomogeneities offered by the adiabatic refocusing pulses is an additional advantage when using the MRSI-semiLASER technique as a substitute to the conventional CSI-PRESS sequence.

Weiss et al [105] have also implemented the semi LASER CSI sequence and compared it with a standard PRESS CSI sequence at high magnetic field (17.6T) with in-vivo application on post-natal wt mouse brain. They reported the implemented semiLASER CSI using weighted k-space averaging as providing high quality spectra and improved spectral profiles as well as reduction in the CSDE and improved quantification of metabolite concentrations. Our application of the implemented MRSI-semiLASER sequence on wt mouse and GB mouse brain tumors studies is in agreement with [88] as we have also demonstrated the reduction in CSDE as well as higher spatial resolution and improved spectral profiles. Apart from that, and at a difference from [88] the CSDE values were much smaller for our implementation owing to the differences in the Magnetic Field. The authors have implemented their work on the older Paravision 4.0 version and the modified sequence was not made available. In our implementation, we have quantitatively compared the SNR as the main performance metric to demonstrate the differences between the implemented MRSI-semiLASER and CSI-PRESS sequences. Furthermore, we have employed the elliptical k-space acquisition strategy and compared its performance with other acquisition strategies. Our sequences will also be made available to interested research groups. Despite its well established utility and results in clinical applications, there remains a huge gap in the preclinical recognition of the semi-LASER sequences. We anticipate that the semiLASER sequences will be made available by major preclinical scanner vendors in future releases of spectroscopy packages. Hence, our results, set the grounds for a wider application of MRSI-semiLASER in preclinical settings.

5.3 Application of SV-semiLASER and MRSI-semiLASER on GB mouse brain bearing tumor monitoring

The SV-semiLASER sequence provided adequate performance in studies involving Tumor tissue and an SNR increase of ca. 1.1-fold over stock CSI-PRESS was recorded in the spectra obtained. Moreover, the metabolite peaks were better resolved and less affected by tumor inhomogeneities. The MRSI-semiLASER sequence can provide better insight into the tumor arquitecture by producing high quality and SNR multi-voxel datasets. In multi-slice acquisitions, the ability to cover the same tumor volume while reducing the partial volume effects, the higher signal-to-noise ratio (SNR) of the MRSI-semiLASER sequence, when compared to the conventional CSI-PRESS, can be used to achieve a higher resolution by reducing the slice thickness from 1mm to 0.8mm. This approach of achieving higher resolution resulted in narrower water peak widths at half height in spectra acquired at 0.8 mm indicating better B_0 homogeneity in thinner slices, which produces narrower and more intense metabolite peaks with SNR larger than predicted based on sampled volume differences.

The spectral pattern evaluation approach for GB tumors, previously developed by our group [44] [83], did not always characterize the spectra acquired using the MRSI-semiLASER correctly, which led to the inconsistent calculation of nosological images and the corresponding TRI. The difference in echo time and baseline noise could be contributing factors which differentiate the MRSI-semiLASER spectra with respect to the training sources used in the Spectraclassifier algorithm. It was hence our deduction that the already available classifier might require to be

retrained using spectra acquired from both the MRSI-semiLASER and CSI-PRESS sequences, in future work.

5.4 Weighted or Elliptical phase encoding?

In the elliptical phase encoding, where corners of k-space are skipped, a higher number of phase encoding steps in each direction can be acquired within the same acquisition time, as compared to standard or weighted acquisition. This causes broadening of the spatial response function but also increases the SNR. In case equal resolution is not intended, the number of phase encoding steps can be reduced, which will in turn reduce the overall scan time of the acquisition and hence can provide faster acquisitions.

The weighted mode has been used by default in our previous studies because of its known improved PSF as compared to standard or elliptical acquisition modes. Nonetheless, the results produced in this work have shown that the elliptical acquisition provided good quality spectra with no apparent artefactual signals and a 16.7 % SNR gain with respect to weighted acquisitions.

5.5 Limitations and challenges of programming on ParaVision 5.1 and multi-site implementations using ParaVision versions 6.1 and 7

Implementation of the semiLASER sequence in the older Bruker software version i.e. ParaVision 5.1 has been a limiting factor and very time-consuming in this PhD project. The programming routine requires frequent logging in and logging out of the software for changes implemented in the method files to take effect. Also, the ParaVision 5.1 does not contain built-in blocks for the adiabatic refocusing pulses which needs to be generated separately. The software support for ParaVision by Bruker is also limited only to version 7 and 360 and above. Hence, the vendor support available was also a limiting factor.

We also experienced the translations of the implemented sequences from the ParaVision 5.1 to ParaVision 6.1 to be very tedious and many parameter definitions needed to be revised. This trouble was faced while implementing the single voxel and multi-voxel semiLASER sequences on the 7T hybrid PET-MR scanner at MoSAIC, KU Leuven during one of the INSPIRE-MED project secondments. However, the sequence written in ParaVision 6.1 could be fairly easily adapted to latest versions such as ParaVision 7 after slight modifications in the make file and others.

It is worth mentioning that the performance of the semiLASER sequence can depend on factors such as the magnetic field strength, gradient strength, and RF pulse characteristics of the scanner. Therefore, it is important to consult with the system requirements to ensure optimal performance and data quality using the implemented sequences.

Although the implemented sequences have been optimized for mouse brain tumor studies, because it is the research focus in our group, these sequences are now available at the SeRMN and will be made publicly available upon publication of the work done, so that other research group studying metabolic brain disorders may benefit from them in the future.

5.6 Future Work

MR systems are improving day by day and new techniques for acquisition, post-processing and quantification are continuously emerging. Nevertheless, the new technology and updates have the attached requirements of cost, maintenance and trained staff. Nevertheless, there exists a pressing need to combine new strategies with the older installations to improve the results

without having to purchase expensive hardware upgrades. The solutions provided in this work can benefit the older installations.

The proposed pipeline may help in reducing the overall post processing time by avoiding redundancy of steps and automatic data conversion into the required format. The manual and automatic phase correction tools will help the user for easy post processing of the acquired datasets as well as providing results for quantitative analysis. These produced tools can be further developed and integrated with our group existing pipelines.

For the generation of Nosological images using the MRSI-semiLASER datasets, the spectra classifier was found to be robust. However, the differences in echo time and baseline of the spectra acquired using the two sequences are parameters that can influence the classification predictions by machine learning tools. The spectra classifier hence may require some retraining by spectral data from both the MRSI-semiLASER and the CSI-PRESS sequences. This is an on-going project in the group.

We did not implement and test simulations for the multi-voxel sequence with the NMR-SCOPE B due to shortage of time and extensive CPU memory requirements. One possible future task could be the implementation of multi-voxel semiLASER sequence using NMR-SCOPE B on a GPU accelerated system and visualize the effects of chemical shift displacement an others on the simulated spectra.

Chapter 6: Conclusions

I. The PRESS_Slice implementation performed as part of the learning process during the PhD work has been shown to be a reliable and accurate method for slice localized spectroscopy, providing reproducible results, and could be used for educational purposes. The PRESS_Slice method exhibited accurate slice selection and the results were evaluated using signal-to-noise ratio (SNR) and Lineshape comparisons. As expected, the SNR increased linearly with the increase in slice thickness.

II. A successful implementation of a SV-semiLASER data acquisition sequence with a 1.3-fold-1.4-fold improvement in SNR in phantoms and 1.2-fold-1.3-fold improvement in SNR of in-vivo animals subjects, in comparison to the stock Bruker PRESS sequence, was achieved.

III. The increased SNR offered by our SV-semiLASER implementation opens the doors to new possibilities in studies of mouse brain diseases such as reduction in voxel size and hence minimization of partial volume effects while maintaining sufficient SNR. The higher SNR can also help reducing the overall scan time of the experiment by acquiring a smaller number of accumulations (averages per scan) and preserving acquisition quality. The reduction in scan time could be a major game changer in overcoming the inherent long scan time limitations of MRS studies. This SV-semiLASER sequence could provide added value in pre-clinical diagnostics and research and substantially increase the data quality achievable by MRS and thereby contribute to the wider utility and use of the technology.

IV. Successful implementation of the MRSI-semiLASER sequence with a 1.2-fold-1.3-fold improvement of SNR in phantoms and in-vivo animal subjects compared to the stock Bruker CSI-PRESS sequence was duly verified and reported. The spectra quality and grids have been evaluated both qualitatively and quantitatively for the implemented MRSI-semiLASER sequence on the basis of consensus parameters reported in literature such as Linewidth, SNR, and other.

V. Increased spatial resolution has been demonstrated by reducing slice thickness acquired with MRSI semiLASER from GL261 GB brain tumor in C57/BL6 mice and hence multi-slice acquisitions can be acquired by increasing the number of slices and reducing the slice thickness from 1 mm to 0.8 mm.

VI. Narrower water peak widths at half height were observed in MRSI semiLASER spectra acquired at 0.8 mm indicating better B_0 homogeneity in thinner slices, which results in narrower and more intense peaks with SNR larger than predicted based on volume differences.

VII. No artefact contamination was observed in the obtained spectra using the elliptical acquisition mode. The significance of the weighted mode cannot be ignored since the spatial resolution of MRSI experiment depends on the width of the spatial response function (SRF) and the acquisition weighting improves the shape of the SRF. However, for spectroscopic uses, we recommend using the elliptical acquisition mode for higher SNR.

VIII. The increased SNR obtained with elliptical phase encoding may allow to further increase the spatial resolution or reduce the experimental time in order to improve pattern spectral analysis in our murine brain tumor models and therefore provides an added value.

IX. An alternate pipeline has been proposed to reduce the post processing time while maintaining the data quality and is integrated with the existing pipeline by replacing the 3DiCSI unmaintained software. Also, several scripts were developed for automatic and

manual phase correction of SV and MRSI datasets.

X. The implemented SV-semiLASER and MRSI-semiLASER sequences, optimized for mouse brain tumor studies along with post processing tools, are now available at the SeRMN and, through manuscript associated publication release, to other research groups studying metabolic brain disorders.

XI. Nosological images were obtained from mouse brain GB using the implemented MRSI-semiLASER acquired spectra, but the already available classifier may require retraining with the additional spectra obtained both from the MRSI-semiLASER and CSI-PRESS sequences for increased robustness.

XII. The sequence simulations were obtained for the single voxel PRESS and SV-semiLASER sequences using the NMR-SCOPE B and the effects on spectra by imposing different test conditions were visualized. The simulations can also be extended to multi-voxel sequences.

XIII. The source codes for the SV-semiLASER and MRSI-semiLASER sequences are now available at the SeRMN and can be provided on request in the meantime. They will be made publicly available associated with the publication of its performance description.

SCIENTIFIC CONTRIBUTIONS

1. Javed Z , Martinez GV , Mulero-Acevedo M, Candiota A.P, Arus C ,Cabañas M, Lope-Piedrafita S "Development and Optimization of MRSI semiLASER acquisitions for mouse brain tumor studies: evaluation of increased spatial resolution and k-space sampling strategies" accepted as Digital Poster at the ISMRM Annual Meeting in June 2023 Toronto Canada.

2. Mulero-Acevedo M, Lope-Piedrafita S, Javed Z, Kübeck O, Arus C, Candiota AP. "Exploring GB models with different immunogenicity: CT-2A preclinical model characterization and its response to IMS-TMZ". Accepted as short talk for the 4th GliMR Annual Meeting 2023, held at Porto, Portugal, May 3rd-5th, 2023.

3. Javed Z, Martinez G, Candiota AP, Cabanas M, Lope-Piedrafita S. "High resolution multi-voxel spectroscopy using CSI-semiLASER for mouse brain preclinical studies", accepted and presented in ISMRM 2022 (abstract 2329) as Digital Poster in May 2022 London UK.

4. Javed Z, Martinez G, Candiota AP, Cabanas M, Lope-Piedrafita S. "High resolution multi-voxel spectroscopy using CSI-semiLASER for mouse brain preclinical studies", accepted and presented in ISMRM Iberian chapter2022 as Conventional Poster in June 2022, Lisbon, Portugal.

5. Javed Z, Martinez G, Candiota AP, Arus, C, Cabanas M, Lope-Piedrafita S. "High resolution multi-voxel spectroscopy using CSI-semiLASER for mouse brain preclinical studies" accepted as oral talk in XVIII *Jornada de Bioquimica*, June 2022, Universitat Autonoma de Barcelona (UAB).

6. Javed Z, Martinez G, Candiota AP, Arus, C, Cabanas M, Lope-Piedrafita S. "PRESS_Slice: Single slice localized 1H spectroscopy", oral talk in *XVII Jornada de Bioquímica*, June 2022 Universitat Autonoma de Barcelona (UAB).

BIBLIOGRAPHY

[1] van der Graaf M. In vivo magnetic resonance spectroscopy: basic methodology and clinical applications. Eur Biophys J. 2010 Mar;39(4):527-40. doi: 10.1007/s00249-009-0517-y. Epub 2009 Aug 13. PMID: 19680645; PMCID: PMC2841275

[2] Arias-Ramos N, Ferrer-Font L, Lope-Piedrafita S, Mocioiu V, Julià-Sapé M, Pumarola M, Arús C, Candiota AP. Metabolomics of Therapy Response in Preclinical Glioblastoma: A Multi-Slice MRSI-Based Volumetric Analysis for Noninvasive Assessment of Temozolomide Treatment. Metabolites. 2017 May 18;7(2):20. doi: 10.3390/metabo7020020. PMID: 28524099; PMCID: PMC5487991

[3] Huszthy PC, Daphu I, Niclou SP, Stieber D, Nigro JM, Sakariassen PØ, Miletic H, Thorsen F, Bjerkvig R. In vivo models of primary brain tumors: pitfalls and perspectives. Neuro Oncol. 2012 Aug;14(8):979-93. doi: 10.1093/neuonc/nos135. Epub 2012 Jun 7. PMID: 22679124; PMCID: PMC3408261.

[4] Kim MM, Parolia A, Dunphy MP, Venneti S. Non-invasive metabolic imaging of brain tumours in the era of precision medicine. Nat Rev Clin Oncol. 2016 Dec;13(12):725-739. doi: 10.1038/nrclinonc.2016.108. Epub 2016 Jul 19. PMID: 27430748; PMCID: PMC5115958.

[5] Al-iedani, O., Lechner-Scott, J., Ribbons, K. et al. Fast magnetic resonance spectroscopic imaging techniques in human brain- applications in multiple sclerosis. J Biomed Sci 24, 17 (2017). https://doi.org/10.1186/s12929-017-0323-2

[6] Purcell EM. Research in nuclear magnetism. Nobel Lecture 1952, pp 219-231 from nobelprize.org accessed on 6 June 2023.

[7] Bloch, F., Hansen, W.W. and Packard, M. The Nuclear Induction Experiment. Physical Review,1946, 70, 474-485. http://dx.doi.org/10.1103/PhysRev.70.474

[8] House, Waylon & Lauterbur, P.C. & Dulcey, C. & Lai, C.M.. "Magnetic Resonance Zeugmatography". Proceedings of the 18th Ampere Congress, Nottingham 1974. Vol1. 27.

[9] Mansfield P, Morris PG, Ordidge RJ, Pykett IL, Bangert V, Coupland RE. Human whole body imaging and detection of breast tumours by n.m.r. Philos Trans R Soc Lond B Biol Sci. 1980 Jun 25;289(1037):503-10. doi: 10.1098/rstb.1980.0069. PMID: 6106225

[10] https://www.chemistrysteps.com/nmr-spectroscopy-an-easy-introduction/ accessed on7 May 2021.

[11] "Shaped RF-Pulses," in Bruker ParaVision5.1 User's Manual, Bruker BioSpin MRI GmbH, 2010, pp. 1–21

[12] Runge VM, Wood ML, Kaufman DM, Silver MS. MR imaging section profile optimization: improved contrast and detection of lesions. Radiology. 1988 Jun;167(3):831-4. doi: 10.1148/radiology.167.3.3363149. PMID: 3363149.

[13] https://u-of-o-nmr-facility.blogspot.com/2011/01/excitation-profiles-for-shaped-pulses.html accessed on 10 May 2021

[14] Gajdošík, M., Hingerl, L., Škoch, A., Freudenthaler, A., Krumpolec, P., Ukropec, J., Ukropcová, B., Šedivý, P., Hájek, M., Itariu, B.K., Maier, B., Baumgartner-Parzer, S., Krebs, M., Trattnig, S. and Krššák, M. (2019), Ultralong TE In Vivo 1H MR Spectroscopy of Omega-3 Fatty Acids in Subcutaneous Adipose Tissue at 7 T. J. Magn. Reson. Imaging,

50: 71-82. https://doi.org/10.1002/jmri.26605

[15] Norris, D.G., Adiabatic radiofrequency pulse forms in biomedical nuclear magnetic resonance., Concepts Magn. Reson.2002, 14: 89-101. https://doi.org/10.1002/cmr.10007

[16] McRobbie, D. W., Moore, E. A., Graves, M., & Prince, M. R. (2017). MRI from picture to Proton. Cambridge University Press.

[17] De Graaf, R.A. and Nicolay, K., Adiabatic rf pulses: Applications to in vivo NMR. Concepts Magn. Reson.1997, 9: 247-268. https://doi.org/10.1002/(SICI)1099-0534(1997)9:4<247::AID-CMR4>3.0.CO;2-Z

[18] Tannús A, Garwood M. Adiabatic pulses. NMR Biomed. 1997 Dec;10(8):423-34. doi: 10.1002/(sici)1099-1492(199712)10:8<423::aid-nbm488>3.0.co;2-x. PMID: 9542739.

[19] Hanson, L. G., & Groth, T., (TRANS.) (2009). Introduction to Magnetic Resonance Imaging Techniques.

[20] Tapper, S. (2019). Neurotransmitter Imaging of the Human Brain : Detecting γ-Aminobutyric Acid (GABA) Using Magnetic Resonance Spectroscopy (PhD dissertation, Linköping University Electronic Press). https://doi.org/10.3384/diss.diva-154904.

[21] Bernstein, M. A., King, K. F., & Zhou, X. J. (2021). Handbook of MRI pulse sequences. Elsevier/Academic Press.

[22] Glunde K, Jiang L, Moestue SA, Gribbestad IS. MRS and MRSI guidance in molecular medicine: targeting and monitoring of choline and glucose metabolism in cancer. NMR Biomed. 2011 Jul;24(6):673-90. doi: 10.1002/nbm.1751. PMID: 21793073; PMCID: PMC3146026.

[23] https://mriquestions.com/ accessed on 10 August 2020.

[24] Bottomley PA. Spatial localization in NMR spectroscopy in vivo. Ann N Y Acad Sci. 1987;508:333-48. doi: 10.1111/j.1749-6632.1987.tb32915.x. PMID: 3326459.

[25] Ordidge RJ, Bendall MR, Gordon RE, Connelly A. Volume selection for in vivo biological spectroscopy.(1985) In: Govil G, KhetrapalCL, Saran A, eds. Magnetic resonance in biology and medicine. New Delhi, India : McGraw Hill ; 387 – 397

[26] Jung, B.A. and Weigel, M. (2013), Spin echo magnetic resonance imaging. J. Magn. Reson. Imaging, 37: 805-817. https://doi.org/10.1002/jmri.24068

[27] Öz G, Deelchand DK, Wijnen JP, Mlynárik V, Xin L, Mekle R, Noeske R, Scheenen TWJ, Tkáč I; Experts' Working Group on Advanced Single Voxel 1H MRS. Advanced single voxel 1 H magnetic resonance spectroscopy techniques in humans: Experts' consensus recommendations. NMR Biomed. 2020 Jan 10:e4236. doi: 10.1002/nbm.4236. Epub ahead of print. PMID: 31922301; PMCID: PMC7347431.

[28] Zur, Y, and Stokar, S. 1987. A phase-cycling technique for canceling spurious echoes in NMR imaging. J. Magn. Reson. 71: 212–228

[29] Landheer K, Gajdošík M, Juchem C. A SV-semiLASER, single-voxel spectroscopic sequence with a minimal echo time of 20.1 ms in the human brain at 3 T. NMR Biomed. 2020 Sep;33(9): e4324. doi: 10.1002/nbm.4324. Epub 2020 Jun 18. PMID: 32557880

[30] Peter.B.Barker, "Clinical MR Spectroscopy,".

[31] Sacolick, Laura & Rothman, Douglas & Graaf, Robin. (2007). Adiabatic refocusing pulses for volume selection in magnetic resonance spectroscopic imaging. Magnetic resonance in medicine : official journal of the Society of Magnetic Resonance in Medicine / Society of Magnetic Resonance in Medicine. 57. 548-53. 10.1002/mrm.21162.

[32] Bulakbasi, N. (2004). Clinical applications of Proton MR spectroscopy in the diagnosis

of brain tumours. Spectroscopy, 18(2), 143–153. https://doi.org/10.1155/2004/38145

[33] Pfeuffer J, Tkáč I, Provencher SW, Gruetter R. Toward an in vivo neurochemical profile: quantification of 18 metabolites in short-echo-time (1)H NMR spectra of the rat brain. J Magn Reson. 1999 Nov;141(1):104-20. doi: 10.1006/jmre.1999.1895. PMID: 10527748.

[34] Cudalbu C, Cavassila S, Ratiney H, Beuf O, Briguet A, Graveron-Demilly D. Metabolite concentrations of healthy mouse brain by Magnetic Resonance Spectroscopy at 7 Tesla. Conf Proc IEEE Eng Med Biol Soc. 2005;2005:1392-5. doi: 10.1109/IEMBS.2005.1616689. PMID: 17282458.

[35] Chen JH, Wu YV, DeCarolis P, O'Connor R, Somberg CJ, Singer S. Resolution of creatine and phosphocreatine 1H signals in isolated human skeletal muscle using HR-MAS 1H NMR. Magn Reson Med. 2008 Jun;59(6):1221-4. doi: 10.1002/mrm.21604. PMID: 18506783; PMCID: PMC2694043.

[36] Harris LM, Tunariu N, Messiou C, Hughes J, Wallace T, DeSouza NM, Leach MO, Payne GS. Evaluation of lactate detection using selective multiple quantum coherence in phantoms and brain tumours. NMR Biomed. 2015 Mar;28(3):338-43. doi: 10.1002/nbm.3255. Epub 2015 Jan 14. PMID: 25586623; PMCID: PMC4681317.

[37] Buckner JC. Factors influencing survival in high-grade gliomas. Semin Oncol. 2003 Dec;30(6 Suppl 19):10-4. doi: 10.1053/j.seminoncol.2003.11.031. PMID: 14765378.

[38] Stupp R, Hegi ME, Mason WP, et al. Effects of radiotherapy with concomitant and adjuvant temozolomide versus radiotherapy alone on survival in glioblastoma in a randomised phase III study: 5-year analysis of the EORTC-NCIC trial. Lancet Oncol. 2009;10(5):459-466.

[39] Dhermain FG, Hau P, Lanfermann H, Jacobs AH, van den Bent MJ. Advanced MRI and PET imaging for assessment of treatment response in patients with gliomas. Lancet Neurol. 2010 Sep;9(9):906-20. doi: 10.1016/S1474-4422(10)70181-2. Epub 2010 Aug 10. PMID: 20705518.

[40] Ortega-Martorell S, Ruiz H, Vellido A, Olier I, Romero E, Julià-Sapé M, Martín JD, Jarman IH, Arús C, Lisboa PJ. A novel semi-supervised methodology for extracting tumor type-specific MRS sources in human brain data. PLoS One. 2013 Dec 23;8(12):e83773. doi: 10.1371/journal.pone.0083773. PMID: 24376744; PMCID: PMC3871596.

[41] García-Gómez, J.M., Luts, J., Julià-Sapé, M. et al. Multiproject–multicenter evaluation of automatic brain tumor classification by magnetic resonance spectroscopy. Magn Reson Mater Phy 22, 5–18 (2009). https://doi.org/10.1007/s10334-008-0146-y

[42] Simões RV, Ortega-Martorell S, Delgado-Goñi T, Le Fur Y, Pumarola M, Candiota AP, Martín J, Stoyanova R, Cozzone PJ, Julià-Sapé M, Arús C. Improving the classification of brain tumors in mice with perturbation enhanced (PE)-MRSI. Integr Biol (Camb). 2012 Feb;4(2):183-91. doi: 10.1039/c2ib00079b. Epub 2011 Dec 23. PMID: 22193155.

[43] Delgado-Goñi T, Ortega-Martorell S, Ciezka M, Olier I, Candiota AP, Julià-Sapé M, Fernández F, Pumarola M, Lisboa PJ, Arús C. MRSI-based molecular imaging of therapy response to temozolomide in preclinical glioblastoma using source analysis. NMR Biomed. 2016 Jun;29(6):732-43. doi: 10.1002/nbm.3521. Epub 2016 Apr 8. PMID: 27061401.

[44] Ortega-Martorell S, Olier I, Julià-Sapé M, Arús C. SpectraClassifier 1.0: a user friendly, automated MRS-based classifier-development system BMC Bioinformatics. 2010 Feb

24;11:106. doi: 10.1186/1471-2105-11-106. PMID: 20181285.

[45] Candiota AP, Arús C. Establishing Imaging Biomarkers of Host Immune System Efficacy during Glioblastoma Therapy Response: Challenges, Obstacles and Future Perspectives Metabolites. 2022 Mar 14;12(3):243. doi: 10.3390/metabo12030243. PMID: 35323686

[46] Li Y, Wang T, Zhang T, Lin Z, Li Y, Guo R, Zhao Y, Meng Z, Liu J, Yu X, Liang ZP, Nachev P. Fast high-resolution metabolic imaging of acute stroke with 3D magnetic resonance spectroscopy. Brain. 2020 Dec 5;143(11):3225-3233. doi: 10.1093/brain/awaa264. PMID: 33141145; PMCID: PMC7719019.

[47] Lam F, Ma C, Clifford B, Johnson CL, Liang ZP. High-resolution (1) H-MRSI of the brain using SPICE: Data acquisition and image reconstruction. Magn Reson Med. 2016 Oct;76(4):1059-70. doi: 10.1002/mrm.26019. Epub 2015 Oct 28. PMID: 26509928; PMCID: PMC4848237.

[48] Cao P, Shin PJ, Park I, et al. Accelerated high-bandwidth MR spectroscopic imaging using compressed sensing. Magn Reson Med. 2016;76(2):369-379

[49] Ozturk-Isik E, Crane JC, Cha SM, Chang SM, Berger MS, Nelson SJ. Unaliasing lipid contamination for MR spectroscopic imaging of gliomas at 3T using sensitivity encoding (SENSE). Magn Reson Med. 2006;55(5):1164-1169

[50] Bogner W, Otazo R, Henning A. Accelerated MR spectroscopic imaging-a review of current and emerging techniques. NMR Biomed. 2021 May;34(5):e4314. doi: 10.1002/nbm.4314. Epub 2020 May 12. PMID: 32399974; PMCID: PMC8244067.

[51] *Bruker TopSpin Acquisition Commands and Parameters User Manual*, 014 ed, vol. 4.x, Bruker Corporation, 2020, pp. 19–20.

[52] Wilson, M, Andronesi, O, Barker, PB, et al. Methodological consensus on clinical proton MRS of the brain: Review and recommendations. Magn Reson Med. 2019; 82: 527– 550. https://doi.org/10.1002/mrm.27742

[53] Meyerspeer M, Scheenen T, Schmid AI, Mandl T, Unger E, Moser E. SemiLASER localized dynamic 31P magnetic resonance spectroscopy in exercising muscle at ultra-high magnetic field. Magn Reson Med. 2011 May;65(5):1207-15. doi: 10.1002/mrm.22730. Epub 2011 Mar 7. PMID: 21384422; PMCID: PMC3272370

[54] Jona, G, Furman-Haran, E, Schmidt, R. Realistic head-shaped phantom with brain-mimicking metabolites for 7 T spectroscopy and spectroscopic imaging. NMR in Biomedicine. 2021; 34:e4421. https://doi.org/10.1002/nbm.4421

[55] Och, J.G., Clarke, G.D., Sobol, W.T., Rosen, C.W. and Mun, S.K., Acceptance testing of magnetic resonance imaging systems: Report of AAPM Nuclear Magnetic Resonance Task Group No. 6., 1992, Med. Phys., 19: 217-229. https://doi.org/10.1118/1.596903

[56] https://www.protocolsonline.com/recipes/phosphate-buffered-saline-pbs/ accessed on 6December 2021.

[57] Simões RV, Delgado-Goñi T, Lope-Piedrafita S, Arús C. 1H-MRSI pattern perturbation in a mouse glioma: The effects of acute hyperglycemia and moderate hypothermia. NMR Biomed. 2010;23(1):23-33. https://doi.org/10.1002/nbm.1421

[58] Dietrich, O., Raya, J.G., Reeder, S.B., Reiser, M.F. and Schoenberg, S.O., Measurement of signal-to-noise ratios in MR images: Influence of multichannel coils, parallel imaging, and reconstruction filters. J. Magn. Reson. Imaging, 2007, 26: 375-385. https://doi.org/10.1002/jmri.20969

[59] Kreis, R, Boer, V, Choi, I-Y, et al. Terminology and concepts for the characterization of in vivo MR spectroscopy methods and MR spectra: Background and experts' consensus recommendations. NMR in Biomedicine. 2021; 34:e4347. https://doi.org/10.1002/nbm.4347.

[60] https://sites.bu.edu/cheminst/files/2021/06/CICNMR_basicconcepts.pdf accessed on

2 June 2023

[61] Bunting KV, Steeds RP, Slater LT, Rogers JK, Gkoutos GV, Kotecha D. A Practical Guide to Assess the Reproducibility of Echocardiographic Measurements. J Am Soc Echocardiogr. 2019 Dec;32(12):1505-1515. doi: 10.1016/j.echo.2019.08.015. Epub 2019 Oct 22. PMID: 31653530.

[62] British Standards Institution. Precision of test methods 1: Guide for the determination and reproducibility for a standard test method. British Standards. 1975;597(Part 1)

[63] Quantitative Imaging Biomarkers Alliance (QIBA). Indices of Repeatability, Reproducibility, and Agreement. 2013. Online.

[64] C., Dutoit, S. H. Graphical exploratory data analysis.,2012, Springer. ISBN 978-1-4612-9371-2. OCLC 1019645745

[65] Giavarina D. Understanding Bland Altman analysis. Biochem Med (Zagreb). 2015 Jun 5;25(2):141-51. doi: 10.11613/BM.2015.015. PMID: 26110027; PMCID: PMC4470095

[66] Runge, V.M., Heverhagen, J.T. Slice Thickness. In: The Physics of Clinical MR Taught Through Images. Springer, Cham.,2022, https://doi.org/10.1007/978-3-030-85413-3_21.

[67] https://mrimaster.com/technique%20SNR.html accessed on 22 June 2020.

[68] Jalnefjord O, Pettersson P, Lundholm L, Ljungberg M. Simulated basis sets for semi-LASER: the impact of including shaped RF pulses and magnetic field gradients. MAGMA. 2021 Aug;34(4):545-554. doi: 10.1007/s10334-020-00900-1. Epub 2020 Dec 23. PMID: 33355720; PMCID: PMC8338815

[69] Deelchand DK, Berrington A, Noeske R, Joers JM, Arani A, Gillen J, Schär M, Nielsen JF, Peltier S, Seraji-Bozorgzad N, Landheer K, Juchem C, Soher BJ, Noll DC, Kantarci K, Ratai EM, Mareci TH, Barker PB, Öz G. Across-vendor standardization of SV-semiLASER for single-voxel MRS at 3T. NMR Biomed. 2021 May;34(5):e4218. doi: 10.1002/nbm.4218. Epub 2019 Dec 18. PMID: 31854045; PMCID: PMC7299834

[70] Giovannetti G, Santarelli MF, Frijia F, Menichetti L, Ardenkjaer-Larsen JH, De Marchi D, Hartwig V, Positano V, Landini L, Lombardi M. Comparison between volume and surface coils for pig cardiac metabolism studies with hyperpolarized 13C MRS. J Cardiovasc Magn Reson. 2011 Feb 2;13(Suppl 1):P343. doi: 10.1186/1532-429X-13-S1-P343. PMCID: PMC3106798

[71] Shams Z, Klomp DWJ, Boer VO, Wijnen JP, Wiegers EC. Identifying the source of spurious signals caused by B0 inhomogeneities in single-voxel 1 H MRS. Magn Reson Med. 2022 Jul;88(1):71-82. doi: 10.1002/mrm.29222. Epub 2022 Mar 28. PMID: 35344600; PMCID: PMC9311141.

[72] Galijasevic M, Steiger R, Mangesius S, Mangesius J, Kerschbaumer J, Freyschlag CF, Gruber N, Janjic T, Gizewski ER, Grams AE. Magnetic Resonance Spectroscopy in Diagnosis and Follow-Up of Gliomas: State-of-the-Art. Cancers. 2022; 14(13):3197. https://doi.org/10.3390/cancers14133197

[73] Rémy, C., Arús, C., Ziegler, A., Lai, E.S., Moreno, A., Fur, Y.L. and Décorps, M., In Vivo, Ex Vivo, and In Vitro One- and Two-Dimensional Nuclear Magnetic Resonance Spectroscopy of an Intracerebral Glioma in Rat Brain: Assignment of Resonances. Journal of Neurochemistry, 1994, 62: 166-179. https://doi.org/10.1046/j.1471-4159.1994.62010166.x.

[74] Rémy C, Fouilhé N, Barba I, Sam-Laï E, Lahrech H, Cucurella MG, Izquierdo M, Moreno A, Ziegler A, Massarelli R, Décorps M, Arús C. Evidence that mobile lipids detected in rat brain glioma by 1H nuclear magnetic resonance correspond to lipid droplets. Cancer

Res. 1997 Feb 1;57(3):407-14. PMID: 9012466.

[75] Assignment of the 2.03 ppm resonance in in vivo 1H MRS of human brain tumour cystic fluid: contribution of macromolecules. Candiota AP, Majós C, Bassols A, Cabañas ME, Acebes JJ, Quintero MR, Arús C. MAGMA. 2004 Sep;17(1):36-46. doi: 10.1007/s10334-004-0043-y. Epub 2004 Aug 31. PMID: 15340855.

[76] Ricci PE, Pitt A, Keller PJ, Coons SW, Heiserman JE. Effect of voxel position on single-voxel MR spectroscopy findings. AJNR Am J Neuroradiol. 2000 Feb;21(2):367-74. PMID: 10696025; PMCID: PMC7975341

[77] Segebarth C.M., Balériaux D.F., Luyten P.R., den Hollander J.A. Detection of metabolic heterogeneity of human intracranial tumours in vivo by 1H-NMR spectroscopic imaging. Magn. Reson. Med. 1990; 13:62–76. doi: 10.1002/mrm.1910130108

[78] Scheenen, T.W.J., Klomp, D.W.J., Wijnen, J.P. and Heerschap, A. , Short echo time ^{1}H-MRSI of the human brain at 3T with minimal chemical shift displacement errors using adiabatic refocusing pulses. Magn. Reson. Med., 59: 1 6. https://doi.org/10.1002/mrm.21302.

[79] Hangel G, Niess E, Lazen P, Bednarik P, Bogner W, Strasser B. Emerging methods and applications of ultra-high field MR spectroscopic imaging in the human brain. Anal Biochem. 2022 Feb 1;638:114479. doi: 10.1016/j.ab.2021.114479. Epub 2021 Nov 24. PMID: 34838516

[80] Javed Z, Martinez G, Candiota AP, Cabanas M, Lope-Piedrafita S. High resolution multi-voxel spectroscopy using CSI- semiLASER for mouse brain preclinical studies accepted and presented in ISMRM 2022 (abstract 2329) as Digital Poster in May 2022 London UK.

[81] Jianmin Wang, A. Reykowski and J. Dickas, "Calculation of the signal-to-noise ratio for simple surface coils and arrays of coils [magnetic resonance imaging]," in IEEE Transactions on Biomedical Engineering ,1995 Sept, vol. 42, no. 9, pp. 908-917, doi: 10.1109/10.412657.

[82] Ramadan, S. and Mountford, C.E., Adiabatic localized correlation spectroscopy (AL-COSY): Application in muscle and brain. J. Magn. Reson. Imaging, 2011, 33: 1447-1455. https://doi.org/10.1002/jmri.22555

[83] Convex non-negative matrix factorization for brain tumor delimitation from MRSI data. Ortega-Martorell S, Lisboa PJ, Vellido A, Simões RV, Pumarola M, Julià-Sapé M, Arús C. PLoS One. 2012;7(10):e47824. doi: 10.1371/journal.pone.0047824. Epub 2012 Oct 23. PMID: 23110107

[84] Oh, T., Fakurnejad, S., Sayegh, E.T. et al. Immunocompetent murine models for the study of glioblastoma immunotherapy. J Transl Med 12, 107 (2014). https://doi.org/10.1186/1479-5876-12-107

[85] Pich O, Muiños F, Lolkema MP, Steeghs N, Gonzalez-Perez A, Lopez-Bigas N. The mutational footprints of cancer therapies. Nat Genet. 2019 Dec;51(12):1732-1740. doi: 10.1038/s41588-019-0525-5. Epub 2019 Nov 18. PMID: 31740835; PMCID: PMC6887544.

[86] Mulero-Acevedo M, Lope-Piedrafita S, Javed Z, Kübeck O, Arus C, Candiota AP. Exploring GB models with different immunogenicity: CT-2A preclinical model characterization and its response to IMS-TMZ. Accepted as short talk for the 4th GliMR Annual Meeting 2023, to be held in Porto, Portugal, May 3rd-5th 2023.

[87] Lin A, Andronesi O, Bogner W, Choi IY, Coello E, Cudalbu C, Juchem C, Kemp GJ, Kreis R, Krššák M, Lee P, Maudsley AA, Meyerspeer M, Mlynarik V, Near J, Öz G, Peek AL, Puts NA, Ratai EM, Tkáč I, Mullins PG; Experts' Working Group on Reporting Standards

for MR Spectroscopy. Minimum Reporting Standards for in vivo Magnetic Resonance Spectroscopy (MRSinMRS): Experts' consensus recommendations. NMR Biomed. 2021 May;34(5):e4484. doi: 10.1002/nbm.4484. Epub 2021 Feb 9. PMID: 33559967; PMCID: PMC8647919.

[88] Javed Z , Martinez GV , Mulero-Acevedo M, Candiota A.P, Arus C ,Cabañas M, Lope-Piedrafita S" Development and Optimization of MRSI semiLASER acquisitions for mouse brain tumor studies: evaluation of increased spatial resolution and k-space sampling strategies" accepted as Digital Poster in ISMRM Annual Meeting in June 2023 Toronto Canada.

[89] Scheenen TW, Heerschap A, Klomp DW. Towards 1H-MRSI of the human brain at 7T with slice-selective adiabatic refocusing pulses. MAGMA. 2008 Mar;21(1-2):95-101. doi: 10.1007/s10334-007-0094-y. Epub 2008 Jan 22. PMID: 18210177; PMCID: PMC2798032

[90] Hu, J., Feng, W., Hua, J., Jiang, Q., Xuan, Y., Li, T. and Haacke, E.M., A high spatial resolution in vivo 1H magnetic resonance spectroscopic imaging technique for the human breast, 2009, at urn:x-wiley:00942405:media:mp3087:mp3087-math-0001. Med. Phys., 36: 4870-4877. https://doi.org/10.1118/1.3213087

[91] Emwas AH, Saccenti E, Gao X, McKay RT, Dos Santos VAPM, Roy R, Wishart DS. Recommended strategies for spectral processing and post-processing of 1D 1H-NMR data of biofluids with a particular focus on urine. Metabolomics. 2018;14(3):31. doi: 10.1007/s11306-018-1321-4. Epub 2018 Feb 12. PMID: 29479299; PMCID: PMC5809546.

[92] Chen, Li & Weng, Zhiqiang & Goh, LaiYoong & Garland, Marc. An efficient algorithm for automatic phase correction of NMR spectra based on entropy minimization. Journal of Magnetic Resonance.,2002, 158. 164–168. 10.1016/S1090-7807(02)00069-1

[93] GABRMN Dynamic MRSI Processing Module (DMPM) [Available at http://gabrmn.uab.es/dmpm]. *2009-2010: GABRMN.Accessed 12 May 2020*

[94] Simpson, R., Devenyi, G.A., Jezzard, P., Hennessy, T.J. and Near, J. Advanced processing and simulation of MRS data using the FID appliance (FID-A)—An open source, MATLAB-based toolkit., 2017, Magn. Reson. Med., 77: 23-33. https://doi.org/10.1002/mrm.26091

[95] https://github.com/CIC-methods/FID-A. accessed on 12 April 2021.

[96] https://nmr.chem.ucsb.edu/protocols/SNR.html accessed on 12 April 2021.

[97] https://github.com/CIC-methods/FID-A/blob/master/LICENSE.txt accessed on 12 April 2021.

[98] In *Bruker TopSpin 4.x Processing commands and Parameters Users Manual*, vol. 007, p. 35.

[99] Near J, Harris AD, Juchem C, Kreis R, Marjańska M, Öz G, Slotboom J, Wilson M, Gasparovic C. Preprocessing, analysis and quantification in single-voxel magnetic resonance spectroscopy: experts' consensus recommendations. NMR Biomed. 2021 May;34(5):e4257. doi: 10.1002/nbm.4257. Epub 2020 Feb 21. PMID: 32084297; PMCID: PMC7442593.

[100] Finsterbusch J, Busch MG, Larson PE. Signal scaling improves the signal-to-noise ratio of measurements with segmented 2D-selective radiofrequency excitations. Magn Reson Med. 2013 Dec;70(6):1491-9. doi: 10.1002/mrm.24610. Epub 2013 Feb 25. PMID: 23440633; PMCID: PMC4987130

[101] Shamaei, A, Starcukova, J, Pavlova, I, Starcuk, Z. Model-informed unsupervised deep learning approaches to frequency and phase correction of MRS signals. Magn Reson

Med. 2023; 89: 1221– 1236. doi:10.1002/mrm.29498

[102] Naressi, A.; Couturier, C.; Devos, J. M.; Janssen, M.; Mangeat, C.; Beer, R. d. & Graveron-Demilly, D. (2001), 'Java-based graphical user interface for the MRUI quantitation package', Magma: Magnetic Resonance Materials in Physics, Biology, and Medicine 12(2-3), 141– 152. doi: 10.1007/bf02668096

[103]   https://magritek.com/2016/06/27/gradients-in-nmr-spectroscopy-part-2-pulsed-gradients/ accessed on 10 February 2023.

[104]   Feldman RE, Balchandani P. A semiadiabatic spectral-spatial spectroscopic imaging (SASSI) sequence for improved high-field MR spectroscopic imaging. Magn Reson Med. 2016 Oct;76(4):1071-82. doi: 10.1002/mrm.26025. Epub 2015 Oct 31. PMID: 26519948; PMCID: PMC4980274.

[105]   Weiss K, Melkus G, Jakob PM, Faber C. Quantitative in vivo 1H spectroscopic imaging of metabolites in the early postnatal mouse brain at 17.6 T. MAGMA. 2009 Feb;22(1):53-62. doi: 10.1007/s10334-008-0142-2. Epub 2008 Sep 20. PMID: 18807078.

APPENDIX A

Generation of sech refocusing pulses using TOPSPIN

In TOPSPIN: type **stdisp** , goto **SHAPES**, select **Adiabatic Shapes** and then **Hyperbolic Secant**.

Editable Parameters:

- **Size of shape: 2048**

ADIABATIC PULSE SHAPE GENERATION USING stdisp TOPSPIN tool

The sech pulse described here is implemented as a full passage pulse with truncation level 1%, phase factor 5, resolved into 4096 points, 2048 for the amplitude and 2048 for the phase.

Select save shape. Select the Flip Angle **180°** and Type of Rotation as **Refocussing.** Save with a filename starting with the keyword "sech", e.g. **sech21_zj.rfc .** ParaVision allows a limited number of characters to be written after the sech keyword.

The file gets saved in the location **/opt/Pv5.1/exp/stan/nmr/lists/wave**

For the shape file to be read in ParaVision it requires a few modifications in the code. The shape tool creates the file readable in TOPSPIN but ParaVision is reading a few headers in the file. To modify those headers within the shape file, select the following:

> **##TITLE: /opt/Pv5.1/exp/stan/nmr/lists/wave/sech**
>
> **SHAPE_EXMODE=(space)Refocussing**

where SHAPE_EXMODE describes the intended use and can have values: *Excitation*, *Inversion*, *Refocussing* (values are case sensitive)

> **SHAPE_Type=adiabatic**

with valid values: *conventional*, *adiabatic* (values are case sensitive)

ShapeRephfac= 0

where ShapeRephfac is the dephasing property and can have values: -100% to 100% for inversion/refocusing pulses, and 0%-100% for excitation pulses.

Shape Integral factor: Area of the waveform compared to a rectangular pulse

Save the changes and close the file. It should appear in ParaVision.

APPENDIX B

MRS/MRSI MATLAB POST PROCESSING SCRIPTS

1. CSI_textexport.m

DESCRIPTION

This script provides a manually phase corrected inner MRSI grid consisting of 144 sub spectra (12x12) matrix. Besides phase correction, exponential multiplication and Line broadening (LB=4) is also applied on the inner grid. The inner grid spectra are also plotted to ppm scale and exported to text file in DMPM format. This script was also written for the purpose of visualizing multi-voxel (MRSI) sub-spectra after applying phase correction manually and processing the phased spectra to calculate SNR, linewidth and Standard deviation. The metabolite of choice is extracted and visualized in a separate figure. Further maps are generated for SNR and intensity of the selected metabolite and the SNR is also plotted as boxplot and histogram.

INPUTS

- Indir1 = pathname for dataset
- Visu1 = read **visu_pars** file
- Spec = Bruker 2dseq image
- Grpdelay = read **acqus** file for group delay value
- method_fid = read method file
- acqp_fid = read acqp file
- phase1 = user defined phase value

OUTPUTS

- sp = complex vector of size [32 32 2048] containing phase corrected spectra
- sp4 = extracted inner grid
- csiphased.txt = exported text file in DMPM format

CODE

```
%%%%code written by zeejay 221202%%%%
%%%To process multi-voxel CSI (MRSI) for SNR and linewidth and export to
%%%text file

%%%%%modified 230220
```

```matlab
%%%% phased CSI spectra exported to DMPM text file
%%%%phasing and linebroadening is applied on full grid
%%%% the inner grid is extracted
%%%%the inner grid is exported to DMPM text format.


close all;
clear all;

indir1='C:\Users\1571788\Desktop\all scans\zoo220623.eB1\200';
%%%CSI phantom dataset
indir2='C:\Users\1571788\Desktop\all scans\zoo220623.eB1\202';
    %indir1='C:\Users\1571788\Desktop\all
scans\zoo221104.gL1\100' %%%CSI tumor dataset

visu1=readBrukerParamFile([indir1,'\pdata\1\visu_pars']); %read
visu_pars file
spec=readBruker2dseq([indir1,'\pdata\1\2dseq'],visu1); % read
2dseq image file (fully processed with CSIdash macro)
%fids=fread(fopen([indir '/ser']),'int');

grpdelay=readBrukerParamFile([indir1,'\acqus']);
save('structureVarMatFile','-struct','grpdelay');
load('structureVarMatFile','GRPDLY')
grpdelay=GRPDLY;

phasec=readBrukerParamFile([indir2 '\pdata\1\procs']);  %load
phasecorrec values
save('structureVarMatFile','-struct','phasec');
load('structureVarMatFile','PHC0');
load('structureVarMatFile','PHC1');
ph0=PHC0;
ph1=0;

%%%%code for ppm scale conversion entered here
%% %%%%phase correction section
phase1=input('Enter phase value=');


%%  %%%%%%PHASE CORRECTION csi-press

figure;

for i=1:32
    for j=1:32
        subspec1=spec(:,i(:),j(:));
        fids_csi=circshift(subspec1,-round(grpdelay));
        LB=4;
        sw=4006.41025641026;

        for c=1:2048
            b(c)= exp(-((c-1).*LB*pi)/(2*sw));
        end

        spec2fid1=fids_csi'.*b;
        fids1=flip(spec2fid1);
```

```matlab
            specs_new1=(fftshift(fft(fids1)));
            %sp_dp1=flip(specs_new);
            sp_dp2=specs_new1.*exp(1i*(phase1*pi/180));
             sp(i,j,:)=sp_dp2';
            %%%%%store the phase corrected spectra as sp
            plot(ppm_s1,real(sp_dp2));
          set (gca, 'xdir' , 'reverse' );
          title('full grid phased spectra');
        hold on;
    end
end
%end

sp3=sp(11:22,11:22,:);
sp4=permute(sp3,[3 2 1]);
figure;

figure;
    meanspectrum=mean(sp4,[2,3]);
        plot(ppm_s1,real(meanspectrum));
        set (gca, 'xdir' , 'reverse' );
        set(gca,'FontSize',12);
        title('mean spectrum')
        xlabel('ppm')
        ylabel('peak intensity')
        xlim([0.5,4])

for i=1:12
    for j=1:12
        spectra=sp4(:,i,j);
        plot(ppm_s1,real(spectra));
        hold on;
         set (gca, 'xdir' , 'reverse' )
         title('inner grid phased spectra'),
    end
end

%%%%% text export%%%%%

fileID = fopen('csiphased.txt','w');
f =(indir1);
fprintf(fileID,'CSI set name: ''%s''\n',f);
q=144;      %Number of voxels
b= '+2048 (+0 , +2047)';    %Npoints per voxel

a='+';
a= repmat(a,q,1);                     %Repetition of Â´+Â´ for 144
times
a =convertStringsToChars(a);     %Convert into charaters data
type
v= (10:21)';                      %These are the indices
values
x =repmat(v,12);                  %Repeating the index values
12 times
x1 =x(:,1);                       %It will give the first
coloumn of TEXT file
```

```matlab
y = x';                                 %Take the Transpose
y= y(:,1:12);                           %Extract coloums from 1 to
12
y=reshape(y, [q,1]);                    %Reshape the Â´yÂ´, it will
give 3rd coloumn of Text file

z= [a num2str(x1) a num2str(zeros(q,1)) a num2str(y)];
%Convert Numeric to String/Character    because we have Â´+Â´ is
character. You cant add numeric and character together. So
convert all into character first
fprintf(fileID,'Number of voxels: %d\n',q);
fprintf(fileID,'Npoints per voxel: %s\n',b);
fprintf(fileID,'\n');
fprintf(fileID,'Voxel Index:\n');
fprintf(fileID,'%c%c%c %c%c %c%c%c\n',z');
fprintf(fileID,'%s %12s\n','Real','Imaginary');
M=[real(sp4(:)) imag(sp4(:))];
fprintf(fileID,'%-5.5e \t %-5.5e\n',M.');
```

2. Autophased_MRSI.m

DESCRIPTION

This script provides a fast and automatic method for extracting phase corrected inner grid spectra from the MRSI dataset and exports the data as text file readable by DMPM. The 2rr and 2ii files are loaded directly from the dataset into MATLAB and the inner grid is extracted. The data is then plotted and exported as text file.

INPUTS:

- Real_spec = read the 2rr file
- Imag_spec = read the 2ii file

OUTPUTS:

- Spec3 = inner grid consisting of 12x12 matrix (144 spectra)
- Autophased.txt = exported text file in DMPM format

CODE:

```matlab
%%%%%%%written by zoona javed%%%%%
%%%%230224%%%%%
%%%UAB,Spain%%%%%%%

close all;
clear all;
```

194

```matlab
%%%%% read pathname for spectra and ppm scale formation
tic;
indir1='C:\Users\1571788\Desktop\all scans\zoo220408.dn1\300';
%%%%  parameters folder
indir2='C:\Users\1571788\Desktop\all scans\zoo220408.dn1\302';
%%%%  processed dataset

%%%%extract inner phased grid from 32 x 32 matrix%%%%%%%%%%%%%%

real_spec=fread(fopen([indir2 '\pdata\1\2rr']),'int');
imag_spec=fread(fopen([indir2 '\pdata\1\2ii']),'int');

spec=real_spec+1i*imag_spec;
spec2=reshape(spec,[2048 32 32]);
spec3=spec2(:,11:22,11:22);

%%%%ppm scale conversion insert here

%%%% plot inner grid spectra

figure;
% for i=1:12
 %   for j=1:12
spec4=spec3(:,5,7);
plot(ppm_s1,real(spec4));
 set (gca, 'xdir' , 'reverse' );
       title('inner grid representative spectra');
     xlim([0,4])
      %ylim([-1*10^7,20*10^7])
       set(gca,'FontSize',12)
       xlabel('ppm');
   ylabel('peak intensity');
   hold on;
  %  end
 %end

%%%%%%%%EXPORT INNER GRID TO DMPM format text
file%%%%%%%%%%%%%%%%%%%%

%%%% PEAK EXTRACTION AND SNR CALCULATION

%%%%% Select spectra chemical shift region%%%%%
Peakppmmin=1.5;
Peakppmmax=2.2;
noiseppmmin=-1;
noiseppmmax=0;

figure

for i=1:12
    for j=1:12

    sp_dp1=spec3(:,i(:),j(:));

    %%%%%%%%%%%%%%%%%%%%peak region extraction%%%%%%%%%%%%%%%%%%
```

```matlab
        NAAwindow1=sp_dp1(ppm_s1>Peakppmmin & ppm_s1<Peakppmmax);
        ppmwindow1=ppm_s1(ppm_s1>Peakppmmin & ppm_s1<Peakppmmax);
        subplot(1,2,1)
        plot(ppmwindow1,NAAwindow1);
        hold on;
        title('extracted peak');
        set (gca, 'xdir' , 'reverse' )
        set(gca,'FontSize',12)
        xlabel('ppm');
        ylabel('peak intensity');
        ylim([-1*10^7,5*10^7])

        %%%%%%%%%%%%%%%noise region extraction%%%%%%%%%%%%%%
        noisewindow1 = sp_dp1(ppm_s1>noiseppmmin &
            ppm_s1<noiseppmmax);
        ppmwindow2_s1=ppm_s1(ppm_s1>noiseppmmin &
            ppm_s1<noiseppmmax);
        subplot(1,2,2)
        plot(ppmwindow2_s1,noisewindow1);
        hold on;
        title('extracted noise');
        % title('extracted noise(CSI-sLASER');
        set (gca, 'xdir' , 'reverse' )
        set(gca,'FontSize',12)
        xlabel('ppm');
        ylabel('peak intensity');
        ylim([-1*10^7,5*10^7])

        %% SNR AND LW calculation

        maxNAA1(i,j)=max(abs(NAAwindow1));
        noisestd1(i,j)=std(noisewindow1);

        SNR1(i,j)=maxNAA1(i,j)/noisestd1(i,j);

        Refwindow1=sp_dp1(ppm_s1>Peakppmmin & ppm_s1<Peakppmmax);
        ppmwindow_s1=ppm_s1(ppm_s1>Peakppmmin & ppm_s1<Peakppmmax);

        maxRef_index1=find(abs(real(Refwindow1)) ==
            max(abs(real((Refwindow1)))));
        maxRef1=real(Refwindow1(maxRef_index1));
        gtHalfMax1=find(abs(real(Refwindow1)) >= 0.5*abs(maxRef1));

        FWHM1(i,j)=ppmwindow_s1(gtHalfMax1(1)) -
            ppmwindow_s1(gtHalfMax1(end));
        FWHM1(i,j)=FWHM1(i,j).*(42.577*Bo);

    end
end

fprintf('Mean SNR CSI-PRESS inner grid')
meanSNRpress=mean(SNR1(:))

fprintf('standard deviation of inner grid SNR')
standarddeviation=std(SNR1(:))
```

```matlab
%%%%%SNR MAPS INNER GRID
figure;
h1 = heatmap(SNR1,'Colormap',jet,'CellLabelColor', 'None');

caxis([0, 30]);
xlabel('x dim');
ylabel('y dim');
set(gca,'FontSize',12)
%title('Lac SNR map for MRSI-semi-LASER');
%title('Lac SNR map for CSI-PRESS');
title('Metabolite peak SNR map');

%%%%%% MEAN SPECTRUM AND STANDARD DEVIATION PLOTS

figure;

meanspectrum=mean(spec3,[2,3]);
plot(ppm_s1,real(meanspectrum));
set (gca, 'xdir' , 'reverse' );
set(gca,'FontSize',12);
title('mean spectrum')
xlabel('ppm')
ylabel('peak intensity')
xlim([0.5,5])
ylim([-1*10^7,5*10^7])

y =meanspectrum;
x = ppm_s1;   % Create: 'y' Data
c= permute(spec3,[3 2 1]);
D= reshape(c,[],size(spec3,1),1);
st1=std(D);
sd =st1';                       % Create: Standard Deviation Vector

figure
hold on
patch([x(:); flipud(x(:))], [y(:)-sd(:);
flipud(y(:)+sd(:))],[0.6 0.7 0.8],'EdgeColor','white')
plot(x,real(meanspectrum), 'LineWidth', 2);
set (gca, 'xdir' , 'reverse' )
hold off
set(gca,'FontSize',12)
title('mean spectrum and standard deviation')
xlabel('ppm')
ylabel('peak intensity')
xlim([0,4])
```

3. ppm scale conversion code

This is a general code adapted from the FID-A pipeline to obtain the ppm scale for spectra plotting.

```
% get the spectralwidth

method_fid = fopen([indir1 '/method']);

line = fgets(method_fid);
index = findstr(line,'$PVM_DigSw=');
while isempty(index)
    line = fgets(method_fid);
    index = findstr(line,'$PVM_DigSw=');
end
equals_index = findstr(line,'=');
spectralwidth = line(equals_index+1:end);
spectralwidth = str2double(spectralwidth);
fclose(method_fid);

% get the transmitter frequency
acqp_fid = fopen([indir1 '/acqp']);
line = fgets(acqp_fid);
index = findstr(line,'$BF1=')
while isempty(index)
    line = fgets(acqp_fid);
    index = findstr(line,'$BF1=');
end
equals_index = findstr(line,'=');
txfrq = line(equals_index+1:end);
txfrq = str2double(txfrq);
txfrq = txfrq*1e6;
fclose(acqp_fid);

% B0size in Tesla(T)
Bo = txfrq/42577000;

% Spectral width in PPM (13.3401 ppm)
spectralwidthppm = spectralwidth/(txfrq/1e6);

% calculate the ppm scale
ppm1 = [4.65+(spectralwidthppm/2):-
spectralwidthppm/(length(spec)-1):4.65-(spectralwidthppm/2)];

%calculate frequency  shift
frqshift = (2.01-1.88)*(txfrq/1e6);
ppm_s1 = ppm1+(frqshift/(txfrq/1000000));
```

4. Code to export phase corrected voxels to DMPM format text file

This code was developed exclusively for this project to convert the processed MRSI datasets to
DMPM text file readable format. This is a general code and can be used with other scripts.

```matlab
fileID = fopen('filename.txt','w');

% pathname of file
f =(indir1);
fprintf(fileID,'CSI set name: ''%s''\n',f);

% Number of voxels
q = 144;

% Npoints per voxel
b = '+2048 (+0 , +2047)';

a = '+';

% Repetition of Â´+Â´ for 144 times
a = repmat(a,q,1);

% Convert into characters data type
a = convertStringsToChars(a);

% These are the indices values
v = (10:21)';

% Repeating the index values 12 times
x = repmat(v,12);

% It will give the first column of TEXT file
x1 = x(:,1);

% Take the Transpose
y = x';

% Extract columns from 1 to 12
y = y(:,1:12);

% Reshape the Â´yÂ´, it will give 3rd column of Text file
y = reshape(y, [q,1]);

% Convert Numeric to String/Character
z = [a num2str(x1) a num2str(zeros(q,1)) a num2str(y)];

fprintf (fileID,'Number of voxels: %d\n',q);
fprintf (fileID,'Npoints per voxel: %s\n',b);
fprintf (fileID,'\n');
fprintf (fileID, 'Voxel Index:\n');
fprintf (fileID,'%c%c%c %c%c %c%c%c\n',z');
fprintf (fileID,'%s %12s\n','Real','Imaginary');
M = [real(spec3(:)) imag(spec3(:))];
fprintf (fileID,'%+.5d \t %+.5d\n',M.');
```

5. Bruker pvmatlab adopted MRSI post processing script for quantitative data analysis (serbruk)

This code was developed using the Bruker PVMATLAB pipeline for processing MRSI datasets.

```matlab
baseDir='C:\Users\1571788\Desktop\all scans\zoo220623.eB2\9';
pathTestData = fullfile(baseDir,'/pdata/1');

% obj=RawDataObject( [basedir '\acqp'], [indir '\ser'],
% [indir '\method']);
obj = RawDataObject(pathTestData);

% rawObj now contains the raw data and parameters associated
% with it, for example the number of images and phase
% encodes:
numSlices = obj.Acqp.NI;

% Use bruker_getAcqSizes to get spatial raw data matrix
% size (equals ACQ_size for pre-PV-360 datasets)
acqSizes=bruker_getAcqSizes(obj.Acqp);
numPhases=acqSizes(2);

display(['  Number of images        = ' num2str(numSlices)]);
display(['  Number of phase encodes = ' num2str(numPhases)]);
display('- Importing Cartesian k-space directly and
displaying');

%reading the method file
kdataObj = CKDataObject(pathTestData);

%kdataObj.viewer
kdataObj = kdataObj.readReco;
kdataObj= kdataObj.readVisu;
new=kdataObj.data;
M = max(new,[],1);
b=squeeze(M);
figure;
imagesc(abs(b))

%==== Reconstructing imported k-space data ===============

reco=kdataObj.Reco;
imageObj = bruker_Reco('all',new,reco);

for i=1:32
    for j=1:32
        specs=imageObj(:,i,j);
    end
end
```

```matlab
%% PLOTTING to ppm code entered here

specs1=imageObj(:,11:22,11:22);

figure

for i=1:12
    for j=1:12
        specs2=specs1(:,i,j);
        plot(ppm2,real(specs2));
        hold on;
        set (gca, 'xdir' , 'reverse' )
        set(gca,'FontSize',12)
        xlabel('ppm');
        ylabel('peak intensity');
        title('inner grid spectra')
    end
end

%% Peak and noise region
Peakppmmin=1.5;
Peakppmmax=2.2;
noiseppmmin=-1;
noiseppmmax=0;

figure;

for i=1:32
    for j=1:32

    sp_dp1=imageObj(:,i(:),j(:));

    %%%%%%%%%%%%%%%%%%%peak region extraction%%%%%%%%%%%%%%%%%
    NAAwindow1=sp_dp1(ppm2>Peakppmmin & ppm2<Peakppmmax);
    ppmwindow1=ppm2(ppm2>Peakppmmin & ppm2<Peakppmmax);
    subplot(1,2,1)
    plot(ppmwindow1,NAAwindow1);
    hold on;
    title('extracted peak');
    % title('extracted peak(CSI-sLASER');
    % xlim([1,1.5]);
    set (gca, 'xdir' , 'reverse' )
    set(gca,'FontSize',12)
    xlabel('ppm');
    ylabel('peak intensity');

    %%%%%%%%%%%%%%%%%noise region extraction%%%%%%%%%%%%%%%%
    noisewindow1=sp_dp1(ppm2>noiseppmmin & ppm2<noiseppmmax);
    ppmwindow2_s1=ppm2(ppm2>noiseppmmin & ppm2<noiseppmmax);
    subplot(1,2,2)
    plot(ppmwindow2_s1,noisewindow1);
    hold on;
    title('extracted noise');
    % title('extracted noise(CSI-sLASER');
    set (gca, 'xdir' , 'reverse' )
```

```matlab
    set(gca,'FontSize',12)
    xlabel('ppm');
    ylabel('peak intensity');

    %% SNR AND LW calculation
    maxNAA1(i,j)=max(abs(NAAwindow1));
    noisestd1(i,j)=std(noisewindow1);
    SNR1(i,j)=maxNAA1(i,j)/noisestd1(i,j);

    Refwindow1=sp_dp1(ppm2>Peakppmmin & ppm2<Peakppmmax);
    ppmwindow_s1=ppm2(ppm2>Peakppmmin & ppm2<Peakppmmax);

    maxRef_index1=find(abs(real(Refwindow1)) ==
        max(abs(real((Refwindow1)))));
    maxRef1=real(Refwindow1(maxRef_index1));
    gtHalfMax1=find(abs(real(Refwindow1)) >= 0.5*abs(maxRef1));
    FWHM1(i,j)=ppmwindow_s1(gtHalfMax1(1)) -
        ppmwindow_s1(gtHalfMax1(end));
    FWHM1(i,j)=FWHM1(i,j).*(42.577*Bo);

    end
end

SNRpress=SNR1(11:22,11:22);
maxpress=maxNAA1(11:22,11:22);

%%%%%%%%%%%%%% to obtain average spectra from inner grid

sp_dp2=imageObj(:,11:22,11:22);

figure;

subplot(7,7,1)
plot(ppm2,sp_dp2(:,4,5))
set (gca, 'xdir' , 'reverse' )
set(gca,'FontSize',12)

figure;

meanspectrum=mean(specs1,[2,3]);
plot(ppm2,real(meanspectrum));
set (gca, 'xdir' , 'reverse' );
set(gca,'FontSize',12);
title('mean spectrum')
xlabel('ppm')
ylabel('peak intensity')

y =meanspectrum;
x = ppm2;   % Create: 'y' Data
c= permute(sp_dp2,[3 2 1]);
D= reshape(c,[],size(sp_dp2,1),1);
st1=std(D);
sd =st1';              % Create: Standard Deviation Vector

figure
```

```matlab
hold on
patch([x(:); flipud(x(:))], [y(:)-sd(:);
flipud(y(:)+sd(:))],[0.6 0.7 0.8],'EdgeColor','white')
plot(x,real(meanspectrum), 'LineWidth', 2);
set (gca, 'xdir' , 'reverse' )
hold off
set(gca,'FontSize',12)
title('mean spectrum and standard deviation')
xlabel('ppm')
ylabel('peak intensity')
xlim([0,4])

%%%%%SNR MAPS INNER GRID
figure;

h1 = heatmap(SNRpress,'Colormap',jet,'CellLabelColor', 'None');
caxis([0, 25]);
xlabel('x dim');
ylabel('y dim');
 set(gca,'FontSize',12)
%title('Lac SNR map for MRSI-semi-LASER');
title('SNR map');
%title('Metabolite peak SNR map');

fprintf('Mean SNR CSI-PRESS inner grid')
meanSNRpress=mean(SNRpress(:))

fprintf('standard deviation of inner grid SNR')
standarddeviation=std(SNRpress(:))

fprintf('Mean LW CSI-PRESS inner grid')
meanlwpress=mean(FWHM1(:));
linewidth=FWHM1(11:22,11:22);
smallestlw= min(linewidth(:))
```

6. Code for single voxel phase correction GUI (svspipeline)

This GUI code for single voxel phase correction was obtained using MATLAB GUIDE.

```matlab
function varargout = svspipeline(varargin)
% SVSPIPELINE MATLAB code for svspipeline.fig
% SVSPIPELINE, by itself, creates a new SVSPIPELINE or
% raises the existing singleton*.
%
% H = SVSPIPELINE returns the handle to a new SVSPIPELINE
% or the handle to the existing singleton*.
%
% SVSPIPELINE('CALLBACK',hObject,eventData,handles,...)
% calls the local function named CALLBACK in SVSPIPELINE.M
% with the given input arguments.
%
```

```
% SVSPIPELINE('Property','Value',...) creates a new SVSPIPELINE
% or raises the existing singleton*.  Starting from the left,
% property value pairs are applied to the GUI before
% svspipeline_OpeningFcn gets called. An unrecognized property
% name or invalid value makes property application stop.
% All inputs are passed to svspipeline_OpeningFcn via varargin.
%
% *See GUI Options on GUIDE's Tools menu.  Choose "GUI allows
% only one instance to run (singleton)".
%
% See also: GUIDE, GUIDATA, GUIHANDLES

% Edit the above text to modify the response to help svspipeline

% Last Modified by GUIDE v2.5 08-Jun-2022 15:47:25

% Begin initialization code - DO NOT EDIT
gui_Singleton = 1;
gui_State = struct('gui_Name',       mfilename, ...
                   'gui_Singleton',  gui_Singleton, ...
                   'gui_OpeningFcn', @svspipeline_OpeningFcn,
...
                   'gui_OutputFcn',  @svspipeline_OutputFcn, ...
                   'gui_LayoutFcn',  [] , ...
                   'gui_Callback',   []);
if nargin && ischar(varargin{1})
    gui_State.gui_Callback = str2func(varargin{1});
end

if nargout
    [varargout{1:nargout}] = gui_mainfcn(gui_State,
varargin{:});
else
    gui_mainfcn(gui_State, varargin{:});
end
% End initialization code - DO NOT EDIT

% --- Executes just before svspipeline is made visible.
function svspipeline_OpeningFcn(hObject, eventdata, handles,
varargin)
% This function has no output args, see OutputFcn.
% hObject    handle to figure
% eventdata  reserved - to be defined in a future version of
MATLAB
% handles    structure with handles and user data (see GUIDATA)
% varargin   command line arguments to svspipeline (see
VARARGIN)

% Choose default command line output for svspipeline
handles.output = hObject;

% Update handles structure
guidata(hObject, handles);

% UIWAIT makes svspipeline wait for user response (see UIRESUME)
% uiwait(handles.figure1);
```

```matlab
% --- Outputs from this function are returned to the
% command line.
function varargout = svspipeline_OutputFcn(hObject, eventdata,
handles)
% varargout  cell array for returning output args
%            (see VARARGOUT);
% hObject    handle to figure
% eventdata  reserved - to be defined in a future version
%            of MATLAB
% handles    structure with handles and user data (see GUIDATA)

% Get default command line output from handles structure
varargout{1} = handles.output;


% --- Executes on button press in pushbutton1.
function pushbutton1_Callback(hObject, eventdata, handles)
% hObject    handle to pushbutton1 (see GCBO)
% eventdata  reserved - to be defined in a future version
% of MATLAB
% handles    structure with handles and user data (see GUIDATA)

indir=get(handles.input1,'String');
handles.indir=indir;
%fid_data=myfunc1(indir)

fid_data =fread(fopen([indir '/fid']),'int');

real_fid = fid_data(2:2:length(fid_data));
imag_fid = fid_data(1:2:length(fid_data));

phasec=readBrukerParamFile([indir '\pdata\1\procs']);  %load
phasecorrec values
save('structureVarMatFile','-struct','phasec');
load('structureVarMatFile','PHC0');
load('structureVarMatFile','PHC1');
ph0=PHC0;
ph1=0;
%%%%Extracted variables

grpdelay=readBrukerParamFile([indir '\acqu']);
save('structureVarMatFile','-struct','grpdelay');
load('structureVarMatFile','GRPDLY');
grpdelay=GRPDLY;

% Apply FFT to the FID to obtain a (complex data points)
% spectrum distorted by the digital filter group delay.
% Plot the real and imaginary parts in separate stacked
% subfigures

fids=real_fid-1i*imag_fid;

fids=circshift(fids,-round(grpdelay));

%apply fourier transform with fftshift
```

```matlab
specs=(fftshift(fft(fids)));

% calculated for total number of data points
for i=1:4096
    %phase correction calculated in radians
    c(i)=(((i-1)).*ph1+ph0).*pi/180;
end

% Apply the 1st order phase correction to the distorted
% spectrum and save the corrected spectrum.

% R0(i) = R(i) cos(a(i))-I(i) sin(a(i))
% where real points R(i) and imaginary points I(i)

for i=1:4096
    X0(i) = real(specs(i)).*cos(c(i)) -
        imag(specs(i)).*sin(c(i));
end

% I0(i) = I(i) cos(a(i)) + R(i) sin(a(i))
for i=1:4096
    Y0(i) = imag(specs(i)).*cos(c(i)) +
        real(specs(i)).*sin(c(i));
end

phasedspec3=X0-1i*Y0;
phasedspec3=phasedspec3.*exp(1i*pi);
phasedspec3=flip(phasedspec3);

spec2fid=(ifft(phasedspec3));
% spec2fid= get(handles.pushbutton1, 'String');
% guidata(hObject, handles);

axes(handles.axes3);
plot real(phasedspec3));
title('phase corrected spectra');
% set(h,'toolbar','figure');
% set(h,'menubar','figure');

% --- Executes on button press in pushbutton2.
function pushbutton2_Callback(hObject, eventdata, handles)
% hObject    handle to pushbutton2 (see GCBO)
% eventdata  reserved - to be defined in a future
% version of MATLAB
% handles    structure with handles and user data (see GUIDATA)
indir=get(handles.input1,'String');
handles.indir=indir;
% fid_data=myfunc1(indir)

fid_data =fread(fopen([indir '/fid']),'int');

real_fid = fid_data(2:2:length(fid_data));
imag_fid = fid_data(1:2:length(fid_data));

% load phasecorrec values
phasec=readBrukerParamFile([indir '\pdata\1\procs']);
```

```matlab
save('structureVarMatFile','-struct','phasec');
load('structureVarMatFile','PHC0');
load('structureVarMatFile','PHC1');
ph0=PHC0;
ph1=0;
% Extracted variables

grpdelay=readBrukerParamFile([indir '\acqu']);
save('structureVarMatFile','-struct','grpdelay');
load('structureVarMatFile','GRPDLY');
grpdelay=GRPDLY;

% Apply FFT to the FID to obtain a (complex data points)
% spectrum distorted by the digital filter group delay.
% Plot the real and imaginary parts in separate stacked
% subfigures

fids=real_fid-1i*imag_fid;
fids=circshift(fids,-round(grpdelay));

% apply fourier transform with fftshift
specs=(fftshift(fft(fids)));

% calculated for total number of data points
for i=1:4096
    % phase correction calculated in radians
    c(i) = (((i-1)) .* ph1+ph0) .* pi/180;
end

% Apply the 1st order phase correction to the distorted
% spectrum and save the corrected spectrum.

% R0(i) = R(i) cos(a(i))-I(i) sin(a(i))
% where real points R(i) and imaginary points I(i)

for i=1:4096
    X0(i) = real(specs(i)).*cos(c(i)) -
        imag(specs(i)).*sin(c(i));
end

% I0(i) = I(i) cos(a(i)) + R(i) sin(a(i))
for i=1:4096
    Y0(i) = imag(specs(i)).*cos(c(i)) +
        real(specs(i)).*sin(c(i));
end

phasedspec3=X0-1i*Y0;
phasedspec3=phasedspec3.*exp(1i*pi);
phasedspec3=flip(phasedspec3);

spec2fid=(ifft(phasedspec3));

LB=str2num(get(handles.edit2,'String'));
handles.LB=LB;
sw=4006.41025641026;
```

```matlab
for i=1:4096
    b(i)= exp(-((i-1).*LB*pi)/(2*sw));
end

spec2fid2=spec2fid.*b;
specs_new=(fft(spec2fid2));
method_fid=fopen([indir '/method']);
line=fgets(method_fid);
index=findstr(line,'$PVM_DigSw=');
while isempty(index)
    line=fgets(method_fid);
    index=findstr(line,'$PVM_DigSw=');
end
equals_index=findstr(line,'=');
spectralwidth=line(equals_index+1:end);
spectralwidth=str2double(spectralwidth);
fclose(method_fid);

% get the transmitter frequency
acqp_fid=fopen([indir '/acqp']);;
line=fgets(acqp_fid);
index=findstr(line,'$BF1=')
while isempty(index)
    line=fgets(acqp_fid);
    index=findstr(line,'$BF1=');
end
equals_index=findstr(line,'=');
txfrq=line(equals_index+1:end);
txfrq=str2double(txfrq);
txfrq=txfrq*1e6;
fclose(acqp_fid);

% B0siz
Bo=txfrq/42577000;  %T

%Spectral width in PPM
spectralwidthppm=spectralwidth/(txfrq/1e6); % 13.3401ppm

%calculate the ppm scale
ppm=[4.65+(spectralwidthppm/2):-spectralwidthppm/
    (length(specs_new)-1):4.65-(spectralwidthppm/2)];

% creatine frequency correction
frqshift=(3.03-2.88)*(txfrq/1e6);
ppm2=ppm+(frqshift/(txfrq/1000000));

% NAA frequency correction
% frqshift=(2.0-1.886)*(txfrq/1e6);
% ppm2=ppm+(frqshift/(txfrq/1000000));

axes(handles.axes4);
plot(ppm2,real(specs_new));
set (gca, 'xdir' , 'reverse' )
title('Phased spectra after Line broadening');
xlabel('ppm');
ylabel('signal intensity');
```

```matlab
function edit1_Callback(hObject, eventdata, handles)
% hObject    handle to edit1 (see GCBO)
% eventdata  reserved - to be defined in a future version
%            of MATLAB
% handles    structure with handles and user data (see GUIDATA)
% Hints: get(hObject,'String') returns contents of edit1 as text
%        str2double(get(hObject,'String')) returns contents
%        of edit1 as a double

% --- Executes during object creation, after setting all
% properties.

function edit1_CreateFcn(hObject, eventdata, handles)
% hObject    handle to edit1 (see GCBO)
% eventdata  reserved - to be defined in a future version
%            of MATLAB
% handles    empty - handles not created until after
%            all CreateFcns called

% Hint: edit controls usually have a white background
% on Windows.
% See ISPC and COMPUTER.
if ispc && isequal(get(hObject,'BackgroundColor'),
        get(0,'defaultUicontrolBackgroundColor'))
    set(hObject,'BackgroundColor','white');
    set ( 0, 'DefaultFigureColor', [1 0 0] )
    set ( gcf, 'Color', [1 0 0] )
end

function edit2_Callback(hObject, eventdata, handles)
% hObject    handle to edit2 (see GCBO)
% eventdata  reserved - to be defined in a future version
%            of MATLAB
% handles    structure with handles and user data (see GUIDATA)

% Hints: get(hObject,'String') returns contents of edit2 as text
%        str2double(get(hObject,'String')) returns contents
%        of edit2 as a double
LB = get(handles.edit2,'String');
%set(handles.pushbutton3,'String', num2str(indir));
guidata(hObject, handles);
display(LB);

% --- Executes during object creation, after setting
%     all properties.
function edit2_CreateFcn(hObject, eventdata, handles)
% hObject    handle to edit2 (see GCBO)
% eventdata  reserved - to be defined in a future version
%            of MATLAB
% handles    empty - handles not created until after
%            all CreateFcns called

% Hint: edit controls usually have a white background
% on Windows.
% See ISPC and COMPUTER.
```

```matlab
if ispc && isequal(get(hObject,'BackgroundColor'),
        get(0,'defaultUicontrolBackgroundColor'))
    set(hObject,'BackgroundColor','white');
end

function input1_Callback(hObject, eventdata, handles)
% hObject    handle to input1 (see GCBO)
% eventdata  reserved - to be defined in a future version
% of MATLAB
% handles    structure with handles and user data (see GUIDATA)

% Hints: get(hObject,'String') returns contents of input1
% as text
% str2double(get(hObject,'String')) returns contents of input1
% as a double
indir = get(handles.input1,'String');
%set(handles.pushbutton3,'String', num2str(indir));
guidata(hObject, handles);
display(indir);

% --- Executes on button press in pushbutton3.
function pushbutton3_Callback(hObject, eventdata, handles)
% hObject    handle to pushbutton3 (see GCBO)
% eventdata  reserved - to be defined in a future version
% of MATLAB
% handles    structure with handles and user data (see GUIDATA)
indir=get(handles.input1,'String');
handles.indir=indir;

fid_data =fread(fopen([indir '/fid']),'int');
real_fid = fid_data(2:2:length(fid_data));
imag_fid = fid_data(1:2:length(fid_data));

fids=real_fid-1i*imag_fid;
fids=flip(fids);
specs=(fftshift(fft(fids)));
%apply fourier transform with fftshift
axes(handles.axes2);
plot(real(specs));
title('original real data');

%indir=str2double(get(hObject,'String'));
%fid_data=fread(fopen([indir '/fid']),'int');

% --- Executes during object creation, after setting
% all properties.
function input1_CreateFcn(hObject, eventdata, handles)
% hObject    handle to input1 (see GCBO)
% eventdata  reserved - to be defined in a future version
%            of MATLAB
% handles    empty - handles not created until after
%            all CreateFcns called

% Hint: edit controls usually have a white background
% on Windows.
% See ISPC and COMPUTER.
```

```matlab
if ispc && isequal(get(hObject,'BackgroundColor'),
        get(0,'defaultUicontrolBackgroundColor'))
    set(hObject,'BackgroundColor','white');
end

% --- Executes on button press in pushbutton3.
function pushbutton5_Callback(hObject, eventdata, handles)
% hObject    handle to pushbutton3 (see GCBO)
% eventdata  reserved - to be defined in a future version
% of MATLAB
% handles    structure with handles and user data (see GUIDATA)
% q = str2num(char(get(handles.input1,'String')));

indir=get(handles.input1,'String');
handles.indir=indir;
fid_data =fread(fopen([indir '/fid']),'int');

real_fid = fid_data(2:2:length(fid_data));
imag_fid = fid_data(1:2:length(fid_data));

phasec=readBrukerParamFile([indir '\pdata\1\procs']);  %load
phasecorrec values
save('structureVarMatFile','-struct','phasec');
load('structureVarMatFile','PHC0');
load('structureVarMatFile','PHC1');
ph0=PHC0;
ph1=0;
% Extracted variables

grpdelay=readBrukerParamFile([indir '\acqu']);
save('structureVarMatFile','-struct','grpdelay');
load('structureVarMatFile','GRPDLY');
grpdelay=GRPDLY;

% Apply FFT to the FID to obtain a (complex data points)
% spectrum distorted by the digital filter group delay.
% Plot the real and imaginary parts in separate stacked
% subfigures

fids=real_fid-1i*imag_fid;
fids=circshift(fids,-round(grpdelay));
% apply fourier transform with fftshift
specs=(fftshift(fft(fids)));

% calculated for total number of data points
for i=1:4096
    % phase correction calculated in radians
    c(i)=(((i-1)) .* ph1+ph0) .* pi/180;
end

% Apply the 1st order phase correction to the distorted
% spectrum and save the corrected spectrum.

% R0(i) = R(i) cos(a(i))-I(i) sin(a(i))
% where real points R(i) and imaginary points I(i)
```

```matlab
for i=1:4096
    X0(i) = real(specs(i)).*cos(c(i)) -
        imag(specs(i)).*sin(c(i));
end

% I0(i) = I(i) cos(a(i)) + R(i) sin(a(i))
for i=1:4096
    Y0(i) = imag(specs(i)).*cos(c(i)) +
        real(specs(i)).*sin(c(i));
end

phasedspec3=X0-1i*Y0;
phasedspec3=phasedspec3.*exp(1i*pi);
phasedspec3=flip(phasedspec3);

spec2fid=(ifft(phasedspec3));

LB=str2num(get(handles.edit2,'String'));
handles.LB=LB;
sw=4006.41025641026;

for i=1:4096
    b(i)= exp(-((i-1).*LB*pi)/(2*sw));
end

spec2fid2=spec2fid.*b;
specs_new=(fft(spec2fid2));

method_fid=fopen([indir '/method']);
line=fgets(method_fid);
index=findstr(line,'$PVM_DigSw=');
while isempty(index)
    line=fgets(method_fid);
    index=findstr(line,'$PVM_DigSw=');
end
equals_index=findstr(line,'=');
spectralwidth=line(equals_index+1:end);
spectralwidth=str2double(spectralwidth);
fclose(method_fid);

% get the transmitter frequency
acqp_fid=fopen([indir '/acqp']);;
line=fgets(acqp_fid);
index=findstr(line,'$BF1=')
while isempty(index)
    line=fgets(acqp_fid);
    index=findstr(line,'$BF1=');
end
equals_index=findstr(line,'=');
txfrq=line(equals_index+1:end);
txfrq=str2double(txfrq);
txfrq=txfrq*1e6;
fclose(acqp_fid);

%B0siz
```

```matlab
Bo=txfrq/42577000;  %T

%Spectral width in PPM
spectralwidthppm=spectralwidth/(txfrq/1e6); % 13.3401ppm

%calculate the ppm scale
ppm=[4.65+(spectralwidthppm/2):-spectralwidthppm /
    (length(specs_new)-1):4.65-(spectralwidthppm/2)];
%ppm= [4.65+3.9:-spectralwidthppm/(length(specs)-1):4.65-3.9];

% freq shift in Hz
% frqshift=(ppmmax-ppmrefval)*(txfrq/1e6);

% creatine frequency correction
frqshift=(2.01-1.87)*(txfrq/1e6);
ppm2=ppm+(frqshift/(txfrq/1000000));

% NAA frequency correction
% frqshift=(2.0-1.886)*(txfrq/1e6);
% ppm2=ppm+(frqshift/(txfrq/1000000));

Peakppmmin=str2num(get(handles.edit7,'String'));
handles.Peakppmmin=Peakppmmin;
Peakppmmax=str2num(get(handles.edit6,'String'));
handles.Peakppmmax=Peakppmmax;
noiseppmmin=-1;
noiseppmmax=0;
%input('Press Enter to continue');

NAAwindow=specs_new(ppm2>Peakppmmin & ppm2<Peakppmmax); % select
the peak in the given range
ppmwindow=ppm2(ppm2>Peakppmmin & ppm2<Peakppmmax);

axes(handles.axes5);
plot(ppmwindow,abs(NAAwindow));
set (gca, 'xdir' , 'reverse' )
ylim([-0.5*10^8,3*10^8]);
xlabel('ppm');
ylabel('signal intensity');
title('extracted peak region');

% select the noise in the given range
noisewindow=specs_new(ppm2>noiseppmmin & ppm2<noiseppmmax);
ppmwindow2=ppm2(ppm2>noiseppmmin & ppm2<noiseppmmax);

% subplot(1,2,2)
% axes(handles.axes5);
% plot(ppmwindow2,abs(noisewindow));
% set (gca, 'xdir' , 'reverse' )
% xlabel('ppm');
% ylabel('signal intensity');
% ylim([0,max(abs(NAAwindow))])
% title('extracted noise region')

% SNR calculation
maxpeak=max(abs(NAAwindow));
```

```matlab
maxpeak=max(abs(NAAwindow));
noisestd=std(noisewindow);
SNR=maxpeak/noisestd;
% noiserms=sqrt((1/numel(noisewindow)) *
%      sum((abs(noisewindow).^2)));
% SNR=maxpeak/(2*(noiserms));

set(handles.edit4, 'String', SNR);
guidata(hObject, handles);


% --- Executes on button press in pushbutton6.
function pushbutton6_Callback(hObject, eventdata, handles)
% hObject    handle to pushbutton6 (see GCBO)
% eventdata  reserved - to be defined in a future version
%            of MATLAB
% handles    structure with handles and user data (see GUIDATA)
indir=get(handles.input1,'String');
handles.indir=indir;
fid_data =fread(fopen([indir '/fid']),'int');

real_fid = fid_data(2:2:length(fid_data));
imag_fid = fid_data(1:2:length(fid_data));

phasec=readBrukerParamFile([indir '\pdata\1\procs']);  %load
phasecorrec values
save('structureVarMatFile','-struct','phasec');
load('structureVarMatFile','PHC0');
load('structureVarMatFile','PHC1');
ph0=PHC0;
ph1=0;
%%%%Extracted variables

grpdelay=readBrukerParamFile([indir '\acqu']);
save('structureVarMatFile','-struct','grpdelay');
load('structureVarMatFile','GRPDLY');
grpdelay=GRPDLY;

% Apply FFT to the FID to obtain a (complex data points)
% spectrum distorted by the digital filter group delay.
% Plot the real and imaginary parts in separate stacked
% subfigures

fids=real_fid-1i*imag_fid;
fids=circshift(fids,-round(grpdelay));

%apply fourier transform with fftshift
specs=(fftshift(fft(fids)));

% apply fourier transform with fftshift
for i=1:4096
    %phase correction calculated in radians
    c(i)=(((i-1)).*ph1+ph0).*pi/180;
end

% Apply the 1st order phase correction to the distorted
```

```matlab
% spectrum and save the corrected spectrum.

% R0(i) = R(i) cos(a(i))-I(i) sin(a(i))
% where real points R(i) and imaginary points I(i)

for i=1:4096
    X0(i) = real(specs(i)).*cos(c(i)) -
        imag(specs(i)).*sin(c(i));
end

% I0(i) = I(i) cos(a(i)) + R(i) sin(a(i))
for i=1:4096
    Y0(i) = imag(specs(i)).*cos(c(i)) +
        real(specs(i)).*sin(c(i));
end

phasedspec3=X0-1i*Y0;
phasedspec3=phasedspec3.*exp(1i*pi);
phasedspec3=flip(phasedspec3);

spec2fid=(ifft(phasedspec3));

LB=str2num(get(handles.edit2,'String'));
handles.LB=LB;
sw=4006.41025641026;
for i=1:4096
b(i)= exp(-((i-1).*LB*pi)/(2*sw));
end
spec2fid2=spec2fid.*b;
specs_new=(fft(spec2fid2));

method_fid=fopen([indir '/method']);
line=fgets(method_fid);
index=findstr(line,'$PVM_DigSw=');
while isempty(index)
    line=fgets(method_fid);
    index=findstr(line,'$PVM_DigSw=');
end
equals_index=findstr(line,'=');
spectralwidth=line(equals_index+1:end);
spectralwidth=str2double(spectralwidth);
fclose(method_fid);

% get the transmitter frequency
acqp_fid=fopen([indir '/acqp']);;
line=fgets(acqp_fid);
index=findstr(line,'$BF1=')
while isempty(index)
    line=fgets(acqp_fid);
    index=findstr(line,'$BF1=');
end
equals_index=findstr(line,'=');
txfrq=line(equals_index+1:end);
txfrq=str2double(txfrq);
txfrq=txfrq*1e6;
fclose(acqp_fid);
```

```matlab
%B0siz
Bo=txfrq/42577000;   %T

%Spectral width in PPM
spectralwidthppm=spectralwidth/(txfrq/1e6); % 13.3401ppm

% calculate the ppm scale
ppm=[4.65+(spectralwidthppm/2):-
spectralwidthppm/(length(specs_new)-1):4.65-
(spectralwidthppm/2)];
% ppm= [4.65+3.9:-spectralwidthppm/(length(specs)-1):4.65-3.9];
% creatine frequency correction
frqshift=(3.03-2.88)*(txfrq/1e6);
ppm2=ppm+(frqshift/(txfrq/1000000));

% NAA frequency correction
% frqshift=(2.0-1.886)*(txfrq/1e6);
% ppm2=ppm+(frqshift/(txfrq/1000000));

Peakppmmin=str2num(get(handles.edit7,'String'));
handles.Peakppmmin=Peakppmmin;
Peakppmmax=str2num(get(handles.edit6,'String'));
handles.Peakppmmax=Peakppmmax;
noiseppmmin=-1;
noiseppmmax=0;

Refwindow=specs_new(ppm2>Peakppmmin & ppm2<Peakppmmax);
ppmwindow=ppm2(ppm2>Peakppmmin & ppm2<Peakppmmax);

maxRef_index=find(abs(real(Refwindow))==max(abs(real((Refwindow)
))));
maxRef=real(Refwindow(maxRef_index));

% plot(ppmwindow,abs(real(Refwindow)),'.');
% set (gca, 'xdir' , 'reverse' );
gtHalfMax=find(abs(real(Refwindow)) >= 0.5*abs(maxRef));

FWHM1=ppmwindow(gtHalfMax(1)) - ppmwindow(gtHalfMax(end));
FWHM1=FWHM1*(42.577*Bo)  %Assumes proton.

sat='n'
waterFreq=ppmwindow(maxRef_index);
while sat=='n'
    parsGuess=zeros(1,5);
    parsGuess(1)=maxRef; % AMPLITUDE
    % FWHM.  Assumes Proton.  LW = 5/3 Hz/T.
    parsGuess(2)=(5*Bo/3)/(42.577*Bo);
    parsGuess(3)=waterFreq; % FREQUENCY
    parsGuess(4)=0; %Baseline Offset
    parsGuess(5)=0; %Phase

    yGuess=op_lorentz(parsGuess,ppmwindow);
    parsFit=nlinfit(ppmwindow,real(Refwindow),
        @op_lorentz,parsGuess);
    yFit=op_lorentz(parsFit,ppmwindow);
```

```matlab
    axes(handles.axes5);
    plot(ppmwindow,Refwindow,'.',ppmwindow,yGuess,
        ':',ppmwindow,yFit);
    legend('data','guess','fit');
    title('fitted peak');
    set (gca, 'xdir' , 'reverse' );
    xlabel('ppm');
    ylabel('signal intensity');
%
    sat=input('are you satisfied with fit? y/n ','s');
    if isempty(sat)
        sat='y';
    end
    if sat=='n';
        waterFreq=input('input new water frequency guess: ');
    end
end

FWHM2=abs(parsFit(2));
FWHM2=FWHM2*(42.577*Bo);   %Assumes Proton.

FWHM=mean([FWHM1 FWHM2])
set(handles.edit5, 'String', FWHM);
guidata(hObject, handles);

function edit4_Callback(hObject, eventdata, handles)
% hObject    handle to edit4 (see GCBO)
% eventdata  reserved - to be defined in a future version
%            of MATLAB
% handles    structure with handles and user data (see GUIDATA)

% Hints: get(hObject,'String') returns contents of edit4 as text
%        str2double(get(hObject,'String')) returns contents
%        of edit4 as a double
SNR = get(handles.pushbutton5,'Value');
set(handles.edit4,'String', num2str(SNR));
guidata(hObject, handles);

% --- Executes during object creation, after setting all
properties.
function edit4_CreateFcn(hObject, eventdata, handles)
% hObject    handle to edit4 (see GCBO)
% eventdata  reserved - to be defined in a future version
%            of MATLAB
% handles    empty - handles not created until after
%            all CreateFcns called

% Hint: edit controls usually have a white background
% on Windows.
% See ISPC and COMPUTER.
if ispc && isequal(get(hObject,'BackgroundColor'),
        get(0,'defaultUicontrolBackgroundColor'))
    set(hObject,'BackgroundColor','white');
end
```

```matlab
function edit5_Callback(hObject, eventdata, handles)
% hObject    handle to edit5 (see GCBO)
% eventdata  reserved - to be defined in a future version
%            of MATLAB
% handles    structure with handles and user data (see GUIDATA)

% Hints: get(hObject,'String') returns contents of edit5
% as text, str2double(get(hObject,'String')) returns contents
% of edit5 as a double

% --- Executes during object creation, after setting
% all properties.
function edit5_CreateFcn(hObject, eventdata, handles)
% hObject    handle to edit5 (see GCBO)
% eventdata  reserved - to be defined in a future version
%            of MATLAB
% handles    empty - handles not created until after
% all CreateFcns called

% Hint: edit controls usually have a white background
%       on Windows.
% See ISPC and COMPUTER.
if ispc && isequal(get(hObject,'BackgroundColor'),
        get(0,'defaultUicontrolBackgroundColor'))
   set(hObject,'BackgroundColor','white');
end

% --- Executes on slider movement.
function slider1_Callback(hObject, eventdata, handles)
% hObject    handle to slider1 (see GCBO)
% eventdata  reserved - to be defined in a future version
%            of MATLAB
% handles    structure with handles and user data (see GUIDATA)

% Hints: get(hObject,'Value') returns position of slider
%        get(hObject,'Min') and get(hObject,'Max') to
%        determine range of slider
sliderValue = get(handles.slider1,'Value');
set(handles.edit7,'String', num2str(sliderValue));
guidata(hObject, handles);

% --- Executes during object creation, after setting all
properties.
function slider1_CreateFcn(hObject, eventdata, handles)
% hObject    handle to slider1 (see GCBO)
% eventdata  reserved - to be defined in a future version
%            of MATLAB
% handles    empty - handles not created until after
%            all CreateFcns called

% Hint: slider controls usually have a light gray background.
if isequal(get(hObject,'BackgroundColor'),
        get(0,'defaultUicontrolBackgroundColor'))
   set(hObject,'BackgroundColor',[.9 .9 .9]);
end
```

```matlab
% --- Executes on slider movement.
function slider2_Callback(hObject, eventdata, handles)
% hObject    handle to slider2 (see GCBO)
% eventdata  reserved - to be defined in a future version
%            of MATLAB
% handles    structure with handles and user data (see GUIDATA)

% Hints: get(hObject,'Value') returns position of slider
%        get(hObject,'Min') and get(hObject,'Max') to
%        determine range of slider
sliderValue = get(handles.slider2,'Value');
set(handles.edit6,'String', num2str(sliderValue));
guidata(hObject, handles);

% --- Executes during object creation, after setting all
properties.
function slider2_CreateFcn(hObject, eventdata, handles)
% hObject    handle to slider2 (see GCBO)
% eventdata  reserved - to be defined in a future version
%            of MATLAB
% handles    empty - handles not created until after
%            all CreateFcns called

% Hint: slider controls usually have a light gray background.
if isequal(get(hObject,'BackgroundColor'),
get(0,'defaultUicontrolBackgroundColor'))
    set(hObject,'BackgroundColor',[.9 .9 .9]);
end


function edit6_Callback(hObject, eventdata, handles)
% hObject    handle to edit6 (see GCBO)
% eventdata  reserved - to be defined in a future version
%            of MATLAB
% handles    structure with handles and user data (see GUIDATA)

% Hints: get(hObject,'String') returns contents of edit6 as text
%        str2double(get(hObject,'String')) returns contents
%        of edit6 as a double
sliderValue = get(handles.edit6,'String');
% convert from string to number if possible, otherwise
% returns empty
sliderValue = str2num(sliderValue);
%if user inputs something is not a number, or if the input is
less than 0
%or greater than 100, then the slider value defaults to 0
if (isempty(sliderValue) || sliderValue < 920 ||
    sliderValue > 1000)
    set(handles.slider1,'Value',940);
    set(handles.edit6,'String','940');
else
    set(handles.slider2,'Value',sliderValue);
end
```

```matlab
% --- Executes during object creation, after setting all
properties.
function edit6_CreateFcn(hObject, eventdata, handles)
% hObject    handle to edit6 (see GCBO)
% eventdata  reserved - to be defined in a future version
%            of MATLAB
% handles    empty - handles not created until after
%            all CreateFcns called

% Hint: edit controls usually have a white background
%       on Windows.
% See ISPC and COMPUTER.
if ispc && isequal(get(hObject,'BackgroundColor'),
        get(0,'defaultUicontrolBackgroundColor'))
    set(hObject,'BackgroundColor','white');
end


function edit7_Callback(hObject, eventdata, handles)
% hObject    handle to edit7 (see GCBO)
% eventdata  reserved - to be defined in a future version
% of MATLAB
% handles    structure with handles and user data (see GUIDATA)

% Hints: get(hObject,'String') returns contents of edit7 as text
%        str2double(get(hObject,'String')) returns contents
%        of edit7 as a double
sliderValue = get(handles.edit7,'String');
% convert from string to number if possible, otherwise
% returns empty
sliderValue = str2num(sliderValue);
% if user inputs something is not a number, or if the input
% is less than 0 %or greater than 100, then the slider value
% defaults to 0
if (isempty(sliderValue) || sliderValue < 920 ||
    sliderValue > 1000)
    set(handles.slider1,'Value',940);
    set(handles.edit7,'String','940');
else
    set(handles.slider1,'Value',sliderValue);
end

% --- Executes during object creation, after setting
% all properties.
function edit7_CreateFcn(hObject, eventdata, handles)
% hObject    handle to edit7 (see GCBO)
% eventdata  reserved - to be defined in a future version
%            of MATLAB
% handles    empty - handles not created until after all
%            CreateFcns called

% Hint: edit controls usually have a white background
% on Windows.
% See ISPC and COMPUTER.
if ispc && isequal(get(hObject,'BackgroundColor'),
        get(0,'defaultUicontrolBackgroundColor'))
    set(hObject,'BackgroundColor','white');
```

```matlab
    end

% --- Executes on button press in pushbutton8.
function pushbutton8_Callback(hObject, eventdata, handles)
% hObject    handle to pushbutton8 (see GCBO)
% eventdata  reserved - to be defined in a future version
%            of MATLAB
% handles    structure with handles and user data (see GUIDATA)
indir=get(handles.input1,'String');
handles.indir=indir;
%fid_data=myfunc1(indir)

fid_data =fread(fopen([indir '/fid']),'int');

real_fid = fid_data(2:2:length(fid_data));
imag_fid = fid_data(1:2:length(fid_data));

% load phasecorrec values
phasec=readBrukerParamFile([indir '\pdata\1\procs']);
save('structureVarMatFile','-struct','phasec');
load('structureVarMatFile','PHC0');
load('structureVarMatFile','PHC1');
ph0=PHC0;
ph1=0;
% Extracted variables

grpdelay=readBrukerParamFile([indir '\acqu']);
save('structureVarMatFile','-struct','grpdelay');
load('structureVarMatFile','GRPDLY');
grpdelay=GRPDLY;

% Apply FFT to the FID to obtain a (complex data points)
% spectrum distorted by the digital filter group delay.
% Plot the real and imaginary parts in separate stacked
% subfigures

fids=real_fid-1i*imag_fid;
fids=circshift(fids,-round(grpdelay));

%apply fourier transform with fftshift
specs=(fftshift(fft(fids)));

% calculated for total number of data points
for i=1:4096
    % phase correction calculated in radians
    c(i)=(((i-1)).*ph1+ph0).*pi/180;
end

% Apply the 1st order phase correction to the distorted
% spectrum and save the corrected spectrum.

% R0(i) = R(i) cos(a(i))-I(i) sin(a(i))
% where real points R(i) and imaginary points I(i)

for i=1:4096
    X0(i) = real(specs(i)).*cos(c(i)) -
```

```matlab
            imag(specs(i)).*sin(c(i));
    end

    % I0(i) = I(i) cos(a(i)) + R(i) sin(a(i))
    for i=1:4096
        Y0(i) = imag(specs(i)).*cos(c(i)) +
            real(specs(i)).*sin(c(i));
    end

    phasedspec3=X0-1i*Y0;
    %phasedspec3=phasedspec3.*exp(1i*pi);
    phasedspec3=flip(phasedspec3);

    spec2fid=(ifft(phasedspec3));
    % spec2fid= get(handles.pushbutton1, 'String');
    % guidata(hObject, handles);

    axes(handles.axes3);
    plot(real(phasedspec3));
    title('phase corrected spectra');
    % set(h,'toolbar','figure');
    % set(h,'menubar','figure');
```

7. Code for manual single voxel phase correction using both ph0 and ph1 (efp_230214.m)

This script applies the stepwise single voxel phase correction as described in the PhD thesis.

```matlab
indir = 'C:\Users\1571788\Desktop\all scans\zoo220321b.d51\9';
%%% %%%read directory

fid_data = fread(fopen([indir '/fid']),'int');%%%%%%% raw data

%load phasecorrec values
phasec = readBrukerParamFile([indir '\pdata\1\procs']);
save('structureVarMatFile','-struct','phasec');
load('structureVarMatFile','PHC0');
load('structureVarMatFile','PHC1');
ph0 = PHC0;
ph1 = PHC1;

grpdelay=readBrukerParamFile([indir,'\acqus']);
save('structureVarMatFile','-struct','grpdelay');
load('structureVarMatFile','GRPDLY')
grpdelay = GRPDLY;

% FID from real and imaginary components of raw data
real_fid = fid_data(1:2:length(fid_data));
imag_fid = fid_data(2:2:length(fid_data));
fids = real_fid+1i*imag_fid;
n = size(fids);
figure;
plot(real(fids));
```

```matlab
title('raw data');

% GRPDELAY CORRECTION ON FID
fids1 = circshift(fids,-round(grpdelay));
%fids2=flip(fids2);
figure;
plot(real(fids1));
title('FID after group delay correction');

% EXPONENTIAL MULTIPLICATION AND LINE BROADENING ON FID
LB = 4;
sw = 4006.41025641026;

for I = 1:n
    b(i) = exp(-((i-1).*LB*pi)/(2*sw));
end

fid2 = fids1 .* b';
figure;
plot(real(fid2));
title('FID after exponential multiplication');

% PH0 and PH1 phase correction
for I = 1:n
    % calculated for total number of data points
    c(i) = (ph0+ph1.*(i-1)/n(1));

    % phase correction calculated in degrees
    % c(i) = (ph0+ph1.*(i-1)/n(1));%.*(180/pi);
end

for  = 1:n
    X0(i) = real(fid2(i)).*cos(c(i)) - 
        imag(fid2(i)).*sin(c(i));
end

% I0(i) = I(i) cos(a(i)) + R(i) sin(a(i))
for i=1:n
    Y0(i) = imag(fid2(i)).*cos(c(i)) + 
        real(fid2(i)).*sin(c(i));
end

phasedspec=X0+1i*Y0;
% phasedspec2=phasedspec.*exp(1i*pi);
% phasedspec3=flip(phasedspec);
figure;
% phased FLIPPED FID
plot(real(phasedspec));
title('phased FID');

% FOURIER TRANSFORMED PHASE CORRECTED SPECTRA
```

```matlab
phasedspec2 = flip(phasedspec);
% apply fourier transform with fftshift
spec1 = (fftshift(fft2(phasedspec2)));
% spec1 = flip(spec1);
figure;
plot(ppm_s1,real(spec1));
set (gca, 'xdir' , 'reverse' )
title('phased spectra');
xlabel('ppm');
ylabel('peak intensity')
xlim([0,5]);
```

8. Topspin imported single voxel post processing script

This script provides the alternate approach of importing TOPSPIN processed data into MATLAB for quantitative analysis.

```matlab
close all;
clear all;

% Read the 'acqu' file and extract the parameters DECIM,
% DSPFVS, and GRPDLY
% C:\Users\1571788\Desktop\all scans\zoo220321.d52\5
indir='C:\Users\1571788\Desktop\all scans\zoo220203.cl1\12'
% read directory
fid_data=fread(fopen([indir '/fid']),'int');

real_spec=fread(fopen([indir '\pdata\1\1r']),'int');
imag_spec=fread(fopen([indir '\pdata\1\1i']),'int');

spectra=real_spec+1i*imag_spec;

% ppm scale conversion is inserted here

% plotting phase corrected spectra
figure;

plot(ppm2,real(spectra),'LineWidth',1);
set (gca, 'xdir' , 'reverse' )
xlabel('ppm');
ylabel('signal intensity');
title('phase corrected spectra');
ylim([-1*10^8,5*10^8]);
xlim([0,5]);
set(gca,'FontSize',12);

% NAA frequency correction
```

```matlab
Peakppmmin=1.5;
Peakppmmax=2.2;
noiseppmmin=-1;
noiseppmmax=0;

% select the peak in the given range
NAAwindow=spectra(ppm2>Peakppmmin & ppm2<Peakppmmax);
ppmwindow=ppm2(ppm2>Peakppmmin & ppm2<Peakppmmax);

figure;

subplot(1,2,1)
plot(ppmwindow,NAAwindow);
set (gca, 'xdir' , 'reverse' )
xlabel('ppm');
ylabel('signal intensity');
title('extracted peak region');
ylim([-0.5*10^8,3*10^8]);

% select the noise in the given range
noisewindow=spectra(ppm2>noiseppmmin & ppm2<noiseppmmax);
ppmwindow2=ppm2(ppm2>noiseppmmin & ppm2<noiseppmmax);

subplot(1,2,2)
plot(ppmwindow2,noisewindow);
set (gca, 'xdir' , 'reverse' )
xlabel('ppm');
ylabel('signal intensity');
title('extracted noise region');
ylim([-0.5*10^8,3*10^8]);
%SNR calculation

maxpeak=max(abs(NAAwindow));
noisestd=std(noisewindow);

SNR=maxpeak/noisestd
```

APPENDIX C

semi-LASER pulse sequence codes for single voxel and multi-voxel

The code in the localization module needs to be modified to implement the changes in the delays, gradients and RF pulses. The sequence design is done in accordance with the minimum time requirements for a pulse and gradient turn on and off.

SV-semiLASER PULSE SEQUENCE CODE:

```
; Copyright (c) 2002-2003
; Bruker BioSpin MRI GmbH
; D-76275 Ettlingen, Germany
;
; All Rights Reserved
;
; semiLASER_v5.ppg - voxel selective spectroscopy  method
;
; code modified by Zoona Javed 2021-2023
; *********************************************************

#include <MRI.include>

#include <PrepModulesHead.mod>

define delay de4
"de4=0.00002s-de"

define delay d7m1_mod
"d7m1_mod=d7-1u"

define delay decodur
"decodur=0.00002s-de"

#include <decoacq.mod>
define loopcounter lds={$NDummyScans}
define loopcounter lnav

preset off

INIT_DEVICES

;-------D/P-----GRAD--------------------RF/ACQ------------

        1u        rpp1
```

```
          1u        rpp2
          1u        rpp3
          1u rpp31

start,    4u
av,  d1                        fq8b:f1
;---------Triggered data-------------------------------
#include <TriggerPerSlice.mod>

;---------noe  module----------------------------------
subr Noe()
;---------ws & ovs module------------------------------
subr WsOvs(ph0,ph0)

;---------localisation  module-------------------------

1u
      d4    grad{  (t1) | (0.0) | (0.0) } fq1:f1
      d6                              gatepulse 1
      (p1:sp1 ph1):f1
      d6
        "lnav=0"
      d7m1_mod  groff
nav, 0.5u
        0.5u
        if "lnav > 0"  {
       if(PVM_ppgFlag4 == Yes)
        {
         ;d4 grad{  (0.0) | (0.0) | (t1) }
      ;d6
      ;(p1:sp0 ph1):f1
      ;d6
      ;d7m1 groff
      }
      1u
      }
      d4      grad{ (Crusher_x) | (Crusher_y) | (Crusher_z)}
        d4 grad{ (0.0) | (t2) | (0.0) } fq1:f1
      d6                              gatepulse 1
      (p2:sp3 ph2):f1
      d6
      d4      grad{ (Crusher_x) | (Crusher_y) | (Crusher_z)}
      d4      groff
      d6
      d4      grad{ (Crusher_x) | (Crusher_y) | (Crusher_z)}
      d4      grad{ (0.0) | (t2) | (0.0) }
      d6                              gatepulse 1
      (p2:sp3 ph3):f1
      d6
      d4      grad{ (Crusher_x) | (Crusher_y) | (Crusher_z)}
      d4      groff
      d6
      d4      grad{ (Crusher_x) | (Crusher_y) | (Crusher_z)}
      d4    grad{ (0.0) | (0.0) | (t3) } fq1:f1
      d6                              gatepulse 1
      (p3:sp3 ph4):f1
```

```
    d6
    d4      grad{ (Crusher_x) | (Crusher_y) | (Crusher_z)}
    d7m1_mod   groff
    d8      grad { (tcomp) | (0.0) | (0.0)}
    d4      grad{ (Crusher_x) | (Crusher_y) | (Crusher_z)}
    d4      grad{ (0.0) | (0.0) | (t3)}
    d6                              gatepulse 1
    (p3:sp3 ph5):f1
    d6
    d4      grad{ (Crusher_x)| (Crusher_y) | (Crusher_z)}
    d4    groff
    d6
    d6
    d6


    ;pulse adjustments:
    if ( PVM_ppgFlag3 == Yes ) {
       d12     grad{ (t11) | (t12) | (t13) }
    d4   groff
    }

    ;d7m1 grad{ (0.0) | (0.0) | (t3) }    fq1:f1
    ;d6                              gatepulse 1
    ;(p3:sp2 ph4):f1
    ;d6 groff
    ;d8     grad{ (t11) | (t12) | (t13)}
    ;d7m1     grad{ (0.0) | (0.0) |  (t3) }
    ;d6
    ;(p3:sp2 ph5):f1
      ;d6     groff
    ;d8 grad{ (t) | (t9) | (t10)}
      ;d7m1 groff

;---------data acquisition-------------------------------
    ;pulse adjustments:
    if ( PVM_ppgFlag3 == Yes )
    {
      d4 grad{ (t14) | (t15) | (t16) }
      de4
                                ADC_INIT_B(ph31, ph0)
      aqq                       ADC_START
    }
    else
    {
subr decoup(decodur,ph31,ph0)
      }
      3m groff
    if(OPT_RFLOnOff == On)
      {
        1m reload B0
    }
    else
    {
       1m
    }
       "lnav = 1"
```

```
      1m                             ADC_END
;---------navigator loop ---------------------------------
      lo to nav times l1



;---------dummy scans ------------------------------------
      "lds = lds - 1"
      if "lds>=0" goto start

;---------averaging & phase cycling-----------------------
      if ( ACQ_scan_type == Scan_Experiment ) {
      1u                             ipp1
      1u                             ipp2
      1u                             ipp3
      1u                             ipp31
      }
      lo to start times NA
      1u                             rpp1
      1u                             rpp2
      1u                             rpp3
      1u                             rpp31

          lo to av times NR
      SETUP_GOTO(av)
exit


ph0 = 0
ph1= 0
ph2= 0
ph3= 0
ph4= 0
ph5= 0
ph31=0
```

MRSI-semiLASER CODE:

```
;*********************************************************
;
;
; pulseprogram for CSI
;
; written by Rolf Pohmann
;
; created on Aug 16, 2002
;
```

```
; Last modification: May 26, 2003

; code modified by Zoona Javed 28 September 2021
;
;************************************************************
;
; d0: TR padding
; d1: first half of echo time
; d3: last half of echo time
; d2: central part of echo time (PRESS only)
; d4: PVM_RiseTime
; d5: phase encoding time
; d8: gradient stabilisation delay  (new!)
; d20: spoiler duration
;
; t0: slice gradient (excitation pulse)
; t1: slice refocusing gradient (for 2D spin echo: also
;     contains second spoiler)
; t2, t3, t4: scaling for phase encode gradients, always 100
; t5: slice gradient (refocusing pulse)
; t6: slice gradient (third pulse, PRESS only)
; t7: spoiler strength (for spin echo)
; t8: spoiler strength
;
;
; PVM_ppgMode1 = 0: FID
;                1: spin echo
;                2: PRESS

#include <MRI.include>
preset off
define delay decodur
"decodur=  d3 - de"
define delay d7m1_mod
"d7m1_mod= d7 - 1u"
#include <PrepModulesHead.mod>
#include <decoacq.mod>



;definitions for the acquisition filter
;*****************************************************+*********
define list<power> ns_list = {$PVM_ppgDoubleArray1}
define loopcounter ns_loop

;definitions for the water suppression scheme
;*************************************************************
define delay NP4
define delay NP5
define delay NP6
define delay de4

INIT_DEVICES

;preparation of the gradient ramps
;*************************************************************
```

```
lgrad PVM_ppgGradAmpArray1 = ACQ_size[1]
zgrad PVM_ppgGradAmpArray1

if( ACQ_dim == 2)
{
  lgrad PVM_ppgGradAmpArray2 = ACQ_size[1]
  zgrad PVM_ppgGradAmpArray2
  lgrad PVM_ppgGradAmpArray3 = ACQ_size[1]
  zgrad PVM_ppgGradAmpArray3
}

if( ACQ_dim >= 3)
{
  lgrad PVM_ppgGradAmpArray2 = ACQ_size[2]
  zgrad PVM_ppgGradAmpArray2
}

if( ACQ_dim >= 4)
{
  lgrad PVM_ppgGradAmpArray3 = ACQ_size[3]
  zgrad PVM_ppgGradAmpArray3
}


lgrad slice = NSLICES
zslice

;**********************************************************
; dummy scans*********************************************
if (DS > 0)
{
dsstart, 5u
subr Noe()
subr WsSat(ph0)
      10u       fq1:f1
      d4        grad{(0)|(0)|(t0)}         ;slice gradient on
      d8 gatepulse 1
      p0:sp0  ph0                          ;excitation pulse
      d4  groff

      if (PVM_ppgMode1 == 1)               ;for spin echo only
      {
        d1      fq2:f1
      d20    grad{(0)|(0)|(t7)}            ;spoiler
      d4     grad{(0)|(0)|(t5)}   gatepulse 1   ;slice gradient
        d8      gatepulse 1
      p1:sp1 ph1                           ;refocusing pulse
        if ( ACQ_dim != 3 )                ;spoiler
        {                                  ;(For 2D the spoiler is
        d20     grad{(0)|(0)|(t8)}         ;contained in slice
refocus)
        }
      }
      if (PVM_ppgMode1 != 2)                       ;not for
PRESS
      {
```

```
        d5      grad{(0)|(0)|(t1)}                      ;slice
refocus gradient
        }


;****************************************************************
*********
        if (PVM_ppgMode1 == 2)                  ;semilaser
        {

        d7m1_mod   groff    fq2:f1
        d20      grad{(0)|(0)|(t8)+(t1)}
;spoiler
        d4      grad{(0)|(t5)|(0)}  fq1:f1         ;second slice
        d8      gatepulse 1
        p2:sp2  ph3
        d8
        d20      grad{(0)|(0)|(t8)}
        d4      groff
        d20      grad{(0)|(t8)|(0)}
        d4      grad{(0)|(t5)|(0)}
        d8    gatepulse 1
        p2:sp2  ph3
        d8
        d4      groff
        d20      grad{(0)|(t8)|(0)}
        d20      grad{(t8)|(0)|(0)}
        d4      grad{(t6)|(0)|(0)}  fq1:f1
        d8        gatepulse 1
        p2:sp2  ph4
        d8
        d20       grad{(t8)|(0)|(0)}
        d4        groff
        d7m1_mod
        d4
        d8
        d4
        d4
        d4
        d4
        d20    grad{(t8)|(0)|(0)}                       ;spoiler
        d4      grad{(t6)|(0)|(0)}
        d8    gatepulse 1
        p2:sp2  ph4
        d8
        d20    grad{(t8)|(0)|(0)}
        d4      groff


}
 ;**************************************************************

        d4      groff fq8b:f1
subr decoup(decodur,ph31,ph30)          ;acquisition
        d20      grad{(0)|(0)|(0)}       ; spoiler
        d4      groff
```

```
        10u     ADC_END
        islice                          ;next slice
        d0                              ;wait for repetition time
        5u
        lo to dsstart times NSLICES     ;slices loop
        zslice
        lo to dsstart times DS          ;dummy scans loop
}




;********************************************************
; end of dummy scans
;********************************************************


;********************************************************
; start of acquisition
;********************************************************

start, 3u
        2u

;---------evaluation of the current NS parameter----------------
--
        if ( ACQ_scan_type == Scan_Experiment )
        {
          ; perform scans if ns_list > 0
          if "ns_list == 0" goto noscan
          1u
          ; set ns_loop to ns_list[i]
          "ns_loop = ns_list"
        }
        if ( ACQ_scan_type == Setup_Experiment )
        {
          "ns_loop = 1"
        }

;---------ws & ovs module--------------------------------
subr Noe()
subr WsSat(ph0)
        10u      fq1:f1
        d4       grad{(0)|(0)|(t0)}     ; slice gradient on
        d8 gatepulse 1
        p0:sp0   ph0                    ; excitation pulse
        d4   groff
        if (PVM_ppgMode1 != 2)          ;not for semilaser
      {
        ;for scan experiment: with phase encoding
        if ( ACQ_scan_type != Setup_Experiment )
          {
            d5
grad{PVM_ppgGradAmpArray1(t2)|PVM_ppgGradAmpArray2(t3)|(t1)+PVM_
ppgGradAmpArray3(t4)}
          }
          ;for setup experiment: no phase encoding
```

233

```
      if ( ACQ_scan_type == Setup_Experiment )
      {
        d5      grad{(0)|(0)|(t1)}
      }
    }

    if (PVM_ppgMode1 == 1)          ;only for spin echo
    {
      d1                            ;echo time
  d20    grad{(0)|(0)|(t7)}       ;spoiler
  d4     grad{(0)|(0)|(t5)}        ;slice gradient
      d8      fq2:f1   gatepulse 1
  p1:sp1 ph1                       ;refocusing pulse
      d8
      if  ( ACQ_dim != 3 )
      {
      d20     grad{(0)|(0)|(t8)}    ;second spoiler
      }
    }
    if (PVM_ppgMode1 != 2)         ;not for PRESS
    {
      ;for scan experiment: with phase encoding
      if ( ACQ_scan_type != Setup_Experiment )
      {
        d5
grad{PVM_ppgGradAmpArray1(t2)|PVM_ppgGradAmpArray2(t3)|(t1)+PVM_
ppgGradAmpArray3(t4)}
      }
      ;for setup experiment: no phase encoding
      if ( ACQ_scan_type == Setup_Experiment )
      {
        d5      grad{(0)|(0)|(t1)}
      }
    }
    ;************************************************
    if (PVM_ppgMode1 == 2)                  ;semilaser

    {
     d7m1_mod   groff    fq2:f1
    d20      grad{(0)|(0)|(t8)+(t1)}        ;spoiler
    d4     grad{(0)|(t5)|(0)}  fq1:f1       ;second slice
    d8      gatepulse 1
    p2:sp2   ph3
    d8
    d20     grad{(0)|(0)|(t8)}
    d4      groff
    d20     grad{(0)|(t8)|(0)}
    d4      grad{(0)|(t5)|(0)}
    d8   gatepulse 1
    p2:sp2   ph3
    d8
    d4      groff
    d20     grad{(0)|(t8)|(0)}
    d20     grad{(t8)|(0)|(0)}
    d4      grad{(t6)|(0)|(0)}  fq1:f1
    d8       gatepulse 1
```

234

```
        p2:sp2  ph4
        d8
        d20      grad{(t8)|(0)|(0)}
        d4        groff
        d7m1_mod
        d4
        d8
        d4
        d4
        d4
        d4
        d20     grad{(t8)|(0)|(0)}                      ;spoiler
        d4      grad{(t6)|(0)|(0)}
        d8    gatepulse 1
        p2:sp2  ph4
        d8
        d20      grad{(t8)|(0)|(0)}
        d4  groff


;****************************************************

     if ( ACQ_scan_type != Setup_Experiment )
       {
            d5
grad{PVM_ppgGradAmpArray1(t2)|PVM_ppgGradAmpArray2(t3)|PVM_ppgGr
adAmpArray3(t4)}
         }
      if( ACQ_scan_type == Setup_Experiment )
         {
         d5
         }
       }

       d4       groff    fq8b:f1


           if (PVM_ppgMode1 == 0)      ;only for fid
       {
subr decoup(decodur,ph31,ph30)               ; acquisition
       }
      if (PVM_ppgMode1 >= 1)             ;only for spin echo
      {
subr decoup(decodur,ph31,ph30)               ;acquisition
      }
      d20      grad{(0)|(0)|(0)}        ; spoiler
      d4       groff
      10u      ADC_END
      islice
      d0                               ;repetition time
      lo to start times NSLICES
      zslice
      5u ipp0 ipp1 ipp3  ipp4         ;increase all phases
      lo to start times NA
      lo to start times ns_loop

;increment the current NS pointer
```

```
noscan, 5u   ns_list.inc
       5u rpp0  rpp1  rpp3  rpp4

; phase encoding loops
if( ACQ_dim >= 3 )
{
;------------------------------1d loop----------------
       igrad PVM_ppgGradAmpArray1
       lo to start times ACQ_size[1]
       zgrad PVM_ppgGradAmpArray1

;------------------------------2d loop----------------
       5u
       igrad PVM_ppgGradAmpArray2
       lo to start times ACQ_size[2]
       zgrad PVM_ppgGradAmpArray2
}
;------------------------------3d loop----------------
if( ACQ_dim >= 4 )
{
       igrad PVM_ppgGradAmpArray3
       lo to start times ACQ_size[3]
       zgrad PVM_ppgGradAmpArray3
}
if(ACQ_dim == 2)
{
       ;for dim == 2 (expMode = file) all gradients are
       ;set for all steps
       igrad PVM_ppgGradAmpArray1
       igrad PVM_ppgGradAmpArray2
       igrad PVM_ppgGradAmpArray3
       lo to start times ACQ_size[1]
       zgrad PVM_ppgGradAmpArray3
       zgrad PVM_ppgGradAmpArray2
       zgrad PVM_ppgGradAmpArray3
}

       5u
       lo to start times NAE
       5u
       lo to start times NR
       SETUP_GOTO(start)
       exit

ph0=0               ; phase pulse 1
ph1=1
ph3 = 1 ;           ;second pulse (PRESS)
ph4 = 1             ;third pulse (PRESS)
ph31= 0             ;receiver phase
ph30=0
```

Changes made to method files

SV-semiLASER pulse sequence

The PVM_ECHO TIME was defined for a single case by removing the 4 cases of Equalize, minTE, FixTE1 and FixTE2, and the default condition is:

TE2= tau3 + tau4 +tau5
PVM_ECHOTIME= MAX_OF(PVM_ECHOTIME, tau)
TE1= PVM_ECHOTIME - TE2

Where **PVM_ECHOTIME = minTE**

This rephasing compensation gradient was named **tcomp** and a routine was defined in the **parsrelations.c** file for the calculation of this gradient. Three variables **tcomp1, tcomp2** and **tcomp** were declared in the **parsdefinition.h** file as double parameters.

The definition for the variables was given in the **parsrelations.c** file where:

tcomp1 = ((VoxPulse1.length/2.0 + 0.1) * PVM_VoxArrGradient [0][0]
tcomp2 = (PVM_RiseTime* 0.5) * PVM_VoxArrGradient [0][0]
tcomp = (tcomp1 +tcomp2) / 1.23 * (1.0)

The **tcomp** variable was then passed as argument to the compensation gradient in the pulse program file (*.**ppg)** .

The **d7m1_mod** delay is defined in the *.**ppg** file as follows:

d7m1_mod= d7-1u

where **d7** is defined in the **BaselevelRelations.c** file as:

d7 = AddDelay[0] - PVM_RiseTime

and AddDelay[0] is equal to the minTE1 parameter:

AddDelay[0] = TE1/2.0

- VoxPulse2.Length/2.0

- SpoilerDuration[0][0]

- GradStabDelay

- GradStabDelay

- GradStabDelay

- 0.02

The GUI of paraVision was modified by changing the name of the method. The parclasses that were modified include:

Parclass {
}method name

where *method name* is the name of the implemented pulse sequence, and

Parclass{
      Method
      Method name
} Methodclass

where *Method* and *Methodclass* are keywords and *method name* is the name of the implemented pulse sequence.

Further, the dephasing part of the slice selection gradient (rephasing gradient) was calculated as follows :

Area of Rephasing gradient (A_r)

Gradient G1

A_r = ((half pulse length + GradStabDelay)
    * (0.5 * RampDownTime) * G_x
    = ((350 µs + 100 µs) +
        (0.5 * 267 µs)) * 17%
    = 9919.5
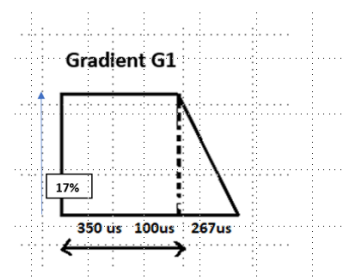
Amplitude of rephasing gradient (Amp_r)

$Amp_r = A_r$ / D8

    = 9919.5 / 1230 µs

    = 8.1%

MRSI-semi-LASER sequence

Echo time and delay calculation

T1(ms)		T2(ms)		T3(ms)		T4(ms)		T5(ms)	
p1/2	0.3	p2/2	1	p3/2	1	p4/2	1	p5/2	1
d4	0.267	d8	0.1	d8	0.1	d8	0.1	d8	0.1
d7m1_mod	0.266	d20	1.53	d20	1.53	d20	1.53	d20	1.53
d20	1.53	d4	0.267	d4	0.267	d7m1_mod	0.266	d5	0.733
d4	0.267	d20	1.53	d20	1.53	d4	0.267	d4	0.267
d8	0.1	d4	0.267	d4	0.267	d4	0.267	d4	0.267
p2/2	1	d8	0.1	d8	0.1	d8	0.1		
		p3/2	1	p4/2	1	d4	0.267		
						d4	0.267		
						d4	0.267		
						d20	1.53		
						d4	0.267		
						d8	0.1		
						d4	0.267		
						p5/2	1		
Tau1 (ms)	3.73	Tau2 (ms)	5.8	Tau3 (ms)	5.8	Tau4 (ms)	7.50	Tau5 (ms)	3.90

P1/2	0.3
pvm_rise time	0.267
CSI spoiler length	1.8
pvm_rise time	0.267
CSIgradstab delay	0.1
p2/2	1
p2/2	1
CSIgradstab delay	0.1
CSISPOILERLENGTH	1.8
CSISPOILERLENGTH	1.8
CSIgradstab delay	0.1
p3/2	1
minEchoTime 1 (ms)	9.534

p3/2	1
CSIgradstab delay	0.1
CSISPOILERLENGTH	1.8
CSISPOILERLENGTH	1.8
CSIgradstab delay	0.1
p4/2	1
p4/2	1
CSIgradstab delay	0.1
CSISPOILERLENGTH	1.8
CSISPOILERLENGTH	1.8
pvm_rise time	0.267
pvm_rise time	0.267
pvm_rise time	0.267
pvm_rise time	0.267
CSIgradstab delay	0.1
p5/2	1
p5/2	1
CSIgradstab delay	0.1
CSISPOILERLENGTH	1.8
csi phase grad	1
CSIgradstab delay	0.1
pvm_rise time	0.267
pvm_rise time	0.267
minEchoTime2 (ms)	17.202

Comparison between MRSI-semi-LASER and CSI-PRESS sequence parameters

The various acquisition parameters for the MRSI-semi-LASER and CSI-PRESS sequences are compared with the help of table. The gradients applied in three orthogonal planes are labelled G1, G2 and G3, corresponding to the axis Gx, Gy and Gz respectively. The excitation pulse for both sequences consists of 600 µs, 9000 Hz conventional Hermite shape. The refocusing pulses in the MRSI-semi-LASER sequence have a longer pulse length of 2000 µs and 9003Hz bandwidth adiabatic pulse. Whereas the CSI-PRESS sequence consists of 600 µs, 5700 Hz conventional Hermite refocusing pulses. The flip angles and voxel dimensions are kept the same. The adiabatic refocusing requires slightly larger gradient strengths in the *y* and *z* directions due to longer RF pulse lengths and bandwidth. Also, the pulse attenuation measured in decibels (dB) for the MRSI-semi-LASER sequence is slightly higher than the CSI-PRESS sequence but well within the acceptable limits (i.e. less than 6 dB).

MRSI-semi-LASER			
Gradients	G1	G2	G3
Axis	Gx	Gy	Gz
RF pulse length(µs)	600	2000	2000
Pulse type	conventional	adiabatic	adiabatic
Bandwidth (Hz)	9000	9003	9003
Flip angle (deg)	90°	180°	180°
Gradient amplitude (%)	58.0	5.0	5.0
Pulse attenuation (dB)	4.4	-1.5	-1.5
Voxel size/ geometry (mm)	6.6	6.6	1

CSI-PRESS			
Gradients	G1	G2	G3
Axis	Gx	Gy	Gz
RF pulse length(µs)	600	600	600
Pulse type	conventional	conventional	conventional
Bandwidth (Hz)	9000	5700	5700
Flip angle (deg)	90°	180°	180°
Gradient amplitude (%)	58.0	3	3
Pulse attenuation (dB)	4.4	-1.4	-1.4
Voxel size/ geometry (mm)	6.6	6.6	1

The area of the gradient can be calculated by finding the area under the curve, which is given by the following equation:

Area of Gradient =

$(\frac{1}{2} x \text{ rampUpTime x } G_x)$
$+ (D x G_x)$
$+ (\frac{1}{2} x \text{ rampDownTime x } G_x)$

Where:

D= (D6 + duration of pulse +D6)

G_x= Amplitude of the gradient

rampUpTime and *rampDownTime* are specific to the gradients. To calculate the rephasing part:

Amplitude of refocusing gradient = $\frac{Area\,of\,gradient}{duration}$

Refocusing gradient =

((Half of pulse length + GradStabDelay) +

(0.5 * rampDowntime)) / (Ts/2)

APPENDIX D

MRSI-semiLASER acquisition protocol
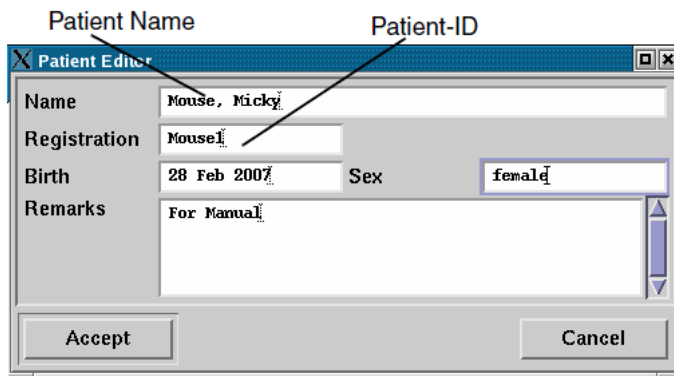
Click on ParaVision 5.1 icon on desktop. The ParaVision 5.1 interface runs on top of Topspin.

To create a new exam, go to New Patient. Create a new patient and study e.g.:

Name (Patient name): Zoona
Registration (Patient-ID): zoo221219

Registration (Patient-ID) format is: {initials}{year}{month}{day}

Create a new study by writing the name of study and folder in which to store the study, e.g.

Study : CSI.brain.SLvsP.w.day1
Location: S_zoona
Coils: Transceiver

To select a scan, click on new scan to select the required protocol to add to the scan Control window. The study protocol is loaded in the following order:

STUDY 1 : MRSI: (weighted mode)

The experiments required to run a complete MRSI acquisition are listed as follows:

1. 01-Tripilot-SMALLER FOV
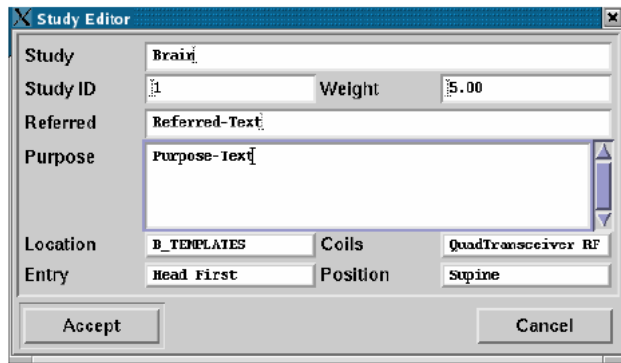2. 02_T2_Ref_RARE8_coronal
3. 03_T2_Ref_RARE8_saggital
4. 04_T2_Ref_RARE8_axial
5. 05_FastMap_4mm
6. 06_PRESS_waterline
7. 07_CSI_T2w_lowRes_ref
8. 08_CSI_T2w_HighRes_ref
9. 09_CSI_14ms_vox12x12_Pixelstandard550micras
10. 10_CSI-semilaser_V3

1.TRIPILOT

The tri-pilot will acquire three reference images going through the center of the gradients (iso-center).

To acquire a TriPilot Scan:

1. Go to folder: **S_zoona**. Load scan **01-Tripilot-SMALLER FOV** in the scan control window.
2. Correctly position the mouse, run **WOBBLE** (Tools (hammer drawing) -> Acq -> Wobble), and perform tuning. Move the lever on the left of CCO (cross-coil, acquire) to SCO (single coil, tune) . Move the rods: M (match, vertical) and T (tuning , horizontal) until reaching one or two points in the center. Then change it back to CCO.

3. Stop **WOBBLE** and acquire with traffic light . The iso-center (cross) should appear in the center of the region of interest. If the position of the iso-center is changed, re-tune probes with wobble and re-run adjustments using Shift + traffic light.

2. CORONAL, SAGGITAL and AXIAL anatomical reference images and voxel placement

The reference images are necessary for positioning of the volume of interest. The anatomical images are acquired in the axial, saggital and coronal orientations in scans 2-4.

Steps:

1. Load the scan low-resolution coronal **02_T2 _Ref_RARE8_coronal** taking the Tripilot as a reference. In the Geometry Editor, move the slices with M + mouse button with arrows and stripe to adjust the Position, Off-centre and Off-centre P1. Once the slices are fully adjusted, acquire with Traffic Light.
2. Load the scan low-resolution saggital **03_T2 _Ref_RARE8_saggital** taking the Tripilot and coronal as a reference. Repeat slice adjustment and acquire with Traffic Light.
3. Load the scan high-resolution axial **04_T2 _Ref_RARE8_axial** taking the coronal and saggital as a reference. Repeat slice adjustment and acquire with Traffic Light.

Once the anatomical references are acquired, the voxel positioning can be done in the CSI sequence.

4. Load scan 9) mark in Tools -> " Edit method " → "CSI inplane geometry " → "Geo editor shows" change " Voxel and position the voxel in the place of interest with the axial image (scan 4) as reference. The size of voxel is kept as Size : 6.6x6.6x1 (mm)^3 for the 12x12 matrix.
5. To put the voxel in the plane of interest, modify the value of " Isodist A" by eye until it is placed in plane. Check the voxel location with saggital and coronal (scan 3 and scan 2) references as well. If there is a continuous line in all 3 reference planes, the voxel is there, if it is discontinuous (dotted line), it is not there.
6. When the voxel is placed, round the values of " Isodist R" and " isodist H" to two decimal places to make them more comfortable for use and copy them.
7. With sequence 9 selected): Tools -> " Edit method " → "CSI inplane geometry " → "Geo editor shows" change " Voxel " to "Field of view " and check that the values of Isodist R (now off-centre read) , Isodist A and Isodist H (now off-centre P1) have not changed. (those of off-centre are in mm).
8. Once the voxel positioning is complete, check the geometry values are identical in both voxel and Field of View modes. Change the values if different and re-check with voxel mode.

3. Shimming with FASTMAP

The Fastmap is used to provide a homogeneous shimming over the voxel. The Fastmap is run with the help of the Bruker FASTMAP scout macro.

1. In scan 9, keeping the Tools -> " Edit method " → "CSI inplane geometry " → "Geo editor→ voxel , import the geometry of the CSI to set the Fastmap Geometry in scan 5.
2. Reduce the shim voxel size so that it covers the volume of interest i.e. (Cube size) is changed to 5.8 mm. This is the same for 10x10 grids than 12x12. Move it with Isodist so that it is not outside the brain with coronal and sagittal view, if it cannot be reduced cube size: 5.6 mm.
3. To acquire FastMap no traffic light.
4. Being in the FastMap sequence . Hat → Bruker → FastmapScout → play -> "adjust 1st and 2nd order". Do not touch anything until it ends.
5. The " estimated evolution time" (in the grey window) should be between 17-22 ms (it can vary from 3 to 40), but it can be seen below these values the process can be repeated several times (to repeat it close the window that comes out with arrows (inspector)) and if it does not work out, you can go back to the geometry and change the position voxel and try again to see if shimming is improved.

4. PRESS waterline

The PRESS waterline is acquired to measure the FWHM (peak width) of the water spectrum. The smaller the peakwidth, the better is the shimming and hence better CSI quality.

1. In scan 6) import the geometry of 9 while staying in voxel mode as in FASTMAP geometry. Go to Tools -> Acq and in current adjustments click on "Protocol ADJ_SHIM adjusting the Field Homogeneity " (Method . Basic Field Homogeneity) and then on "Protocol ADJ_SF adjusting the Basic Frequency" (Method specific Local Field Homogeneity). Then acquire with traffic light.
2. The acquired spectrum is exported to TopSpin : selecting the spectrum and export to Topspin. In the bar below: Bruker TopSpin -> Get water peakwidth. Width (Hz / ppm) : LB 0, ef , apk , peakw 0.5 and take the value of the width of the water peak.
3. The narrower the peak, the better. If the peakw 0.5 is below 20 Hz then okay otherwise, repeat the shimming and waterline acquisition.

5. Low and high resolution reference images

The low and High resolution images help as references for saturation band placement and CSI acquisition.

1. In scan 9, mark in Edit Method " Field of view " to be able to import the geometry to the images.
2. Go to 7) (CSI ref) and import the geometry of 9). Change Readout HF and check the H switches to R. Acquire the low resolution image (scan 7) with Traffic light.

3. Go to sequence 8) and import the geometry of 9) in the same Field of View mode. Also change the readout from LR to HF and acquire the high resolution image (scan 8) with Traffic Light.

6. Saturation bands placement and water suppression

Saturation bands are placed outside the CSI grid to eliminate unwanted signal entering the area of interest

1. To place the saturation bands in scan 9. Tools -> Edit methods -> CSI Inplane Geometry. Go to the geometry and reference the low resolution image (7).
2. The geometry editor and Parameter editor windows must stay open simultaneously.
3. In the " voxel " mode , expand (Z + left mouse button) until there is a row of frames on the outside (1 or 2, write down the ones on each side).
4. In the " field of view " mode, return to geometry and mark " saturation ". Adjust the B0 around the voxel (m + left mouse button), it can also be moved in Saturation slice.
5. In Field of View mode , with Saggital reference (Ref_sag_tRARE). Switch to voxel mode and give saturation. Adjust it by moving M + left button. Leave in " voxel " mode to acquire and with the high resolution reference image.
6. Adjust the water suppression pulses : Pulses. Tools -> Edit method -> Number of scans: 512 to 1. Number of dummy scans: 0. Receiver gain: 203. Lock -> TPQQ [4] and TPQQ [5]. Tx attenuat 4: 40 and Tx attenuat 5:30. Remove independent scale and there must be 10 units of difference between one and the other. GSP Window Setup scan: 4 at least. Tx attenuator 4: 40 1 down to 0.2 or 0.1. You go down with Tx attenuator 4 of 40, 38, 37 ... You stay right in the previous one in which water disappears. STOP
7. Back to change : Edit method. Number of scans: 512 and number of dummy scans: 4. Estimated scan time: 21min30s.

7. MRSI-semi-LASER sequence

1. In scan 10 copy the voxel geometry set in scan 9 to acquire the MRSI at the same position. Check with both voxel and Field of view modes the geometry coordinates are the same.
2. Place the low resolution image as reference to place saturation bands as described in section 6.
3. Acquire after water suppression with high resolution image as reference. If a new voxel position is required, repeat scan 5, 6, 7 and 8 with the new geometry copied.

8. Post-processing CSI

The CSI Dashboard Tool is started via the Macro Manager with the BRUKER macro CsiDash.tcl. In the Chemical Shift processing package, the TOPSPIN spectroscopic processing is used to

process the spectrum of each voxel of the CSI image. It is necessary to transfer the data from the ParaVision environment to the TOPSPIN environment. The whole CSI data set is transferred into the 2D TOPSPIN buffer file after reconstruction of the spatial directions. Each line of the 2D TOPSPIN ser file buffer corresponds to the raw data of the spectrum of a voxel of the CSI image. Each spectrum can be processed in the 1D TOPSPIN menu and replaced in the buffer. The buffer will be re-imported at the end into the ParaVision environment for display.

For these operations three EXPNOs are created:

- expno+e0, a copy of the original data,
- expno+e1, 2D TOPSPIN buffer for treatment,
- expno+e2, 1D TOPSPIN buffer for processing of each spectrum.

For the three new EXPNOs the next free numbers are chosen. In the simplest case these are the next subsequent numbers in the Scan Overview list. After processing, the data is re-imported into the expno+e0/procno2 in ParaVision environment. The values of e0, e1, e2 are saved in the ParaVision curdir directory of the user in the file csi_4e4_<name>_<expno>. After the acquisition, the CSI data are reconstructed as magnitude data. The Spatial Manipulation button opens a window in which the spatial sizes and the window filters for Reco are displayed.

STEPS:

1. The high resolution image with the voxel must be in the geometry of the acquired CSI. It is dragged to the image viewer with the middle mouse button. The image is zoomed until the edges of the voxel match the edges of the image.
2. Then in " Processing " select "CSI visualization ". The reference image is dragged (PV51_11_CSI_Ref) and the CSI data where it corresponds. Click on "pixel scan " and the cross is at the center of the image. When this is done right button and "ok" in the image viewer.
3. Then you go to Hat → Bruker → CSI.Dash.tcl → play. In the window that opens, click processing → Spatial manipulation → Apply. It becomes a mark processing → Manipulation for single voxel → get from CSI display → Baseline correction → Exponential multiplication Line broadening 4 → EXECUTE ft spectral.
4. Go to topspin and fasar → ok → (wait) apply to all. Go back to processing and check Update CSI display.
5. The process is then dragged into the "CSI visualization " slot and clicked on the " display matrix ".
6. To process another: Processing: Process new data.

For the post processing of MRSI-semi-LASER acquired dataset, the macro **csidash_v3_zoo** is selected from the Bruker methods folder. The post processing steps are identical to the csidash macro.

STUDY 2: MRSI (Multiple acquisition modes)

MRSI:

1. Tripilot
2. T2 Ref cor-tRARE
3. T2 Ref sag-tRARE
4. T2 Ref ax-tRARE (high res)
5. CSI fastmap (PV51_FastMap)
6. CSI_PRESS_WL (PV51_PRESS_waterline)
7. CSI ref (low resolution) (PV51_10_CSI_ref)
8. CSI REF (high resolution) (PV51_11_CSI)
9. CSI_14ms (ppcsi_14ms_OI_vpx12x12_pixelstandard550micras) standard
10. CSI_14ms (ppcsi_14ms_OI_vpx12x12_pixelstandard550micras) weighted
11. CSI_14ms (ppcsi_14ms_OI_vpx12x12_pixelstandard550micras) elliptical
12. CSI-semilaser_V3(standard)
13. CSI-semilaser_V3(weighted)
14. CSI-semilaser_V3(elliptical)

Note: The acquisition protocol is the same for a normal CSI acquisition. To acquire in multiple acquisition modes, the geometry is first set in scan 9 with the acquisition mode set as standard and the number of encoding steps = 8. After placement of saturation bands, the scan can be cloned to obtain 10 and 11. The acquisition modes and encoding steps are only changed according to the corresponding acquisition modes. The same steps are repeated from scan 12-14. The acquisition parameters should be in accordance with the tables.

CSI-PRESS	STANDARD	ELLIPTICAL	WEIGHTED
TE(ms)	14	14	14
TR(ms)	2500	2500	2500
Number of acquisitions	512	520	512
Number of encoding steps	8	13	12
Dummy scans (DS)	4	4	4
Slice dimensions	6mm x 6mm x 1mm	6mm x 6mm x 1mm	6mm x 6mm x 1mm
Acquisition time	21 min 30 s	21m 50s	21m 30 s
Spectral width	13.34	13.34	13.34
FOV(mm)	17.6	17.6	17.6
Resolution(mm)	2.2	2.2	2.2

MRSI-semi-LASER	STANDARD	ELLIPTICAL	WEIGHTED
TE(ms)	27	27	27
TR(ms)	2500	2500	2500
Number of acquisitions	512	520	512
Number of encoding steps	8	13	12
Dummy scans (DS)	4	4	4
Slice dimensions	6mm x 6mm x 1mm	6mm x 6mm x 1mm	6mm x 6mm x 1mm
Acquisition time	21 min 30 s	21m 50s	21m 30 s
Spectral width	13.34	13.34	13.34
FOV(mm)	17.6	17.6	17.6
Resolution(mm)	2.2	2.2	2.2